Cranfield University

Scott Harada

Issues related to the processing of ferroelectric nanostructures via ex situ and in situ methods

School of Applied Sciences

PhD

Cranfield University

School of Applied Sciences

Department of Materials

Microsystems and Nanotechnology Centre

PhD

2008

Scott Harada

Issues related to the processing of ferroelectric nanostructures via ex situ and in situ methods

Supervisor: Dr. Steve Dunn
8th January 2008

This thesis is submitted in partial fulfilment of the requirements for the Degree of PhD.

Abstract

This study investigates the impact of several processing parameters on the production of PZT and lead titanate nanostructures, by two different synthesis routes. The first aimed to produce freestanding, nanoscale PZT crystals via a simple, hydrothermal technique. Phase-pure, 52:48 PZT was synthesised within 2 hr at 160 °C in a hydrothermal autoclave. The morphology of the resultant crystals was cubic and micron-sized. Efforts were thus directed at reducing crystal size, by altering several processing conditions. Reaction time and temperature were found to have little effect on crystal size and instead resulted in incomplete reaction below the threshold values shown above. Introducing a 100% excess of Pb precursor led to an improvement in the faceting of the crystals, but again did not lead to a change in average crystal size. However, by using a 2% solution of the surfactant Triton-X, the average crystal size fell from 5 μm to 2 μm.

The use of anatase TiO_2 in the general hydrothermal procedure imposed a lower limit on the mineraliser concentration that was necessary for dissolution to occur. To overcome this restriction, a hybrid sol-gel/hydrothermal technique was attempted. This had the unexpected result of producing pyramidal microfibres that tapered to nano-sized points.

Since the attempts to synthesise freestanding, nanoscale PZT crystals using the hydrothermal method were unsuccessful, work focussed on growing nanoislands on single crystal (100)- $SrTiO_3$ substrates. Heteroepitaxial PZT films up to 1 μm thick, as well as micro- and nanoislands were observed, after extended 24 hr reactions at 160 °C. In some cases, the islands appeared to nucleate along scratches in the $SrTiO_3$ substrate, leading to the formation of microwires up to a millimetre in length. Ferroelectric analysis of the microwires by PFM revealed them to be weakly piezoelectric.

The second synthesis route to nanoscale ferroelectrics relied upon the solid phase reaction between Pb and Ti thin films to produce lead titanate. The optimum condition for the crystallisation of the perovskite phase was found to be 1 hr at 650

°C, under an air atmosphere. However, examination of the film morphology revealed large distortions and blistering across the surface. As such, it was not possible to acquire polarisation loop measurements, due to shorting between the top and bottom electrodes. EDAX confirmed that PbO vapour from the film was diffusing into the Si substrate leading to the formation of voids and the production of lead silicate glasses.

Alternative adhesion layers for the Pt back electrodes were investigated, in an attempt to limit the diffusion of PbO. Electrical measurements on the films were made possible by substituting Zr for Ti. However, the shape of the hysteresis loops corresponded to a lossy dielectric as opposed to a ferroelectric response from the film.

Films annealed on alternative substrates also suffered from blistering, but without the intrusion of PbO. This result suggested that the distortion present in the films was not as a consequence of the interaction between volatile species and the substrate. Instead, blistering and delamination was attributed to stresses generated during the transformation into the $PbTiO_3$ perovskite phase.

The solid phase synthesis method was extended to produce $PbTiO_3$ nanoislands by utilising flash thermal evaporations. Deposition times below 1 s resulted in Pb nanoislands with a size range of 5 – 30 nm. Annealing the nanoislands under the same regime as used during the thin film experiments led to the loss of their morphology through melting. To overcome this problem an extended low temperature annealing was adopted.

PFM was conducted on various nanoisland and thin film samples produced by the in situ technique. Nanoisland samples subjected to prolonged conventional annealings at 300 °C and brief hot plate annealings at 550 °C exhibited a non-zero piezoresponse. Definitive evidence of ferroelectricity in the nanoisland samples could not be demonstrated, however, as attempts to pole them were unsuccessful.

$PbTiO_3$ thin films produced by annealing Pb/Ti bilayers displayed clear *c*+ and *c*- ferroelectric domains that were mostly pinned by the grain boundaries. Little evidence of self-polarisation was found, since the average piezoresponse across the image was

close to zero. Localised poling resulted in piezoresponse images showing the presence of intermediate contrast. This was interpreted as partial, 90 ° switching or evidence for “tail-to-tail” domain structure formation.

Acknowledgements

I wish to thank all of my colleagues at the Microsystems and Nanotechnology Centre, for helping to foster a pleasant and supportive work environment. I am particularly indebted to my supervisor Dr. Steve Dunn, who offered excellent support and guidance throughout my time at Cranfield. His enthusiasm and optimistic outlook were a source of great inspiration to me, especially during the difficult writing-up period.

I was fortunate enough to meet many kind and generous people at Cranfield and I wish to thank the following, in no particular order, for their valued friendship: Dr. Diego Gallardo, Mr. Paul Jones, Dr. Chris Shaw, Dr. Florent Dauchy, Dr. Glenn Leighton, Mr. Sameer Bargir and Mr. Garfay Liu. Many on that list also went out of their way in providing technical assistance and I am particularly appreciative of Mr. Paul Jones for his AFM/PFM expertise and Drs. Chris Shaw and Glenn Leighton for their help in resolving issues related to sputter deposition and thermal evaporation. Chris deserves further mention for his inimitable ability to spot questionable double entendre in the most innocuous of phrases and statements!

I wish to express my gratitude to the technicians and support staff within the department and school, including Mr Andy Stallard at the Microsystems and Nanotechnology Centre and Mr Andrew Dyer and Dr Matt Kershaw in the Centre for Water Science. Thanks are also due to Mrs Enza Giaracuni for her tireless efforts as our department secretary.

Last and by no means least, I must thank my parents for their unwavering support and affection over the years, without which none of this would have been possible.

TABLE OF CONTENTS

List of Figures

List of Tables

Introduction

In recent years the field of nanotechnology has received widespread attention from the scientific community, as well as the general public, for its great potential impact on future society.[1- 5] At the heart of this exciting discipline is the ability to manipulate matter at the nanoscale. Many physical properties associated with a material in bulk form are subject to dramatic change as dimensions are reduced. These so-called size effects often arise as a result of the quantum nature of matter that dominates the character of materials, at or below the nanoscale. One such phenomenon, directly attributable to a quantum size effect, is the tunable photoluminescence from semiconductor nanoparticles.[6] By altering the radius of CdSe nanoparticles in the range 0.7 – 5 nm, for example, it is possible to induce light emission across most of the visible spectrum.[7] Another interesting size effect is the quantum conductance exhibited by metallic nanowires[8] and carbon nanotubes[9]. This behaviour is likely to have important implications for the design of molecular electronic circuits. However, if these unusual and often beneficial properties are to be exploited and commercialised in future technologies, there must be a concerted effort towards developing new, innovative materials processing techniques.

This thesis focuses on the synthesis and characterisation of lead titanate and lead zirconate titanate (PZT) ferroelectric nanostructures. Ferroelectric materials are used in a wide variety of important applications due to their unique combination of physical properties. The defining characteristic of a ferroelectric material is the possession of a permanent dipole moment that can be switched by applying an external electric field. This property has been exploited, with some success, in the production of non-volatile ferroelectric memories (FeRAM). Conceptually, the binary logic states "1" and "0" are assigned arbitrarily to the two polarisation states of a ferroelectric element. The advantages of FeRAM in comparison to competing non-volatile memory technologies include: lower power requirements, faster read/write speeds and greater endurance (number of write/erase cycles before failure).[10] Up to the present date the market for FeRAM has remained small, due in large part to the success of its major rival, Flash memory. To fulfil its potential and remain competitive, the lengthscale at which FeRAM is currently fabricated must be reduced.

This will bring with it interesting technological challenges requiring solutions, as it is not yet clear whether such small memory elements can remain stable.

The ferroelectric material studied in this thesis, PZT, has found use in FeRAM, but is perhaps most commonly encountered in electroceramic form. Being a ferroelectric it is also piezoelectric, meaning it develops an electric potential upon the application of mechanical stress. applied to will induce a voltage between its two faces. and has been It has several advantages is one of the most popular ferroelectric materials for several reasons. Firstly, it is a very low cost material that is comparatively easy to synthesise with properties that remain stable after manufacture. from a chemical point of view its constituent elements are abundant and easy to handle, making perhaps the most

If we are to exploit and harness these unusual properties in future technologies considerable effort must be invested in developing the relevant materials processing techniques. In particular the so called bottom-up method of generating nanoscale m

The wavelength of light emitted by the nanoparticles depends on the diameter By adjusting the diameter tunable emission of superparamagnetism, whereby a normally ferromagnetic material displays paramagnetic behaviour on lengthscales of several nm. This is a challenge faced by the hard drive industry as they strive to increase data storage density. usually have an unimportant influence can dominate the character of certain materials at the nanoscale. These so-called size effects have important implications for the development of new technologies as well as for fundamental research. One of the most familiar The goal of this thesis is to investigate two promising synthesise routes for producing ferroelectric nanostructures. branch of applied science control , both due to its the potential promise The ability to produce materials at the nanoscale is at the heart of the emerging field of Nanotechnology study of material properties at the nanoscale is of interest from both a fundamental and technological point of view. By controlling the size of

This thesis is presented in six chapters. Chapter one begins with an introduction to ferroelectric materials with a particular focus on the perovskite solid solution, lead zirconate titantate (PZT). The existing literature related to the ex situ and in situ synthesis of ferroelectric nanostructures is then reviewed. A critical appraisal of the

various strengths and weaknesses associated with each method is given. An analysis section follows, which discusses one of the most important techniques currently in use to investigate ferroelectricity at the nanoscale: namely, piezoresponse force microscopy. Finally, chapter one ends with a review of the size effects specifically related to ferroelectric materials together with the aim and objectives of this study.

Chapter two, entitled *Methodology*, describes the experimental details of the ex situ hydrothermal method and the in situ solid phase synthesis technique. The various forms of analysis applied throughout the study are then discussed.

The findings of this thesis are presented in chapters three, four and five. Chapter three describes the attempts at synthesising PZT nanostructures using a one-stage hydrothermal technique. Several modifications are made in order to better understand the reaction mechanisms and to reduce the size of particles produced. to use the hydrothermal method for producing PZT nanostructures. report the findings of this study related to the hydrothermal method, the solid phase technique and ferroelectric analysis of nanostructures, respectively.

References

[1] P. Ball, *Nature*, 408, 904 (2000)
[2] M. Helmer M, *Nature*, 408, 531 (2000)
[3] P. Vettiger, G. Cross, M. Despont et al. *IEEE Trans. Nanotechnol.* 1, 1, 39 (2002)
[4] W. S. Bainbridge, *J. Nanopart. Res.* 4, 6, 561 (2002)
[5] S. C. Currall, E. B. King, N. Lane et al. *Nat. Nanotechnol.* 1, 153 (2006)
[6] C. Bertoni, D. Gallardo, Steve Dunn et al. *Appl. Phys. Lett.* 90, 034107 (2007)
[7] C. B. Murray, D. J. Norris and M. G. Bawendi, *J. Am. Chem. Soc.* 115, 8706 (1993)
[8] S. Csonka, A. Halbritter, G. Mihály et al. *Phys. Rev. Lett.* 90, 11, 116803 (2003)
[9] S. Frank, P. Poncharal, Z. L. Wang, and W. A. de Heer *Science*, 280, 1744 (1998)
[10] H. Takasu, *J. Electroceram.* 4, 327 (2000)

Chapter 1: Literature Review and Objectives

1.1 Perovskite Ferroelectrics

1.1.1 History

A material is termed ferroelectric when it has two or more orientational states in the absence of an electric field and can be switched between these states by an electric field.[1] The history of ferroelectrics begins with the water-soluble crystal sodium potassium tartrate tetrahydrate, or Rochelle Salt. This mineral was first identified by the apothecary Elie Seignette in 1655 and used for over 200 years as a mild purgative. The detailed investigation of its physical properties took place during the 19th century, beginning with the work by Brewster who observed the pyroelectric effect in various crystals, including Rochelle salt, in 1824. Pyroelectricity is the ability of certain materials to generate an electric potential when they are heated or cooled. The related phenomenon of piezoelectricity, in which a material exposed to mechanical stress generates an electrical polarisation, was discovered by Pierre and Paul-Jacques Curie in 1880. Of the several crystals tested by the brothers, Rochelle Salt and quartz exhibited the largest piezoelectric response. One of the first studies to identify an anomalous dielectric response from Rochelle Salt was conducted by Pockels in the closing years of the 19th century. However, it was not until 1920 that Valesek discovered that the polarisation direction of Rochelle Salt could be switched by applying an electric field. His later work showed that there was a hysteresis effect in the field-polarisation curve of the crystal. This led to the establishment of the term ferroelectricity by analogy to ferromagnetism.[2]

Arguably, the most important development in ferroelectrics came about with the discovery of the ferroelectric phase in barium titanate.[3] Up until this point, it was thought that hydrogen bonds were a crucial requirement for the onset of ferroelectric behaviour. The slow progress in developing a theoretical background for ferroelectricity came about as a direct result of the structural complexity of the ferroelectrics discovered prior to barium titanate. Researchers now had a comparatively simple unit cell to study that consisted of just five atoms arranged in the perovskite structure (Fig. 1.1). Furthermore, barium titanate proved a very facile

material to work with since it exhibited a ferroelectric response at room temperature, was chemically and mechanically stable and could be prepared as a ceramic.[1] These factors combined to make barium titanate the most studied ferroelectric material and led to the discovery of several other perovskite-based ferroelectrics, including potassium niobate and lead titanate.[2]

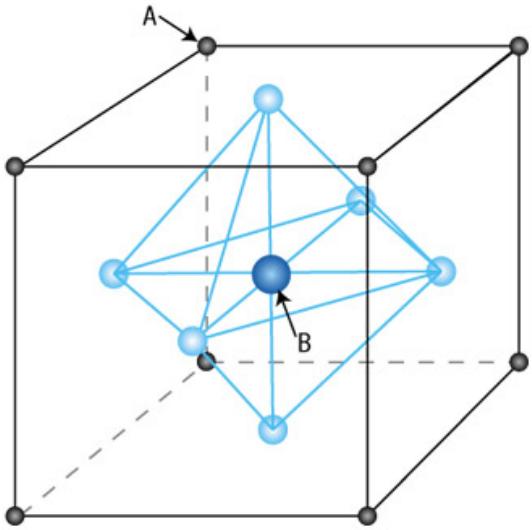

Fig. 1.1 The perfect perovskite structure named after the mineral $CaTiO_3$. The general formula for the structure is ABO_3, where A is a monovalent or divalent metal and B a tetra- or pentavalent one.[4]

1.1.2 Lead zirconate titanate

Lead zirconate titanate (PZT) is a perovskite ferroelectric solid solution formed from lead titanate and lead zirconate. Its structure is composed of one Ti^{4+} or Zr^{4+} ion on the B-cation site, six O^{2-} ions at the face centres of the cube and a Pb^{2+} ion at each A site. However, the picture is more complicated than it first appears since the B-cations are not centralised within their oxygen octahedra and the Pb^{2+} and O^{2-} ions are similarly displaced from their perfect perovskite positions. It is this local disorder, within the framework of the ordered perovskite lattice, that lends PZT its interesting properties.[5]

PZT is one of the most commonly used electroceramics due to its very large piezoelectric coupling constants (ratios that describe how efficiently a piezoelectric material converts mechanical energy into electrical energy or vice-versa). Table 1.1 compares the properties of PZT with several other ferroelectric perovskites.

Table 1.1 Properties of several perovskite ferroelectrics.

Formula	Spontaneous Polarisation (P_s) /μCcm^{-2} (T /°C)	Curie Point (T_c) /°C	Coupling constant (k_{33})
$PbZr_{0.52}Ti_{0.48}O_3$	31 (23)	386	0.67
$PbTiO_3$	>50 (23)	490	0.07
$BaTiO_3$	26.0 (23)	135	0.32
$KNbO_3$	30.0 (250)	435	0.16

The crystal structure of PZT depends on the Zr/Ti ratio. Fig. 1.2 shows the phase diagram for the PZT system. Above a certain temperature, known as the Curie point, a material loses its ferroelectric characteristics and becomes paraelectric. The electric dipoles within the material lose their order and the internal field becomes weak. In the case of PZT, the paraelectric phase is cubic. As temperatures are reduced below the Curie point, the structure transforms into a rhombohedral or tetragonal phase, depending on composition. This phase change results in a displacive transition whereby the Pb^{2+} and Zr^{4+}/Ti^{4+} ions are displaced relative to the O^{2-} ions. The unit cell thus acquires a dipole moment and an associated spontaneous polarisation.

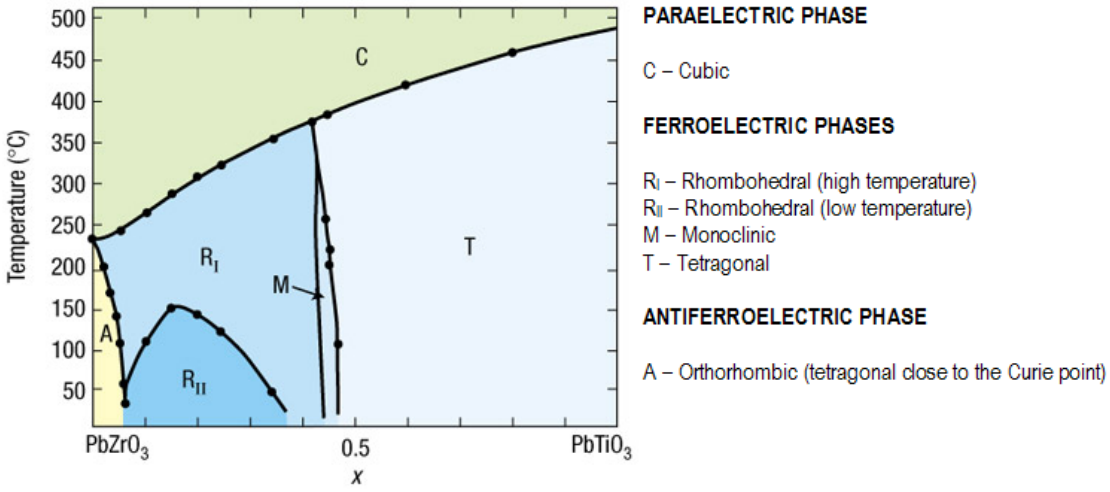

Fig. 1.2 Phase diagram for the $Pb(Zr_{1-x}Ti_x)O_3$ (PZT) solid solution.[4]

Recently Noheda et al. discovered the existence of a monoclinic phase at the morphotropic phase boundary (MPB) between the rhombohedral and tetragonal phases.[6] A highly homogenous sample of $PbZr_{0.52}Ti_{0.48}O_3$ was cooled from 736 K

down to 20 K while simultaneously taking high-resolution x-ray powder diffraction measurements. Upon cooling, the cubic to tetragonal phase transition was reached at ~660 K and the structure remained tetragonal down to 300 K. Further decreases in temperature see the formation of a structure that is not compatible with either a rhombohedral phase or a mixture of rhombohedral and tetragonal phases but rather that of a monoclinic phase. The monoclinic structure can be constructed by shifts of the Pb and Zr/Ti cations along a tetragonal [110] direction; hence, the monoclinic phase serves to connect the tetragonal and rhombohedral phases (Fig. 1.3). Glazer and Thomas suggest that all three ferroelectric phases can be considered monoclinic at the local level, provided one considers the structures on a suitably small length scale.[7] Under these conditions, the idea of discrete phase boundaries spanning the MPB can be dispensed with.

PZT compositions close to the MPB are known to give the largest piezoresponse and this is thought to be due to the unit cell elongating in the directions associated with the monoclinic distortion.[8]

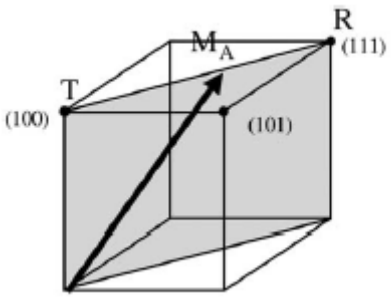

Fig. 1.3 Representation of a perovskite unit cell with the polarisation vector in the monoclinic phase (M_A) rotating between the rhombohedral (R) and tetragonal (T) phases in the (1 $\bar{1}$ 0) plane (shaded).[9]

At the lead zirconate end of the PZT phase diagram there exists an orthorhombic antiferroelectric phase. The structure of an antiferroelectric crystal can be thought of as two sublattices polarised spontaneously in antiparallel directions and in which a ferroelectric phase can be induced by applying an electric field. This distinction can most clearly be visualised by contrasting the single hysteresis loop, characteristic of polarisation reversal in ferroelectrics, with the double hysteresis loop associated with the induced phase transition of an antiferroelectric (Fig. 1.4).[10]

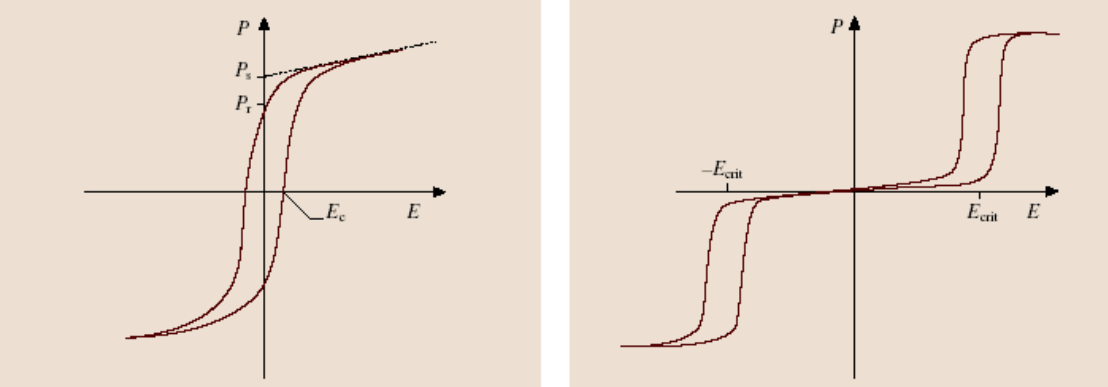

Fig. 1.4 Hysteresis behaviour associated with ferroelectric (left) and antiferroelectric (right) sample response.[10]

Hysteresis in ferroelectric materials arises from the energy required to reverse the dipoles during each sweep of the electric field.[11] An ordinary dielectric material does not show significant hysteresis when an electric field is slowly increased and then reversed.[12] Therefore, the acquisition of a hysteresis loop is a key test for ferroelectricity. The area of the loop represents energy that is dissipated as heat within the sample.[11] Three important parameters, which help to characterise the behaviour of ferroelectric materials, are shown in Fig. 1.4. The spontaneous polarisation, P_s, is obtained by extrapolating the saturation polarisation back to zero along a tangent.[11] The remnant polarisation, P_r is defined as the value of the polarisation that remains after the applied electric field has been removed. Finally, the coercive field, E_c, is the electric field strength necessary to reduce the polarisation to zero.

1.1.3 Ferroelectric domains

Ferroelectric domains are regions within a crystal that share the same polarisation orientation. Adjacent domains are oriented in different directions. Domain structure originates as a way of reducing the free energy in the system.[12] To understand why, consider a spherical, perfect, insulating ferroelectric crystal in vacuum that has a uniform spontaneous polarisation throughout. Charges will be induced on its surface thus leading to a depolarising electric field whose energy is proportional to the volume of the crystal and the square of the polarisation. The magnitude of this depolarising field is such that the uniform spontaneous polarisation originally envisaged becomes unsustainable.[13] Consequently, the crystal is subdivided into domains having antiparallel directions of spontaneous polarisation, a state that is

energetically favourable since it reduces the depolarising field. This process of subdivision is halted when the energy stored in the walls, between domains, balances the decrease in energy of the depolarising field. The result is a stable domain configuration for a given temperature.[13]

In practice, the domain configuration in real ferroelectric crystals is rarely stable at any temperature. Real crystals are never perfectly insulating so the charges induced by spontaneous polarisation are partially compensated by bulk and surface conductivity. Furthermore, imperfections within the crystal lattice disturb the uniformity of the polarisation and hence the depolarising field. Lastly, most crystals are subject to a non-uniform strain because of the processing conditions during their growth. Therefore, the domain configuration of a real crystal is a balance between the energetic requirements of an ideal crystal and the perturbing effects of conductivity, strain and imperfections in the lattice. The latter effects evolve slowly with time leading to a metastable domain configuration. This phenomenon is known as ageing.[13]

It is interesting to consider the effect of particle size on domain formation and the appearance of ferroelectricity. As mentioned previously, domains form to minimise the depolarising field within a crystal. However, domain wall energy is a surface energy and as the surface to volume ratio is large for small particles, this term becomes important. Therefore, below a critical size, it becomes energetically more favourable for a crystal to dispense with domain walls and switch to a single domain configuration. When this happens, the depolarising field will annihilate the polarisation and the crystal will no longer be ferroelectric.[13] In 2003, Junquera and Ghosez calculated from first principles the critical thickness for ferroelectricity in $BaTiO_3$ thin films.[14] Their simulated system consisted of an ultrathin $BaTiO_3$ film between two $SrRuO_3$ electrodes epitaxially grown on a thick $SrTiO_3$ substrate. This was a new approach since preceding first principles studies[15, 16] had neglected the influence of the metal-perovskite interface on polarisation and atomic relaxation – an essential part of any ferroelectric device. Below a critical thickness of 26 Å, approximately six unit cells, the ferroelectric properties disappeared and the energy was minimised for the paraelectric configuration. The authors demonstrated that the depolarising field due to dipoles at the ferroelectric-metal interface was the main

reason for the disappearance of the ferroelectric instability and that the interface chemistry, in this case, played a minor role. A more thorough discussion of the sources and types of size effects that exist in ferroelectric materials is given in *Section 1.4.2*.

The polarisation directions of domains are the high temperature symmetry axes (<001> and <111> for tetragonal and rhombohedral structures, respectively). The angles between the polarisation directions in adjacent domains are hence the same as those between the symmetry axes (90º and 71º), with a slight modification to account for the ferroelectric distortion.[13] Fig. 1.5 shows the possible domain arrangement in a pseudo-cubic (001) plate of tetragonal $PbTiO_3$. Domains with polarisations oriented perpendicular to the plane of the plate are termed *c*-domains, whilst those oriented in-plane are called *a*-domains. In Fig. 1.5 each domain is separated by a 90º wall since neighbouring domains are polarised perpendicularly however, anti-parallel domains, separated by 180º walls, can also form in $PbTiO_3$ and the other tetragonal perovskite ferroelectrics. As the tetragonality of $PbTiO_3$ at room temperature is approximately 6%, the angle between polar axes of adjacent 90º domains is altered by: $2\tan^{-1}(c/a) - 90º \approx 3.6º$ (Fig. 1.6).[13] Domain wall motion alters the total domain volume and therefore leads to a change in the total polarisation within a ferroelectric material.

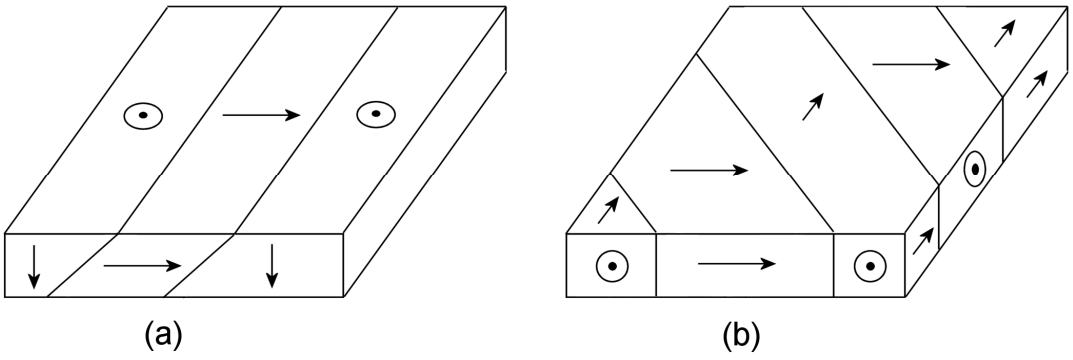

Fig. 1.5 Domain arrangements in a (001) plate of tetragonal $PbTiO_3$. Arrows represent the direction of the polar axis. The plate surface shows: (a) *a*-domain between two *c*-domains, (b) *a*-domains only.[13]

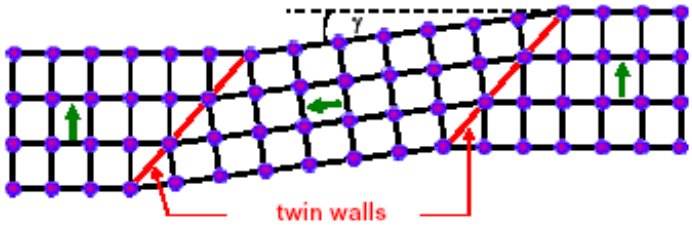

Fig. 1.6 A typical *c*/*a*/*c* domain arrangement in tetragonal $PbTiO_3$. The inclination angle γ between adjacent domains is due to the tetragonal distortion. Twinning is a crystallographic term that refers to the intergrowth of two crystals that share the same structure.

When a crystal is cooled from a paraelectric to a ferroelectric phase, in the absence of an electric field, the depolarising fields are usually of sufficient magnitude to prevent a net polarisation in the crystal. The process of poling is used to remove the domain configuration that would otherwise form in the ferroelectric state. This is achieved by applying a DC E-field along one of the polar crystallographic axes as the crystal is cooled through the Curie point. The single-domain state is then thermodynamically stable in an unstressed crystal because the depolarisation fields are neutralised by charge flow in the external circuit.[1]

1.1.4 Piezoelectricity

Piezoelectricity originates from the non-centrosymmetric (not having a centre of symmetry) nature of certain crystal structures. Of the 32 crystal classes, or point groups, 21 are non-centrosymmetric, and of these, 20 are piezoelectric. The one exception is the cubic class 432, which, although lacking a centre of symmetry, has other symmetrical elements that rule out piezoelectric activity.[13] Of the 20 piezoelectric classes, 10 possess a unique polar axis, or dipole moment, and exhibit pyroelectricity. If this dipole can be reversed, the material is ferroelectric. All crystals in a ferroelectric state are piezoelectric, but the inverse is not always true. Examples of crystals that exhibit a piezoelectric response but lack a ferroelectric one include quartz and gallium orthophosphate.

When a stress T is applied to ordinary solids a proportional strain is S induced, related by an elastic modulus, $T = YS$. The *direct* piezoelectric effect is the additional generation of electric charge by the application of stress. Since the charge is

proportional to the force, its sign is opposite for compression and tension. An equation can be generated for the direct piezoelectric effect in terms of the dielectric displacement D and stress T:

$$D = Q/A = dT \qquad \text{Eqn. 1.1}$$

There is also a *converse* or *indirect* piezoelectric effect in which an applied field E produces a strain S leading to an expansion or contraction, depending on polarity:

$$S = dE \qquad \text{Eqn. 1.2}$$

The proportionality constant is the piezoelectric constant d and is numerically identical in both cases, however it is expressed in coulombs/Newton for the direct case and metres/Volt in the converse case. Other piezoelectric constants include g that relates the field produced for a given stress and e, which relates the stress induced by a given field.

The piezoelectric equations of state are obtained by combining the electrical properties of a material (field, displacement and polarisation) with its elastic properties (stress and strain), in a variety of ways. The form linking strain and charge is shown below:

$$\{S\} = \left[s^E\right]\{T\} + [d_t]\{E\}$$
$$\{D\} = [d]\{T\} + \left[\varepsilon^T\right]\{E\} \qquad \text{Eqn. 1.3 \& 1.4}$$

where s is the elastic compliance, superscript E refers to a constant or zero E-field, subscript t the transposition of a matrix, ε is the permittivity and superscript T refers to a constant or zero stress field. It is necessary to describe the piezoelectric equations of state using tensorial notation since the elastic, dielectric and piezoelectric constants of single crystals and ceramics are axis dependant.

The internal dipole moment of a pyroelectric crystal at rest is compensated by surface charges on the crystal faces. If a stress is applied parallel to the dipole direction, the

strength of the dipole is altered which leads to the appearance of surface charges on the ends of the crystal. In non-pyroelectric piezoelectric crystals, dipolar arrangements can still exist but, in the unstressed state, they are arranged in several compensating directions. As a result, the crystal exhibits no overall dipole moment at rest, but when a stress is applied along one of the polar axes, the dipoles oriented in this direction are compressed at the expense of the rest and a charge is created.[12]

1.1.5 Electroceramics

Ferroelectric ceramics consist of many spontaneously polarised crystallites or grains packed together in a random way. A ferroelectric ceramic must first be poled before it can exhibit piezoelectric properties since the polar axes of the individual grains are randomly oriented with respect to each other. Practically, this is achieved in a similar way to poling a ferroelectric single crystal. An E-field of greater magnitude than the coercive field is applied to the ceramic, which leads to the reorientation of the domains within each grain into a polarisation direction closest to that of the applied field (Fig. 1.7). The ceramic is often heated to a temperature close to the Curie point during poling since the coercive field decreases with temperature. After poling, the ceramic behaves like a pyroelectric single crystal, and will respond linearly to an applied E-field or mechanical pressure, as long as the field or pressure is well below that needed to switch the polar axis. Because the crystallites in the ceramic were oriented at random prior to poling, alignment of the polar axes to the same degree as in a single crystal cannot be achieved. The imperfect nature of ceramic materials leads to strains within grains that prevent switching. Likewise, intergranular stresses tend to fix the polarity of the domains in their initial orientation.[11]

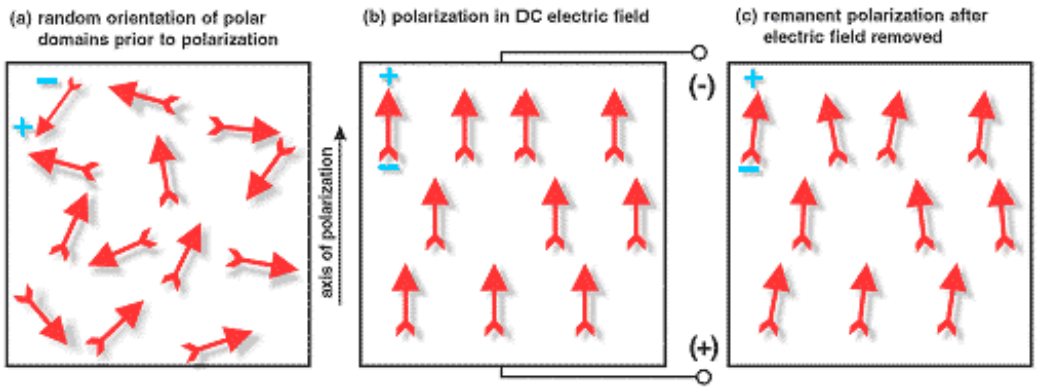

Fig. 1.7 Domain orientation within an piezoelectric ceramic: (a) before, (b) during and (c) after applying a DC field.

In the unpoled state, a piezoelectric ceramic is isotropic in all directions. After poling, this isotropy is destroyed in the direction of the poling field but remains in the plane at right angles to it. The symmetry of a poled ceramic, expressed using Hermann-Mauguin notation, is ∞mm, or cylindrical polar.[11] When describing the piezoelectric constants a 6-fold symmetry axis is equivalent to the infinite-fold axis. Hence, the piezoelectric constant d_{ij} matrix for a piezoelectric ceramic is given by:

$$\begin{pmatrix} 0 & 0 & 0 & 0 & d_{15} & 0 \\ 0 & 0 & 0 & d_{15} & 0 & 0 \\ d_{31} & d_{31} & d_{33} & 0 & 0 & 0 \end{pmatrix}$$

The first subscript of each element refers to the field or displacement direction while the second gives the component of mechanical deformation or stress. Subscripts ranging from 1 to 3 represent a set of orthogonal axes with 3 usually reserved as the poling axis. Shear stresses and strains around axes 1, 2 and 3 are denoted by subscripts ranging from 4 to 6, respectively. Since only three of the elements within the d_{ij} matrix are unique, this implies the existence of just three mechanical modes. Fig. 1.8 illustrates these three modes. Application of an E-field in the same direction as the polarisation results in a longitudinal extension, this is termed the longitudinal or d_{33} mode. Simultaneously, under the same field and polarisation conditions, a transverse contraction occurs which is labelled the transverse or d_{31} mode. Finally, when an E-field is applied in direction 1 across a sample polarised in direction 3 a shear strain is induced around axis 2. This is termed the shear or d_{15} mode.

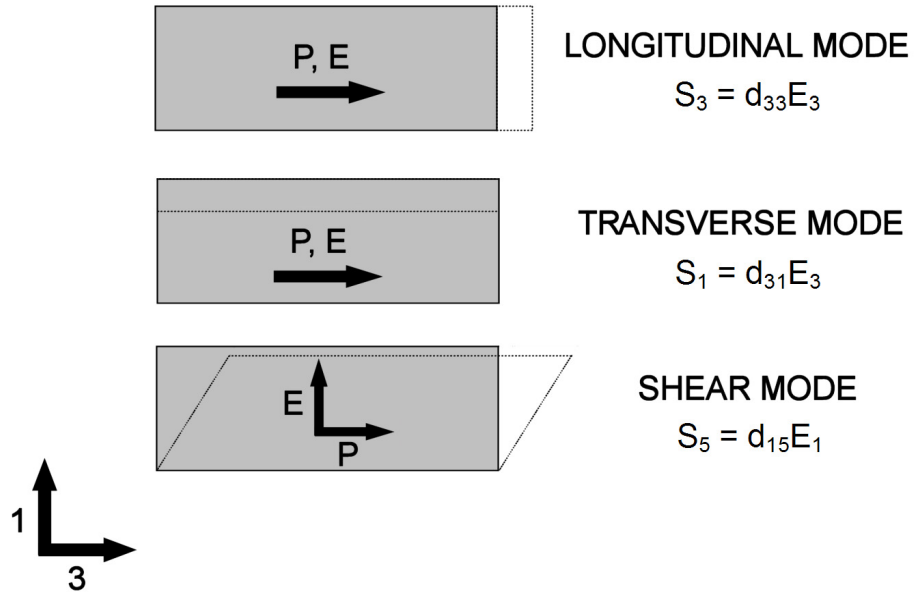

Fig. 1.8 The three mechanical modes associated with the piezoelectric constant d_{ij}.

As mentioned previously, the alignment of the crystallites within a poled ceramic can never be as perfect as in a single crystal. However, the measured piezoelectric constants of many materials are greater in ceramic as opposed to single crystal form. This is due to extrinsic contributions to the piezoresponse from domain wall vibrations. An analysis by Luchaninov et al. found such contributions were responsible for between 60-70% of the measured piezoresponse in ceramic $BaTiO_3$ samples.[17] A value of similar magnitude was estimated for ceramic PZT, by the same authors, that included a contribution from interphase boundary motion.[18]

1.2 Ex situ synthesis of P(Z)T

Ex situ synthesis, in the context of this investigation, is defined as the nucleation and/or growth of free-standing perovskite P(Z)T particles. In this section, the literature associated with the ex situ method of choice for the project, namely hydrothermal synthesis, will be discussed and critically assessed. Comparisons with competing techniques will also be made. Towards the end of the section, the hydrothermal synthesis of perovskite thin films and nanostructures will be discussed.

This area shares common elements with in situ processing (see *Section 1.3*), however, as it is still a form of hydrothermal synthesis, it has been included in this section instead.

1.2.1 Hydrothermal Synthesis

1.2.1.1 Introduction

The term hydrothermal originates from the science of geology and refers to the action of superheated water on the Earth's crust, leading to the production of various rocks and minerals. The accepted definition for the laboratory hydrothermal technique is "any heterogenous chemical reaction in the presence of a solvent (whether aqueous or nonaqueous) above room temperature and at pressure greater than 1 atm in a closed system".[19] Its history can be traced back to the steam digester invented by Denis Papin in the late 17th century. This device was primarily used to soften bones and was the forerunner to the modern pressure cooker.[20] The first artificial hydrothermal synthesis took place in 1845 when Schafthaul used a Papin digester to transform freshly precipitated silicic acid into quartz crystals.[19] Important industrial applications followed later including the hydrothermal treatment of bauxite in the production of aluminium[21] and the hydrothermal synthesis of zeolites for molecular sieving applications.[22]

Nowadays, one of the most active areas of hydrothermal research is in advanced materials processing. The latest technologies that exploit quantum effects impose tight restrictions on the morphology and size of their active components. Hydrothermal synthesis has been used to make InP[23], CaF_2 [24] and LaF_3 [25] light-emitting nanocrystals. Fig. 1.9, showing LaF_3 nanocrystals that have self-assembled into a 2D array, bears testament to the level of control over morphology and size distribution afforded by the hydrothermal technique.

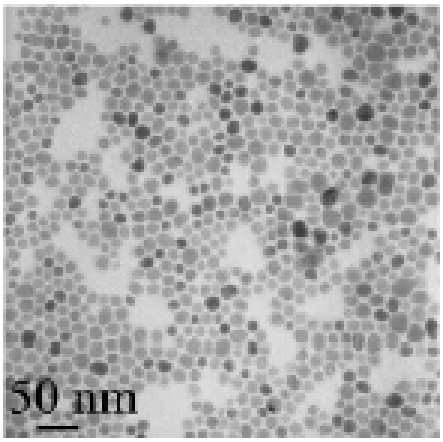

Fig. 1.9 A TEM image of hydrothermally synthesised LaF_3 nanocrystals.[25]

1.2.1.2 Comparison of hydrothermal synthesis with competing techniques

Several features of the hydrothermal technique make it ideal for the production of ferroelectric crystals. Perhaps foremost amongst these is the comparatively low processing temperatures (< 250 °C) required to achieve phase purity. When ferroelectric crystals are produced via the conventional mixed oxide method they must undergo a calcination step to remove impurities and initiate the necessary thermochemical reactions. Temperatures in the region of 1200 °C are not uncommon.[26] Alternative wet chemical techniques for the synthesis of ferroelectrics, such as sol-gel[27] and coprecipitation[28], also require relatively high calcination temperatures (between 500 – 900 °C). These high temperatures can lead to the formation of O^{2-} vacancies within the lattice of the ferroelectric because of the volatility of PbO. When making thin films or bulk ceramic ferroelectrics the PbO-loss can be compensated for by maintaining a partial pressure of the oxide in the atmosphere. This is usually achieved by annealing some $PbZrO_3$ pellets alongside the sample in the furnace.[11] Alternatively, a Pb-excess can be introduced at the precursor stage, if a wet chemical technique is used.[29] Although these solutions help to alleviate the degradation of macroscale ferroelectric properties, when analysing the behaviour of individual micro and nanoscale single crystals, PbO-loss can still be a problem.

Table 1.2 lists several other parameters associated with powder processing and makes a comparison between the competing techniques. As can be seen, hydrothermal synthesis compares favourably in nearly all areas. In fact, the only major disadvantage

to the hydrothermal technique is the inability to follow a reaction in situ due to the hostile conditions present within an autoclave. Attempts to use autoclaves with pressure-resistant ruby windows were met with limited success.[19] This situation has helped to drive the remarkable progress made by physical chemists in modelling hydrothermal reactions and studying their kinetics. As such, reaction parameters can now be optimised through a precise knowledge of hydrothermal chemistry.

Table 1.2 Comparison of several competing techniques used for the production of advanced oxide powders[30]

	Conventional	Sol-gel	Coprecip-itation	Hydrothermal
Cost	**Low-moderate**	**High**	**Moderate**	**Moderate**
State of development	Commercial	R & D	Commercial/ demonstration	Demonstration
Compositional control	Poor	Excellent	Good	Good-excellent
Morphology control	**Poor**	**Moderate**	**Moderate**	**Good**
Powder reactivity	Poor	Good	Good	Good
Purity (%)	< 99.5	> 99.9	> 99.5	> 99.5
Calcination step	Yes	Yes	Yes	No
Milling step	**Yes**	**Yes**	**Yes**	**No**

1.2.1.3 Hydrothermal synthesis of perovskite ferroelectrics

The hydrothermal method has been used to synthesis perovskite ferroelectric crystals since the 1970s.[31, 32] However, serious efforts to utilise the technique did not start until the mid-1980s and continue up to the present day. Kutty and Balachandran

synthesized PZT across the entire compositional range of Zr and Ti ratios using a precursor mixture that consisted of PbO and a $TiO_2 \cdot ZrO_2$-nH_2O gel dispersed in distilled water.[33] The authors found that the temperature required for complete phase formation was proportional to the Zr:Ti ratio of the product. Complete formation of perovskite lead titanate and lead zirconate took place within 6-8 hr at 160 °C and 340 °C, respectively. The resultant PZT crystals, with compositions around the MPB, had an acicular morphology and were micron-sized. Larger, more cube-like particles were produced by introducing a 20% PbO-excess.

Beal produced PZT solid solutions at 300 °C with the aid of alkali hydroxide and halide mineralisers.[34] The effects of pH and mineraliser type on particle morphology and phase purity were studied. Mineralisers that contained Na^+, Li^+ and F^- ions led to impurities being retained within the product. Fluorides were also found to increase particle size. In related work, Lee et al. managed to reduce the synthesis temperature of MPB PZT to 100 °C by employing a high concentration (10 M) of the mineraliser KOH.[35] However, a considerable 25% PbO-excess was necessary to obtain stoichiometric PZT. Developing these ideas further, Ohba et al. investigated the effects of precursor and KOH mineraliser concentration on PZT particle morphology and size.[36] The solubility of each of the precursors (titania gel, zirconia gels and lead oxide) and PZT was first measured over a range of temperatures (25 – 180 ºC) and at three KOH concentrations (0 M, 2 M and 4 M). This data was then used to explain the morphology and size of PZT particles synthesised at 150 ºC and 180 ºC. The authors found that undissolved PbO acted as a buffer to the precipitation of PZT, and the growth of particles was supported by the consumption of Pb supplied by the dissolved PbO. Cube-like particles were formed at 150 ºC when the concentrations of PbO and KOH reached 0.1 M and 2 M, respectively. Rounded, sub-micron particles were produced when the concentration of PbO was increased to 0.275 M and the KOH concentration to 4 M.

In the majority of papers involving the hydrothermal synthesis of PZT the titanium and zirconium precursor gels are derived from co-hydrolysed metal alkoxides[37] or metal chlorides.[38] However, these compounds are expensive and difficult to handle, due to their hydroscopic nature. To overcome these difficulties Traianidis et al.

proposed a two-stage hydrothermal synthesis route to form PZT using inexpensive oxide precursors.[39] In the first stage, amorphous $ZrO_2 \cdot nH_2O$ and nanocrystalline TiO_2 were hydrothermally treated at 265 ºC for 2 hr in a 5 M KOH solution. This led to the formation of tetragonal ZrO_2 and fibres of a potassium-titanate compound that was not formally identified. These compounds were then mixed with $Pb(NO_3)_2$, dissolved in a 1 M KOH solution and treated for a second time at 265 ºC for 2 hr. The resultant PZT particles were phase pure and composed of micron sized cubes and large agglomerates of nanosized grains. A 12% Pb deficiency was present in the grains despite a 100% stoichiometric lead precursor excess being introduced at the second stage. In an extension to this work, Deng et al. substituted the amorphous $ZrO_2 \cdot nH_2O$ with $ZrOCl_2 \cdot 8H_2O$ and used a one stage hydrothermal synthesis to form phase-pure, nanoscale PZT particles.[40] Again, high mineraliser concentrations (5M KOH) were necessary, but no lead excess was required and lower temperatures (160 – 265 ºC) were used. The order in which the precursors were combined was found to be critical for the formation of crystalline PZT. Only when KOH was added to a previously well-mixed solution of $Pb(NO_3)_2$, TiO_2 and $ZrOCl_2 \cdot 8H_2O$, did the authors achieve phase purity. If KOH was added simultaneously, unreacted TiO_2 and amorphous $PbZrO_3$ were produced instead. Omitting $ZrOCl_2 \cdot 8H_2O$ from the reaction led to the production of tetragonal $PbTiO_3$ with unreacted TiO_2 as an impurity phase. However, mixing these products with $ZrOCl_2 \cdot 8H_2O$ and conducting a second hydrothermal treatment gave the desired PZT phase. These results suggested that a reactive form of Zr was essential to breakdown the relatively unreactive TiO_2 and allowed the authors to propose the following reaction mechanism. Prior to the hydrothermal treatment, dissolved Zr^{4+} and Pb^{2+} ions are adsorbed onto the surface of TiO_2 particles. Addition of the KOH mineraliser leads to the formation of $ZrO_2 \cdot nH_2O$ and $Pb(OH)_3^-$. During the hydrothermal process the adsorbed species facilitate the dissolution of the TiO_2 which, together with Pb(OH)3-, diffuse into the insoluble $ZrO_2 \cdot nH_2O$ to form a precursor gel. Finally, this precursor gel itself dissolves and re-precipitates as crystalline PZT. Fig. 1.10 shows TEM images of the PZT nanocrystals obtained after 4 hr processing at 160 ºC and 2 hr processing at 260 ºC. In general, grain size was proportional to processing time and temperature with the smallest grains having an average diameter of 5-10 nm.

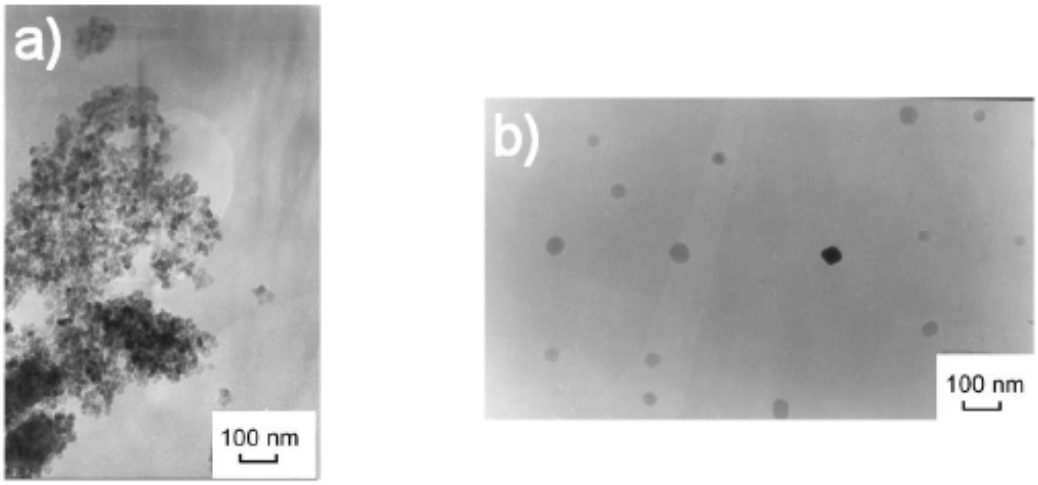

Fig. 1.10 TEM images of hydrothermal PZT particles obtained after (a) 4 hr at 160 ºC and (b) 2 hr at 260 ºC.[40]

Lencka and Riman have made significant contributions to our understanding of the thermodynamics involved in the hydrothermal synthesis of ferroelectric perovskites. They have generated experimentally verified phase stability diagrams, which predict the optimum synthesis conditions (e.g. pH, precursor concentrations and temperature) necessary to produce phase pure lead titanate[41], barium titanate[42] and PZT[43].

Ferroelectric perovskite thin films have also been synthesised using a hydrothermal technique. Shimomura et al. deposited PZT onto TiO_2 substrates using a two-stage technique with $Pb(NO_3)_2$, $ZrOCl_2 \cdot 8H_2O$ and $TiCl_4$ precursors in a KOH solution.[44] In the first stage, a layer of $PbZrO_3$ was hydrothermally deposited onto the TiO_2 substrate during a 24 hr run at 150 ºC. The second treatment, over 48 hr but at a reduced temperature of 120 ºC, introduced the $TiCl_4$ precursor and resulted in the nucleation and growth of crystalline PZT on the $PbZrO_3$ seeding layer. The two-stage method led to improved adhesion of the PZT film but at the same time introduced a level of chemical inhomogeneity. Morita et al. followed the work of Shimomura et al. but managed to obviate the first stage by halving the concentration of the same precursors.[45] The adhesion of the films was described as sufficient and they were shown to possess a spontaneous polarisation. In a later study, Ndiaye et al. used TiO_2 as a precursor in the reaction and managed to produce high quality PZT films with a good piezoresponse when analysed using a laser interferometric technique.[46]

1.2.1.4 Epitaxial growth of films and nanoislands

The term epitaxy is used when the crystallographic ordering of a film or nanostructure is significantly influenced by the substrate on which it is grown.[47] The simplest form of epitaxy is homoepitaxy – the growth of crystals of one material on the crystal face of the same material. Conversely, heteroepitaxy involves growing crystals of one type of material on the crystal face of another material. In general, for epitaxy to occur, the atomic spacings along some direction in the film crystal must match those of the substrate to within 10%.[47] If this condition is not met then defects are liable to form at the interface to accommodate for the mismatch. Alternatively, if the mismatch is small, the film lattice can sometimes be strained to fit the substrate. Fig. 1.11 shows bulk lattice parameters for a range of perovskite ferroelectric films and substrates. The level of strain present in a ferroelectric thin film can have a large impact on its dielectric properties. As an example, Haeni et al. harnessed the epitaxial strain provided by a $DyScO_3$ substrate to raise the Curie point of a $SrTiO_3$ thin film up to room temperature – an increase of over 200 K.[48]

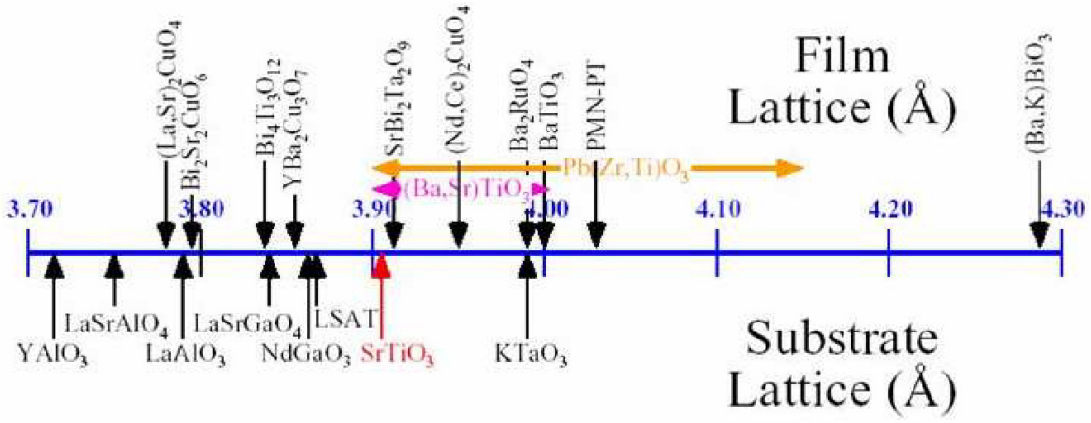

Fig. 1.11 Lattice parameters for several perovskite thin films and associated substrates.[49]

Hydrothermal synthesis has been used to grow epitaxial perovskite thin films on a variety of single crystals substrates. These include $BaTiO_3$ on $SrTiO_3$[50], $BaTiO_3$ on $LiAlO_3$[51] and PZT on $SrRuO_3$[52]. In general, epitaxial hydrothermal thin films grow via a Volmer-Weber (island) 3D nucleation mechanism due to lattice mismatch. By reducing hydrothermal treatment times, Szafraniak and Alexe utilised this mechanism to produce epitaxial $PbTiO_3$ nanoislands on $SrTiO_3$ and $LiAlO_3$ single crystal substrates of varying orientation (Fig. 1.12).[53] They found the growth rate of $PbTiO_3$

on $LiAlO_3$ was slower in comparison to $SrTiO_3$ with partial film coverage and isolated nanoislands being present, even after a 20 hr synthesis. The reduced nucleation rate and the subsequent reluctance of the nanoislands to coalesce were attributed to the greater lattice mismatch between $PbTiO_3$ and $LiAlO_3$.

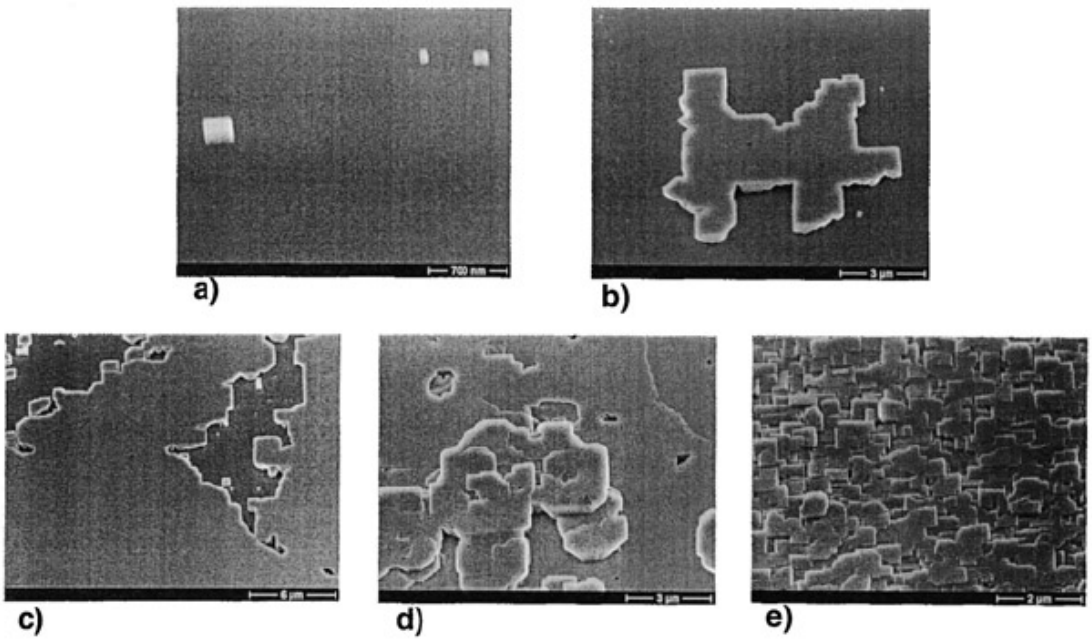

Fig. 1.12 Growth stages of an epitaxial PbTiO3 film on (100)-oriented SrTiO3: (a) nucleation, (b) coalescence, (c) primary layer, (d) secondary nucleation, (e) thick film.[53]

Ahn et al. used a hydrothermal technique to grow epitaxial, mono-*c*-domain $PbTiO_3$ nanoislands on conductive Nb-doped $SrTiO_3$ substrates.[54] They found that the initial polarisation direction of the nanoislands was size dependent and proposed the following mechanism, involving the electrical boundary conditions, to account for this observation. Under hydrothermal conditions the mobility of OH^- ions from the KOH mineraliser increases with reaction temperature whilst the electron mobility in the $Nb:SrTiO_3$ decreases due to dominant polar optical mode scattering. As nanoislands nucleate and grow their initial polarisation direction is positive (facing towards the surface), since the mobile OH^- ions completely screen the depolarising field and the $Nb:SrTiO_3$ substrate has lost its semiconductive properties (Fig. 1.13a). Under ambient conditions, the substrate properties are restored and the OH^- ions no longer influence the polarisation direction. The depolarising field is now completely screened

by the negative charges of the Nb:$SrTiO_3$ substrate, leading to a situation whereby negative polarisation is the stable state. However, the energy associated with 180º domain switching is thought to depend on volume because the change involves shifting oxygen ions along the [100]/[010] direction (Fig. 1.13b). Therefore, when the nanoisland exceeds a critical size (lateral area ~10^4 nm^2 and height ~12 nm) the energy barrier to domain switching becomes too large and the initial positive polarisation state is maintained (Fig. 1.13c).

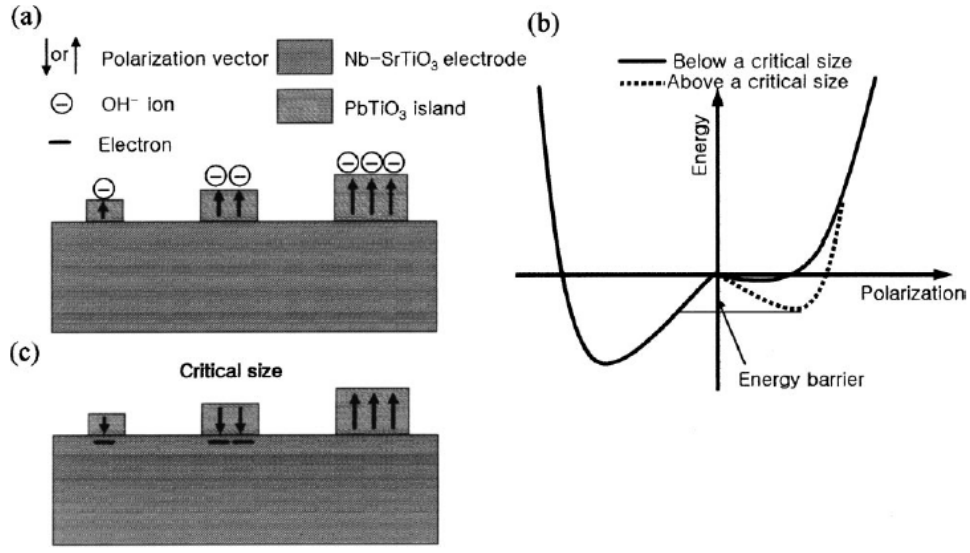

Fig. 1.13 Diagrams showing (a) the positive polarisation state of PbTiO3 nanoislands under hydrothermal conditions; (b) the size dependence of the potential well associated with domain switching (from the Ginzburg-Landau-Devonshire model) and (c) the critical size above which nanoislands retain their initial, positive polarisation state.[54]

1.3 In situ synthesis of P(Z)T

In contrast to ex situ synthesis methods, an in situ method involves forming the ferroelectric phase whilst the nanostructure is in contact with a substrate. Analysis of dielectric properties is made simpler since a conductive substrate can act as a back electrode to which the nanostructure is already well attached. However, an unwanted consequence of this synthesis route is the possibility of the substrate affecting the ferroelectric properties of the nanostructure.

This section will follow a similar pattern to the last with an extended discussion of the in situ method chosen for the project, namely solid-phase synthesis, followed by a comparison with competing techniques.

1.3.1 Solid-phase synthesis

This technique involves the sequential deposition of Pb and Ti metal layers onto a substrate and annealing the resulting heterostructure in the presence of oxygen. It was first proposed by Sidorkin et al. to produce thin films of $PbTiO_3$.[55] The authors used (100) Si substrates in the first set of experiments onto which they deposited Pb and Ti, sequentially, in the thickness ratio Pb:Ti = 2:1 using magnetron sputtering. This ratio was chosen to give the desired $PbTiO_3$ stoichiometry.

Annealing of the films took place in a conventional furnace with an oxygen flow of 40 l/h. After annealing for 60 min at 320 ºC, PbO_2 and a $PbO\text{-}3TiO_3$ solid solution were detected using powder XRD. Increasing the annealing time to 90 min led to the formation of $PbTiO_3$ and $PbTi_3O_7$, however a significant quantity of Pb remained unreacted. A stepped annealing of 335 ºC for 60 min, 410 ºC for 30 min and finally 600 ºC for 5 min ended the formation of the $PbTiO_3$ and $PbTi_3O_7$ phases.

The dielectric properties of the films were measured by depositing a conductive In-Ga eutectic onto the Si to act as a back electrode. Silver top electrodes, with a diameter of 1 mm, were deposited onto the surface of the films post-annealing. Hysteresis loops for 150 nm films were taken at four temperatures (25 ºC, 250 ºC, 370 ºC, and 480 ºC) using a Sawyer-Tower circuit Fig. 1.14a. The loops were unsaturated and broad and this was attributed to diffusion occurring at the film-substrate interface. This is a reasonable assumption since the stability of the In-Ga eutectic back electrode during annealing is questionable. To overcome this problem, Si was substituted for Ti plate as the substrate. Pb was deposited directly onto this plate and the system annealed under the same regime as the films on Si. Using Ti as the substrate meant a separate bottom electrode was unnecessary. Hysteresis loops from 150 nm films on Ti were similarly unsaturated, most probably due to an excessively high coercive field beyond the electrical strength of the film. However, when 1 μm films were tested, a qualitatively different loop was observed Fig. 1.14b. The form is typical of $PbTiO_3$

films prepared by other methods such as metalloorganic decomposition.[56] The spontaneous polarisation and coercive field taken from the loop were 15 μC/cm^2 and 18 kV/cm, respectively. Dielectric measurements of 1 μm films on Si were not shown, but the temperature induced changes in the response, shown in Fig. 1.14, were taken as further evidence of the ferroelectric nature of the films, on both types of substrate. Questions remain over the validity of these results, however, since two follow-up studies from the same group appear to suggest that ferroelectric properties could only be measured from Pb/Ti/Si structures, as opposed to the Ti/Pb/Si structures produced in the initial work [57,58]

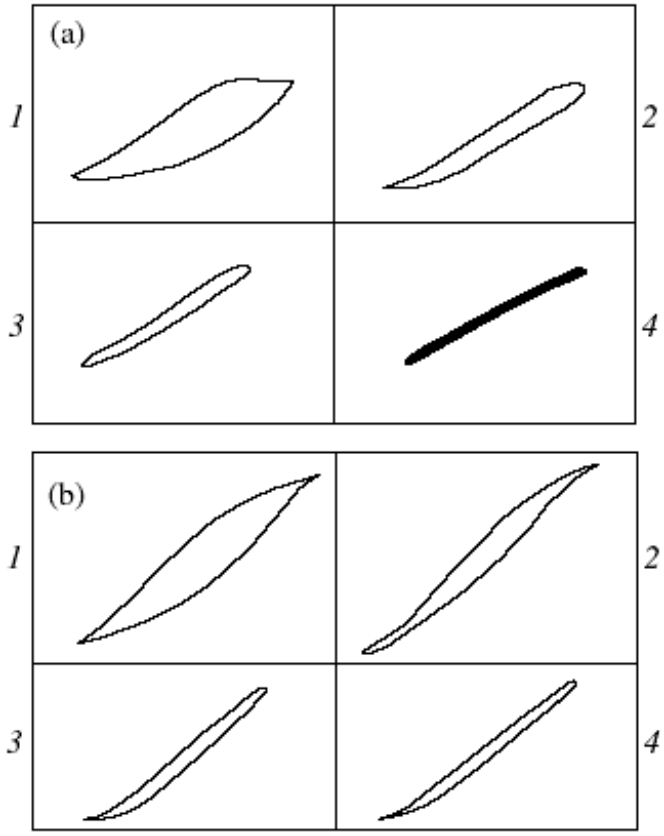

Fig. 1.14 P-E hysteresis loops for $PbTiO_3$ films on (a) Si and (b) Ti substrates measured at various temperatures (1) 25 ºC, (2) 250 ºC, (3) 370 ºC, (4) 480 ºC.[55]

Stankus et al. have also studied the formation of perovskite $PbTiO_3$ thin films through solid-phase reactions.[59] They too used magnetron sputtering to deposit Ti and Pb layers onto Si substrates, but annealed the heterostructures in air as opposed to oxygen. Perovskite $PbTiO_3$ formed, with pyrochlore $Pb_2Ti_2O_6$ present as a secondary phase, after annealing a 1 μm bilayer for 20 min at 650 ºC. Increasing the annealing time to 60 min gave phase pure $PbTiO_3$. Similar results were found with samples

annealed at 600 ºC, but the XRD peak intensities were reduced. The films were composed of relatively loosely arranged, micron-sized grains that lent a rough texture had a loose grain structure uneven morphology were composed of morphology and were composed of micron-sized $PbTiO_3$ grains. Fig. 1.15 shows an SEM image of the $PbTiO_3$ film after annealing at 650 ºC for 60 min.

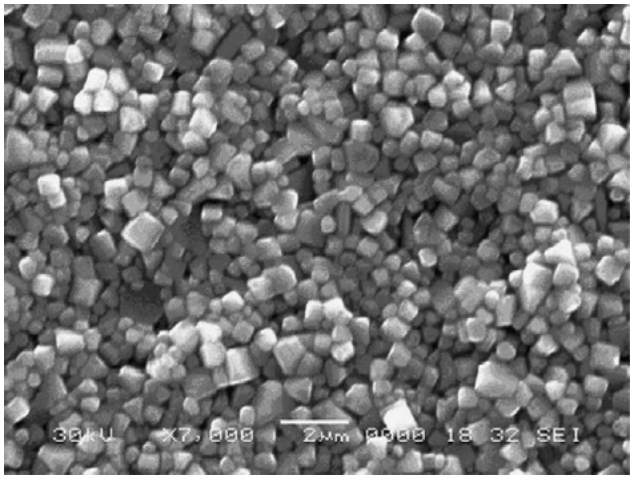

Fig. 1.15 SEM image of a $PbTiO_3$ film formed after annealing a Ti/Pb bilayer for 60 min at 650 ºC.[59]

From these results, the authors deduced that the pyrochlore phase was an intermediary formed from a reaction between PbO and TiO_2 in the temperature range 20 – 500 ºC. Pyrochlore $Pb_2Ti_2O_6$ then transforms into perovskite $PbTiO_3$ at temperatures between 600 – 650 ºC. This reaction can be modelled using the Avrami equation, which describes the overall kinetics of crystallisation:

$$\alpha(t) = 1 - e^{-kt^n} \qquad \text{Eqn. 1.5}$$

where $t = \tau/\tau_{0.5}$ is the normalised time, k the reaction rate, α the phase amount and n the nucleation rate. The reaction rate constant k is itself equal to:

$$k(T) = N_0 e^{-\frac{E_a}{RT}} \qquad \text{Eqn. 1.6}$$

where E_a is the activation energy for the reaction and N_0 the empirical coefficient. This is the well-known Arrhenius equation relating reaction temperature to reaction

rate. By measuring the increase in the perovskite phase (from XRD data) over time, the authors derived the rate of reaction at the two temperatures, 600 ºC and 650 ºC. This allowed them to calculate a figure for the activation energy for the pyrochlore to perovskite reaction E_a = 43.41 kJ/mol.

The authors also investigated the behaviour of $(Ti/Pb)_{20}$ multilayer heterostructures. The resultant films, when annealed under the same regime as the bilayers, consisted of perovskite $PbTiO_3$ and unreacted Pb and Ti. Increasing the reaction time led to the consumption of Pb and Ti but no intermediate pyrochlore phase was identified. The reason for this difference is unclear, but the authors postulate that the growth mechanism of perovskite $PbTiO_3$ is dependent on the thickness of the Pb and Ti layers. When they are very thin, as is the case with $(Ti/Pb)_{20}$ multilayers, a stoichiometric mixture for the perovskite phase is present close to the surface and a thin layer of $PbTiO_3$ forms. Fig. 1.16 $(Ti/Pb)_{20}$ multilayer after annealing for 20 minutes at 650 ºC. The circular plate-like structures are indicative of crystalline nucleation and growth in 2D. Over time, O_2 diffuses through the surface layer and reacts with successive (Ti/Pb) bilayers to form a series of flat $PbTiO_3$ structures towards the substrate. Cross-sectional SEM images of the multilayer films were not provided, but could have given more insight into this reaction mechanism.

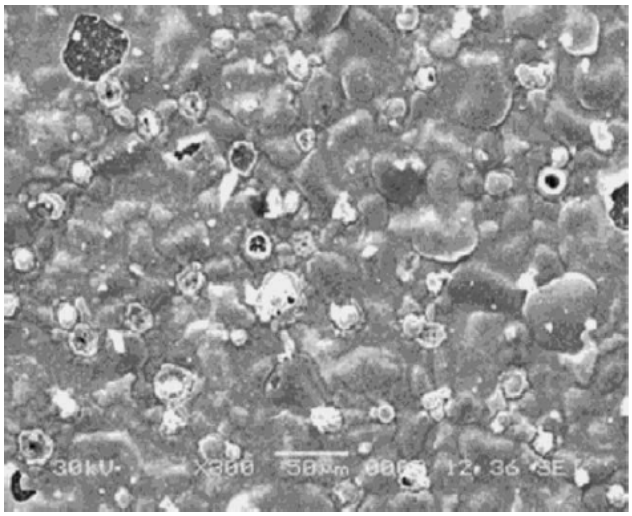

Fig. 1.16 SEM image of a $(Ti/Pb)_{20}$ multilayer structure after annealing at 650 ºC for 20 minutes.[59]

1.3.2 Chemical solution deposition (CSD)

The chemical solution deposition technique has been used to make perovskite thin films since the mid-1980s.[60] Fabrication of thin films by this technique requires four basic steps: (i) synthesis of a precursor solution, (ii) deposition onto a substrate using dip- or spin-coating, (iii) a low-temperature annealing (300 – 400 ºC depending on the oxide material) in air or oxygen for drying, removal of organic species and the formation of an amorphous film, and (iv) high temperature annealing (500 – 1100 ºC) in air or oxygen in order to crystallise and densify the thin film into the appropriate phase.[61] Among the first publications in this area came from Fukushima et al who used metalloorganic decomposition (MOD) to produce PZT thin films.[62] MOD involves dissolving large metal carboxylate compounds in a common solvent, typically xylene, and combining the solutions to give the desired film stoichiometry.[60] When synthesising PZT, suitable carboxylates would be lead 2-ethylhexanoate, zirconium neodecanoate, and titanium dimethoxy dineodecanoate.[56] Solution synthesis is straightforward since the carboxylates are moisture insensitive. However, the large organic ligands, associated with the commonly used starting reagents, can cause cracking during the annealing stages due to the large weight loss and shrinkage that can occur. Overcoming this problem requires careful control of solution concentration and thermal processing conditions.[60]

The sol-gel method, discussed briefly in the preceding section, is another popular CSD technique. Budd et al. are credited with one of the earliest papers on the successful application of the sol-gel technique to produce PZT thin films.[63] Most sol-gel routes use the solvent 2-methoxyethanol (2ME) due to its high reactivity and dissolving power.[64] The key reactions that lead to the formation of precursor species are the hydrolysis and condensation of metal alkoxide reagents, in which metal-oxygen-metal (M – O – M) bonds are formed[60]:

Hydrolysis:

$$M(OR)_x + H_2O \rightarrow M(OR)_{x-1}(OH) + ROH$$

Condensation (alcohol elimination):

$$2M(OR)_{x-1}(OH) \rightarrow M_2O(OR)_{2x-3}(OH) + ROH$$

Condensation (water elimination):

$$2M(OR)_{x-1}(OH) \rightarrow M_2O(OR)_{2x-2} + H_2O$$

where R is an alkyl group. Lead carboxylate compounds are commonly used in preference to lead alkoxides since the former are more stable and readily available. In a typical sol-gel process lead acetate and the alkoxide compounds (titanium (IV) isopropoxide and zirconium (IV) isopropoxide, when synthesising PZT[65]) will be refluxed separately in 2ME. They will then be combined, refluxed further, distilled and finally diluted to the correct volume. Before applying the stock solution to the substrate, it must first be hydrolysed in order to initialise oligomerisation (partial depolymerisation).

In contrast to MOD techniques, the precursor species involved in sol-gel synthesis are relatively reactive. This gives researchers plenty of scope to manipulate the reactions and ultimately to influence the material properties of the films. However, this also means that sol-gel processing can be complex and must be carefully controlled in order to maintain reproducibility.[60]

1.3.2.1 Microstructural instability

For some time it has been known that continuous thin films can be thermodynamically unstable.[66] This can lead to film breakdown and the uncovering of the underlying substrate.[67] Seifert et al. produced epitaxial $PbTiO_3$ thin films by depositing a Pb-Ti alkoxide precursor, via spin-coating, onto a $SrTiO_3$ (001) substrate.[68] Film thickness was dictated by precursor concentration. After deposition, the films were annealed under O_2 at 800 ºC for 1 hr in order to crystallise the $PbTiO_3$ phase. Films with a thickness of ~120 nm were continuous and stable but thinner films (< 80 nm) showed a tendency to develop holes after annealing. When the thickness was reduced to 15 nm the film broke down into isolated, single-crystal islands (Fig. 1.17).

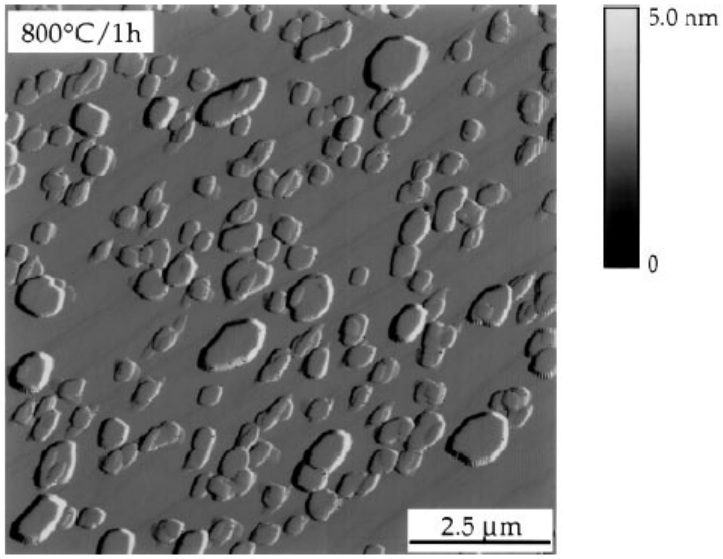

Fig. 1.17 AFM image of PbTiO3 islands produced after annealing a 15 nm Pb-Ti alkoxide precursor thin film[68]

The source of the microstructural instability in the thinnest films was related to pre-existing pores formed during the CSD process. A free energy model taking into account surface energy anisotropy and the spacing between holes was developed that matched the experimental results.[68]

Waser et al. exploited microstructural instabilities in CSD thin films to produce nanoscale $PbTiO_3$ grains on $Pt(111)/TiO_2/SiO_2/Si$ substrates.[69] It was found that the $PbTiO_3$ grains grew preferentially at the Pt electrode grain boundaries. The ferroelectric properties of the $PbTiO_3$ grains were analysed by Roelofs et al. using a technique known as piezoresponse force microscopy (discussed further in *Section 1.3*).[70] It was found that below a critical size of approximately 20 nm (2000 nm^3) the grains appeared to lack piezoresponse, both in- and out of the film plane (Fig. 1.18). This was taken as evidence of a size induced phase change from the ferroelectric to the superparaelectric phase. Although, at first, this value appears to contradict the findings of Tyball et al.[15], who observed ferroelectricity in 4 nm perovskite thin films, there are several differences between the two studies. Foremost amongst these is that a nanoisland is effectively a 0D structure, being constrained in three dimensions, whilst a thin film is only constrained in one dimension. Bearing in mind that ferroelectricity is a collective phenomenon, when searching for its limit it is important to constrain a test structure in all dimensions.

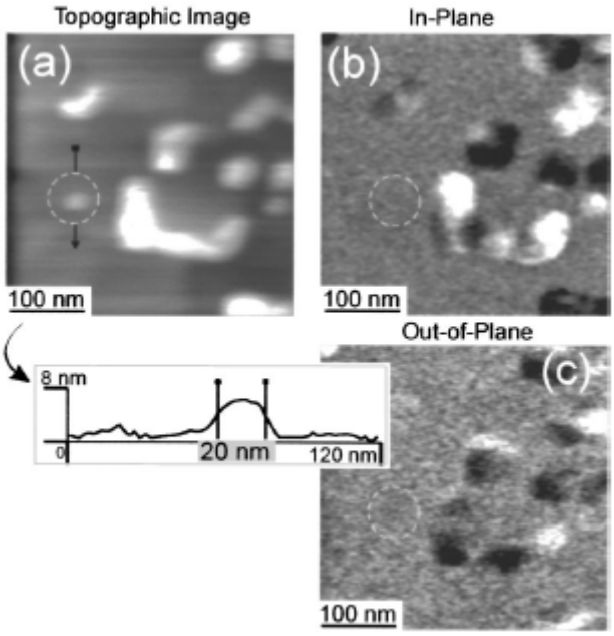

Fig. 1.18 AFM images showing the (a) topography and associated (b) in-plane and (c) out-of-plane piezoresponse from a $PbTiO_3$ nanoisland sample. Note the absence of any piezoresponse from the circled grain. This is evidence of a potential ferroelectric to superparaelectric phase transition.[70]

1.3.3 Metalloorganic chemical vapour deposition (MOCVD)

MOCVD has been used to grow perovskite thin films since the early to mid-1980s.[71] The MOCVD of oxide thin films involves evaporating volatile precursors that subsequently decompose on a hot substrate. Careful control of the atmosphere in which the precursors evaporate is essential. Its major advantages include excellent film uniformity over large areas, easy and reproducible control of film stoichiometry and relatively high deposition rates.[61] It also has the unique ability to deposit conformal films on 3D structures, down to the sub-micron range.[72] However, it is technically more challenging than CSD techniques, in terms of both equipment complexity and precursor costs.[73]

One similarity that MOCVD shares with CSD is the ability to grow nanoscale ferroelectric structures; however, the growth mechanisms differ.[74] Shimizu et al. deposited PZT and $PbTiO_3$ thin films onto Pt (111)/SiO2/Si substrates using a MOCVD technique.[75] They noticed that the films grew laterally across the substrate from flat triangle-shaped nanoislands (Fig. 1.19). XRD measurements confirmed that

the triangular shape corresponded to the (111) orientation of the perovskite lattice, with its three-fold symmetry.

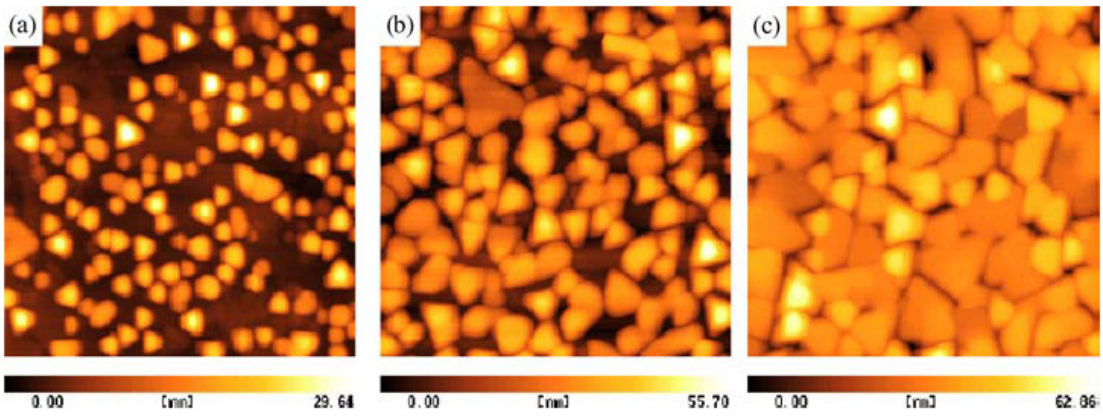

Fig. 1.19 AFM images showing the growth of a MOCVD PZT film from triangular nanoislands. Deposition times: (a) 1 min, (b) 3 min and (c) 7 min. Scan size = 1 µm × 1 µm.[75]

In later work by Fujisawa et al., $PbTiO_3$ nanoislands synthesised via a MOCVD technique were analysed using PFM.[76] The authors measured the piezoresponse of various nanoislands deposited at two different substrate temperatures, 390 ºC and 560 ºC. Plotting ferroelectricity as a function of nanoisland height and width enabled them to ascertain a critical nanoisland volume of 1900 nm^3, below which, no ferroelectric response was found (Fig. 1.20). This value agrees well with the one ascertained by Roelofs et al. for CSD $PbTiO_3$ nanoislands (discussed in the preceding section).[70] However, both values are approximately three times larger than the critical volume measured by Ishikawa et al. for isolated $PbTiO_3$ grains.[77] In this study, Raman spectroscopy and XRD were used to study the dependence of the phase transition temperature on particle size. Crystal lattice vibrations are quantised in units known as phonons. $PbTiO_3$ displays low frequency (soft) optical phonon mode behaviour due to its perovskite structure.[12] However, the paraelectric phase cannot support these modes. Therefore, by using Raman spectroscopy the Curie point can be determined by noting the temperature at which the soft-mode disappears.

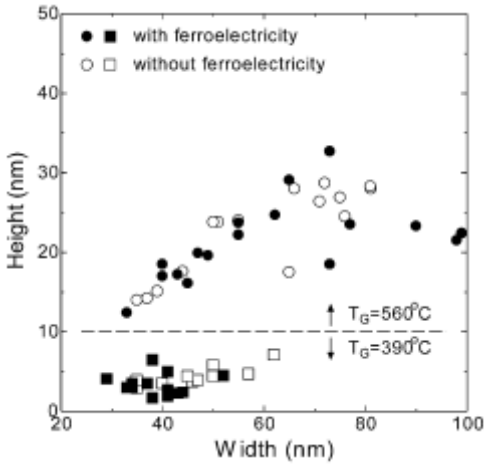

Fig. 1.20 The presence of ferroelectricity plotted as a function of nanoisland width and height. Closed (■,●) and open (□,○) marks indicate $PbTiO_3$ islands with and without ferroelectricity, respectively. Squares (■,□) and circles (●,○) correspond to $PbTiO_3$ islands grown at 390 and 560 ºC, respectively.[76]

Two possible sources of the critical volume discrepancy were discussed by Fujisawa et al.[76] Firstly, limitations in the piezoresponse force measurement technique (discussed in *Section 1.3*) such as sample breakdown at high electric field, tip wear and scanner drift meant the actual critical volume may have been smaller than that measured. Secondly, the nanoislands were subject to a thermal strain whilst in contact with the Si substrate due to the difference in the thermal expansion coefficients of the two materials. The *a*-axis thermal expansion coefficient of $PbTiO_3$ is approximately 3.5 times larger than that of Si between 27 – 400 ºC. The resultant in-plane stress at room temperature elongated the *a*-axis parameter and shortened the *c*-axis parameter. Consequently, the spontaneous polarisation and tetragonality of the unit cells were reduced.

1.4 Analysis

1.4.1 Scanning Probe Microscopy

Scanning probe microscopy (SPM) is the general term given to techniques that involve scanning a sharp tip, in a raster pattern, across the surface of a sample. The development of SPM began with the invention of the scanning tunnelling microscope (STM) by Binnig and Rohrer in 1981.[78] This instrument was capable of inferring the position of individual atoms and molecules on the surface of a lattice through

quantum mechanical tunnelling. Since the establishment of STM, numerous other scanning probe techniques have been developed. They are used to study a variety of surface properties over a range of length scales from the atomic up to the micron level.

In principle, every scanning probe microscope shares the same basic components:

- Sharp tip (radius of curvature < 10 nm) attached to a cantilever
- Method of coarse probe positioning
- Piezoelectric transducer for fine positioning and scanning
- Writefield area ≤ 100 μm × 100 μm
- Probe detection mechanism
- Feedback system to control vertical motion of tip
- Display to output visual/numeric data

In the following section, one specific SPM technique, known as atomic force microscopy (AFM), will be discussed.

1.4.1.1 Atomic Force Microscopy

1.4.1.1.1 Introduction

STM can only be used to image conducting or semiconducting surfaces since it involves the detection of tunnelling currents. To overcome this limitation Binnig et al. invented the AFM in 1985.[79, 80]. In its original inception a diamond shard, acting as a tip, was attached to a gold foil cantilever and scanned across an insulating surface. The authors reportedly measured forces as small as 10^{-18} N with lateral and horizontal resolutions down to 3 nm and 0.1 nm, respectively.

Modern AFM probes generally consist of a single crystal Si or Si_3N_4 cantilever with an integrated single crystal tip. Dopants, such as phosphorous, are often added to the Si in order to increase conductivity and thus overcome electrostatic charging.

1.4.1.1.2 Applications

AFM is primarily used to give information about the surface topography of a sample. Forces between the tip and sample cause the cantilever, on which the tip is mounted, to deflect vertically. These movements are detected as the tip is scanned across the sample, or the sample is moved beneath the tip. A computer then generates a topographical map of the surface being analysed (Fig. 1.21).

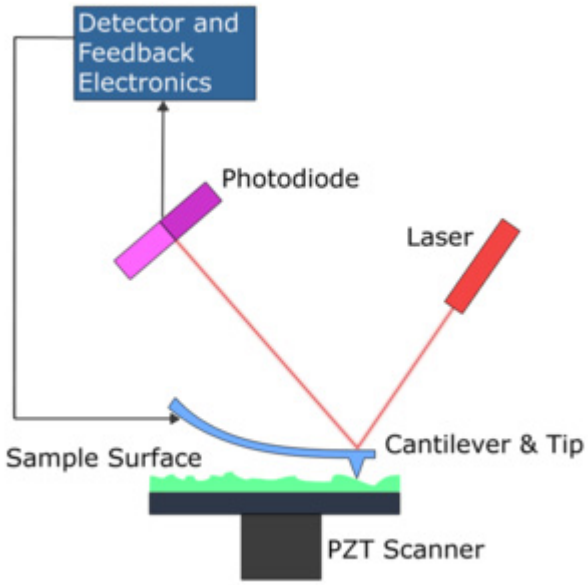

Fig. 1.21 Schematic diagram of an AFM system.[81]

The type of force or combination of forces, responsible for the cantilever deflection, depends on how closely the tip interacts with the surface. Fig. 1.22 illustrates the van der Waals force vs. distance curve for two distance regimes: contact and non-contact. Within the contact regime (< 1 nm), the interatomic force between the tip and sample is repulsive. While further away (1-10 nm), in the non-contact regime, the interaction is attractive. In the contact area of the tip apex repulsion occurs due to the overlapping electronic shells of the tip and sample atoms. Since these interatomic repulsive forces are short-range forces and confined to an extremely small area, they can be utilized to trace the surface topography with atomic resolution.[82]

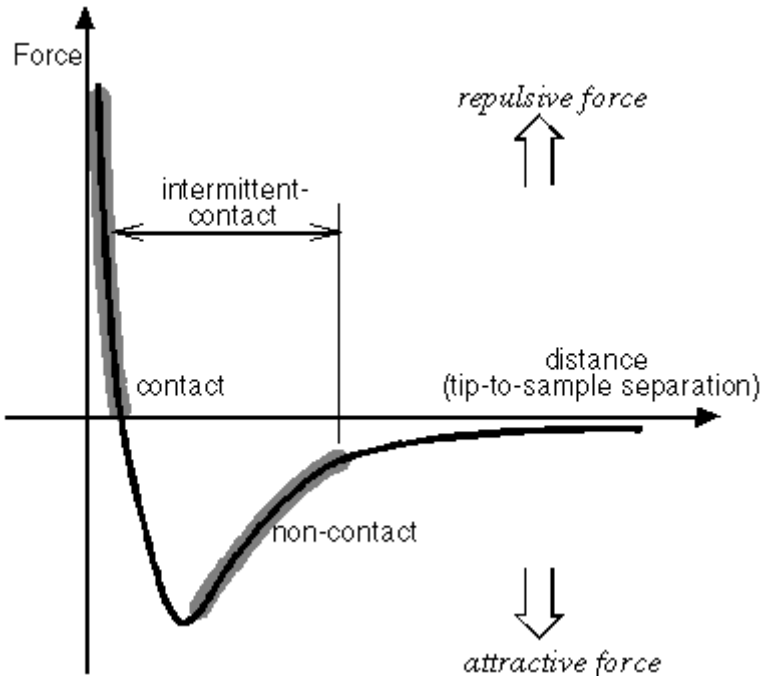

Fig. 1.22 Interatomic van der Waals force vs. distance curve.[83]

1.4.1.1.3 Contact mode

In contact mode AFM the tip is scanned in soft physical contact with the sample. Most contact mode cantilevers are relatively soft and have a spring constant, $k < 1$ N/m. The repulsive van der Waals force is so strong in the contact regime that any attempt to bring the tip closer to the sample will result in bending of the cantilever. However, if a very stiff cantilever ($k > 1$ N/m) is used plastic deformation of the sample can take place.

Position detection of the cantilever is usually achieved via optical methods.[84] A laser beam is focused onto a mirrored section of the cantilever and any vertical movement is detected by a position-sensitive photodetector (PSPD). The resolution of the PSPD tends to be better than 1 nm. However, due to mechanical amplification caused by the beam path length ratios, a typical AFM system can detect sub-angstrom changes in vertical topography.

Topographical data can be gathered in one of two modes – constant-height or constant-force mode. In constant-height mode the probe scans across the sample at a fixed height and an image is generated corresponding to spatial changes in cantilever deflection. Constant-force mode works by altering the probe or scanner ride height in order to keep cantilever deflection constant. A feedback circuit is required when in constant-force mode and variations in probe height generate the topographical image.

Constant-height mode is more suited for producing atomic-scale images of atomically flat surfaces. Constant-force mode is suited to general-purpose applications.

1.4.1.1.4 Intermittent contact mode

Tapping or intermittent contact mode overcomes some of the difficulties associated with imaging in contact mode. Under ambient conditions, sample surfaces are covered by a layer of adsorbed gases consisting primarily of water vapour and nitrogen that is typically several nanometres thick.[85] When the probe touches this contaminant layer, a meniscus forms and the cantilever is pulled by surface tension toward the sample surface. Trapped electrostatic charge on the tip and sample can contribute additional adhesive forces (Fig. 1.23). These downward forces increase the overall force on the sample and, when combined with lateral shear forces caused by the scanning motion, can distort measurement data and damage soft samples such as polymers. Tapping mode imaging works by alternately placing the tip in contact with the surface to provide high resolution and then lifting it to avoid the interaction forces associated with dragging the tip across the surface.[86] The tip is driven at its resonance frequency, which is typically between 50 – 500 kHz. Another secondary benefit of tapping mode is its large, linear operating range. This makes the vertical feedback system highly stable, allowing for routinely reproducible sample measurements.

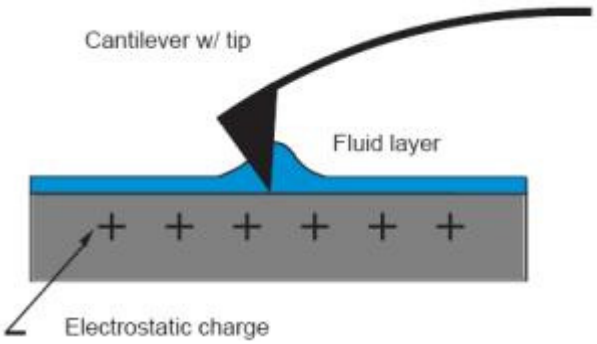

Fig. 1.23 Unwanted tip-sample interactions associated with contact mode AFM.[85]

1.4.1.2 Piezoresponse Force Microscopy

Piezoresponse force microscopy (PFM) is achieved by using a modified AFM system. It can be used to image nanoscale ferroelectric domains[87] and to produce hysteresis measurements[88], which relate to the ferroelectric response of a sample. As a technique, it is still in its infancy so improvements and developments occur continuously. In the following section, the various modifications necessary to implement PFM will be discussed, along with the capabilities of different systems and modes.

1.4.1.2.1 Lock-in techniques

PFM relies on lock-in techniques to extract information about the sample. A lock-in amplifier is an instrument that provides a DC output that is proportional to an AC input signal. It does this by using a phase sensitive detector (PSD), which suppresses noise and interference and only rectifies the signal of interest. An ordinary rectifier does not make the distinction between signal and noise, thus producing errors at the output. In a PSD the noise component appears as an AC fluctuation, thereby allowing the desired signal response (a DC level) to be isolated at the output using a low-pass filter.

In order to recognise the signal of interest, the PSD is fed a reference voltage at the same frequency and with a fixed phase difference to that of the signal. This is usually

achieved by ensuring the signal and reference originate from the same source. Therefore, any changes to the frequency of interest will be tracked, because the reference circuit is "locked" to it.[89]

1.4.1.2.2 Imaging ferroelectric domains using PFM

The principle of ferroelectric domain imaging via PFM is relatively straightforward. It relies upon the piezoelectric deformation of a ferroelectric material under an applied electric field. PFM works by detecting the surface vibrations caused by an external AC field applied to the sample through the tip. Because the system works in contact mode, there is a large mechanical coupling between the tip and sample. This results in the cantilever vibrating together with the sample, following the surface oscillations caused by the inverse piezoelectric effect.[90] Fig. 1.24 shows a schematic representation of this type of domain imaging system.

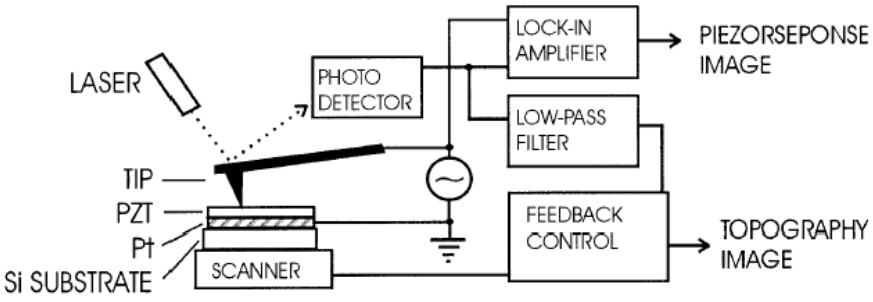

Fig. 1.24 Example apparatus used in PFM domain imaging.[88]

PFM requires the use of conductive tips and the most commonly used varieties are heavily *n*- or *p*-doped Si [91] and $PtIr_5$-coated Si [92]. The use of a $PtIr_5$ coating helps to reduce tip wear whilst maintaining a high level of conductivity.[93]

During a PFM experiment the tip is biased with $V_{tip} = V_0\cos(\omega t)$, and brought into contact with the surface. The electromechanical response of the sample is detected as the first harmonic component, $d_{1\omega}\cos(\omega t + \varphi)$, of the bias-induced tip deflection. The phase, φ, indicates the polarisation direction of the localised area beneath the tip, whilst the amplitude is proportional to the local d_{33} piezoelectric coefficient. For c^+ domains (polarisation vector pointing away from the substrate), the application of a positive tip bias leads to a contraction of the sample and the oscillations are $\varphi = 180$ °

out of phase with the applied field. The situation is reversed for c^- domains, whereby the sample expands and oscillates in phase with the applied field (Fig. 1.25). Often the phase shift between antiparallel domains is less than 180 º due to the presence of an electrostatic offset or cross-talk inevitable at high (500 kHz – 5 MHz) imaging frequencies.[94]

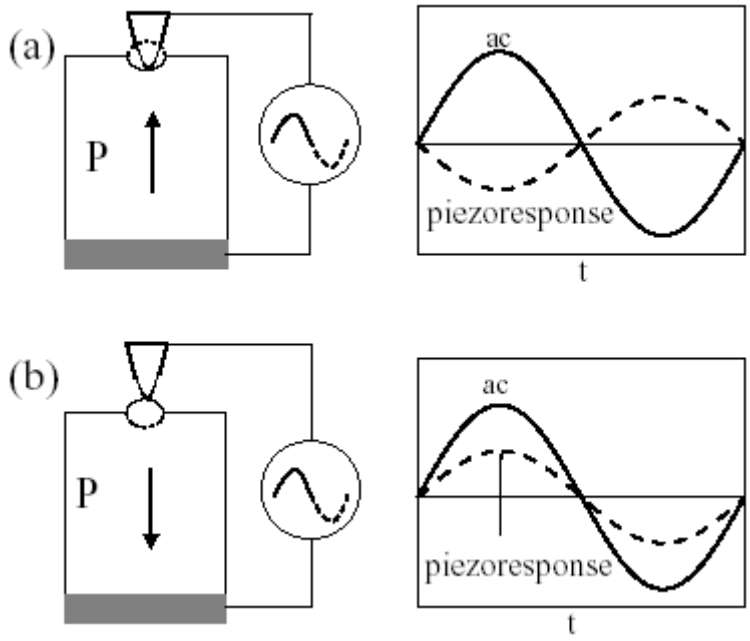

Fig. 1.25 Tip response to a) upward (-) polarisation and b) downward (+) polarisation and the associated in-phase piezoresponse.[95]

The periodic modulation associated with the piezoresponse is superimposed on the static deflection of the cantilever and is detected by the lock-in amplifier. Meanwhile, the low-pass filtered static deflection signal is used to control probe ride height (as in constant force contact-AFM). In this way, simultaneous measurements can be made in order to compare topographic with piezoresponse data from a particular location of the sample. The lock-in amplifier measures the in-phase components of the tip oscillation amplitude. Therefore, the out-of-plane polarisation state can be determined by monitoring the polarity of the output signal. As a result, regions with opposite orientation of polarization can be imaged without being influenced by topographical features.[90] Fig. 1.26 shows the topography and associated piezoresponse from a PZT/LSCO thin film.[96] Note the white and black regions in the right-hand image that correspond to negative and positive domains, respectively.

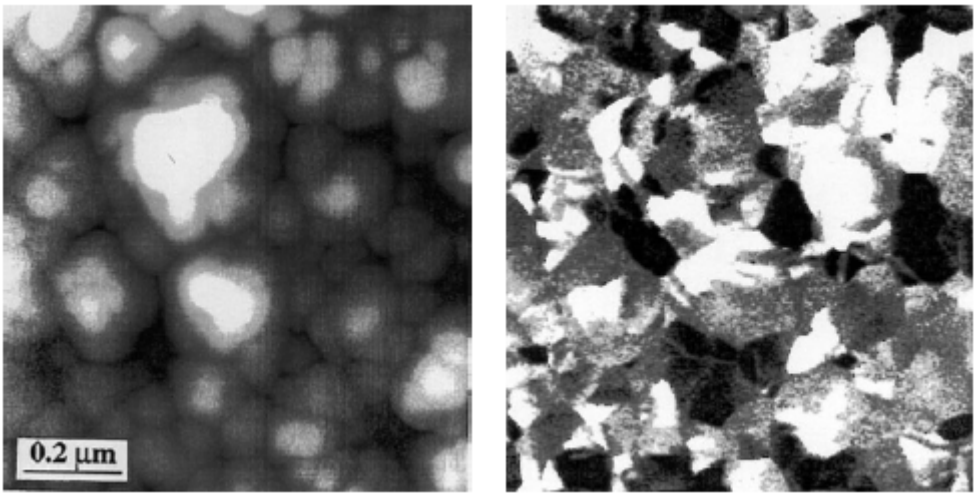

Fig. 1.26 AFM image of a PZT/LSCO thin film showing topography (left) and associated piezoresponse (right)[96]

The advantage of imaging domains without interference from topography can be illustrated with the following analysis. A relatively smooth, sol-gel PZT thin film, for example, may have a surface roughness between 20-30 nm. Assuming the film possesses a d_{33} coefficient of 10^{-10} m/V, a 10 V applied voltage would lead to a change in thickness of 2 nm.[97] Thus, the alteration in surface topography, due to the piezoresponse, would be indistinguishable from the background roughness. The sensitivity of PFM, in comparison, corresponds to a vertical resolution of 5 pm.[98]

PFM images often show areas with intermediate contrast alongside the bright and dark regions associated with *c*-domains. If a polycrystalline film is being analysed it is possible that the material in these regions remained amorphous after processing and is thus non-ferroelectric. Alternatively, there may be several randomly polarised grains stacked in the direction normal to the plane of the film. Since the PFM technique integrates the piezoresponse over the entire range of the film thickness, it is possible that the expansion of certain grains will be compensated for by the contraction of others, leading to no overall response. This tends to occur when the grain size of a film is small relative to its thickness.[13] Finally, the region being analysed may contain *a*-domains, which are domains polarised in the film plane, or domains that have their polarisation vector deviating from the direction normal to the plane.[99]

Abplanalp and Günter used PFM to make simultaneous measurements of in-plane and out-of-plane polarisation in $BaTiO_3$ crystals.[100] An E-field applied across a region containing domains polarised in the plane will cause local shearing, due to the d_{15} mode (Fig. 1.8). During PFM, this movement is transferred to the tip by friction and leads to torsional forces in the cantilever. These forces can be detected using an optical system equipped with a four-quadrant PSD. The laser spot will move either vertically or horizontally depending on whether the polarisation is aligned parallel to the cantilever (y-axis) or normal to it (x-axis) (Fig. 1.27).

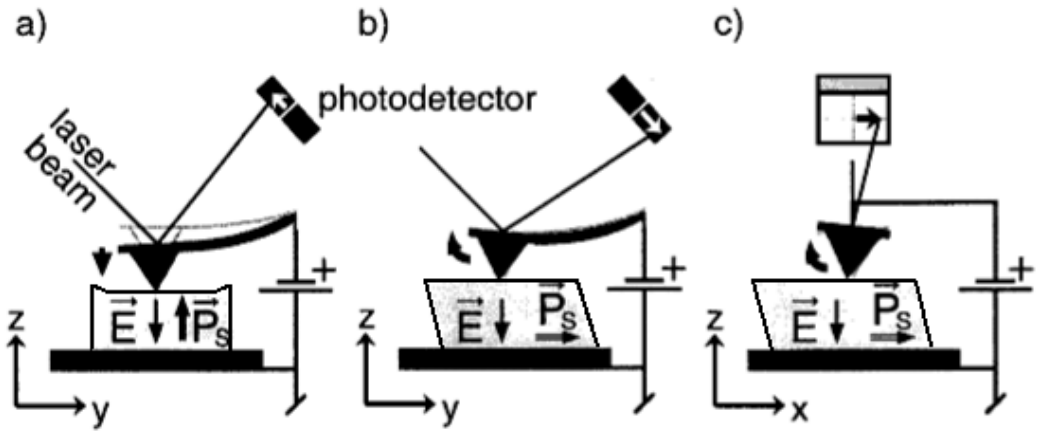

Fig. 1.27 Schematic for (a) vertical and (b)+(c) lateral PFM. Polarisation out-of-plane leads to a vertical deflection of the laser beam whilst polarisation in-plane can give vertical and horizontal deflections.[100]

A second lock-in amplifier is required to demodulate the horizontal signal from the PSD. Separation of the in-plane and out-of-plane components of the vertical deflection is achieved by phase analysis. This is possible since the friction forces, associated with the in-plane components, are strongly dependent on scanning speed.[100]

1.4.1.2.3 Confirming ferroelectricity using PFM

Although a PFM image showing domain structure is compelling evidence for the presence of ferroelectricity, it is not conclusive proof. The criterion for ferroelectricity is a dipole moment that can be reversed in direction by 180 °.[11] Two methods of demonstrating this via PFM are shown below.

1.4.1.2.3.1 Localised poling

This technique involves applying a DC bias that exceeds the coercive field in the local region beneath the tip. This will lead to the formation of stable domains which can be imaged during a PFM scan of the area. Dunn et al. conducted a poling experiment on a sol-gel PZT/Pt/MgO(100) film.[99] The highly (100)-oriented PZT film displayed excellent poling characteristics, with well-defined domain boundaries owing to the small grain size (Fig. 1.28). The greater contrast between the unpoled regions and the black poled areas, in comparison to the white poled areas, was taken as evidence for an internal bias in the film (discussed further in *Section 1.4.2.2*).

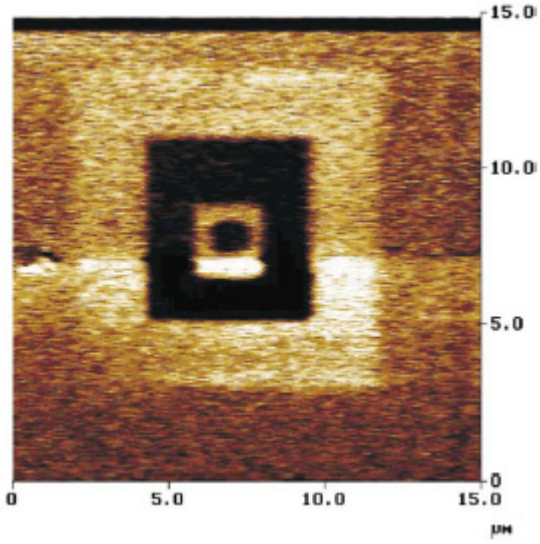

Fig. 1.28 PFM image of a PZT/Pt/MgO film after poling.[99]

1.4.1.2.3.2 Localised hysteresis measurements

When characterising any ferroelectric samples, one of the most important tests involves measuring a hysteresis loop. From this, the magnitude of the remnant and coercive fields can be ascertained. Under macroscopic conditions, this is achieved by measuring an area on the order of 1 mm^2.[11] If we are to gain an insight into how ferroelectric properties scale, it is necessary to have some means of measuring hysteresis effects on the nanoscale. The principle of the measurement, using PFM, is

to monitor the sample displacement (using the lock-in amplfier) under the application of a DC voltage ramp to the tip.

In order to derive the polarisation from measurements of displacement, Durkan and Welland developed an analytical model of the electric field distribution within a sample.[88] This was required since the tip-sample geometry deviates strongly from the plane electrode case, whereby the relationship between the electric field and applied voltage is simply $E = V / t$ (where t is the sample thickness). The region close to the tip will experience a large field enhancement compared with the lower section of the sample.

As the size of the sample is reduced, parasitic capacitance associated with the system linearly distorts the hysteresis loop. To overcome this, Schmitz et al. have developed a hardware-based method that extracts physical data about the tip-sample system in order to compensate directly for the unwanted capacitance.[101] The advantage to this over other methods, such as finite element analysis, is that the influence of noise is significantly reduced (Fig. 1.29). Using this method of correction, ferroelectric capacitors down to 300×300 nm have been measured, with the potential to reach 100×100 nm in the near future.

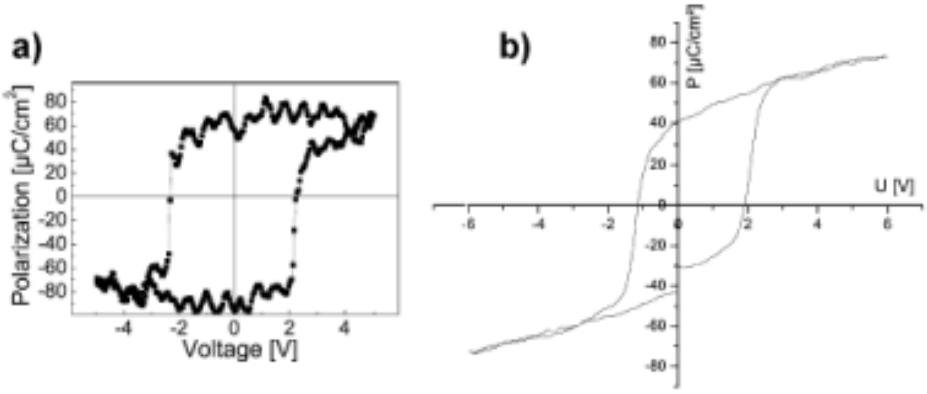

Fig. 1.29 Comparison of hysteresis loops produced via a) a numerical method and b) inverse current compensation.[101]

1.4.1.2.4 Disadvantages of PFM

Three factors limit the ultimate resolution achievable by PFM:

1. Electrostatic contributions to the signal
2. Large (> 100 nN) tip-surface forces present during contact mode imaging
3. Capillary forces due to condensed atmospheric moisture

Electrostatic effects can be minimised with the use of stiff cantilevers, however, this increases indentation forces and reduces resolution.

In an attempt to overcome the problems listed above, Rodriguez et al. conducted PFM experiments in a NaCl solution environment.[102] The authors found that the ions in solution screened the long-range electrostatic interactions, thus localising the AC field to the tip-surface junction. Spatial resolutions of ~3 nm were achieved which approaches the intrinsic domain wall width of several unit cells, or 1 – 1.5 nm.

1.4.2 Size effects

When the dimensions of a ferroelectric crystal are reduced, several size effects manifest themselves. Ferroelectricity is a cooperative phenomenon that originates from the alignment of local dipole moments via short-range chemical and long-range physical interactions. Competition between these temperature-dependent forces results in a specific alignment transition temperature. It is reasonable to expect a size effect associated with this transition, i.e. a decrease in the transition temperature and spontaneous polarization along with an increase in the coercive field, when the physical dimensions of ferroelectric structures are reduced. The range at which size effects become prominent is determined by the correlation length. To a first approximation, this length is defined by the width of the domain walls within the ferroelectric.[103] Meyer and Vanderbilt, in an ab initio study of domain wall widths in bulk $PbTiO_3$, found them to be of the order of one or two lattice constants (0.5 – 1 nm).[104] This is far smaller than the domain walls found in magnetic materials and highlights the potential of ferroelectric materials at reduced length-scales.[105]

Size effects in ferroelectric materials take two forms: intrinsic and extrinsic. Intrinsic effects are related to changes in the atomic polarisation at the small scales. Extrinsic effects are related to the external physical and chemical influences on the ferroelectric structure. Sources of extrinsic effects include patterning and processing of ferroelectric materials, inhomogeneous strain, incomplete polarisation screening at interfaces and defect microstructure.[103] The effect of scaling in the context of PFM analysis of ferroelectric materials is discussed below.

1.4.2.1 Clamping and the removal of a-domains

Ferroelectric thin films exhibit clamping due to their negligible thickness in comparison to the substrate. This manifests itself as a reduction in the piezoresponse of ferroelectric thin films in comparison to bulk ferroelectrics.[106]

Bühlmann et al. produced sub-micron structures by patterning an epitaxial PZT thin film, grown on a (001)-oriented Nb:$SrTiO_3$ substrate, using e-beam lithography and a combination of chemical and physical etching.[107] The unpatterned film and resultant ferroelectric structures were analysed using PFM. The authors found that the piezoresponse increased as the lateral size of the ferroelectric structures decreased (Fig. 1.30). The critical size of the observed effect was approximately 200 nm, which corresponded to the thickness of the unpatterned film.

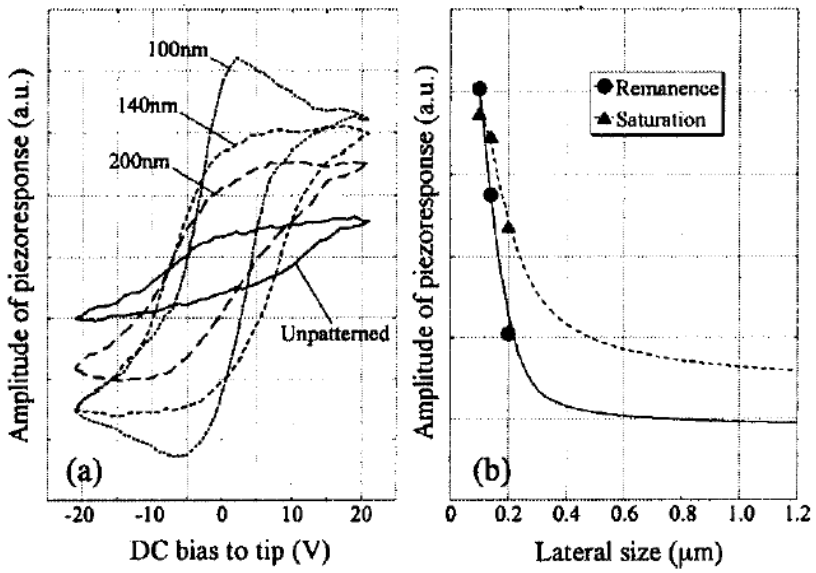

Fig. 1.30 Hysteresis measurements showing an increase in piezoresponse with shrinking size. (a) Loops for ferroelectric structures between 100 – 200 nm across and unpatterned film, and (b) remanent polarisation and saturation as a function of lateral size.[107]

Two separate contributions to the increase in the piezoresponse were highlighted by the authors. Clamping could only account for a 50% increase in the unpatterned piezoresponse, however an increase of 300% was recorded for the smallest structures. Therefore, the major contributor was thought to come from a rearrangement in the domain configuration – specifically, the removal of *a*-domains. Stress resulting from thermal mismatch and spontaneous ferroelectric strain were released as lateral dimensions fell. The *a*-domains that would otherwise form, to compensate for the thermal strain, no longer did so. Furthermore, *a*-domains could be eliminated from the structures entirely since *c*-domains match the Nb:$SrTiO_3$ substrate lattice more closely.

In later work by Nagarajan et al. they argued that the primary cause of the increase in piezoresponse observed in sub-micron PZT structures was in fact clamping and not the removal of *a*-domains.[108] Both papers reported valid conclusions, however the methods of synthesis and processing used by the authors differed. This case highlights how important extrinsic effects can be when measuring the piezoresponse of sub-micron ferroelectric structures.

1.4.2.2 Imprint and fatigue

When the remanent polarisation of a ferroelectric thin film is maintained for extended periods, the hysteresis loop starts to shift with respect to the applied voltage (Fig. 1.31). This behaviour is known as imprint and is analogous to internal bias – an effect that occurs in bulk ferroelectric materials.[109] When fabricating ferroelectric random access memories (FeRAM), imprint is an unwanted characteristic for two reasons. Firstly, if the voltage shift exceeds the write voltage then the memory can become non-switchable. Secondly, the sense amplifier may be unable to distinguish between the two polarisation states due to the loss of remanent polarisation.[110]

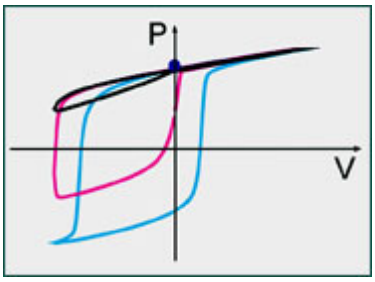

Fig. 1.31 The effect of imprint on polarisation hysteresis loop shape.[110]

Warren et al. found that the internal space charge field, associated with trapped charges near the ferroelectric-electrode interface, was mainly responsible for the imprint in thin films.[111] Defect dipoles associated with O_2 vacancies can enhance the charge trapping and therefore amplify the imprint effect.

Alexe et al. used PFM to study PZT structures with lateral sizes from 0.1 – 1 μm patterned on Nb:$SrTiO_3$ substrates.[112] The structures mainly exhibited an initial downward pre-polarisation, an effect that increased as the lateral size fell. Hysteresis loops from the structures were qualitatively similar regardless of size but a negative vertical offset was present that was inversely proportional to lateral size (Fig. 1.32). This offset was interpreted as a form of imprint since a vertical shift of piezoelectric loop can be associated with regions of non-switching polarisation and, therefore, a preferred polarisation direction (see discussion on fatigue, below). In epitaxial ferroelectric films, the lattice mismatch is responsible for in-plane strains that build up a region of fixed polarisation (pinned domain layer) at the substrate-ferroelectric interface.[113] As film thickness is reduced, the influence of this non-switching layer increases, leading to a measurable size effect. However, the PZT structures prepared by Alexe et al. were not epitaxial but polycrystalline with an average grain size of 20 nm.[112] Therefore, they speculate that the pinning was due to the effects of O_2 vacancies and surface/interface defects. By generating a simple model, derived from the hysteresis loop offsets, the authors were able to make an estimate of the thickness of the pinned domains at the electrode interface (15 ± 8.9 nm) and at the sidewalls of the structures (68.9 ± 7.4 nm).

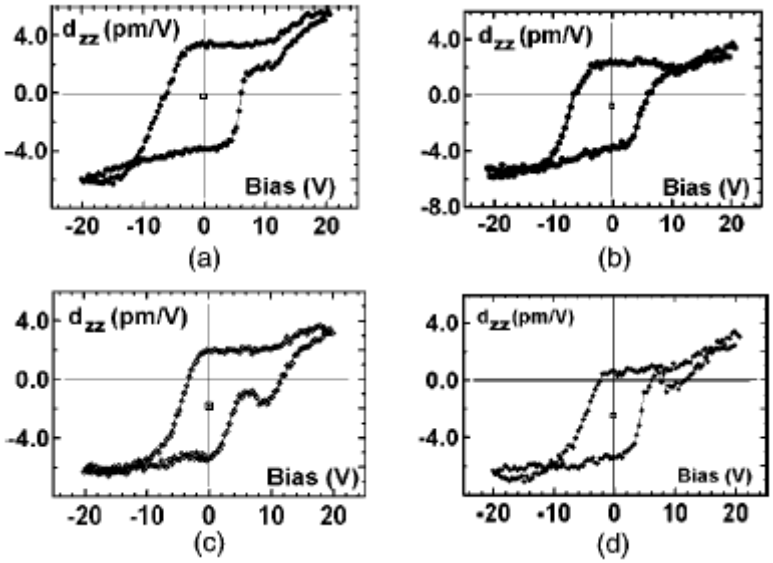

Fig. 1.32 Remanent hysteresis loops for PZT structures patterned on Nb:$SrTiO_3$ substrates. Lateral size: (a) 1 μm, (b) 0.5 μm, (c) 0.25 μm and (d) 0.1 μm.[112]

In a follow-up study, Harnegea et al. compared the behaviour of 350 nm PZT cells patterned on Nb:SrTiO3 and Pt bottom electrodes.[114] The hysteresis loops from samples with Pt bottom electrodes did not show any imprint effects, in contrast to cells patterned on Nb:$SrTiO_3$. Also, the cells on Nb:$SrTiO_3$ showed signs of incomplete crystallisation of the ferroelectric phase. Both of these issues were rectified by using a thin PbTiO3 seeding layer prior to depositing the PZT film. This is known to enhance the nucleation process, which lowers the pyrochlore to perovskite transformation temperature and promotes complete crystallisation.[115]

Fatigue is the reduction in the remanent polarisation of a ferroelectric material after many switching cycles.[116] Like imprint, it has severe implications for the production of reliable FeRAM memories. It is a complex problem involving many interrelated physical and chemical phenomena that occur mainly at the electrode-ferroelectric interface.[103] PFM has been used to study the development of fatigue in both electrode-free films[117] and thin film capacitors[118]. These studies found that fatigue developed over small regions or individual grains before spreading across the entire surface of the ferroelectric (Fig. 1.33). Local hysteresis measurements show a progressive shift in the loops both vertically and horizontally thus demonstrating the imprint of the non-switching regions. The size of the frozen or pinned regions varies between 100

nm to several micrometres, which means there are significant technical repercussions as ferroelectric capacitors approach these length scales.[103]

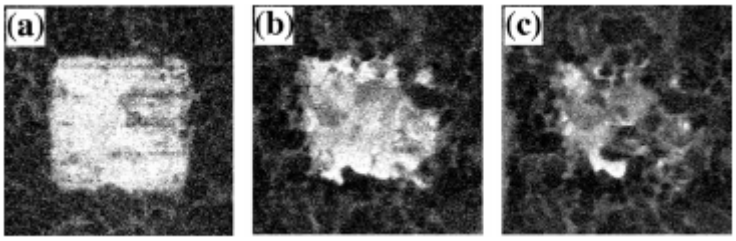

Fig. 1.33 PFM images of a PZT film showing the progression of fatigue over time. In (a) the white region is a 1 μm × 1 μm square poled using a –15 V DC tip voltage. The same region after scanning for (b) 1 hr and (c) 2 hrs with the tip held at 8 V AC peak-to-peak. Unswitchable crystallites appear as dark areas inside the square region that was scanned again using a –15 V DC tip voltage.[103]

Fatigue can be controlled in PZT capacitors by replacing Pt electrodes with conductive oxide electrodes, such as the superconducting cuprate $YBa_2Cu_3O_7 - \delta$ (YBCO)[119] and the metallic perovskite $La_{0.5}Sr_{0.5}CoO_x$ (LSCO)[120]. These materials share a closer lattice match to epitaxial PZT and as such, the number of O_2 vacancies at the interface is reduced in comparison to Pt/PZT/Pt capactitors.[121]

1.4.2.3 Coercive field and fringe effects

The coercive field of a ferroelectric thin film is proportional to $d^{-\frac{2}{3}}$, where d is the film thickness, for films between 0.1 – 100 μm.[116] However, this semi-empirical scaling law assumes that there are no electric fields present within the sample.[122] This is only true for idealised ferroelectric capacitor, which has perfectly conducting electrodes. In that situation, charge is held on a plane at the electrode-ferroelectric interface and the spontaneous polarisation is completely compensated. In reality, the charge extends some way into the metal and hence incomplete screening occurs and a depolarising field is generated. Dawber et al. found that this depolarising field leads to a distinction between the measured and true coercive fields within very thin (< 100 nm) ferroelectric films.[123] The authors developed a model which agreed well with coercive field measurements on thin films of the polymer ferroelectric PVDF[124], down to a thickness 1 nm (Fig. 1.34). The same principles were also applied to thin films of PZT and KNO_3.

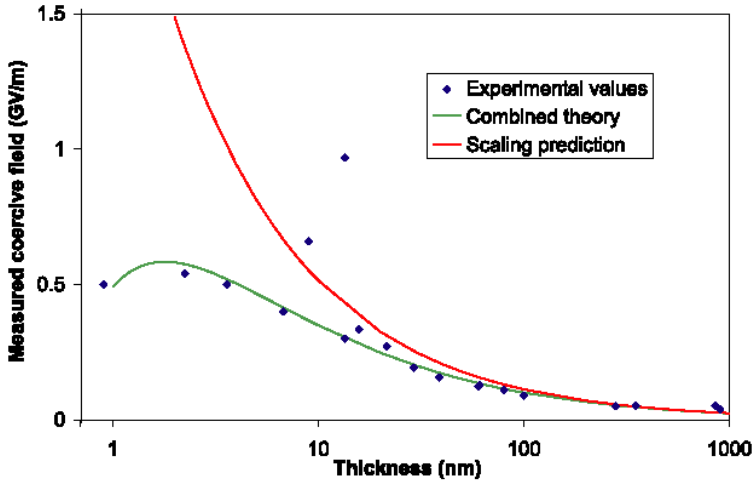

Fig. 1.34 Coercive field data for PVDF plotted alongside the empirical scaling law (Kay-Dunn) and the modified theory that includes depolarisation field contributions.[123]

These results have implications for the design of ferroelectric devices and quantitative measurements using PFM. The oxide electrodes used to combat fatigue would be unsuitable for ultrathin (< 10 nm) ferroelectric devices due to large field penetration in the capacitor plates. As such, the screening properties of the electrodes will have to be optimised for the next generation of ferroelectric devices. Likewise, the screening properties of SPM tips will depend on the material they are made from (metal, diamond etc.) so quantitative measurements of nanoscale ferroelectrics may prove problematic.[123]

The electric field between two parallel-plate electrodes deviates from uniformity, especially at the edges, due to fringing effects. This leads to an underestimation of the true capacitance if fringing fields are neglected.[125] As the aspect ratios (lateral area/height) of ferroelectric structures fall, the fringing fields may initiate domain nucleation.[126]

1.4.2.4 Superparaelectric limit

The superparaelectric limit was discussed in some detail in *Section 1.3.3* with regard to $PbTiO_3$ nanoislands grown on Pt. Research into the superparaelectric limit in isolated perovskite particles is ongoing since fabrication techniques such as sol-gel and hydrothermal synthesis continue to be refined. Measurement techniques usually involve assessing the crystal structure of the grains using XRD[127] or searching for the

disappearance of soft-optical modes using Raman spectroscopy[128]. In one of the latest studies, Erdem et al. used electron paramagnetic resonance (EPR) spectroscopy, alongside the more established techniques, to ascertain the tetragonal to cubic transition in nano-sized $PbTiO_3$ grains.[129] Their results suggest that the phase transition occurs at dimensions below 7 nm. As synthesis techniques of ultrafine perovskite particles continue to develop, it is likely that this limit will be revised. Suffice to say that most of the experimental observations to date have been associated with extrinsic as opposed to intrinsic size effects.

1.5 Aim and objectives

As the literature review has demonstrated, control over the size and morphology of ferroelectric nanostructures is important both from the point of view of emerging applications and fundamental studies. It also highlights the continued relevance of PZT and $PbTiO_3$ to the future success of the field. The aim of this investigation was therefore to investigate factors affecting the processing of nanoscale PZT and $PbTiO_3$ ferroelectrics. Two different synthesis routes were proposed to achieve this aim. The first was the ex situ technique of hydrothermal synthesis. The motivation behind much of the literature pertaining to the hydrothermal synthesis of freestanding ferroelectric perovskites relates to the production of bulk electroceramics. Many of the criteria for electroceramic powders, such as high crystallinity, minimal defects and low agglomeration are also desirable attributes for fundamental research, albeit at a larger lengthscale. As such, the hydrothermal technique would seem an ideal candidate for ferroelectric size effect research in terms of both novelty and feasibility.

The second half of this study was dedicated to the in situ technique of solid phase synthesis. Although this method was not capable of producing freestanding ferroelectric particles and required high annealing temperatures, it possessed several advantages over the ex situ, hydrothermal route. Firstly, it was anticipated that the level of fine control afforded by the technique, in terms of the thickness and nature of the deposited layers, would allow for greater flexibility. Secondly, the method relied upon conventional semiconductor processing techniques, which is advantageous for integration into future technologies and microelectronic devices. Finally, ferroelectric

analysis of the resultant nanostructures was simplified since a bottom electrode could be incorporated directly into the heterostructure.

References

[1] M. E. Lines and A. M. Glass, *Principles and Applications of Ferroelectrics and Related Materials*, Clarendon, Oxford (1977)

[2] L. E. Cross and R. E. Newnham, *Ceramics and Civilization, Volume III. High-Technology Ceramics-Past, Present, and Future*, The American Ceramic Society. Inc. History of Ferroelectrics (1987).

[3] M. Wul and I. M. Goldman, *Dokl. Akad. Nauk. SSSR*, 46, 154 (1945)

[4] K. M. Rabe, *Nat. Mater.* 1, 147 (2002)

[5] V. R. Cooper, I. Grinberg, N. R. Martin and A. M. Rappe, *AIP Conference Proceedings*, vol. 626, iss. no. 1, p. 26-35 (08/2002)

[6] B. Noheda, D. E. Cox, G. Shirane, J. A. Gonzalo, L. E. Cross and S-E. Park, *Appl. Phys. Lett.* 74, 14, 2059 (1999)

[7] A. M. Glazer and P.A. Thomas, *Phys. Rev. B*, 70, 184123 (2004)

[8] R. Guo, L. E. Cross, S-E. Park, B. Noheda, D. E. Cox and G. Shirane. *Phys. Rev. Lett.* 84, 23, 5423 (2000)

[9] B. Noheda, *Curr. Opin. Solid State Mater. Sci.* 27–34 (2002)

[10] Martienssen and Warlimont, *Springer Handbook of Condensed Matter and Materials Data*, Springer, Berlin (2005)

[11] B. Jaffe, W. R. Cook Jr and H. Jaffe, *Piezoelectric Ceramics*, Academic Press, New York, London (1971)

[12] C. Kittel, *Introduction to Solid State Physics 7th Ed.* Wiley, New York (1995)

[13] F. Jona and G. Shirane, *Ferroelectric Crystals*, Pergamon Press, Oxford (1962)

[14] J. Junquera and P. Ghosez, *Nature*, 422, 506 (2003)

[15] T. Tybell, C. H. Ahn and J-M. Triscone, *Appl. Phys. Lett.* 75 856 (1999)

[16] A. V. Bune, V. M. Fridkin, S. Ducharme, L. M. Blinov, S. P. Palto, A. V. Sorokin, S. G. Yudin, A. Zlatkin et al. *Nature*, 391, 874 (1998)

[17] A. G. Luchaninov et al. *Sov. Phys. Tech. Phys*. 25, 368 (1980)

[18] A. G. Luchaninov, A. V. Shil'Nikov, L. A. Shuvalov and Shikova, *Ferroelectrics*, 98, 123 (1989)

[19] K. Byrappa and M. Yoshimura, *Handbook of Hydrothermal Technology*, Noyes (2001)

[20] S. Inwood, *The Man Who Knew Too Much: The Inventive Life of Robert Hooke*, Pan Books, London (2003)

[21] F. Habashi, Recent Advances in Pressure Leaching Technology, in: *Proc. First Intl. Conf. Solvothermal Reactions,* 13–16, Takamatsu, Jpn. (1994)

[22] R. M. Barrer, Some Features of Ion Exchange in Crystals, in: *Molecular Sieves, Soc. Chem. Ind*., 1258 (1962)

[23] S. Wei, J. Lu, W. Yu and Y. Qian, *J. Appl. Phys.* 95, 7, 3683 (2004)

[24] X. Sun and Y. Li, *Chem. Commun.* 1768 (2003)

[25] X. Wang, J. Zhuang, Q. Peng and Y. Li et al. *Inorg. Chem.* 45, 6661 (2006)

[26] Y. Matsuo and H. Sasaki, *J. Am. Ceram. Soc.* 48, 289 (1965)

[27] K. S. Jacob, N. R. Panicker, I. P. Selvam and V. Kumar, *J. Sol-Gel Sci. and Technol.* 28, 289 (2003)

[28] J-H. Choy, Y-S. Han and J-T. Kim, *J. Mater. Chem.* 5, 65 (1995)

[29] Y. Sun Y, Ayabe T and Miyasato T, *Jap. J. Appl. Phys P. 1*, 38, 9 B, 5342 (1999)

[30] S. Somiya, *Hydrothermal Reactions for Materials Science and Engineering: An Overview of Research in Japan*, Elsevier Science Publishers Ltd. UK (1989)

[31] V. A. Kuznetsov, *Iss. Prof. Krist Gidroterm, Vsloniyaka* 75 (1970)

[32] S. Kaneko and F. Imoto, *Bull. Chem. Soc. Jpn.* 51, 6, 1739 (1978)

[33] T. R. N. Kutty and R. Balachandran, *Mater. Res. Bull.* 19, 1479 (1984)

[34] K. C. Beal, *Advances in Ceramics, Vol. 21: Ceramic Powder Science*, 33 (1987)

[35] K. H. Lee, K. Asaga, T. Ichihara and M. Daimon, *Yogyo Kyokaishi,* 95, 736 (1987)

[36] Y. Ohba, T. Rikitoku, T. Tsurumi and M. Daimon, *J. Ceram. Soc. Japan,* 104, 1, 6 (1996)

[37] S-B. Cho, M. Oledzka and R. E. Riman, *J Cryst. Growth*, 226, 313 (2001)

[38] R. M. Piticescu, A. M. Moisin, D. Taloi, V. Badilita and I. Soare, *J. Euro. Ceram. Soc.,* 24, 931 (2004)

[39] M. Traianidis, C. Courtois and A. Leriche, *J. Euro. Ceram. Soc.* 20, 2713 (2000)

[40] Y. Deng, L. Liu, Y. Cheng, C-W. Nan and S-J. Zhao, *Mat. Lett.* 57, 1675 (2003)

[41] M. M. Lencka and R. E. Riman, *J. Am. Ceram. Soc.* 76, 2649 (1993)

[42] M. M. Lencka and R.E. Riman, *Chem. Mater.* 5, 1, 61 (1993)

[43] M. M. Lencka, A. Anderko and R. E. Riman, *J. Am. Ceram. Soc.* 78, 10, 2609 (1995)

[44] K. Shimomura, T. Tsurumi, Y. Ohba and M. Daimon, *Jpn. J. Appl. Phys.* 30, 9B, 2174 (1991)

[45] T. Morita, T. Kanda, M. Kurosawa, Y. Yamagata and T. Higuchi, *Jpn. J. Appl. Phys.* 36, 5B, 2998 (1997)

[46] P. A. Ndiaye, B. Loiseau, S. Minaud, P. Pernod and J.C. Tricot, *Microsystem Technologies*, 6, 15 (1999)

[47] D. L. Smith, *Thin Film Deposition: Principles & Practice*, McGraw-Hill, New York (1995)

[48] J. H. Haeni, P. Irvin, W. Chang, R. Uecker, P. Reiche, Y. L. Li, S. Choudhury, W. Tian, M. E. Hawley, B. Craigo, A. K. Tagantsev, X. Q. Pan, S. K. Streiffer, L. Q. Chen, S. W. Kirchoefer, J. Levy and D. G. Schlom, *Nature*, 430, 758 (2004)

[49] C. Lichtensteiger, *PhD Thesis*, University of Geneva (2006)

[50] A. T. Chien, J. S. Speck, F. F. Lange, A. C. Daykin, and C. G. Levi, *J. Mater. Res.* 10, 1784 (1995)

[51] E. Ciftci, M. N. Rahaman and F. D. Blum, *J. Mater. Sci.* 37, 16, 3361 (2002)

[52] T. Morita, Y. Wagatsuma, Y. S. Cho, H. Morioka, H. Funakubo and N. Setter, *Appl. Phys. Lett.* 84, 25, 5094 (2004)

[53] I. Szafraniak and M. Alexe, *Ferroelectrics*, 291, 19 (2003)

[54] S. H. Ahn, W. W. Jung and S. K. Choi, *Appl. Phys. Lett.* 86, 172901 (2005)

[55] A. S. Sidorkin, A. S. Sigov, A. M. Khoviv, S. O. Yatsenko and O. B. Yatsenko, *Phys. Solid State*, 42, 4, 745 (2000)

[56] R. W. Vest and J. Xu, *IEEE Trans. UFFC*, 35, 6 (1988)

[57] V. A. Logacheva, E. A. Turenko, A. M. Khoviv and O. B. Yatsenko, *Inorg. Mater.* 37, 5, 466 (2001)

[58] A. S. Sidorkin, L. P. Nesterenko, I. A. Bocharova,V. A. Sidorkin, and G. L. Smirnov, *Ferroelectrics*, 286, 335 (2003)

[59] V. Stankus and J. Dudonis, *Mat. Sci. Eng. B*, 109 178 (2004)

[60] R. W. Schwartz, *Chem. Mater.* 9, 2325 (1997)

[61] J. Schwarzkopf, R. Fornari, Prog. Cryst. Growth Charact. Mater. 52 (2006) 159-212

[62] J. Fukushima, K. Kodaira and T. J. Matsushita, *Mater. Sci.* 19, 595 (1984)

[63] K. D. Budd, S. K. Dey and D. A. Payne, *Brit. Ceram. Soc. Proc.* 36, 107 (1985)

[64] S. K. Dey, K. D. Budd and D. A. Payne, *IEEE Trans. UFFC*, 35, 1, 80 (1988)

[65] Q. Zhang, R. W. Whatmore and M. E. Vickers, *J. Sol-Gel Sci. and Technol.* 15, 13-22 (1999)

[66] M. L. Gimpl, A. D. McMaster and N. Fuschillo, *J. Appl. Phys.* 35, 12, 3572 (1964)

[67] R. E. Hummel, R. T. Dehoff. S. Matts-Goho and W. M. Goho, *Thin Solid Films*, 78, 1 (1981)

[68] A. Seifert, A Vojta, J. S. Speck and F. F. Lange, *J. Mater. Res*., 11, 6, 1470 (1996)

[69] R. Waser, T. Schneller, S. Hoffmann-Eifert and P. Ehrhart, *Integ. Ferro.* 36, 3 (2001)

[70] A. Roelofs, T. Schneller, K. Szot and R. Waser, *Appl. Phys. Lett.* 81, 5231 (2002)

[71] M. Kojima, M. Okuyama, T. Takagawa and Y. Hamakawi, *Jpn. J. Appl. Phys.* 22, 22-2, 14 (1983)

[72] T. Schneller and R. Waser, *Ferroelectrics*, 267, 293 (2002) 293

[73] C. J. Brierley , C. Trundle, L. Considine, R. W. Whatmore and F. W. Ainger, *Ferroelectrics*, 91, 181 (1989)

[74] M. Alexe and D. Hesse, *J. Mater. Sci.* 41, 1 (2006)

[75] M. Shimizu, M. Sugiyama, H. Fujisawa, T. Hamano, T. Shiosaki and K. Matsushige, *Journal of Cryst. Growth* 145, 226 (1994)

[76] H. Fujisawa, M. Okaniwa, H. Nonomura, M. Shimizu and H. Niu, *J. Euro. Ceram. Soc.* 24, 1641 (2004)

[77] K. Ishikawa, T. Nomura, N. Okada and K. Takada, *Jpn. J. Appl. Phys.* 35 Pt 1, 9B 5196 (1996)

[78] G. Binnig, H. Rohrer, Ch. Gerber and E. Weibel, *Appl. Phys. Lett.* 40, 178 (1982)

[79] G. Binnig, *US Patent RE 33 387* (1985)

[80] G. Binnig, C.F. Quate and Ch. Gerber, *Phys. Rev. Lett.* 56, 930 (1986)

[81] T. Chang, *MSc thesis*, UC Berkley (2002)

[82] G. Friedbacher and H. Fuchs, *Pure Appl. Chem.* 71, 7, 1337 (1999)

[83] *Theory and Simulation of SPM*, http://invsee.asu.edu/nmodules/spmmod/afm.html

[84] D. Sarid, *Scanning Force Microscopy*, OUP, New York (1991)

[85] *The common AFM modes*, http://www.chembio.uoguelph.ca/educmat/chm729/afm/details.htm

[86] *Atomic Force Microscopy Of Soft Or Fragile Materials*, http://www.azom.com/details.asp?ArticleID=3279#_TappingMode_Imaging_in_Air

[87] K. Franke, J. Besold, W. Haessler and C. Seegebarth, *Surf. Sci. Lett.* 302, 283 (1994)

[88] C. Durkan and M. E. Welland, *Ultramicroscopy* 82, 141 (2000)

[89] Perkin Elmer Instruments, *Technical Note 1000*

[90] A. Gruverman, O. Auciello and H. Tokumoto, *Integ. Ferro.* 19 (1998), 49

[91] C. Franck, G. Ravichandran and K. Bhattacharya, *Appl. Phys. Lett.* 88, 102907 (2006)

[92] S. Dunn, C. P. Shaw, Z. Huang and R. W. Whatmore, *Nanotechnology* 13, 456 (2002)

[93] *Electrostatic Force Microscopy - $PtIr_5$ coating*, http://www.nanoworld.com/print/I-01.html

[94] S. V. Kalinin, S. Jesse, B. J. Rodriguez, J. Shin, A. P. Baddorf, H. N. Lee, A. Borisevich and S. J. Pennycook, *Nanotechnology*, 17, 3400 (2006)

[95] D. Fu, K. Suzuki and K. Kato, *Jpn. J. Appl. Phys.* 41, Pt. 2, 10A, 1103 (2002)

[96] A. Gruverman, O. Auciello, R. Ramesh and H. Tokumoto, *Nanotechnology*, 8, A38 (1997)

[97] Q. M. Zhang, W. Pan and L. E. Cross, *J. Appl. Phys*. 62 , 2492 (1988)

[98] A. Gruverman, O. Auciello, J. Hatano and H. Tokumoto, *Ferroelectrics*, 184, 11 (1996)

[99] S. Dunn and R.W. Whatmore, *J. Euro. Ceram. Soc.* 22, 825 (2002)

[100] T. Abplanalp and P. Günter, *Proceedings of the Eleventh IEEE ISAF*, 423 (1998)

[101] T. Schmitz, K. Prume, B. Reichenberg, A. Roelofs, R. Waser and S. Tiedke, *J. Euro. Ceram. Soc.* 24, 1145 (2004)

[102] B. J. Rodriguez, S. Jesse, A. P. Baddorf, and S. V. Kalinin, *Phys. Rev. Lett.* 96, 237602 (2006)

[103] A. Gruverman and A. Kholkin, *Rep. Prog. Phys.* 69, 2443 (2006)

[104] B. Meyer and D. Vanderbilt, *Phys. Rev. B*, 65, 104111 (2002)

[105] C. H. Ahn, K. M. Rabe and J.-M. Triscone *Science* 488, 303 (2004)

[106] K. Lefki and G. J. M. Dormans, *J. Appl. Phys.* 76, 1764 (1994)

[107] S. Bühlmann, B. Dwir, J. Baborowski and P. Muralt, *Appl. Phys. Lett.* 80, 3195 (2002)

[108] V. Nagarajan, A. Stanishevsky, L. Chen, T. Zhao, B.-T. Liu, J. Melngailis, A. L. Roytburd, R. Ramesh, J. Finder, Z. Yu, R. Droopad and K. Eisenbeiser *Appl. Phys. Lett.* 81, 22 (2002)

[109] G. Arlt and H. Neumann, *Ferroelectrics*, 87, 109 (1988)

[110] *Imprint Effects in Ferroelectric Thin Films for FeRAMs*, http://www.fz-juelich.de/iff/e_iem_research_4/

[111] W. L. Warren, D. Dimos and R. M. Waser, *MRS Bull.* 21, 40 (1996)

[112] M. Alexe, C. Harnagea, D. Hesse and U. Gösele, *Appl. Phys. Lett.* 79, 242 (2001)

[113] Y. Saya, S. Watanabe, M. Kawai, H. Yamada and K. Matsushige, *Jpn. J. Appl. Phys.* 39, 3799 (2000)

[114] C. Harnagea, M. Alexe, J. Schilling, J. Choi, R. B. Wehrspohn, D. Hesse and U. Gösele, *Appl. Phys. Lett.* 83, 1827 (2003)

[115] C. K. Kwok and S. B. Desu, *J. Mater. Res.* 8, 2, 339 (1993)

[116] J. F. Scott, *Ferroelectric Memories*, Springer, Berlin (2000)

[117] A. Gruverman, O. Auciello and H. Tokumoto, *Appl. Phys. Lett.* 69 3191 (1996)

[118] E. L. Colla, S. Hong, D. V. Taylor, A. K. Tagantsev, N. Setter and K. No, *Appl. Phys. Lett.* 72, 2763 (1998)

[119] R. Ramesh, W. K. Chan, B. Wilkens, H. Gilchrist, T. Sands, J. M. Tarascon, V. G. Keramidas, D.K. Fork, J. J. Lee and A. Safari, *Appl. Phys. Lett.* 61, 1537 (1992)

[120] F. L. Ramesh, H. Gilchrist, T. Sands, V. G. Keramidas, R. Haakenaasen and D. K. Fork, *Appl. Phys. Lett.* 63, 26 (1993)

[121] J. Gao, L. Zheng, X. Duo, J. Huang, L. Yang, C. Lin and R. Yan, *Thin Solid Films* 340, 1-2, 132 (1999)

[122] H. F. Kay and J. W. Dunn, *Phil. Mag.* 7, 2027 (1962)

[123] M. Dawber, P. Chandra, P. B. Littlewood and J. F. Scott, *J. Phys.: Condens. Matter* 15, L393 (2003)

[124] S. Ducharme, V. M. Fridkin, A. V. Bune, S. P. Palto, L. M. Blinov, N. N. Petukhova and S. G. Yudin, *Phys. Rev. Lett.* 84, 175 (2000)

[125] G. J. Sloggett, N. G. Barton and S. J. Spencer, *J. Phys. A: Math. Gen.* 19, 2725 (1986)

[126] A. Rüdiger, T. Schneller, A. Roelofs, S. Tiedke, T. Schmitz and R. Waser, *J. Appl. Phys. A* 80, 1247–1255 (2005)

[127] K. Uchino, E. Sadamaga and T. Himse, *J. Am. Ceram. Soc.* 72, 1555 (1989)

[128] U. Ishikawa, T. Yoshikawa and N. Okada, *Phys. Rev. B*, 37, 5852 (1988)

[129] E. Erdem, H-C. Semmelhack, R. Böttcher, H. Rumpf, J. Banys, A. Matthes, H-J. Gläsel, D. Hirsch and E. Hartmann, *J. Phys.: Condens. Matter* 18, 3861 (2006)

Chapter 2: Methodology

2.1 Hydrothermal synthesis

2.1.1 Autoclave

To accommodate the high pressures involved in hydrothermal synthesis a commercially available, oven heated, acid digestion bomb was used.[1] The device consisted of a 45 ml PFTE liner, into which the precursor materials were inserted, surrounded by a screw top steel casing (Fig. 2.1). The absolute maximum rated temperature of the bomb was 250 °C, although when used at temperatures above 200 °C the Teflon liner degraded rapidly. This is because Teflon has a tendency to creep at high pressures making it hard to attain a tight seal.[2] For this reason hydrothermal experiments were restricted to temperatures at or below 200 °C.

A water-based solution heated to 250 °C occupies a 25% larger volume than at room temperature, so it is essential accommodate for this expansion during hydrothermal experiments. If not, the immense hydrostatic pressures would destroy the bomb. Therefore, in all hydrothermal experiments, the total volume of the charge was kept below 30 ml.

A thermostatically controlled laboratory oven was used to heat the bomb. The oven was pre-heated to the reaction temperature before the start of each experiment. The temperature of the bomb was taken at the surface of the steel casing using a K-type thermocouple and meter accurate to ± 0.05 °C. Timing started when the meter recorded the desired reaction temperature. Reaction times ranged from 0 minutes (oven shutdown as soon as the reaction temperature was reached) up to 24 hr. At the end of each experiment the oven was switched off and the door left open to increase the cooling rate of the bomb. All runs were repeated twice to verify the reproducibility of the results.

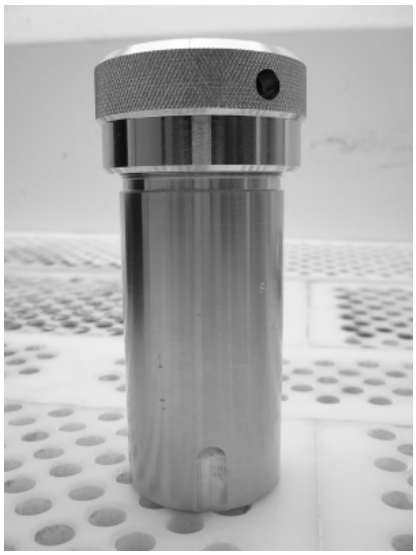

Fig. 2.1 Parr acid digestion bomb used for the hydrothermal experiments.

2.1.2 General hydrothermal procedure for the synthesis of perovskite P(Z)T powder

The basic hydrothermal procedure used in this project was first proposed by Deng et al. for the synthesis of PZT.[3] It is a relatively simple one-step technique that utilises the following precursors in powdered form:

- Lead nitrate - $Pb(NO_3)_2$
- Zirconyl oxychloride - $ZrOCl_2 \cdot 8H_2O$
- Titanium dioxide (anatase) - TiO_2

In their paper, Deng et al. produced 52:48 PZT by adding stoichiometric quantities of the precursors to a home-built autoclave with 100 ml capacity. Next, 80 ml of deionised water were added and the mixture stirred vigorously. Finally, potassium hydroxide flakes were added slowly, with continuous stirring, to give an initial mineraliser concentration of 5 mol/l. After the hydrothermal treatment the powders were filtered and washed with distilled water and ethanol and then dried in an oven at 80 °C. These procedures were replicated exactly during this project. However, since a smaller bomb was used, a scaling factor of 5/16 = 0.3125 was applied to all the quantities. Table 2.1 shows the adjusted precursor masses for 52:48 PZT and several other stoichiometries, across the solid solution range, that were attempted in this

project. The precursors were mixed with 25 ml deionised water and 7.013 g KOH to reproduce the 5 M initial mineraliser concentration used by Deng et al.[3]

Table 2.1 Hydrothermal precursor masses for stoichiometries across the PZT solid solution.

STOICHIOMETRY→ / **PRECURSOR ↓**	$PbTiO_3$	20:80	52:48	60:40	70:30	$PbZrO_3$
$Pb(NO_3)_2$	2.070 g	2.070 g	2.070 g	2.070 g	2.070 g	2.070 g
$ZrOCl_2 \cdot 8H_2O$	-	0.403 g	1.047 g	1.208 g	1.410 g	2.014 g
TiO_2	0.499 g	0.399 g	0.240 g	0.200 g	0.150 g	-

All chemicals were analytical grade and obtained from Sigma-Aldrich, UK (TiO_2 and KOH) or Fisher Scientific, UK ($ZrOCl_2 \cdot 8H_2O$ and $Pb(NO_3)_2$). A standard Buchner vacuum filtration system was used in conjunction with Whatman No. 6 (3 μm pore size) filter paper, to isolate the product. This trapped the majority of the particles since they had agglomerated after processing. The powders were rinsed using deionised water.

2.1.3 Adaptations to the general hydrothermal procedure

Several attempts were made to adapt the general hydrothermal procedure discussed in the previous section. The motivation behind these adaptations is discussed in *Chapter 4*; however, the technical details of some of the modifications are shown below.

2.1.3.1 Alternative Ti precursor

Amorphous hydrous titania was trialled as an alternative Ti precursor in this project to replace the commercial anatase TiO_2 powder used in the general hydrothermal procedure. It was synthesised according to the procedure by Kamat et al.[4] Firstly, a solution containing 100 ml absolute ethanol (Aldrich, UK), 20 ml deionised water and 2 ml glacial acetic acid (Aldrich, UK) was prepared. Next, 3 ml of titanium isopropoxide (Aldrich, UK) was added, dropwise, under continuous stirring. After 24 hr the reaction was stopped and the solvent left to evaporate at ambient temperatures. This produced a gel that was substituted for anatase in the general hydrothermal

procedure. A sample of the gel was weighed before and after dehydrating at 200 °C for 12 hrs in a conventional oven. From the mass lost it was calculated that the gel contained 73% TiO_2. Powder XRD and EDAX analyses (techniques discussed in *Sections 2.3.1* and *2.3.2.1*, respectively) confirmed that amorphous TiO_2 had been produced.

2.1.3.2 Alternative mineraliser

The effects of substituting the KOH mineraliser with NaOH were tested.

2.1.3.3 Surfactant-assisted hydrothermal synthesis

Several compounds were tested for their ability to inhibit the hydrothermal growth rate of PZT crystals. These were: the non-ionic surfactant Triton X-100, the chelating agent ethylenediaminetetraacetic acid (EDTA), oleic acid and stearic acid. Aldrich, UK supplied all the chemicals.

Triton X-100 was dissolved in warm deionised water under continuous stirring to make two solutions of 2% and 5% v/v concentration. Saturated EDTA solutions were prepared by dissolving 1.5 g in 150 ml warm deionised water, again under continuous stirring. The resultant solutions were used in separate hydrothermal experiments as a replacement for pure deionised water.

The surfactant properties of oleic acid and its saturated counterpart stearic acid were compared in separate hydrothermal experiments. Aqueous solutions containing 2% v/v of each acid were used in place of pure deionised water.

2.1.3.4 Hydrothermal treatment of PZT sol

A PZT gel was used as a replacement for the precursors in the general hydrothermal method. The synthesis of the sol proceeded as follows: Firstly, $Pb(OAc)_2{\cdot}3H_2O$ (Aldrich, UK) was dissolved in methanol with gentle warming. Next, $Zr(O^nPr)_4{}^nPrOH$ (Aldrich, UK) and $Ti(O^nBu)_4$ (Aldrich, UK), in a 52:48 ratio, were dissolved in a mixed solution of acetic acid and methanol. This solution was stirred at room temperature for 1 hr. The Pb solution was added to the Zr/Ti solution and the

mixture refluxed for 2 hr. Acetic acid (Aldrich, UK) was added to adjust the pH and the PZT concentration to 0.4 M. The resulting yellow solution was passed through a filter (0.2 μm pore size) and ethylene glycol (Aldrich, UK) was added. A gel was obtained by drying the above sol at 70 ºC for 24 h. After grinding the gel to a fine powder, 2 g was added to the bomb along with 25 ml deionised water and the mixture stirred well. Finally, 4.63 g of KOH was added slowly to make an initial mineraliser concentration of 3.3 M.

2.1.4 Hydrothermal deposition of epitaxial PZT nanostructures and thin films

Epitaxial PZT nanostructures and films were hydrothermally deposited on single-crystal (100) $SrTiO_3$ and 1% Nb-doped (100) $SrTiO_3$ substrates, measuring 10 × 5 × 0.5 mm (L × W × T). The substrates were single-side polished, sourced from MTI Corporation (USA) and were used without further preparation. PZT precursor solutions were prepared following the general hydrothermal technique. The substrates were placed polished side up at the bottom of the bomb after mixing the precursors.

2.2 Solid phase synthesis

The in situ method of producing P(Z)T was developed from the work of Sidorkin et al.[5] and Stankus et al[6]. In this project the Ti thin films were deposited via sputtering and the Pb thin films by thermal evaporation. The techniques of conventional and rapid thermal annealing, under air, were used to crystallise the perovskite $PbTiO_3$ phase. A hotplate was also used for a small number of experiments. Attempts were made, post-annealing, to analyse the ferroelectric properties of the films.

The solid phase synthesis technique was adapted in a bid to produce ferroelectric nanoislands, whose properties were subsequently tested using PFM. Finally, the feasibility of generating PZT with the technique was attempted by adding a Zr layer to the original Pb/Ti bilayer system.

2.2.1 Substrates

A variety of substrates were tested during the in situ synthesis investigation and these are listed below:

- Mechanical-grade, 4" (100) Si wafers (500 μm thick) that were p-type, boron-doped and single-side polished (SSP). The wafers were cleaned with acetone then IPA before use.

- Prime-grade, 4" (100) SiO_2/Si wafers (500 μm thick), p-type, boron-doped and SSP. The thickness of the thermal oxide layer was 400 nm. The wafers were used without further treatment.

- Soda lime glass coated with a polished SiO_2 layer and then 125 nm of ITO. Substrates were cleaned in an ultrasonic bath, first under soap solution and subsequently with IPA.

- Nb:SrTiO3 single-crystal wafers of the same specification as discussed in *Section 2.1.4*.

2.2.2 Sputter deposition

Sputter deposition involves the bombardment of a target material with energetic ions in order to generate a vapour that subsequently deposits onto a substrate. In this project two types of sputtering were used: DC magnetron sputtering for depositing Pt (source: PI-KEM, UK 99.9 % purity) and RF magnetron sputtering for depositing Zr (PI-KEM, UK 99.9 %) and Ti (PI-KEM, UK 99.7 %). The basic principle behind both techniques is the same and begins with an evacuated chamber into which Ar gas, at a low pressure, is introduced. A glow-discharge plasma is struck between the target (cathode) and an adjacent shield (anode) by applying either a steady voltage (DC sputtering) or an AC voltage (RF sputtering). Positive Ar ions are accelerated towards the target and "sputter" atoms, through momentum exchange, out into the chamber. Those that hit the substrate condense to form a thin film. Secondary electrons are also emitted through the bombardment of the target and these maintain the plasma by ionising further Ar atoms. Permanent magnets behind the target form a toroidal field

that confines the plasma to a ring close to the target. Because the path length of electrons within the plasma is increased, the minimum gas pressure to sustain the plasma is reduced. This helps to boost sputtering rates since the sputtered atoms are subjected to fewer collisions on their way to the substrate. RF sputtering is advantageous for insulating targets or targets with reduced conductivity as it prevents charge build up and also reduces the drive voltage necessary to maintain the plasma.

A Nordiko 2000 sputtering system was used during this investigation (Fig. 2.2). This machine was equipped with three magnetrons (two for RF sputtering and one for DC sputtering). Samples were loaded onto one of six substrate holders, which, in turn were fitted to a motorised central spindle. A computer was used to rotate the samples into the correct position above the relevant target. Fig. 2.3 shows a photograph of one of the RF magnetrons together with the spindle and shutter assemblies. In this picture the substrate holder has been removed and the shutter left open to show the target.

Fig. 2.2 Nordiko 2000 sputtering system.

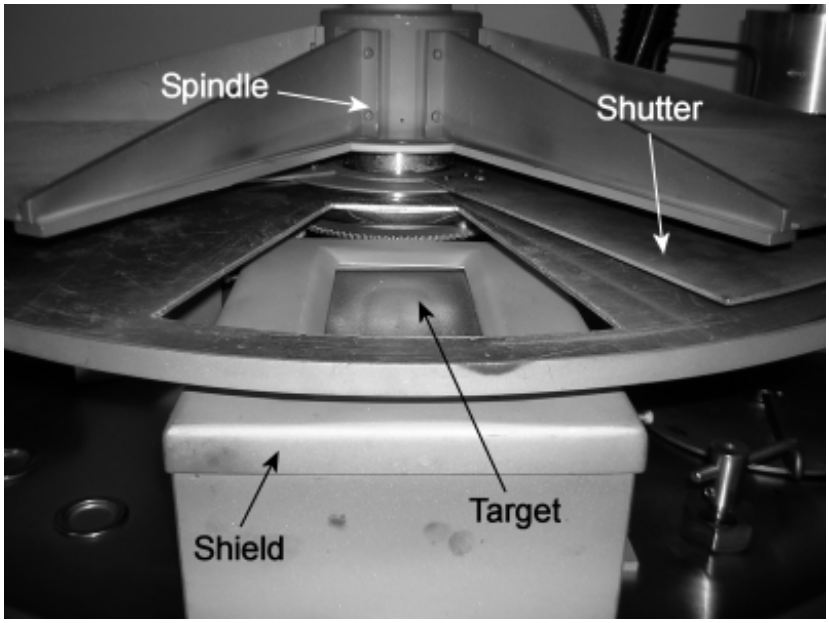

Fig. 2.3 Photograph of the sputtering chamber (substrate holder was removed for clarity).

As there was no in situ means of measuring deposition rates, two post deposition methods were used to determine the average sputtering rate. The first was step height measurement using a Dektak 3ST profilometer (for Ti and Pt) and the second was film cross-sectional measurement using an SEM (Zr). Table 2.2 shows the established average sputtering rates for the three targets in question. The Si wafers were cleaved into quarters before sputtering to ensure a consistent coating across the entire surface. Also, care was taken to position samples in the centre of the substrate holder, since the sputtering rates decreased significantly towards the edges.

Table 2.2 Sputtering rate data for the Nordiko 2000 system.

Target	Type	Power /watts	Rate /nm·s^{-1}
Pt	DC magnetron	300	2.38 ± 0.05
Ti	RF magnetron	300	0.28 ± 0.01
Zr	RF magnetron	300	0.82 ± 0.05

The Nordiko system was evacuated to base pressures below 1.3×10^{-3} Pa (10^{-3} mtorr) before sputtering commenced. Ar gas was then introduced at a flow rate that maintained a pressure of 1.3 Pa (10 mtorr). A 10 min pre-sputter was employed to remove surface oxide and/or contaminants from the Ti and Zr targets. In the case of Pt, a shorter, 2 min pre-sputter was used that took into account the reduced reactivity of the material and its significant monetary value.

Back electrodes were deposited onto the non-conductive substrates in order to test the ferroelectric properties of the heterostructures. The standard procedure involved depositing an 8 nm Ti adhesion layer, followed by 100 nm of Pt, without breaking vacuum. Adhesion layers are used to join layers in a thin film system that would otherwise be incompatible. Since Ti is a relatively reactive metal it can break an O-Si bond on the surface of a Si or thermal oxide wafer and form a Ti-O or Ti-Si bond. Conversely, Pt, being a noble metal, cannot do this and thus has limited adhesion to Si wafers. However, Pt *can* form strong metallic bonds with unoxidised Ti. Hence, with an intermediate reactive layer, Pt can be made to adhere well to Si wafers.

2.2.3 Thermal evaporation

Thermal evaporation was used to deposit Pb for the in situ technique and Cr/Au top electrodes onto ferroelectric thin films. The technique is very simple and involves heating an evaporation source, under vacuum, by passing a large current through it (Joule effect). Refractory (high melting point) metals, such as W, Ta and Mo are examples of commonly used evaporation sources. The evaporant, which has a lower melting point, is inserted into the source and the chamber evacuated. As the current is increased, the evaporant vaporises and condenses on a substrate placed above the source. Vacuum pressures below 1.33×10^{-3} Pa are necessary to prevent the atoms in the vapour oxidising before coming into contact with the substrate and to ensure a large mean free path.

The amount of heat generated through Joule heating is I^2R, where R is the parallel resistance of the source and evaporant at the evaporation temperature, T. T is nonuniform because some heat is conducted down the electrodes. Therefore, unlike sputter deposition, it is essential to monitor the evaporation rate in situ as it is highly variable. One common method is to use a crystal rate monitor. These utilise the resonant properties of piezoelectric quartz wafers to detect a vapour flux and thus give an estimate of the amount of material that is deposited on a substrate during the evaporation. A quartz wafer generates an oscillating voltage across itself when vibrating at its resonant frequency, and this voltage can be amplified and fed back to drive the crystal at this frequency. Metal electrodes on opposite faces of the wafer act as electrical coupling. During a deposition one side of the wafer is exposed to the

vapour flux and proceeds to accumulate mass, which subsequently reduces the resonant frequency, ν_r, of the crystal. By comparing the reduced frequency with the ν_r of a reference crystal, located in the control unit, the mass of the deposit can be calculated. Measurements of any quantity relative to a reference value of similar magnitude is always more accurate than making an absolute measurement and as such the instrument has a submonolayer resolution.[7]

An Edwards E480 thermal evaporator was used for the evaporation experiments in this project (Fig. 2.4). The system was pumped down to pressures below 3×10^{-4} Pa (2.25×10^{-6} torr) before commencing the experiments. Table 2.3 lists the evaporants deposited together with their associated parameters.

Fig. 2.4 Edwards E480 thermal evaporator.

Table 2.3 Evaporation parameters for the metals deposited in the project.

Evaporant	Source (max I)	Evaporation current /A
Pb sheet	Mo boat (70 A)	30
Cr granules	W wire (40 A)	30
Au wire	Mo boat (25 A)	25

During the solid phase synthesis experiments a shutter was fitted above the source. This meant it was possible to pre-evaporate the Pb (source: Goodfellow, UK) for 30 s in order to remove oxides and contaminants. It also lent a finer degree of control over the deposition, since the vapour flux could be shut off almost instantaneously.

A W wire source was used to evaporate Cr granules in place of a Mo boat. This was to enhance the source-evaporant contact to compensate for the lack of wetting associated with the sublimation of Cr. Top electrodes were produced by evaporating 15 nm of Cr (adhesion layer) and 100 nm of Au through a mask that had holes with an area of 0.48 mm^2.

Flux monitoring was achieved using a crystal rate monitor that measured the instantaneous rate and total thickness to an accuracy of $\pm$ 0.1 nm. Fig. 2.5 shows the arrangement of the electrodes, shutter and rate monitor within the evaporating chamber. The sample stand was removed for clarity.

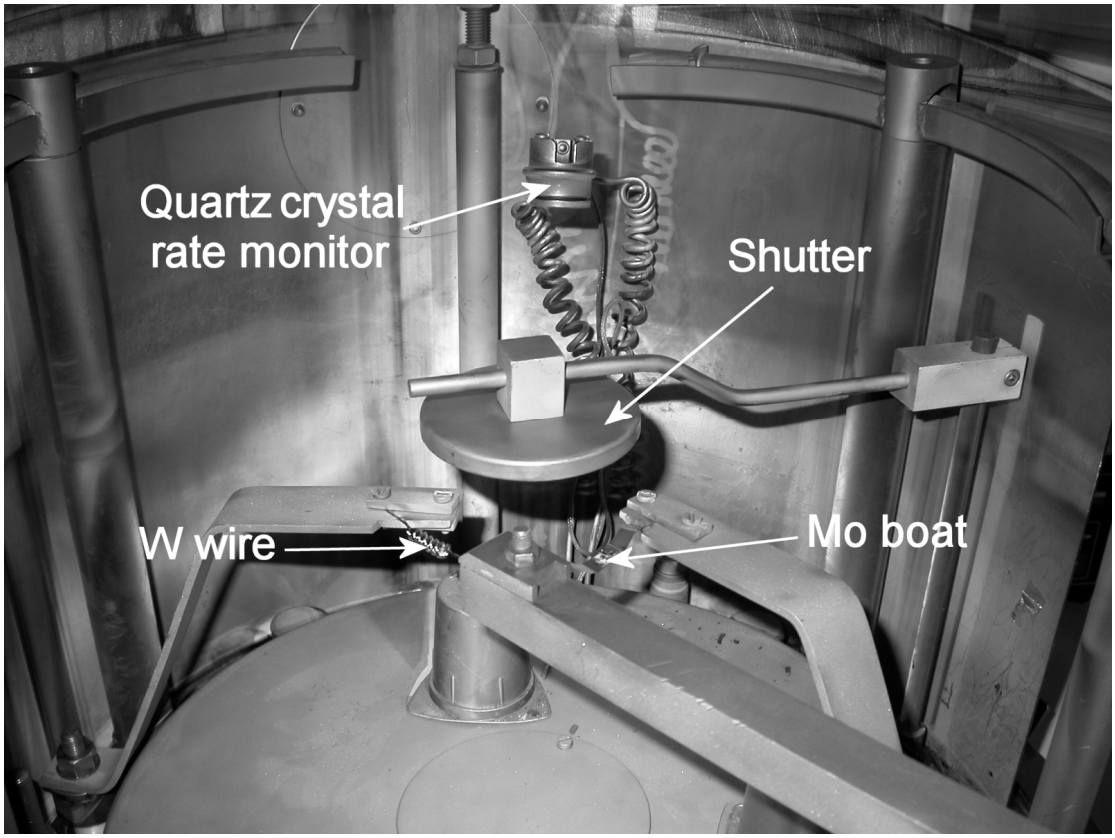

Fig. 2.5 Photograph of the evaporating chamber.

2.2.4 Annealing

2.2.4.1 Conventional chamber furnace

A conventional chamber furnace (Carbolite ELF 11/6B) was used for the majority of the in situ annealing experiments. The temperatures and reaction times investigated ranged from 300 – 900 °C and 5 min to 72 hrs, respectively. Samples were loaded into the furnace while cold. The furnace had a programmable electronic control unit with a number of inbuilt heating profiles. In general, unless stated otherwise, the ramp rate used for the annealing experiments was 5 °C/min. The power of the furnace was reduced to 40% for temperatures below 400 °C to minimise temperature overshoot. Timing started once the desired operating temperature had been reached.

2.2.4.2 Rapid thermal annealing

An AG Associates Heatpulse 210 rapid thermal annealer was used for a minority of the in situ annealing experiments. The device consisted of a small quartz chamber

sandwiched between two banks of water-cooled quartz-tungsten-halogen lamps. The tray-type door of the chamber incorporated a quartz plate, onto which a wafer was mounted. A K-type thermocouple was brought into contact with the wafer to give accurate in situ temperature measurements. An O-ring fitted to the door isolated the chamber allowing samples to be annealed under different atmospheres (compressed air, N_2 and Ar). Heating control was fully automated and handled by a computer. Wafers were annealed between 500 – 800 °C for up to 2 min, with ramp rates fixed at 60 °C/s.

2.3 Analysis

2.3.1 Powder x-ray diffraction

The phase composition and degree of preferential orientation in powders and thin films was determined by powder x-ray diffraction (XRD) using the Bragg-Brentano goniometer geometry (Fig. 2.6). In this geometry the sample is moved through an angle θ whilst the detector is scanned through an angle 2θ – producing a so-called θ-2θ scan. At values of 2θ for which the lattice spacing *d* of the sample satisfies the Bragg condition, $n\lambda = 2d\sin\theta$, a peak appears from which *d* can be derived. The peak intensity gives a qualitative measure of the preferential orientation.

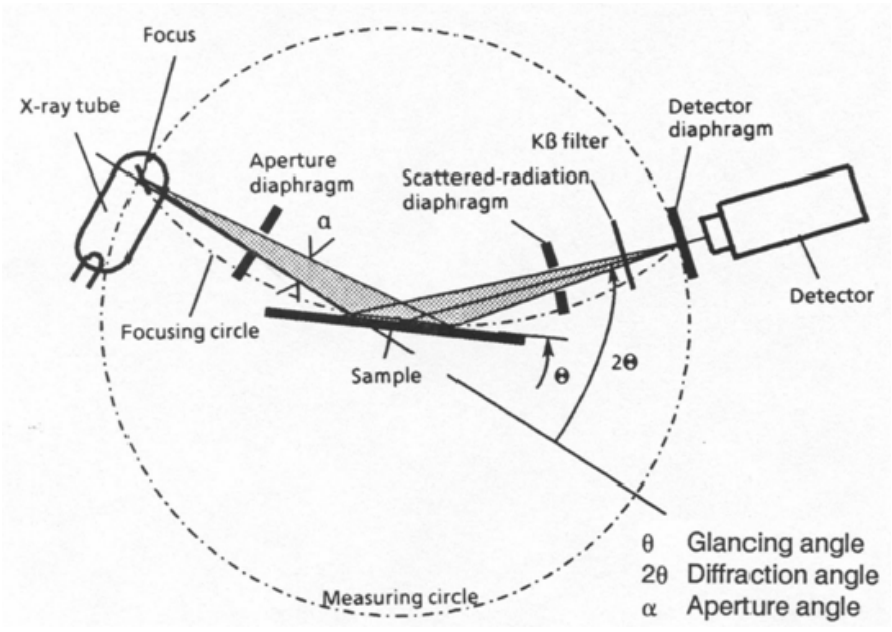

Fig. 2.6 Schematic of the Bragg-Brentano diffractometer geometry.[8]

A Siemens D5005 diffractometer was used for all the XRD experiments. The x-ray tube emitted CuKα (λ = 1.5406 Å) radiation at 40 kV and 30 mA. In general, θ-2θ scans were conducted between 20 – 90° in increments of 0.04° with a dwell time of 1 s per increment. Powder samples were prepared by grinding in a pestle and mortar to limit the possibility of preferential orientation. Phase identification involved matching peaks from a given scan with the accepted values for compounds found in the Powder Diffraction File (PDF-2) database, produced by the International Centre for Diffraction Data (ICDD). The PCPDFWIN software was used to search the database to find patterns that matched specified sample parameters, e.g. known elements or the d-values of intense peaks. This reduced the number of possible phase candidates to a more manageable size.

2.3.2 Scanning electron microscopy

Scanning electron microscopy (SEM) was the primary imaging technique used throughout the project. Its many benefits include minimal sample preparation requirements, a wide magnification range and the ability to resolve features below 10 nm. The system used during the investigation was a Sirion XL30 Schottky Field Emission Gun (SFEG) SEM. This type of SEM utilises a sharp, tungsten-based tip at which a very high electric field concentrates ($> 10^7$ Vm^{-1}). Under these circumstances electrons can tunnel through the reduced potential barrier and are then accelerated up to the required beam voltage. Field emission SEMs have a very high brightness (current density per solid angle) compared to conventional thermionic emitters. This means that they can provide a high electron density over a smaller spot area, obtaining high resolutions (better than 1.5 nm under ideal conditions) at relatively low accelerating voltages (5 kV).

Samples inspected under the SEM were prepared in such a way as to minimise the effects of charging on the images. In the case of powders this meant depositing very small quantities on adhesive carbons stubs. Wafers were attached to the sample holder using aluminium tape. For low resolution imaging (< 5,000 ×) an Everhart-Thornley secondary electron detector was used. Higher resolutions were achieved by setting working distances to ≤ 5 mm and using the through-the-lens secondary electron

detector (TLD). This detector was mounted within the lens and received electrons in the immediate vicinity of the scanned area.

2.3.2.1 Energy dispersive analysis by x-rays

If a high energy particle, such as an electron, strikes a bound atomic electric within a sample, and the energy of the particle is greater than the binding energy of the atomic electron, it is possible for the atomic electron to be ejected from the atom. This vacancy in the atomic shell leaves the atom in an unstable state and leads to one of two possible outcomes. The first involves a rearrangement that results in the emission of another electron – the so-called Auger effect. The second process by which the atom can regain stability is by the transfer of a higher orbital electron into the vacancy left by the ejected electron. This can result in the emission of an x-ray characteristic of the element and is expressed by Moseley's Law:

$$\frac{1}{\lambda} = K(Z-\sigma)^2 \qquad \text{Eqn. 2.1}$$

where K is a constant that depends on the spectral series, Z is the atomic number and σ is a shielding constant. Fig. 2.7 shows the characteristic x-rays associated with the K, L and M spectral series.

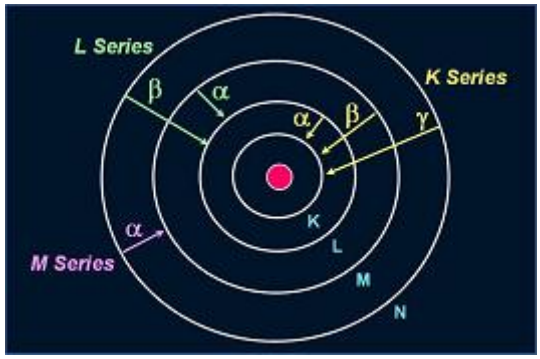

Fig. 2.7 Characteristic x-rays associated with electronic transitions.[9]

Energy dispersive analysis by x-rays (EDAX) involves measuring the characteristic energy, as opposed to wavelength, of incident atomic x-rays. The SEM used in the project was fitted with an integrated EDAX detector to make localised x-ray

fluorescence measurements. Field emission SEMs, with their reduced spot areas, are particularly suited for making nanoscale EDAX measurements. When analysing nanostructures, a compromise must be made when choosing a suitable electron beam voltage. The interaction volume of the electron beam inside the sample scales with the beam voltage, so a large voltage may produce many characteristic x-rays from the substrate. This unwanted background noise might mask the signal produced by the atoms in the nanostructure. Furthermore, quantitative analysis of the elements can become difficult. However, if a low beam voltage is used, the electrons may not have sufficient kinetic energy to remove atomic electrons from within the nanostructure. In this project EDAX analysis was conducted using beam voltages in the range 10 – 20 kV with the working distance set to 5 mm.

2.3.3 Focussed-ion beam milling

A focussed-ion beam (FIB) system uses a gallium ion beam to raster scan a sample in a similar way to an electron beam in a SEM. Ions, originating from a liquid-metal ion source, are accelerated from a tungsten tip towards the sample using electric fields in the range 30 – 50 kV. Images are formed by detecting the secondary electrons emitted as a result of the interaction between the beam and the sample. Alternatively, parts of a sample can be selectively etched by using higher beam energies. In this investigation an FEI Sirion 200 XP FIB system was used to section cubic PZT crystals in order to analyse their internal structure.

2.3.4 Polarisation hysteresis measurements

An RT66A Standardized Ferroelectric Test System was used to analyse the ferroelectric hysteresis properties of thin film samples produced during the project. This instrument combines the features of a function generator, an electrometer and a digital oscilloscope in a single PC controlled unit. Details of the sample, such as thickness and electrode size, are inputted into the software, which then executes the appropriate hardware commands and collects and processes the data. The results are displayed in the form of polarisation vs. field curves.

The system can produce polarisation hysteresis curves in one of two ways: conventional Sawyer-Tower circuit mode or virtual ground circuit mode. The Sawyer-Tower circuit consists of a linear sense capacitor connected in series to the sample. The voltage across the sense capacitor measures the charge stored on the sample, which is related back to the polarisation. This is a simple technique but requires an accurately known sense capacitance of far greater magnitude than the sample capacitance. In contrast, the virtual ground circuit is composed of a current integrator connected in series with the sample. By measuring the charge collecting on the integrating capacitor, the polarisation is easily calculated. This circuit improves reproducibility and allows smaller capacitances to be measured with greater accuracy than the Sawyer-Tower method. All measurements in this investigation were made using the virtual ground circuit mode.

The inbuilt power supply of the system can apply a maximum of ± 20 V across a sample. If the thickness of a sample exceeds 1 μm then it is unlikely that this drive voltage will be able to overcome the coercive field. In these circumstances a high voltage interface was used in combination with a Trek 610D amplifier.

The RT66A system can also test for fatigue in ferroelectric samples. It does this by performing a large ($> 10^6$) number of hysteresis cycles and measuring the remanent polarisation at preset intervals. A fatigued sample will show a decrease in the remanent polarisation over time.

2.3.5 Atomic force microscopy

A Digital Instruments Dimension 3000 AFM (Fig. 2.8) was used to analyse the surface topography and ferroelectric properties of samples during the project. Contact mode was used to make high-resolution topographical images of nanoisland samples and combined topography-PFM scans.

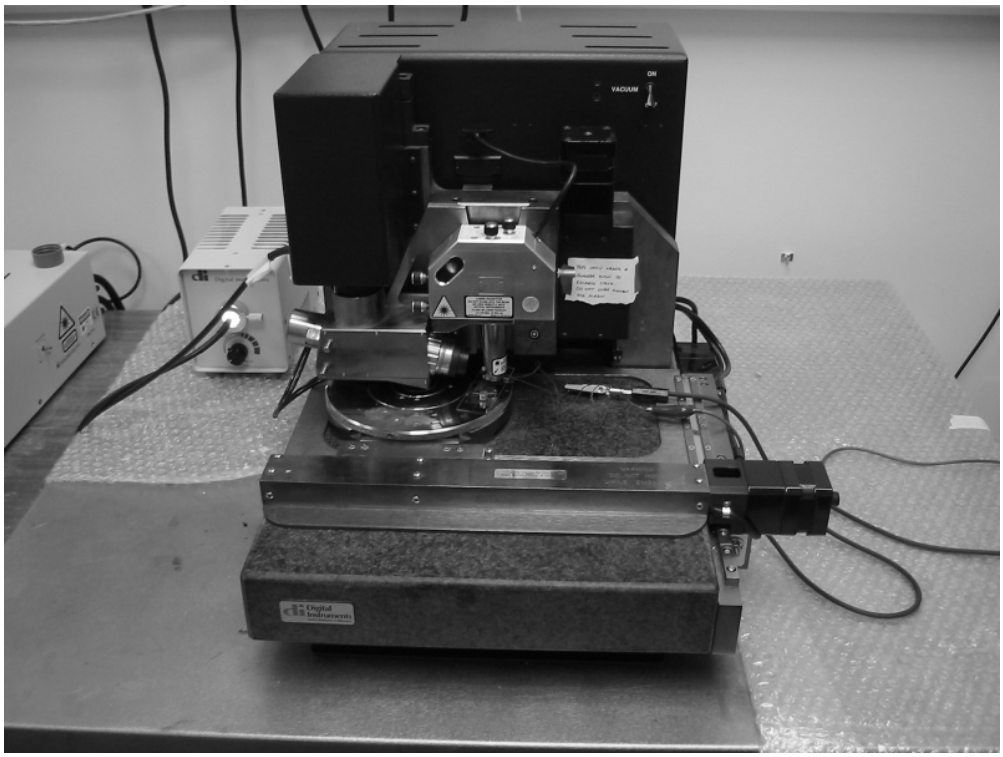

Fig. 2.8 Digital Instruments Dimension 3000 atomic force microscope.

The tips used during the investigation were composed of boron-doped p-type Si and manufactured by NANOSENSORS (NanoWorld AG). For electrical measurements, tips coated with a 25 nm double layer of $PtIr_5$/Cr were used.

2.3.5.1 Piezoresponse force microscopy

The modifications necessary to operate the AFM in PFM mode are illustrated schematically in Fig. 2.9. In order to map the piezoresponse from a particular area of a sample, the following method was adopted. An AC drive voltage was applied between the conducting tip and the back electrode of the sample using an HP33120A function generator. A lock-in amplifier (EG&G Instruments 7260) was provided with the same reference frequency from the function generator, together with the signal from the AFM, via the signal access module. The vibrations generated by the converse piezoelectric effect were isolated by the lock-in amplifier and sent back to the signal access module. A PC, also connected to the signal access module, then displayed the topography and associated piezoresponse of the region being scanned, simultaneously.

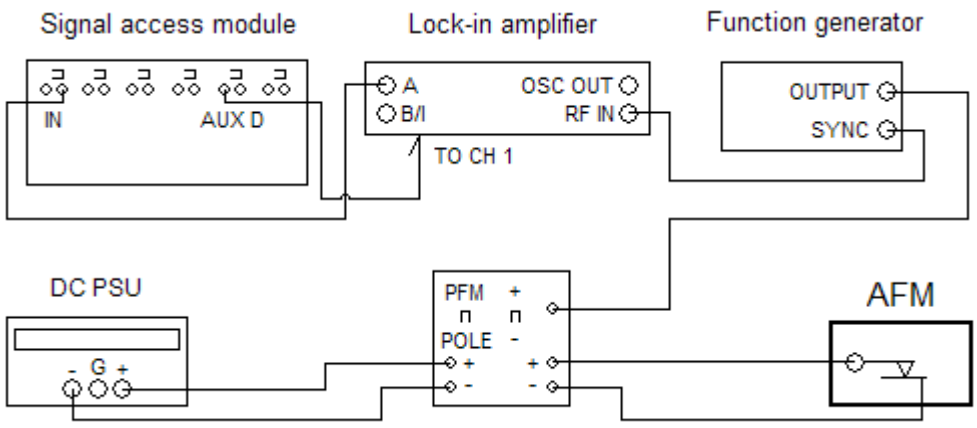

Fig. 2.9 Schematic diagram of the PFM apparatus.

Poling was accomplished by applying a positive or negative DC voltage from an Isotech IPS1603D PSU, between the tip and the bottom electrode, whilst scanning an area of the sample. Evidence of switching was detected by conducting a before-and-after piezoresponse scan of a larger area that incorporated the poled region.

2.3.5.1.1 Infield hysteresis loop measurements

Localised infield hysteresis measurements were attempted by positioning the tip over a single grain and setting the scan size to zero. A DC voltage was then applied slowly, in 0.1 V increments, whilst simultaneously monitoring the piezoresponse amplitude displayed on the lock-in amplifier. At the positive saturation point the voltage was decreased, again in 0.1 V increments, until the negative saturation point was reached. To complete the loop the voltage was raised to zero.

References

[1] Parr Instrument Company, Illinois, Model 4744 (45 ml capacity)

[2] Operating Instructions – Parr Acid Digestion Bombs

[3] Y. Deng, L. Liu, Y. Cheng, C.W Nan and S. Zhao, *Mater. Lett.* 57, 1675 (2003)

[4] P. V. Kamat, I. Bedja, and S. Hotchandanit, *J. Phys. Chem.* 98, 9137 (1994)

[5] A. S. Sidorkin, A. S. Sigov, A. M. Khoviv, S. O. Yatsenko and O. B. Yatsenko, *Phys. Solid State*, 42, 4, 745 (2000)

[6] V. Stankus and J. Dudonis, *Mat. Sci. Eng. B*, 109 178 (2004)

[7] D. L. Smith, *Thin Film Deposition: Principles & Practice*, McGraw-Hill, New York (1995)

[8] Operating Instructions – Siemens D5000 X-ray diffractometer

[9] *EDX Analysis and WDX Analysis*, http://www.siliconfareast.com/edxwdx.htm

Chapter 3: Hydrothermal Synthesis of PZT Nanostructures

3.1 Introduction

Initially, attempts were made to replicate the work by Deng et al. in synthesising PZT nanocrystals using a hydrothermal method.[1] Stoichiometric quantities of the precursors described in *Section 2.1.2*, necessary to produce 52:48 PZT, were added to the bomb and heated for 4 hr at 160 °C. The morphology of the resultant particles is shown in Fig. 3.1. There was a wide size distribution; however, the major particles were cubic and micron-sized. Irregularly shaped agglomerates were also present. This contradicted the findings of Deng et al. who, under the same conditions, described nearly homogeneous spherical particles with an average diameter of 5 – 10 nm, in their paper. The powder XRD results (Fig. 3.2) were in better agreement however, with a single identifiable phase that was a reasonable qualitative match to the accepted ICDD PDF card no. 33-0784 for tetragonal 52:48 PZT. The *c*/*a* ratio, determined from the (200) and (002) peaks in the XRD pattern, was found to be equal to 1.03. This suggests that the actual phase synthesised lay closer to the 50:50 PZT composition.[2]

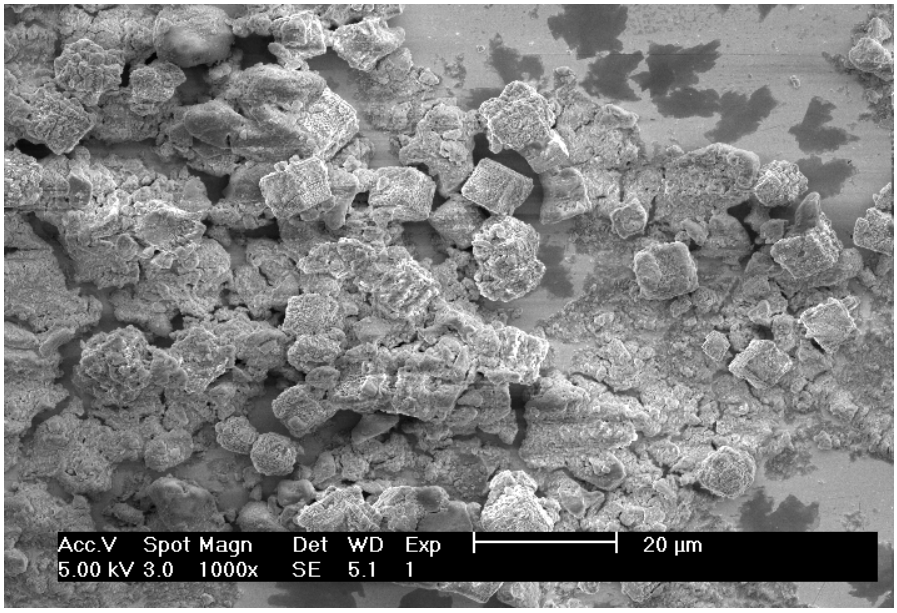

Fig. 3.1 A SEM image showing the morphology of particles produced after a 4 hr hydrothermal reaction at 160 °C.

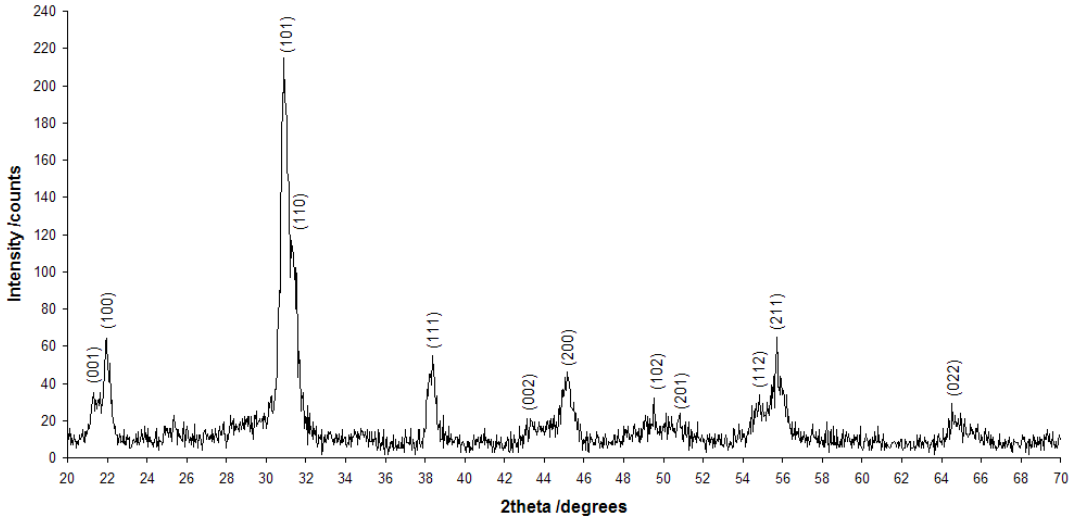

Fig. 3.2 XRD data for the powder produced after a 4 hr hydrothermal reaction at 160 °C (indexed peaks correspond to the accepted values for 52:48 PZT, PDF card no. 33-0784).

These results demonstrated the feasibility of producing phase-pure PZT powders using the method proposed by Deng et al. However, the particle size was two orders of magnitude larger than that required for the investigation. Therefore, efforts were concentrated on finding ways to reduce particle sizes.

3.2 Attempts to reduce PZT crystal size

3.2.1 Altering processing time

The first variable to be altered in the general hydrothermal synthesis technique was the processing time. Since it is established that PZT crystals synthesised using the hydrothermal technique form via a dissolution-precipitation mechanism, if the reaction could be quenched during the growth stage it should be possible to tailor particle size. The XRD results for reaction times from 30 min up to 4 hr at 160 °C are shown in Fig. 3.3. As can be seen, MPB PZT becomes the dominant phase after 30 minutes of processing. Full crystallisation is attained after somewhere between 1.5 – 2 hr of processing.

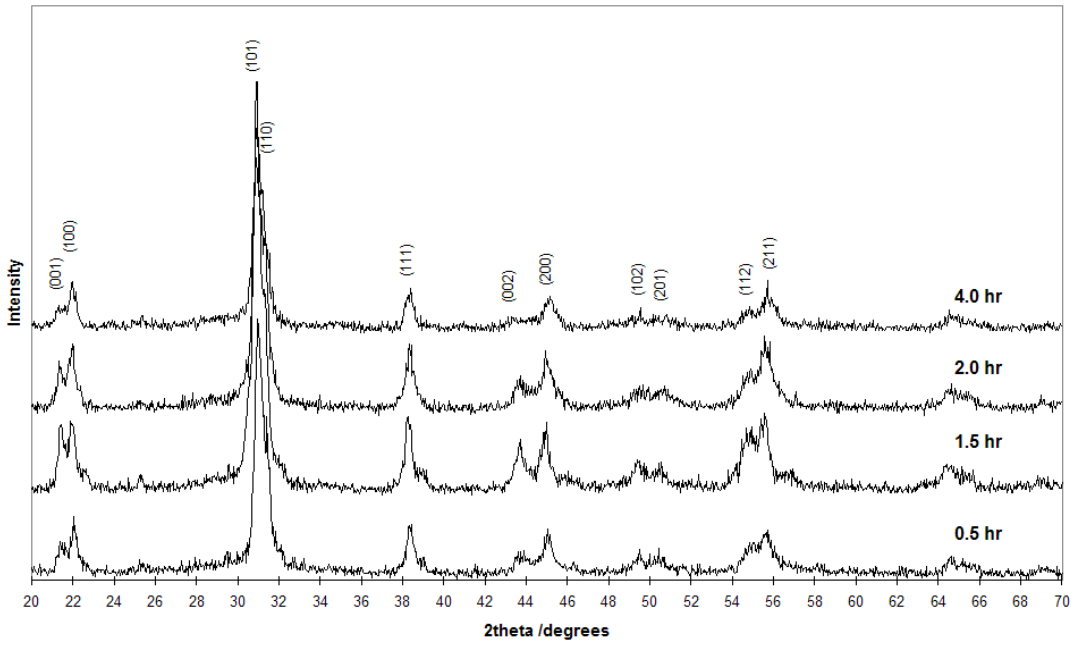

Fig. 3.3 XRD data for PZT powder synthesised at 160 °C over a range of times from 30 min to 4 hr (indexed peaks correspond to the accepted values for 52:48 PZT, PDF card no. 33-0784).

The resultant particle morphology for each processing time is shown in Fig. 3.4, parts a) – d). The cubic particles ranged in size from 2.5 – 5 μm for the 30 min – 2 hr reactions. In the case of the 4 hr reaction, the average particle size was slightly larger, but this was most likely due to a local inhomogeneity in the precursor solution, since later experiments involving 6 hr reaction times produced powders that shared the same size range as the shorter reaction times. Therefore, it would appear that systematic changes in morphology do not appear to take place with increasing processing time – cubic particles, once formed, undergo little change. The results also suggest that reducing processing times is not a feasible method of inhibiting crystal growth during the precipitation stage.

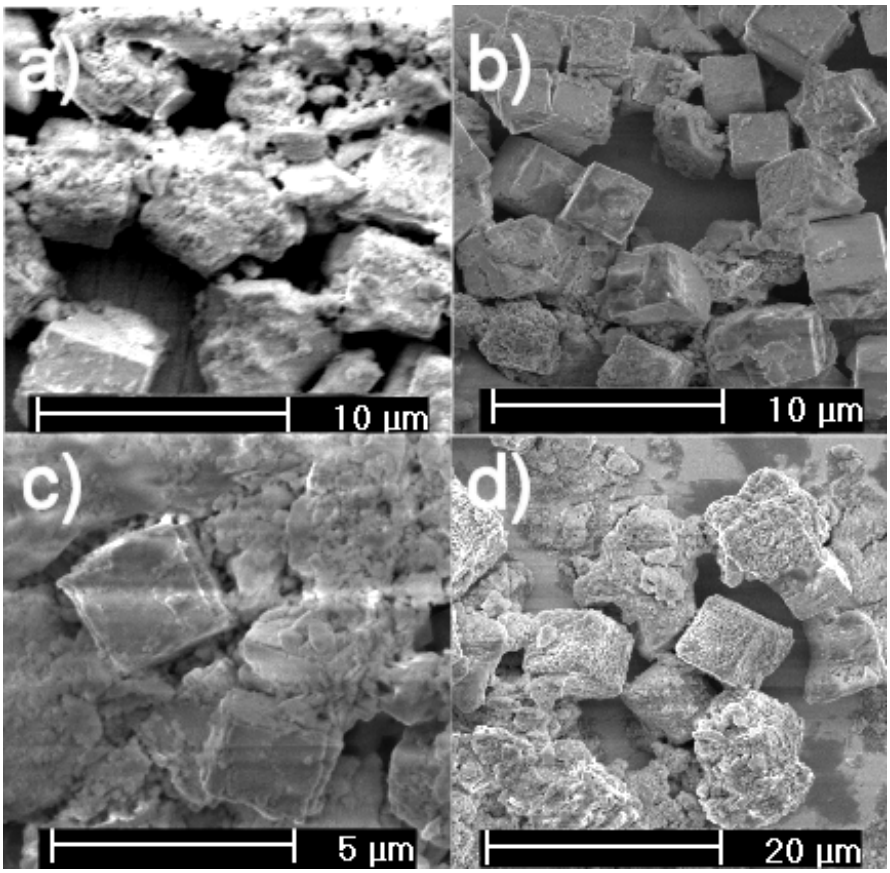

Fig. 3.4 SEM images showing the morphology of powders produced after a) 0.5 hr b) 1.5 hr c) 2 hr and d) 4 hr of processing.

Traianidis et al. proposed a two-stage reaction mechanism to account for the existence of two types of particle morphology encountered in their hydrothermal experiments.[3] In the first stage a Zr-Ti co-precipitate forms, into which Pb ions diffuse. This leads to irregularly shaped agglomerates. As the reaction progresses these agglomerates are dissolved leading to the nucleation and growth of cubic PZT particles. Although different precursors were used in this investigation, the nature of the Zr-Ti co-precipitate, as analysed by XRD, was similar, albeit with more TiO_2, which would have dissolved, had Pb ions been present (Fig. 3.5). We therefore conclude that a similar dissolution-precipitation mechanism occurs and that it is unlikely that the PZT phase has been generated in the irregularly shaped agglomerates. Instead they represent an intermediate chemical stage between the precursor gel and the fully crystallised cubes.

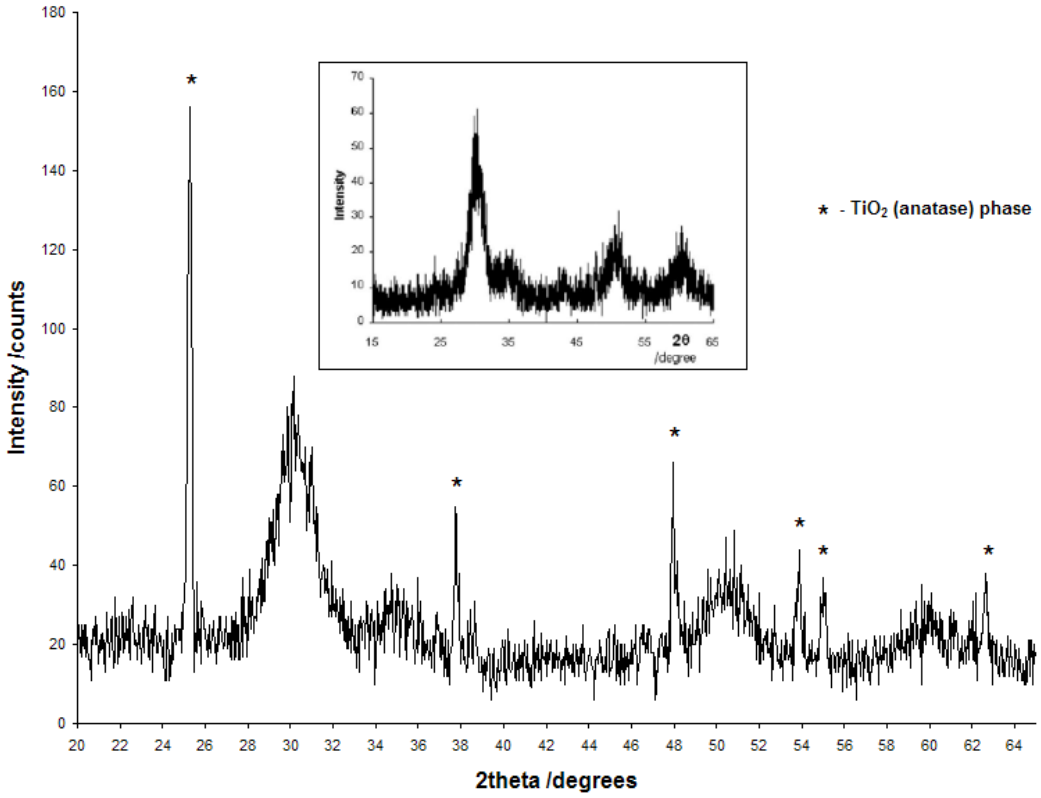

Fig. 3.5 XRD data for Zr-Ti precipitates formed after reacting the Zr and Ti precursors for 4 hr at 160 °C under 5 M KOH . Inset is the result from Traianidis et al.3

3.2.2 Altering processing temperature

In this series of experiments the effects of processing temperature on the morphology and size of hydrothermal powders were analysed. The justification for this study was similar to that for reducing processing times in that it was hypothesised that lower temperatures would lead to a reduction in the rate at which PZT crystals precipitated. Since PZT was shown to be the dominant phase after a 30 min reaction at 160 °C, this processing time was retained for the following experiments. Fig. 3.6 shows XRD data for hydrothermal reactions conducted between 140 – 160 °C. The TiO_2 precursor is present as an impurity phase that steadily diminishes until it is barely detected at 160 °C. However, MPB PZT is still able to form at the reduced temperatures. Fig. 3.7 shows a PZT crystal from the 140 °C reaction. The round particles in the background were confirmed as unreacted TiO_2 by EDAX analysis and SEM studies of the precursors. These results imply that the dissolution part of the hydrothermal reaction has been retarded, but the precipitation half is more or less unaffected. Hence, the

PZT crystals that do form are of a similar size and morphology, regardless of the processing temperature.

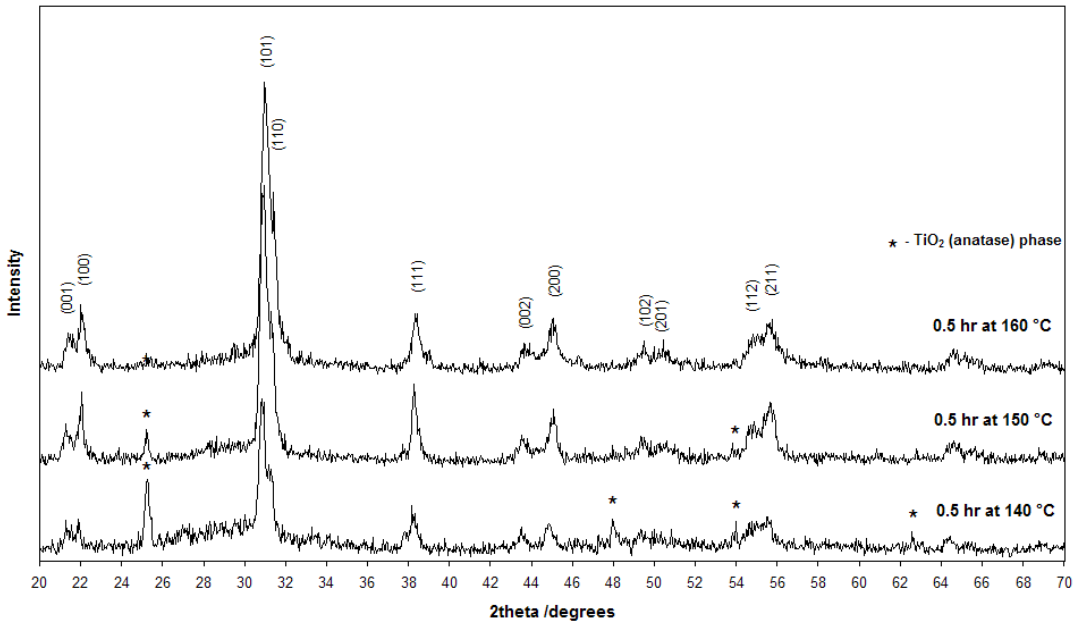

Fig. 3.6 XRD data for PZT powder synthesised for 30 min over a range of temperatures from 140 – 160 °C (indexed peaks correspond to the accepted values for 52:48 PZT, PDF card no. 33-0784).

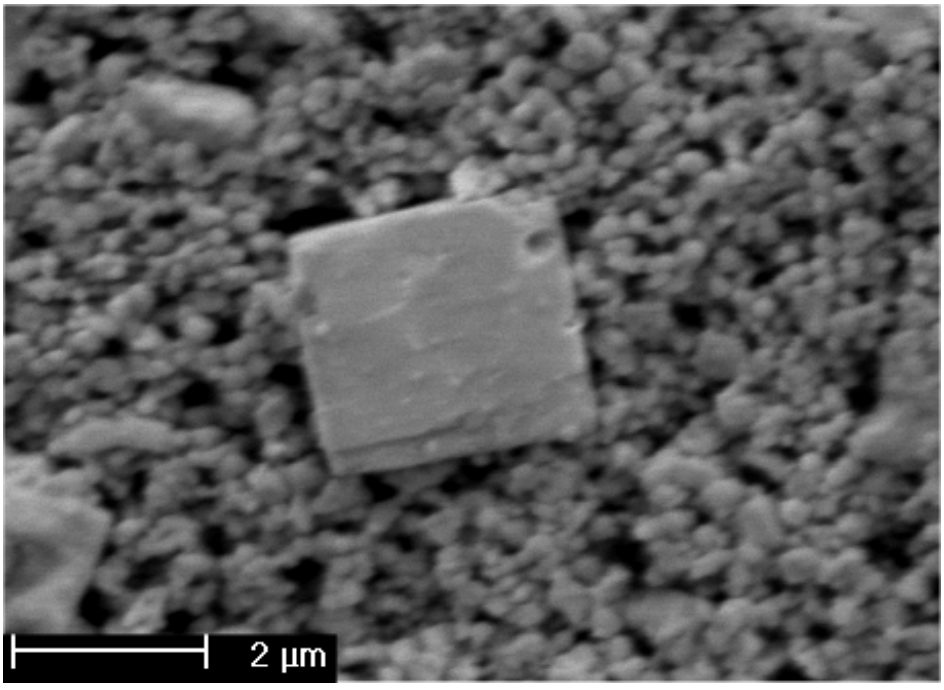

Fig. 3.7 SEM image of a PZT crystal formed after 30 min at 140 °C.

3.2.3 Attempts to synthesise alternative PZT stoichiometries

In an effort to better understand the hydrothermal reaction mechanism, attempts were made to synthesise PZT stoichiometries on either side of the MPB by altering the Zr/Ti precursor ratio. Fig. 3.8 shows XRD data for powders produced using precursor ratios from 20:80 – 70:30. Synthesis conditions were identical in each case, with processing temperatures and times fixed at 160 °C and 4 hr, respectively. Once again, the now ubiquitous MPB tetragonal phase was visible in all patterns. Determining whether multiple PZT phases have formed can be difficult, since many of the peaks corresponding to rhombohedral compositions overlap those of tetragonal compositions. What is clear, however, is that under these hydrothermal conditions it has not been possible to produce phase-pure PZT compositions away from the MPB. If an initial precursor ratio of 70:30 *had* led to the production of rhombohedral 70:30 PZT then we would expect to see a single (200) peak as opposed to the split (002) – (200) peaks, characteristic of the tetragonal structure. Likewise, a mixture of rhombohedral and tetragonal phases would be characterised by a triplet of peaks in the 42° – 47° 2theta range.[4] Instead, we find a strong match to the tetragonal MPB composition along with a broad peak attributable to amorphous $PbZrO_3$ and a reflection that can be indexed to ZrO_2 (PDF card no. 41-0017).

A similar situation arose when attempting to synthesise compositions below the MPB. The tetragonality (*c*/*a* ratio) of the PZT unit cell is proportional to the Ti content. As such, the separation between split tetragonal peaks in the XRD patterns increases as the Zr content falls. For 20:80 PZT, the accepted lattice constants are: $a = 3.952$ and $c = 4.151$.[2] Taking the (101) – (110) split peaks as an example, their theoretical 2theta separation for the 20:80 composition should be approximately equal to 0.8°. This level of splitting was not witnessed in the attempted synthesis of 20:80 PZT. What's more, the presence of TiO_2 in the XRD pattern provides further evidence to suggest that the extra titanium has failed to incorporate into the PZT lattice. In summary, the XRD data appears to show that only one PZT phase forms, which lies close to the MPB, regardless of the initial precursor ratio. The subsequent excess of Zr or Ti manifests itself as amorphous $PbZrO_3$ and ZrO_2 above the MPB and TiO_2 below the MPB.

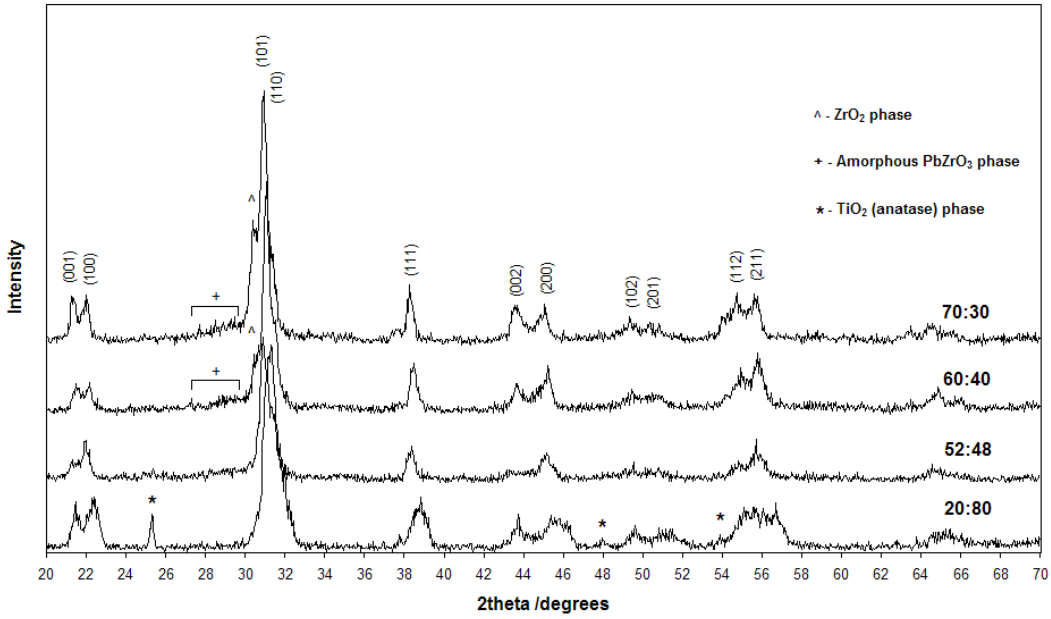

Fig. 3.8 XRD data for powders synthesised at 160 °C for 4 hrs from various precursor stoichiometries (indexed peaks correspond to the accepted values for 52:48 PZT, PDF card no. 33-0784).

Kutty and Balachandran found that the reaction temperature necessary to synthesise PZT was proportional to the Zr/Ti ratio.[5] In other words, the rhombohedral phase required more energy to form than the tetragonal phase. Attempts to synthesize $PbTiO_3$ (the tetragonal end member of the PZT system) in this investigation have been successful, whereas similar attempts to produce crystalline $PbZrO_3$ have failed (Fig. 3.9). These results agree with the findings of Kutty and Balachandran and suggest that there was insufficient thermal energy available to form compositions above the MPB. Furthermore, Cheng et al. argued that the formation of PZT was favoured in preference to $PbZrO_3$ and $PbTiO_3$, under the same hydrothermal conditions, due to the greater entropy associated with the PZT system.[6] Their justification for this viewpoint was that an increase in entropy leads to a decrease in the Gibb's free energy of formation of PZT, since $\Delta G = \Delta H - T\Delta S$. This could explain why the $PbTiO_3$ phase is absent whenever Zr is present in the precursor solution (Fig. 3.8).

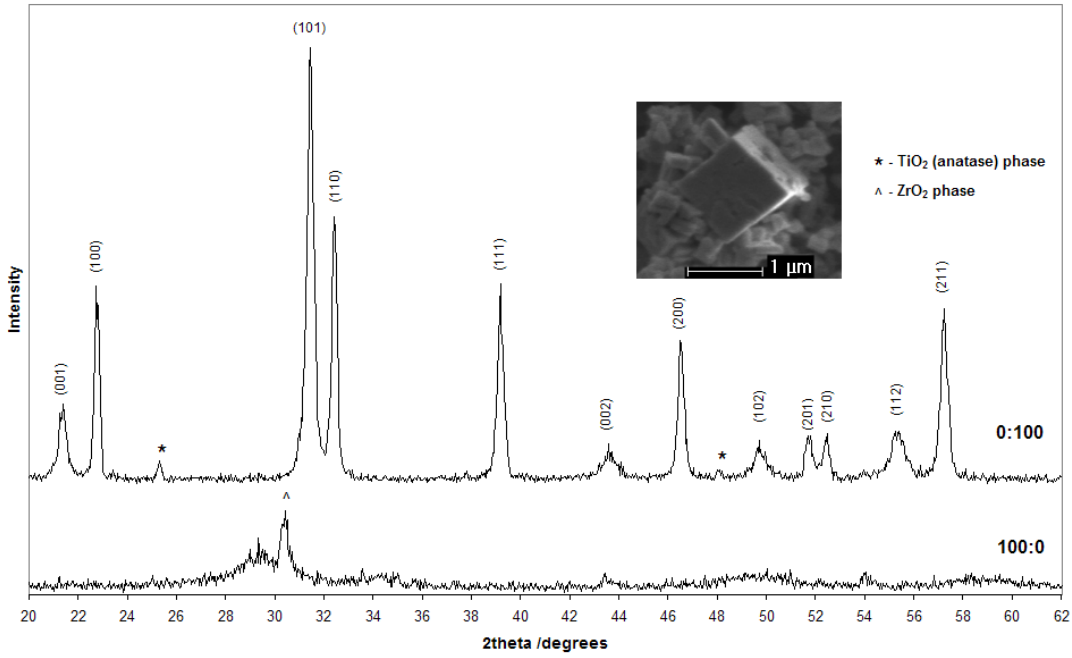

Fig. 3.9 XRD data for powders synthesised at 160 °C for 4 hrs with Zr/Ti precursor ratios of 100:0 and 0:100 (indexed peaks correspond to the accepted values for tetragonal $PbTiO_3$, PDF card no. 06-0452). The inset SEM image shows the morphology of the $PbTiO_3$ powder.

Incidentally, the hydrothermal $PbTiO_3$ particles, shown in Fig. 3.9 (inset) had a cubic morphology and in some cases were sub-micron in size. However, the smaller particles were either strongly agglomerated or intergrown which could have made analysing their electrical properties difficult.

In a final attempt to synthesise 20:80 PZT, amorphous titania (synthesised via the hydrolysis of titanium isopropoxide) was used as an alternative Ti precursor in place of crystalline anatase. Titania in this form is known to be more reactive[7], so it was hoped that its use could initiate the crystallisation of phases below the MPB. Fig. 3.10 shows the XRD data for a powder synthesised using the amorphous titania precursor. The standard reaction conditions were employed (4 hr at 160 °C) and the Zr/Ti precursor ratio was 20:80. It can be seen that this resulted in the formation of a PZT phase close to the MPB as opposed to the desired 20:80 phase.

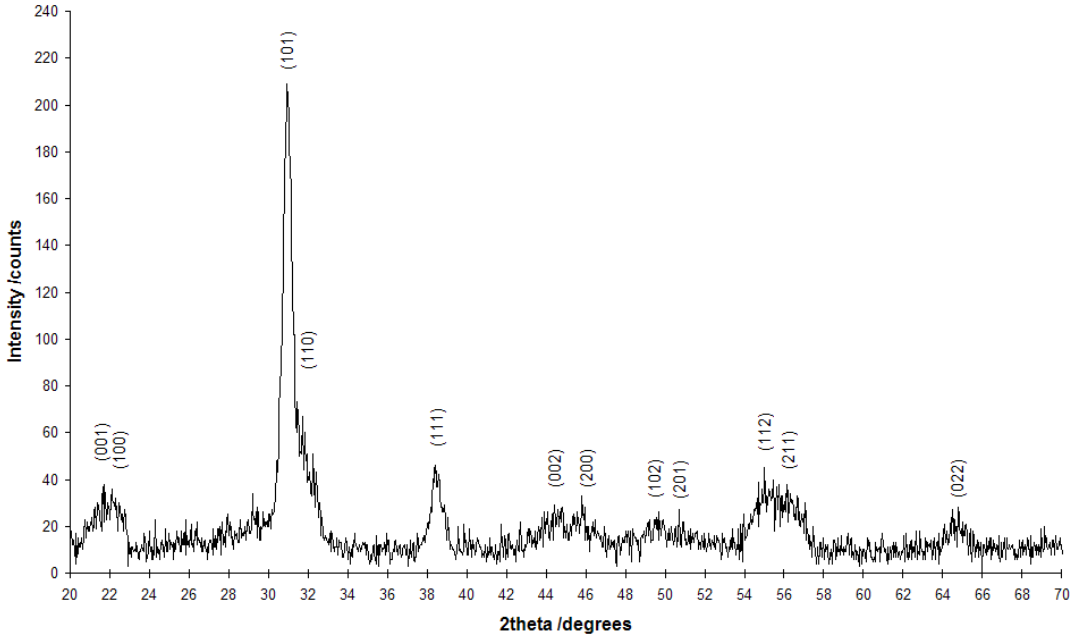

Fig. 3.10 XRD data for the powder synthesised using an amorphous titania precursor in the Zr/Ti ratio of 20:80 (indexed peaks correspond to the accepted values for 52:48 PZT, PDF card no. 33-0784).

The morphology of the powder synthesised using the amorphous titania precursor was varied. It was predominantly composed of micron-sized cubic crystals (Fig. 3.11a) that were smaller than those seen during equivalent experiments where crystalline anatase was used as a Ti source. Unfortunately the crystals agglomerated into large masses that also contained amorphous or partially crystallised material. Other morphologies were seen including circular platelets (Fig. 3.11b). These variations are most probably due to inhomogenieties in the precursor mixture. A similar platelet morphology was observed by Cho et al. during the hydrothermal synthesis of $PbTiO_3$ using the organic mineraliser TMAH. As with the current study, the titania in their precursor mixture was produced via the hydrolysis of titanium isopropoxide.[8]

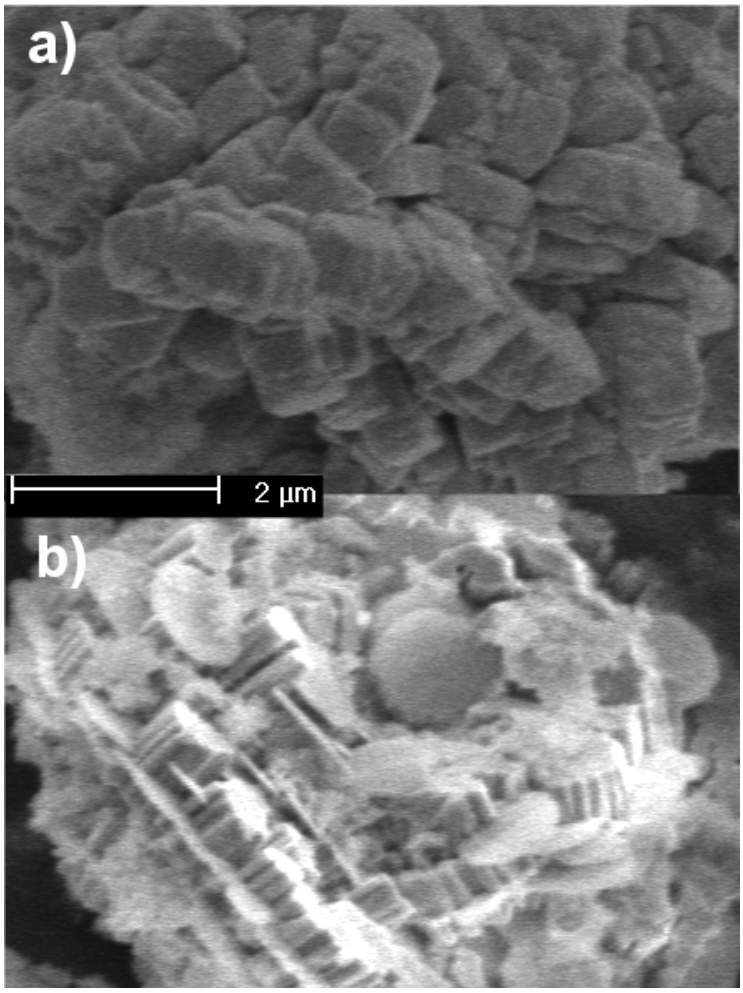

Fig. 3.11 SEM images showing two types of particle morphology observed after substituting crystalline anatase with amorphous titania in the attempted hydrothermal synthesis of 20:80 PZT: (a) agglomerated micron-sized cubes and (b) circular platelets.

3.2.4 The effects of $Pb(NO_3)_2$ precursor concentration

Experiments were conducted to determine the effects of Pb precursor concentration on the formation of PZT in the general hydrothermal reaction. It was found that a 100% $Pb(NO_3)_2$ excess produced unagglomerated PZT particles with a cubic morphology under the standard synthesis conditions of 4 hr processing at 160 °C (Fig. 3.12). The particles were well faceted and little amorphous/unreacted material remained after processing, in contrast to the previous experiments conducted without Pb-excess. Crystal intergrowth was also observed in some cases, as was the precipitation of crystallised particles in close proximity to the precursor gel (Fig. 3.13). The average size of the particles was around 5 µm. During the early stages of the hydrothermal reaction Pb ions play an important role in infiltrating and helping to dissolve the

coprecipitated Zr-Ti gel. As PZT crystals precipitate the Pb ion concentration in solution starts to fall, hence reducing the rate of dissolution. An excess of Pb precursor compensates for this deficiency and ensures more complete dissolution of the gel.

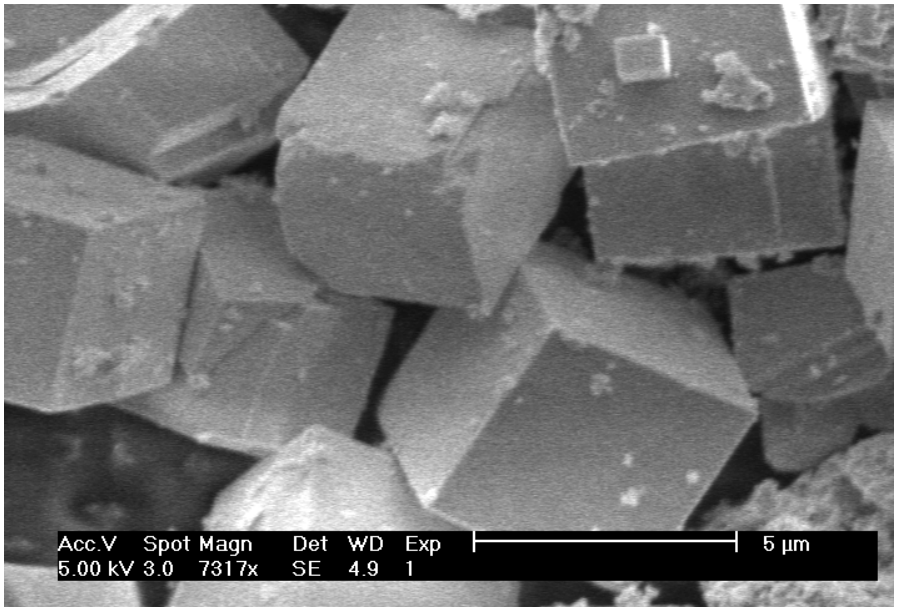

Fig. 3.12 SEM image of PZT particles produced using a 100% Pb precursor excess.

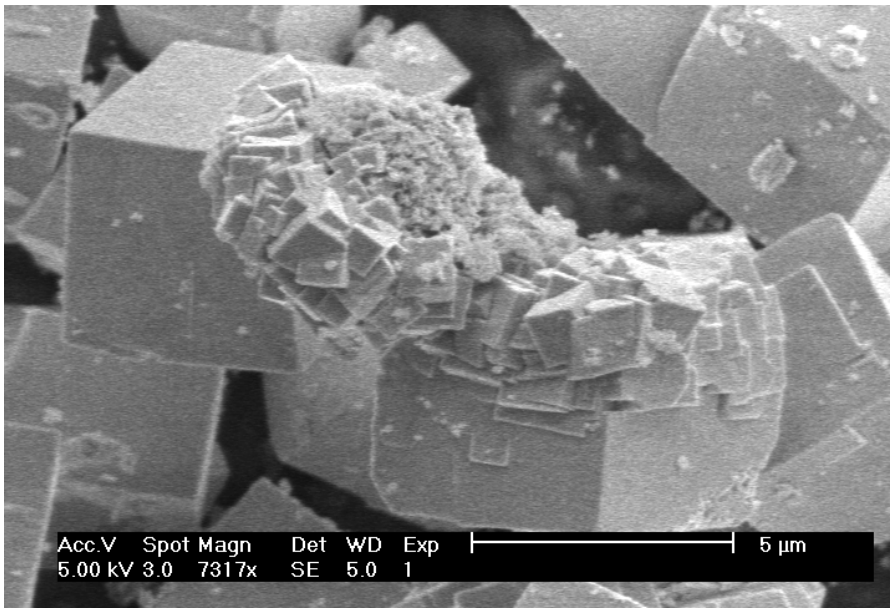

Fig. 3.13 SEM image showing intergrowth and the precipitation of crystals near to the precursor gel.

FIB milling of PZT crystals produced using a 100 % Pb precursor excess showed a dense, almost homogeneous internal structure in comparison to crystals synthesised without a Pb excess (Fig. 3.14). This evidence would suggest that a Pb-excess helps to improve crystallisation during the precipitation phase.

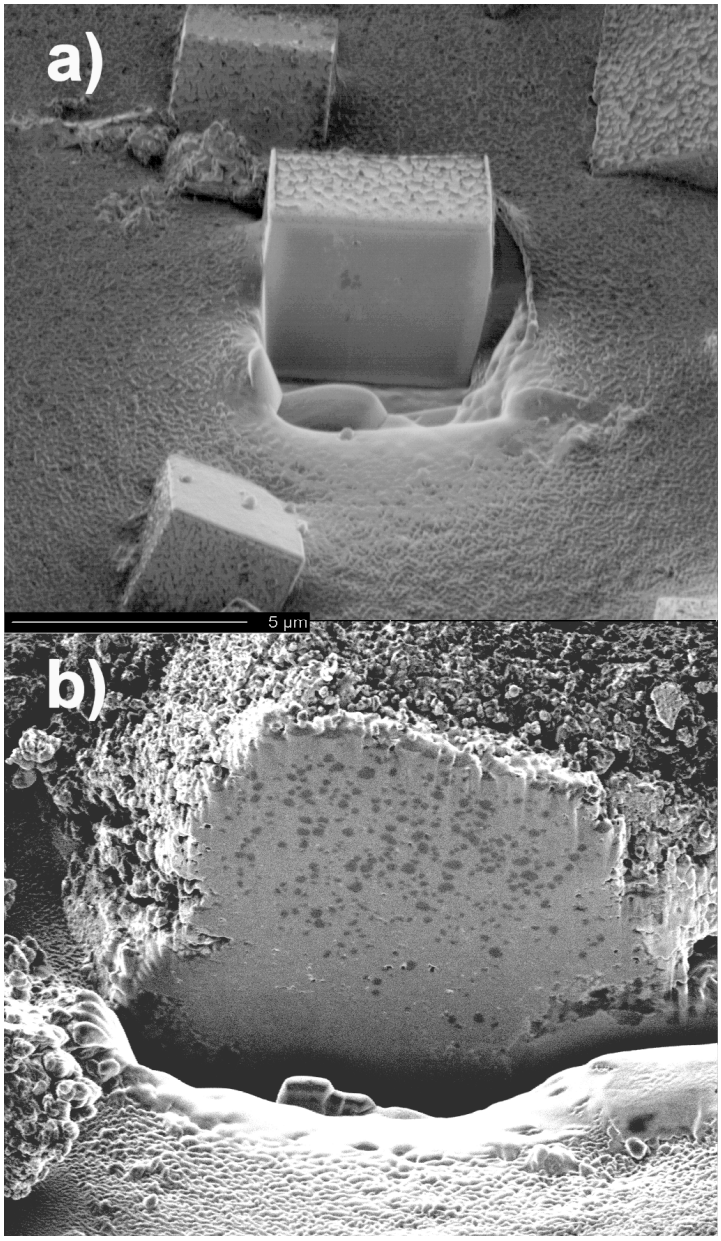

Fig. 3.14 FIB images of PZT crystals synthesised (a) with and (b) without a Pb-excess and subsequently sectioned using FIB milling. Note the greater degree of crystallisation exhibited by the crystal processed using a Pb excess.

3.2.5 Alternative mineraliser

A brief investigation was conducted to determine the effects of using NaOH as an alternative mineraliser in the general hydrothermal technique. Most of the papers in the literature concentrate on KOH; however there is some evidence to suggest that NaOH produces PZT particles with a smaller average size and narrower size distribution than KOH.[9]

The decision was made to use a 100% Pb precursor excess in the following experiments. Changes to the average particle size were easier to distinguish due to a reduction in the amount of partially reacted precursor gel. The Pb-excess also helped to make the morphology of PZT particles more uniform. Fig. 3.15, parts a) + b), show the resultant powders produced under standard conditions (4 hr processing at 160 °C) using 5 M KOH and 5 M NaOH, respectively. The average size of the PZT crystals produced using 5 M NaOH, under standard conditions (4 hr processing at 160 °C), fell by a third in comparison to crystals synthesised using 5 M KOH (Fig. 3.15). However, there was little difference in the morphology of the crystals produced with both mineralisers producing well-faceted, unagglomerated crystals (cf. Fig. 3.16 and Fig. 3.12). As such, it can be concluded that the nature of the mineraliser does not play a significant role in the formation of hydrothermal PZT, when a large excess of Pb precursor is used.

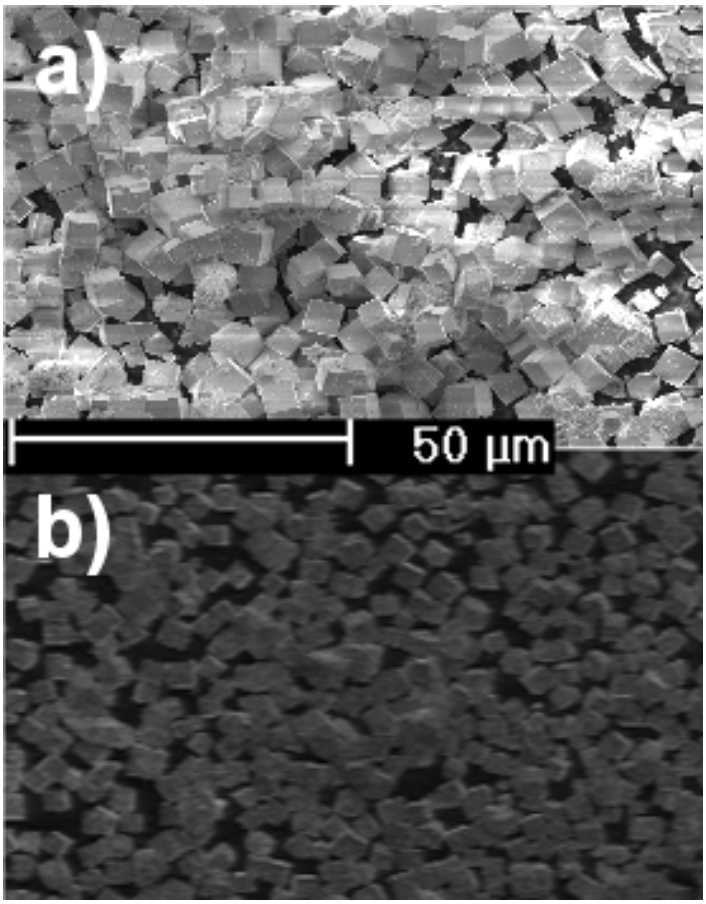

Fig. 3.15 SEM images comparing powders produced using a) 5 M KOH and b) 5 M NaOH mineraliser concentrations.

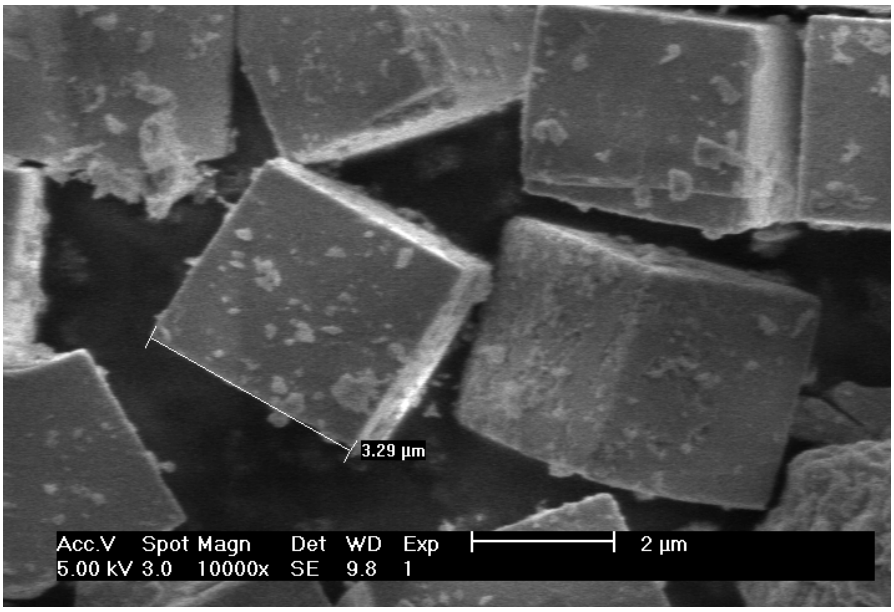

Fig. 3.16 SEM image showing the morphology of PZT particles synthesised using NaOH.

Both mineralisers produced single-phase PZT powders, close to the MPB, as indicated by the XRD data in Fig. 3.17. The absolute intensity of the peaks in the KOH pattern was greater than that seen in the NaOH pattern, however the relative intensities between peaks in the same pattern were similar. This suggests simply that the quantity of powder analysed in both cases was different. As such, some peaks in the NaOH pattern (i.e. (200) and (201)) are of such low intensity that they appear absent altogether. Plotting the logarithmic intensity revealed these missing peaks and confirmed the phase purity of the powders.

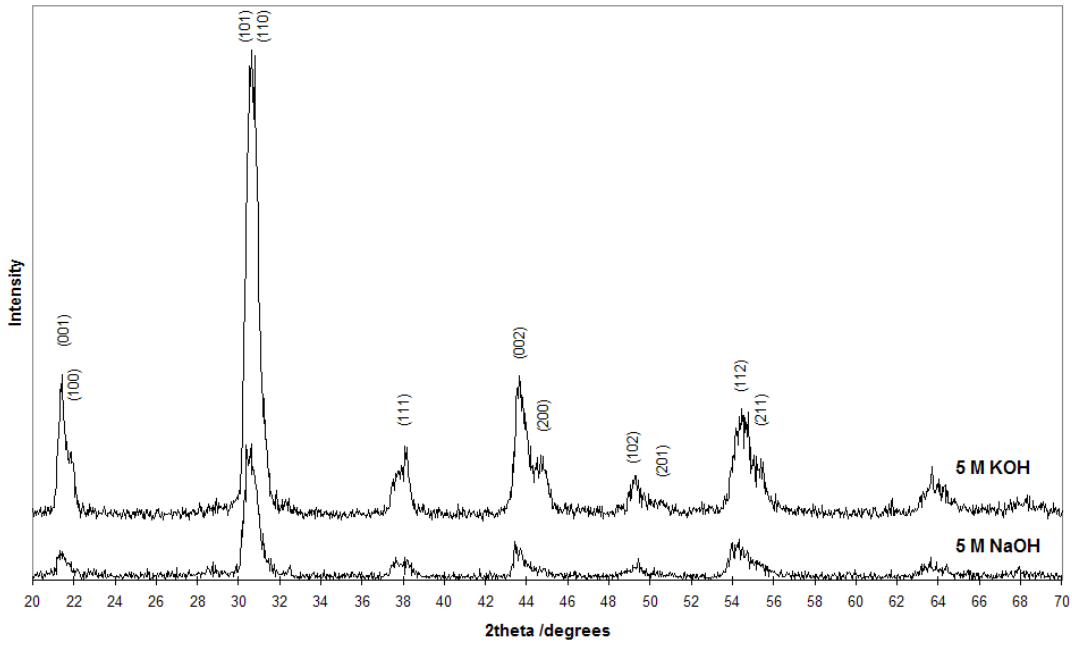

Fig. 3.17 XRD data for powders produced using NaOH and KOH mineralisers (indexed peaks correspond to the accepted values for 52:48 PZT, PDF card no. 33-0784).

3.2.6 Surfactant-assisted hydrothermal synthesis

Surfactants have been used in various hydrothermal synthesis experiments to tune the size, morphology and agglomeration of the crystals produced.[10, 11, 12] In this investigation, the aim of the surfactant experiments was to impede crystal growth at the precipitation stage. All experiments in this section utilised a 100% Pb precursor excess to ensure complete crystallisation of any PZT that was produced. Unless stated otherwise, the reactions took place under standard conditions (4 hr processing at 160 °C using 5 M KOH mineraliser concentration).

3.2.6.1 Triton X-100

The non-ionic surfactant, Triton X-100, has been used occasionally in the past to control the morphology of nanocrystals produced using wet chemical synthesis techniques.[13] The morphology of the PZT crystals was unaffected by the presence of Triton X-100 in the precursor solution (Fig. 3.18). However, a reduction in average crystal size was apparent when solutions containing Triton X-100 were used. In the case of a 2% solution the average size of the crystals was 2 μm – a reduction of 60% in comparison to surfactant-free solutions. Increasing the concentration to 5% produced particles with an average size of 2.5 μm. The critical micelle concentration (CMC) of Triton X-100 is approximately 2×10^{-4} M at 25 °C [14], which corresponds to a solution concentration slightly greater than 0.01%. Optimum encapsulation occurs at concentrations slightly above the CMC. As concentrations are raised above the CMC agglomeration can occur. However, the solubility of non-ionic surfactants falls with temperature, so it can be expected that the Triton-X concentration during the hydrothermal treatment was much lower than 2%.

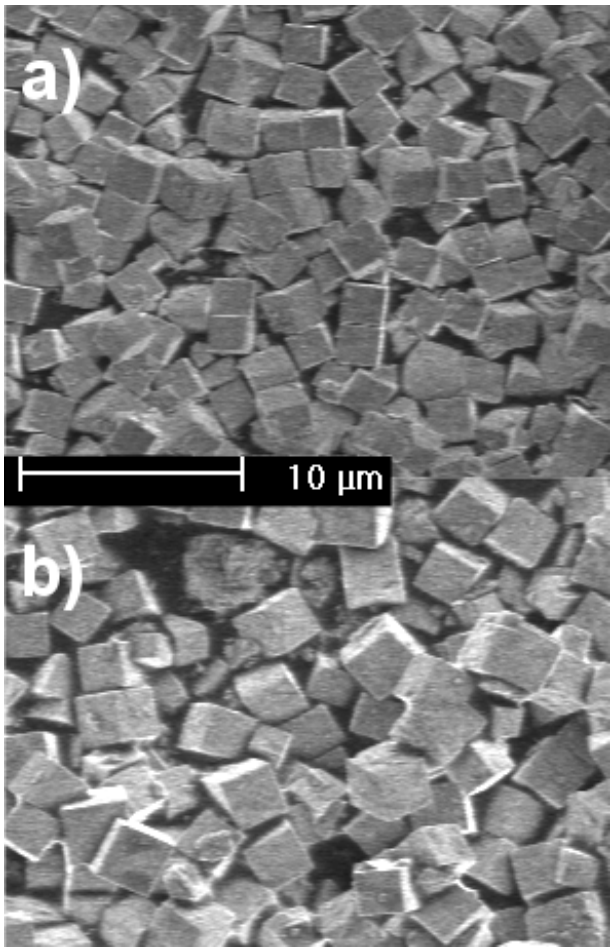

Fig. 3.18 SEM images showing PZT particles produced using a) 2% and b) 5% Triton X solutions.

3.2.6.2 EDTA

EDTA is a molecule that can form complexes with metal ions. According to the classical LaMer model, one of the keys to forming monodisperse particles is to separate the nucleation and growth stages.[15] EDTA has been used in the past to control the size and morphology of rare earth fluoride nanocrystals synthesised using a hydrothermal technique.[16] Shortly after nucleation, EDTA molecules in solution were found to cap the surface of nanocrystals, thus preventing further growth and inhibiting agglomeration. It was hoped that a similar effect would occur during the hydrothermal synthesis of PZT, especially since EDTA is known for its strong chelation with Pb ions. Alternatively, the removal of Pb ions at the initial stages of the hydrothermal process might inhibit secondary nucleation on pre-existing existing seed particles.

Precursors, with a 100% Pb excess, hydrothermally processed under saturated EDTA solutions for 4 hr at 160 °C produced powders with varied morphology (Fig. 3.19). The cubic crystals were micron-sized but, unlike most experiments involving a Pb excess, were not well-faceted. Under alkaline conditions the EDTA molecule becomes deprotonated (all the acidic hydrogen atoms are removed) and can bind to metal ions to form a complex. The efficiency of chelation (or complexation) can be quantified by a term known as the K_f formation constant:

$$K_f = \frac{MY^{n-4}}{M^{n+}Y^{-4}} \qquad \text{Eqn. 3.1}$$

where MY^{n-4} is the EDTA-metal complex concentration, M^{n+} is the metal ion concentration and Y^{-4} is the deprotonated EDTA concentration. The efficiency of complexation (or chelation) is proportional to the charge on the metal ion and inversely proportional to ionic radius, for constant charge. For Pb ions the formation constant is particularly large – over 17 orders of magnitude greater than the formation constant for K ions, for example. Consequently, a significant quantity of the initial Pb-excess used during the hydrothermal procedure would have been sequestered by the deprotonated EDTA. This could account for the eroded faces of the cubic crystals – something that was observed during hydrothermal experiments without a Pb-excess (cf. Fig. 3.1). A free Pb ion deficiency can also explain the appearance of amorphous material alongside the cubic crystals.

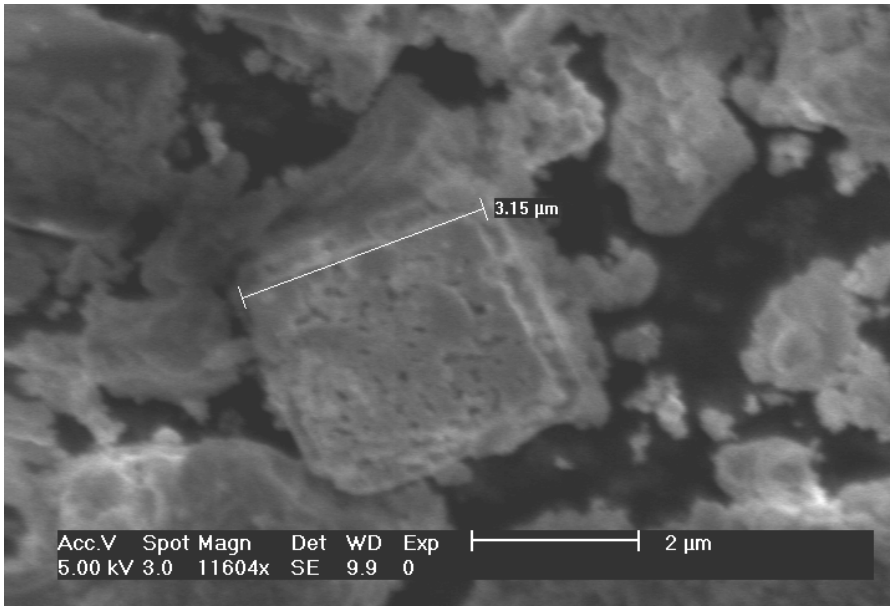

Fig. 3.19 SEM image showing the influence of EDTA on the powder morphology.

XRD measurements showed that a PZT phase close to the MPB had been produced in the EDTA-assisted synthesis (Fig. 3.20).

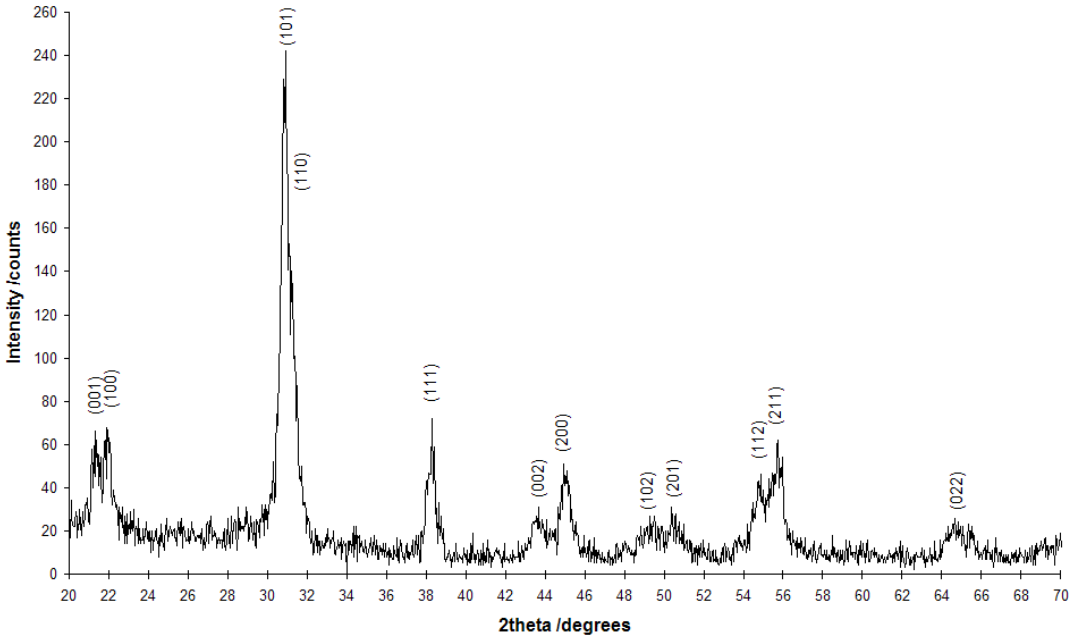

Fig. 3.20 XRD data for the powder synthesised in the EDTA experiment (indexed peaks correspond to the accepted values for 52:48 PZT, PDF card no. 33-0784).

3.2.6.3 Oleic and stearic acid

When precursor solutions containing 2% oleic acid were processed for 30 min at 160 °C the resultant powder was predominantly amorphous with no PZT phase detected using XRD (Fig. 3.21). However, the fact that peaks corresponding to unreacted TiO_2 precursor were not observed indicated that dissolution had taken place. Processing precursor solutions without surfactants for 30 min led to the almost complete crystallisation of the perovskite PZT phase (Fig. 3.3). Therefore, we can hypothesise that, under the same conditions, the addition of oleic acid has inhibited the precipitation rate of PZT crystals. This hypothesis would seem to have been confirmed when, after processing an oleic precursor solution for 4 hr, a significant quantity of the amorphous coprecipitate was transformed into crystalline PZT (Fig. 3.22b). The morphology of the crystals varied from relatively well faceted, micron-sized, disperse cubes to large partially-crystallised agglomerates.

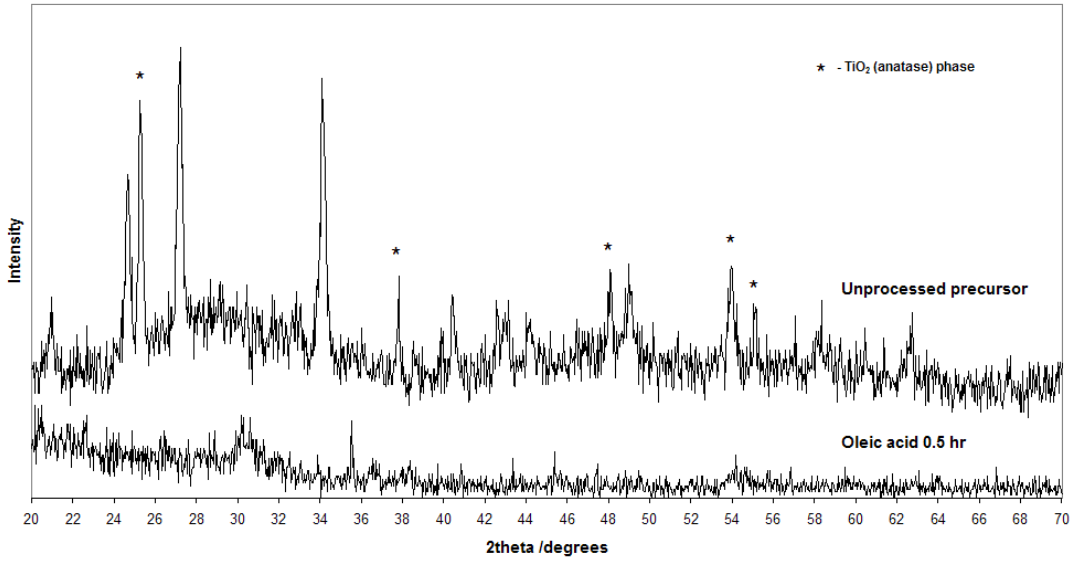

Fig. 3.21 XRD data for powder synthesised using an oleic acid solution and the unreacted precursor mixture.

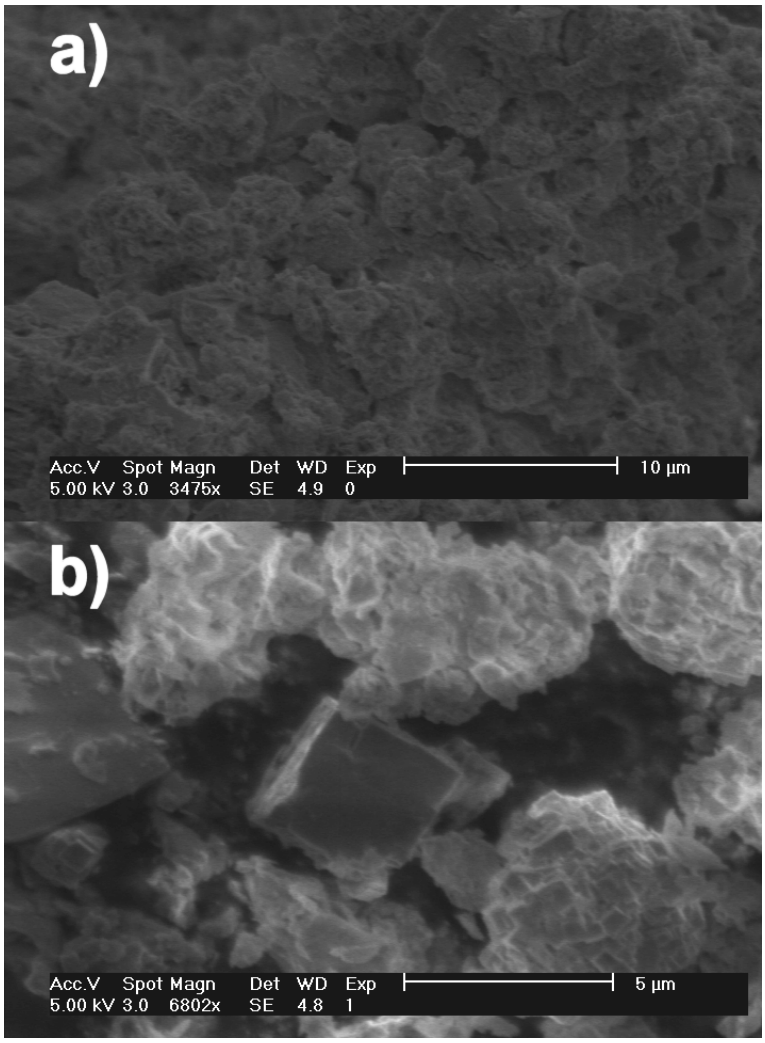

Fig. 3.22 SEM images of powders processed for a) 0.5 hr and b) 4 hr using a 2% oleic acid solution.

Stearic acid, the saturated form of oleic acid, has been used in a number of hydrothermal synthesis experiments to impede crystal growth. It was shown by Xu et al. that stearic acid adsorbed onto the surface of TiO_2 nuclei that formed after the hydrothermal treatment of titanyl sulphate.[17] This was successful in preventing further growth and subsequent agglomeration of the TiO_2 particles, which had an average diameter of 8 nm. Wei et al. used potassium stearate to similar effect in the hydrothermal synthesis of InP nanocrystals.[18] The morphology of the surfactant-assisted particles was spherical or rod-like, and an order of magnitude smaller than equivalent nanocrystals synthesised without surfactant. Finally, Xu et al. synthesised BaTiO3 via a hydrothermal method in solutions containing stearic acid and found a 40% reduction in the size of the nanoparticles that were produced.[19]

In the current investigation, the morphology of PZT powders processed for 4 hr using a 2% solution of stearic acid was similar to that observed during the oleic acid experiments (Fig. 3.23). Some crystallised micron-sized PZT cubes were seen, but there was plenty of amorphous material still present.

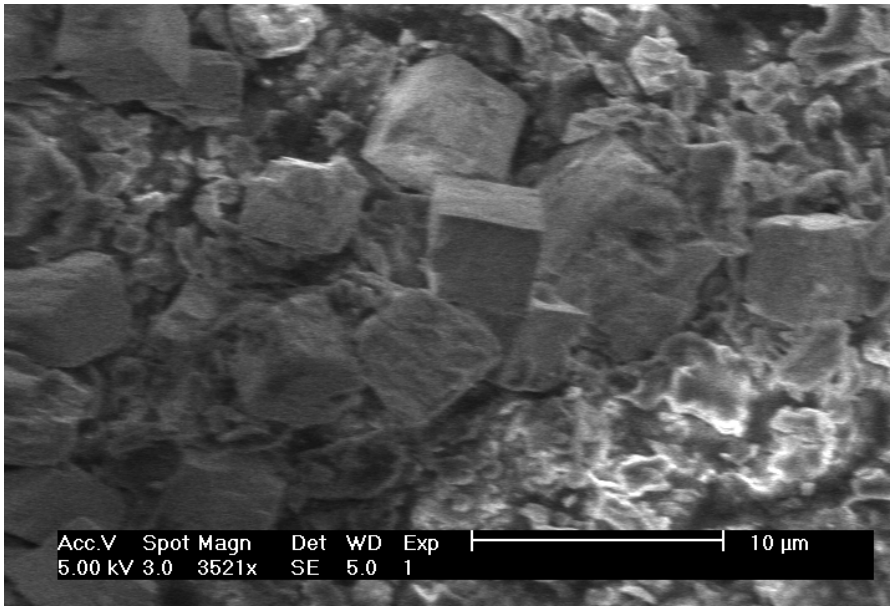

Fig. 3.23 SEM image showing the partial crystallisation of PZT powder that occurred after the hydrothermal treatment of a precursor solution containing 2% stearic acid.

3.2.7 Hydrothermal treatment of a PZT sol

The use of anatase TiO_2 in the general hydrothermal procedure imposed a lower limit on the mineraliser concentration that was necessary for dissolution to occur. As an example, Fig. 3.24 shows the result of processing a standard 52:48 precursor solution with a 0.5 M KOH concentration for 18 hr at 160 °C. Even with such extended processing times the PZT phase fails to crystallise and significant quantities of anatase are present. To overcome this restriction, and also to investigate the effects of hydrothermal processing on a more homogeneous precursor mixture, a hybrid sol-gel/hydrothermal technique was attempted. This involved preparing a sol-gel derived precursor to replace the standard precursors used during the general hydrothermal method. The KOH mineraliser was still retained, however a reduced concentration of 3.3 M was used. The motivation behind this change lay in a paper by Wendelbo et al. who conducted a combinatorial investigation into the hydrothermal synthesis of

various perovskites, including PZT.[20] They identified a mineraliser concentration close to 3 M as being the optimum for reducing the average size of PZT particles.

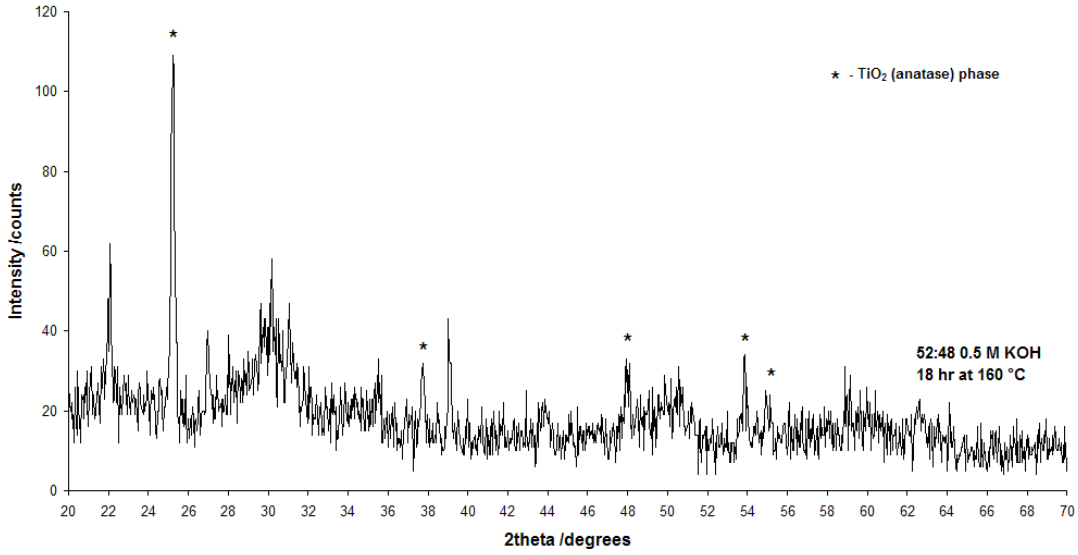

Fig. 3.24 XRD data for 52:48 precursor solution processed for an extended time using a reduced, 0.5 M KOH concentration.

The resultant morphology after processing the sol-gel derived precursor for 24 hr at 160 °C was unexpected (Fig. 3.25). Alongside agglomerates of submicron cubic particles were found pyramidal fibres that ranged in length from 1-10 μm. The smaller fibres tapered to nanoscale points (Fig. 3.26). EDAX analysis of the fibres showed them to be Ti-rich in comparison to the composition of the cubic crystals. Cho et al. found acicular PZT was produced when Zr-Ti coprecipitate gels were hydrothermally processed using low concentrations (≤ 0.75 M) of the organic mineraliser TMAH.[21] However, the authors also observed an acicular intermediate phase, something that was not seen when reaction times were reduced to 30 min in the current investigation. Instead the morphology of the powder was a combination of cubic agglomerates and amorphous gel (Fig. 3.27). XRD results for powders produced after 30 min and 24 hr indicate the presence of a PZT phase close to the MPB, in both cases (Fig. 3.28). Since the quantity of pyramidal particles, produced during the 24 hr synthesis, was significantly less than the quantity of cubic particles, it is likely that the phase of the latter has masked that of the former.

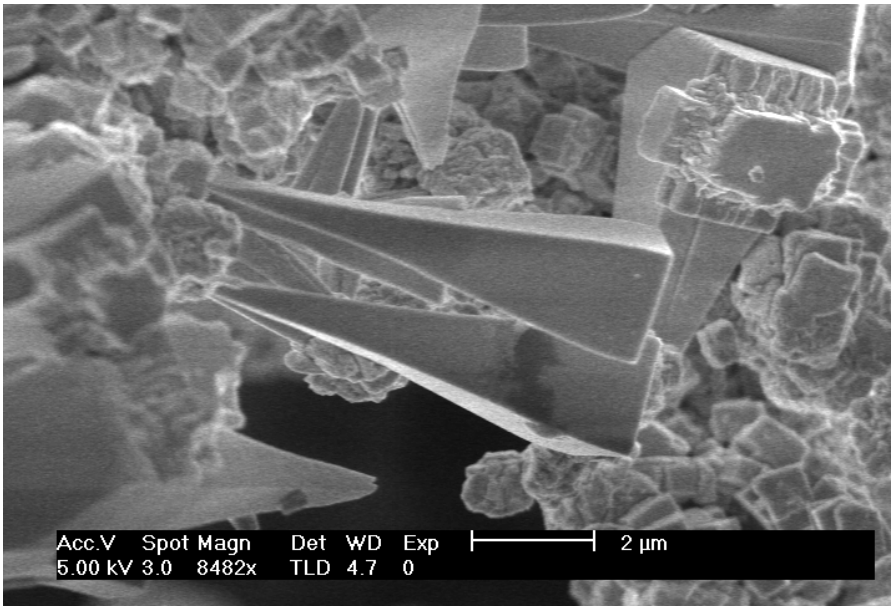

Fig. 3.25 SEM image showing the unusual morphology of particles synthesised using a sol-gel derived precursor.

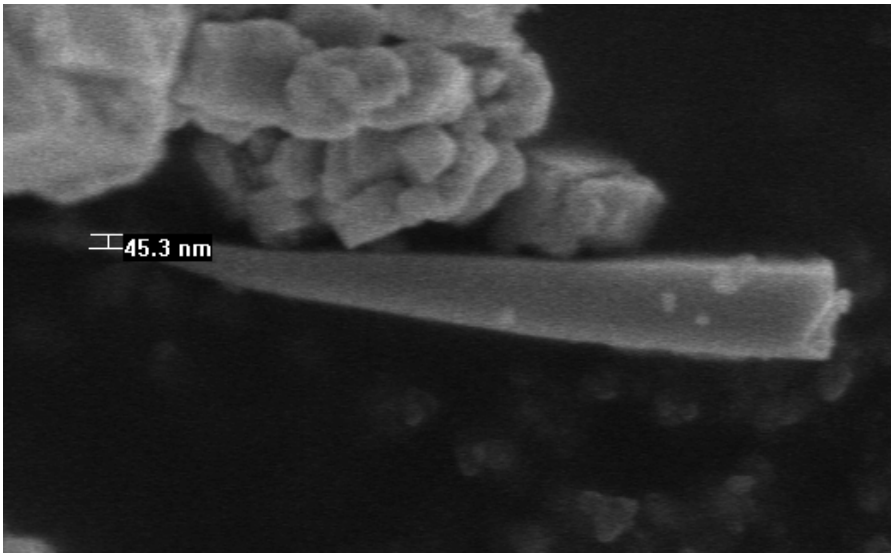

Fig. 3.26 SEM image showing a PZT fibre that tapers to a nanoscale point.

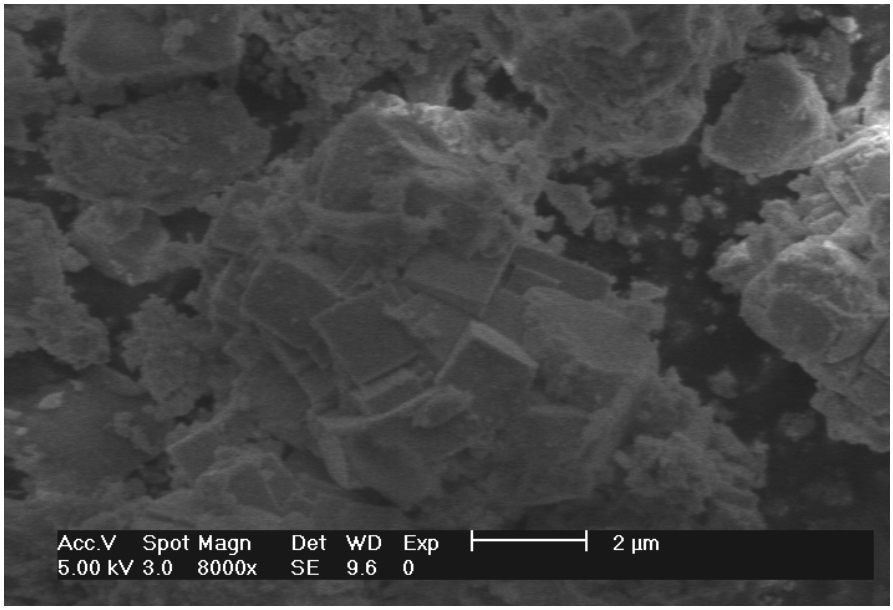

Fig. 3.27 SEM image of powders produced after processing the sol-gel derived precursor for 0.5 hr.

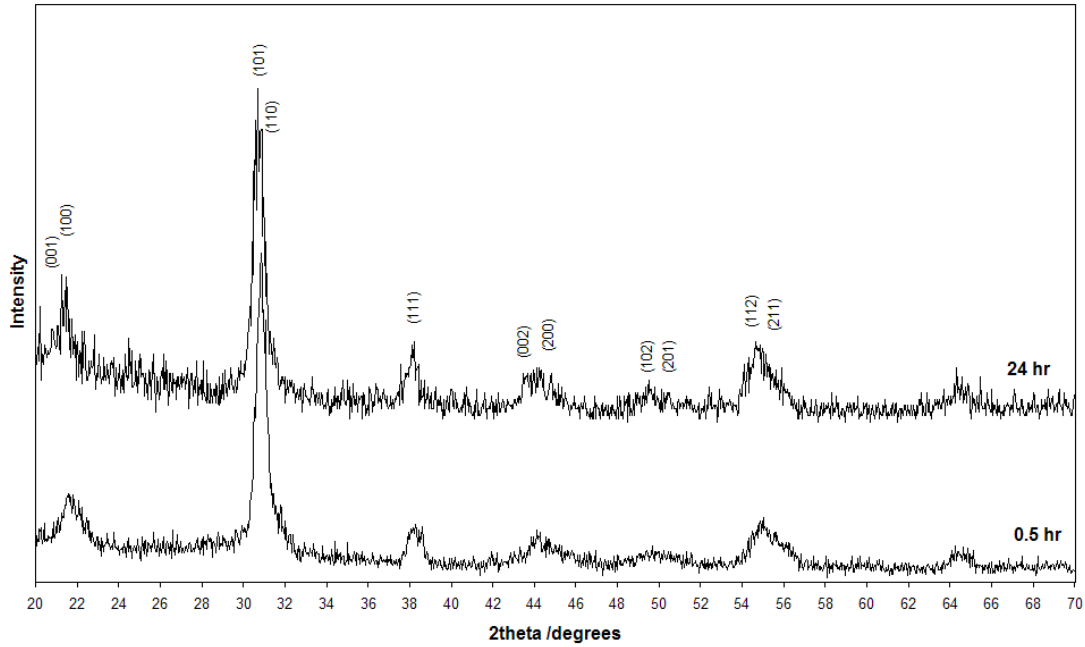

Fig. 3.28 XRD data for powders produced after 0.5 hr and 24 hr using the sol-gel derived precursor (indexed peaks correspond to the accepted values for 52:48 PZT, PDF card no. 33-0784).

3.2.8 Hydrothermal deposition of epitaxial PZT nanostructures and thin films

Since the attempts to synthesis freestanding, nanoscale PZT crystals using the hydrothermal method were unsuccessful, work focussed on growing nanoislands on single crystal $SrTiO_3$ substrates. Ahn et al. showed that epitaxial $PbTiO_3$ nanoislands

with diameters below 50 nm could be grown on Nb-doped STO substrates using a hydrothermal technique.[22] This work inspired attempts to produce epitaxial PZT nanoislands, of similar dimension, using the general hydrothermal method adopted in previous experiments.

3.2.8.1 PZT grown on $SrTiO_3$

The initial experiments involved observing the growth mechanism of PZT on single-crystal (100) $SrTiO_3$ substrates under hydrothermal conditions. Long processing times were used together with a 100% Pb-precursor excess. The PZT coverage across the surface of the substrate, after 24 hr at 160 °C, was inhomogeneous. Some areas remained relatively bare, but for the occasional well faceted, rectangular-shaped nanoisland (Fig. 3.29a). Other parts were covered in a dense film, up to a micron in thickness (Fig. 3.29b). The films appeared to grow in stages that began with the coalescence of nanoislands (Fig. 3.30). After the coalescence stage, film thickness increased through the nucleation and growth of fresh layers on top of the original film. Szafraniak and Alexe also observed this behaviour during the hydrothermal synthesis of $PbTiO_3$ films on $SrTiO_3$ substrates.[23] The inhomogeneous film coverage was most probably due to local variations in precursor concentration at the bottom of the hydrothermal bomb.

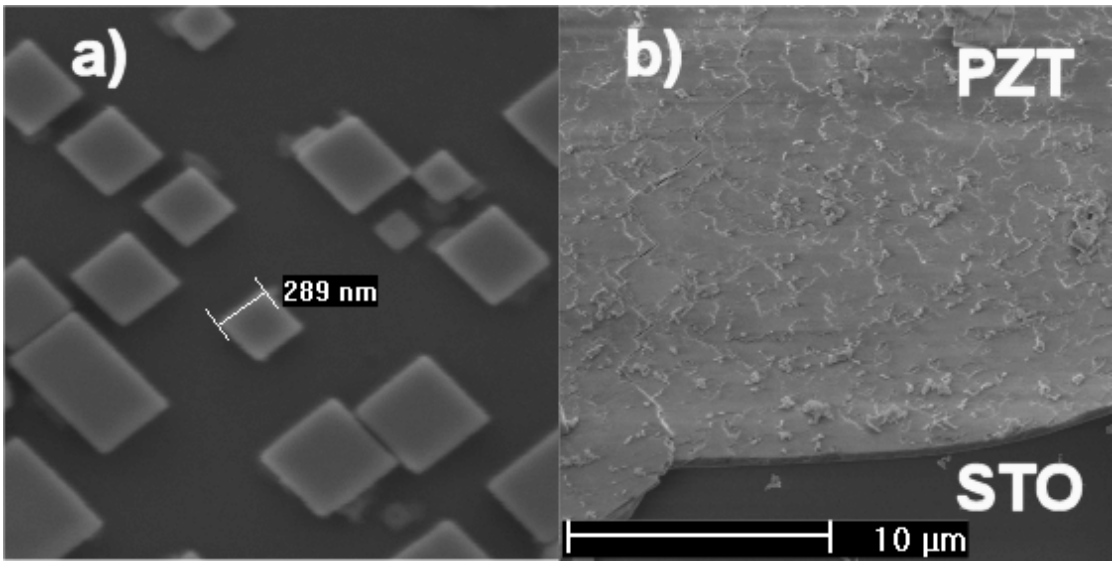

Fig. 3.29 SEM images showing hydrothermal PZT (a) island and (b) film growth on a single-crystal $SrTiO_3$ substrate.

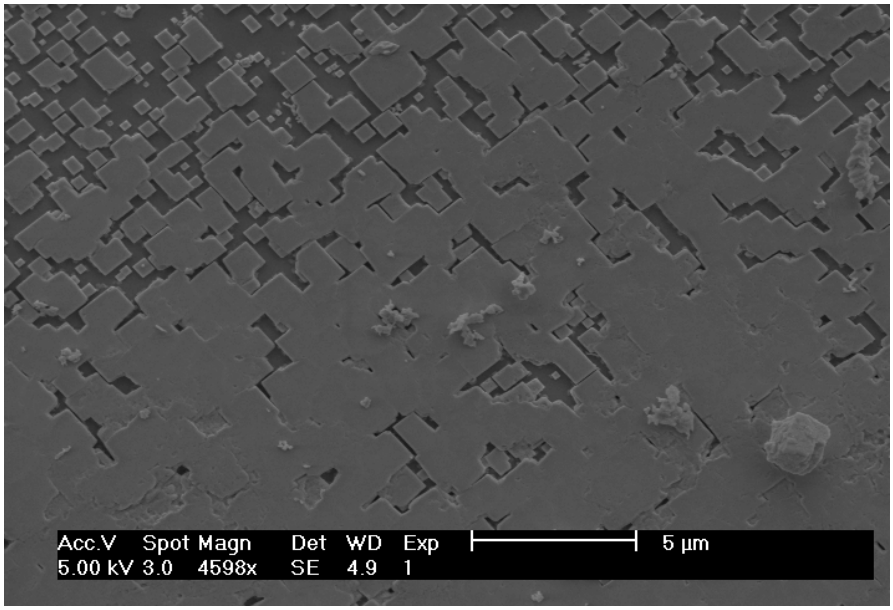

Fig. 3.30 SEM image showing the coalescence of PZT nanoislands leading to the formation of a film.

The epitaxial nature of the nanoislands and thin films was confirmed through XRD analysis. Strong preferential orientation in the [001] direction was a clear indication that the (100) $SrTiO_3$ substrate had influenced PZT growth (Fig. 3.31). Peaks corresponding to three alternative PZT orientations were also visible, but their intensities were over an order of magnitude less than that of the preferred orientation. These reflections can be attributed to stray PZT particles that had formed in solution before coming to rest arbitrarily on the surface of the substrate.

The peaks in the XRD data for the PZT film matched particularly well to the accepted values for the 52:48 composition. Since the *a*-axis lattice parameters of PZT and $SrTiO_3$ are different there will be some degree of epitaxial strain within the film, which can be expressed as:

$$\frac{\Delta a}{a} = \frac{a_s - a_f}{a_s} \qquad \text{Eqn. 3.2}$$

where a_s and a_f are the *a*-axis lattice parameters for the substrate and film, respectively. The stress within a given film is compressive for $\Delta a/a < 0$ and tensile for $\Delta a/a > 0$. Inserting the accepted values for 52:48 PZT and $SrTiO_3$ into the equation gives a lattice mismatch equal to –2.2%. This figure is sufficient to account for the

island growth mode observed during the initial stages of hydrothermal PZT film formation.

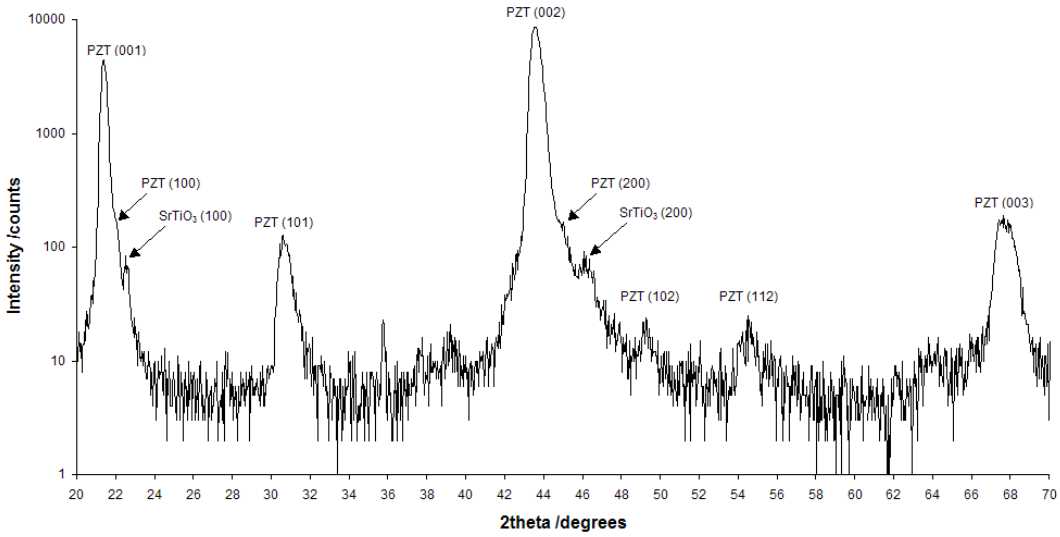

Fig. 3.31 XRD data for PZT grown on a (100) SrTiO3 single-crystal substrate via the hydrothermal method (indexed peaks correspond to the accepted values for 52:48 PZT, PDF card no. 33-0784 and $SrTiO_3$, PDF card no. 35-0734)

An unusual crystal morphology was observed in one small area of a (100) $SrTiO_3$ substrate that was processed for 24 hr at 160 °C. Platelets were found that grew perpendicular to the substrate surface and were orientated parallel to the $SrTiO_3$ crystallographic axes (Fig. 3.32). They possessed a semi-circular morphology and grew with their curved surfaces in contact with the substrate (Fig. 3.33). Quantitative compositional analysis of the platelets via EDAX proved difficult due to a combination of the small interaction volume and an abundance of contaminant species across the surface of the substrate following the hydrothermal reaction. However, the data suggested a large quantity of Pb was present indicating the possibility that the platelets were in fact composed of lead oxide. Prior hydrothermal tests that involved reacting the $Pb(NO_3)_2$ precursor alone with KOH produced platelet particles of PbO with a similar morphology (Fig. 3.34). If the structures found on the $SrTiO_3$ substrate are indeed composed of PbO their location is puzzling. They were found in a region that separated two large areas of well-crystallised PZT film. What's more, no sign of island growth was present in the vicinity, which would appear to rule out the possibility that the platelets act as a template to PZT island growth. Instead, it is more

likely that the area in question was exposed to a particularly high concentration of Pb ions leading to the nucleation and growth of PbO on the substrate surface. Furthermore, the well-crystallised PZT film found close to the platelets is consistent with a large excess of Pb ions.

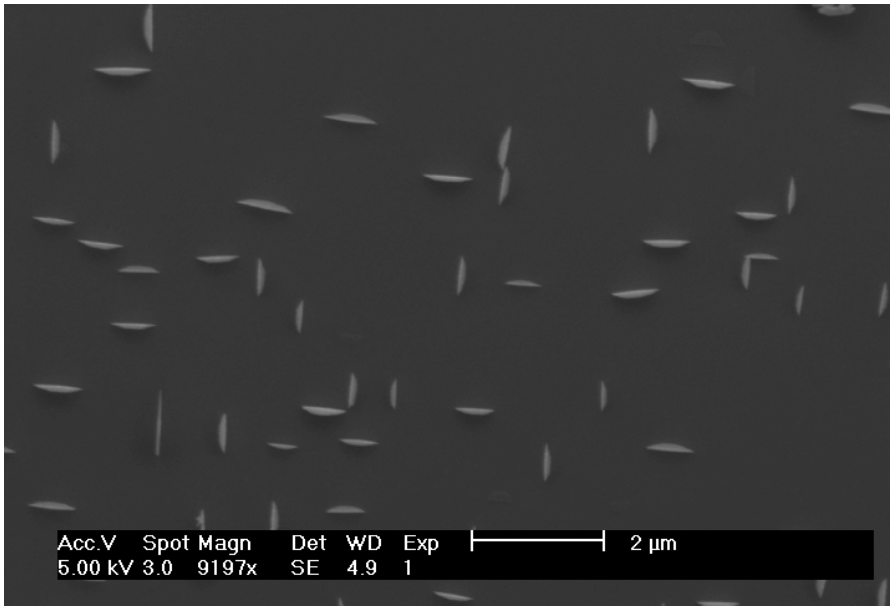

Fig. 3.32 SEM image of platelets oriented to the crystallographic axes of the substrate.

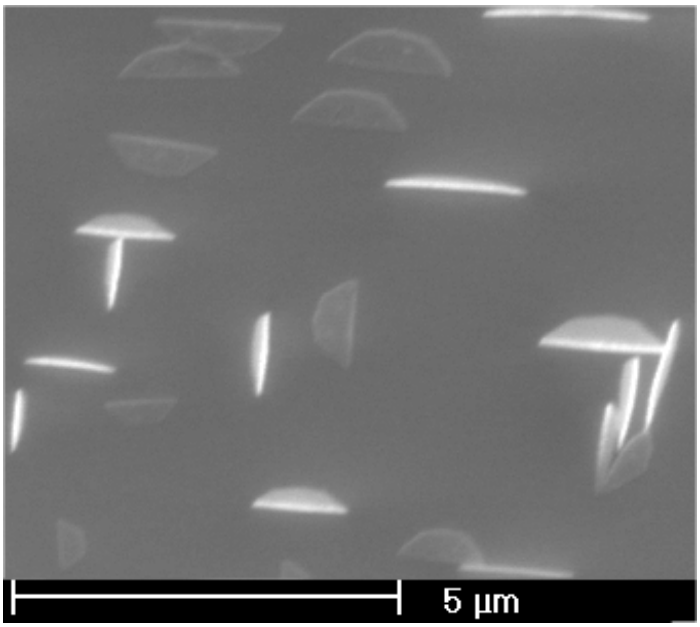

Fig. 3.33 SEM image showing the semi-circular morphology of the platelets.

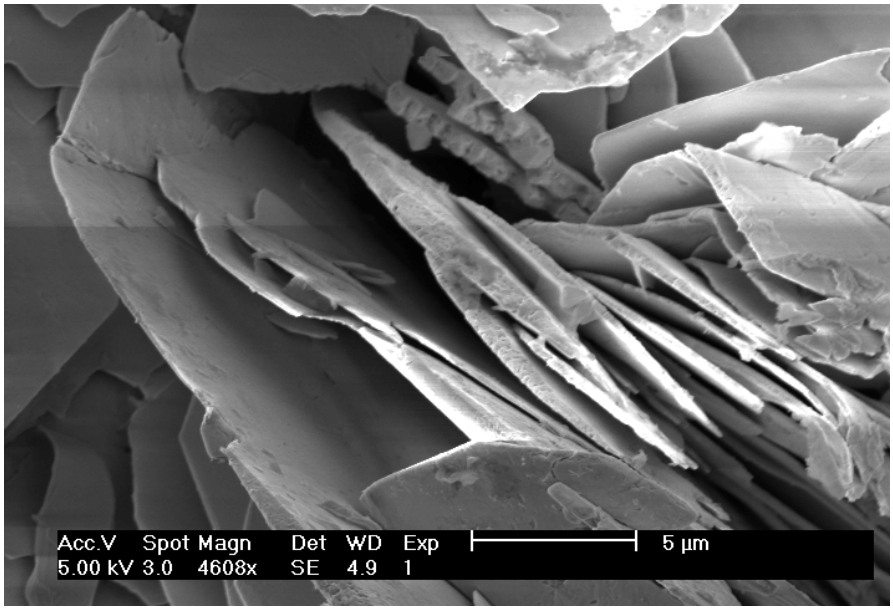

Fig. 3.34 SEM image of PbO platelets produced after the reaction between $Pb(NO_3)_2$ and KOH.

3.2.8.2 PZT grown on Nb:$SrTiO_3$

After establishing the mechanism involved in the growth of hydrothermal PZT on (100) $SrTiO_3$, the next stage was to reduce reaction times to produce nanoislands of the desired size. Conductive Nb-doped (100) $SrTiO_3$ substrates were used in place of pure (100) $SrTiO_3$ so that the electrical properties of the resultant nanoislands could be assessed.

Fig. 3.35 shows a large area of a Nb:$SrTiO_3$ substrate processed for 30 min at 160 °C without a Pb excess. No continuous film coverage was visible; instead the PZT structures consisted of isolated and partially coalesced cubic islands as well as lines of interconnected islands that formed unbroken "microwires", sometimes over a millimetre in length. The rough morphology of the islands (Fig. 3.36) was similar to that witnessed during the hydrothermal synthesis of freestanding PZT cubes without a Pb-excess. Furthermore, in contrast to the Pb-excess experiments, the islands appeared to display a layered structure. Unfortunately the size of the islands did not scale with reaction time, which suggests growth rates for PZT crystals on the $SrTiO_3$ substrates and in solution (freestanding) were comparable.

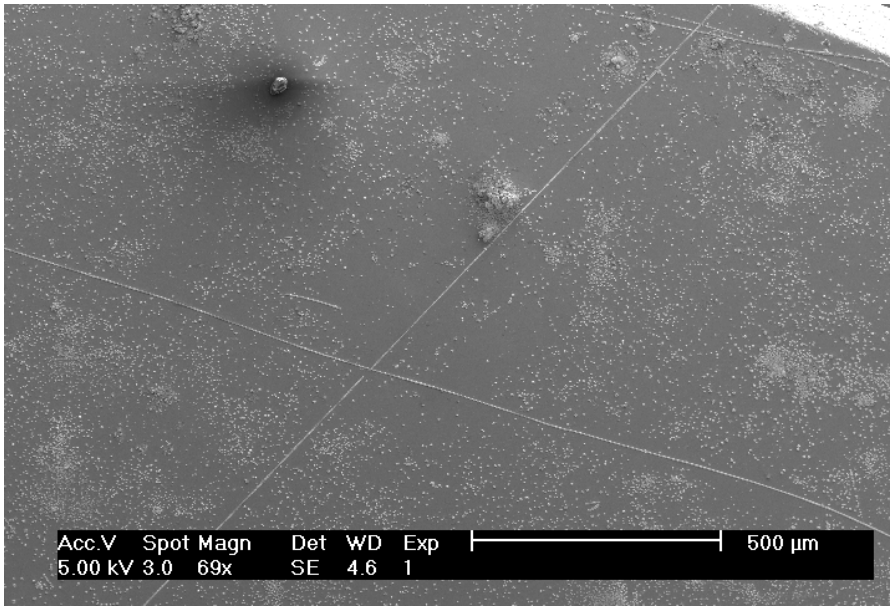

Fig. 3.35 SEM image showing the extent of PZT coverage on a Nb:$SrTiO_3$ substrate after 30 min processing at 160 °C.

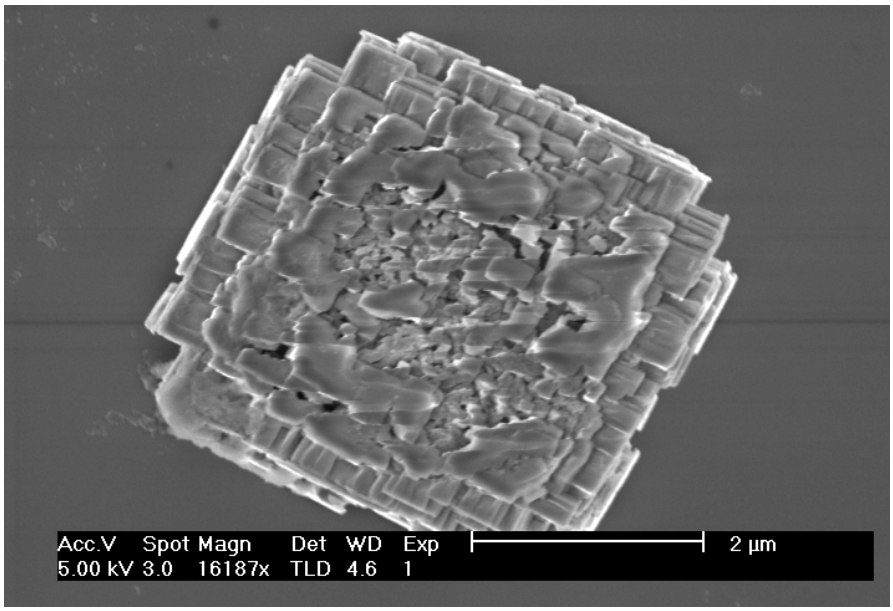

Fig. 3.36 SEM image of a PZT island grown on Nb:$SrTiO_3$ without a Pb-excess.

The origin of the PZT microwires across the substrate is unclear, however certain attributes of the lines favour one explanation in particular. Firstly, their length, sometimes in excess of 1 mm, would appear to rule out crystallographic defects such as step edges, which persist over much shorter lengthscales in $SrTiO_3$ substrates, even after etching.[24] Secondly, the individual islands, of which the microwires are composed, aligned themselves to the crystallographic directions of the substrate

surface, even if the microwire itself followed a different path (Fig. 3.37). These observations point to the existence of preferred nucleation sites on the surface of the substrate, which are independent of the underlying crystal structure. Single-crystal substrates are subjected to a chemical-mechanical polishing process during their fabrication that introduces scratches into the surface. Particles from the polishing paste (often diamond-based) can become embedded in these scratches and later act as potential nucleation sites during the hydrothermal treatment. After nucleation, the PZT islands grow epitaxially and coalesce with neighbouring crystals to form a continuous wire. Fig. 3.38 shows the remnants of a PZT microwire that detached from the substrate through mechanical contact. The outline of the scratch can clearly be seen, bounded by the remaining crystalline material.

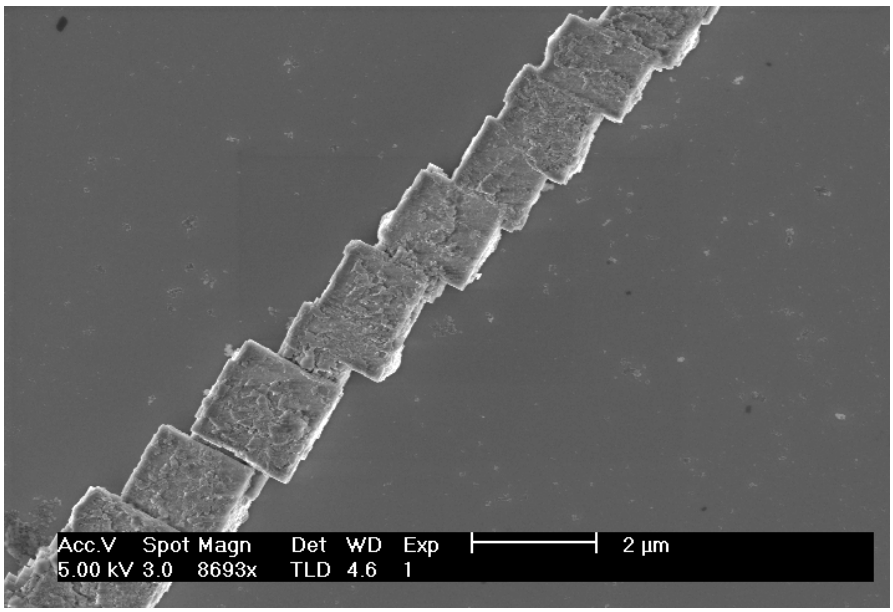

Fig. 3.37 SEM image showing the misalignment between the epitaxial PZT islands and the axial direction of the microwire. Scratches in the substrate exert an influence over the location of islands whilst the crystallographic orientation of the substrate affects their growth.

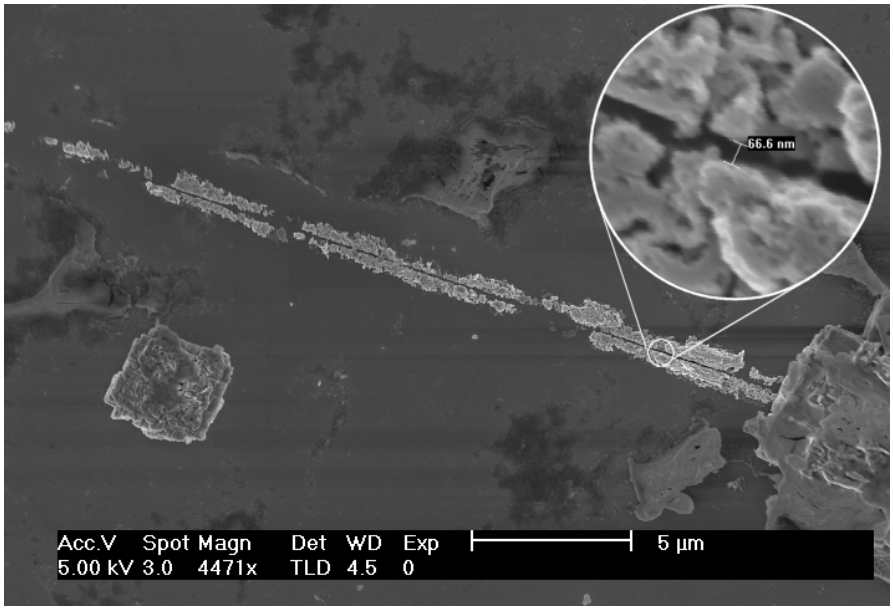

Fig. 3.38 SEM showing the remnants of a microwire after mechanical removal

The limited adhesion of the microwires to the $SrTiO_3$ surface opens up the possibility of using intentionally scratched substrates as a templated growth mechanism for generating ferroelectric structures via the hydrothermal method.

3.2.8.3 Piezoresponse from PZT islands and microwires

PFM was used to produce piezoresponse images of the structures found on the surface of the Nb:$SrTiO_3$ substrates after a 30 min hydrothermal treatment without Pb-excess. Piezoresponse images were acquired by applying an AC voltage with a magnitude of 1.5 V and frequency of 62 kHz between a conductive $PtIr_5$-coated Si tip and the bottom electrode of the sample. The tip had a nominal resonant frequency and spring constant of 14 kHz and 0.2 N/m, respectively. Fig. 3.39 shows the topography and associated out-of-plane piezoresponse of an isolated, cubic PZT island, scanned using the AFM. No domain patterns are seen; instead the cube displays a uniform, weak piezoresponse as evidenced by the low contrast. Greater piezoresponse is detected around the edges of the cube, however this is most likely due to topographic cross-talk of the type encountered by Tiruvalem et al. during their PFM analysis of relaxor nanocrystals.[25] They found an apparent dipolar ordering of the piezoresponse along the cantilever axis, which was attributed to the interaction between the tip and the sloping sides of the nanocrystals. The net effect being that positive slopes produced a strong in-phase response whilst negative slopes gave an out-of-phase signal. This

behaviour is replicated to an extent in Fig. 3.39, whereby the left-hand and right-hand edges of the cube show strong in-phase and out-of-phase response, respectively. The use of stiffer cantilevers can diminish this effect, however the limited adhesion of islands to the substrate surface precluded this option.

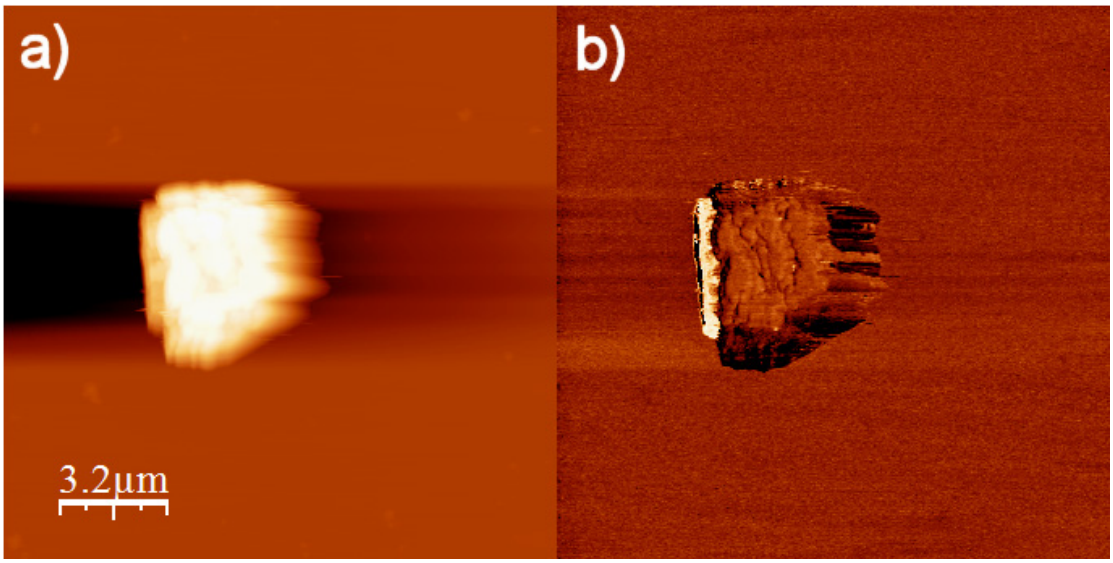

Fig. 3.39 AFM image showing the (a) topography and associated (b) out-of-plane piezoresponse of a PZT island.

Further evidence that the PZT islands were indeed ferroelectric came a larger area of the sample was scanned (Fig. 3.40). In the piezoresponse image we can see that the cubic crystals display a response, whilst adjacent regions, containing amorphous material, do not.

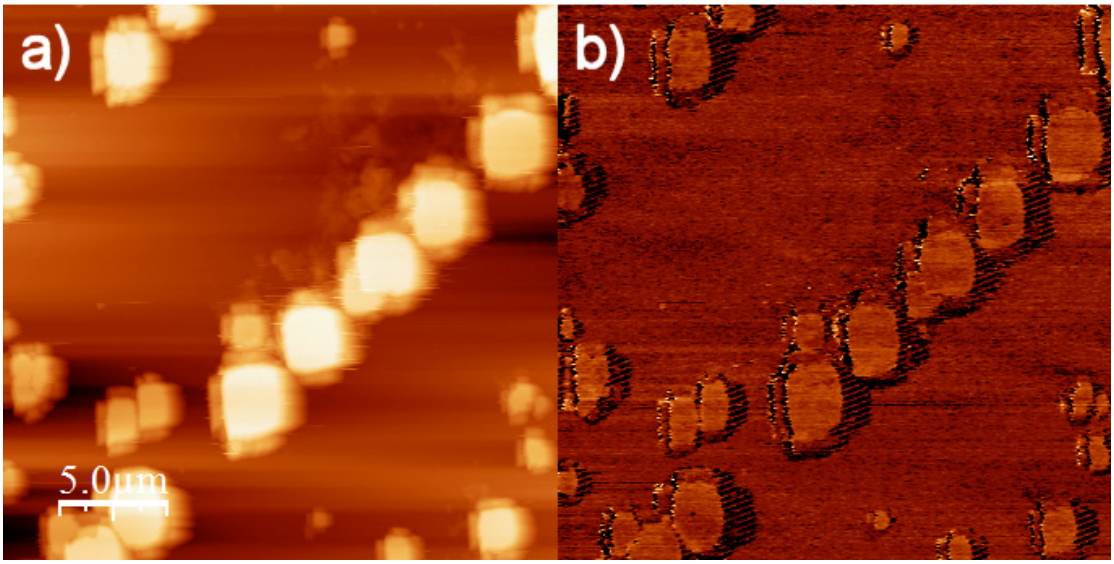

Fig. 3.40 AFM image showing the (a) topography and associated (b) out-of-plane piezoresponse of a collection of PZT islands and amorphous material. Note the apparent lack of piezoresponse from the amorphous material.

Acquiring piezoresponse images of microwires proved challenging because of their aforementioned relatively weak adhesion to the substrate. Consequently, during a scan the AFM tip had a tendency to remove them. However, in a limited number of cases it was possible to acquire images (Fig. 3.41). It can be seen that the detected piezoresponse is consistent with the theory that the microwires formed through the coalescence of individual islands, each bearing their own piezoresponse.

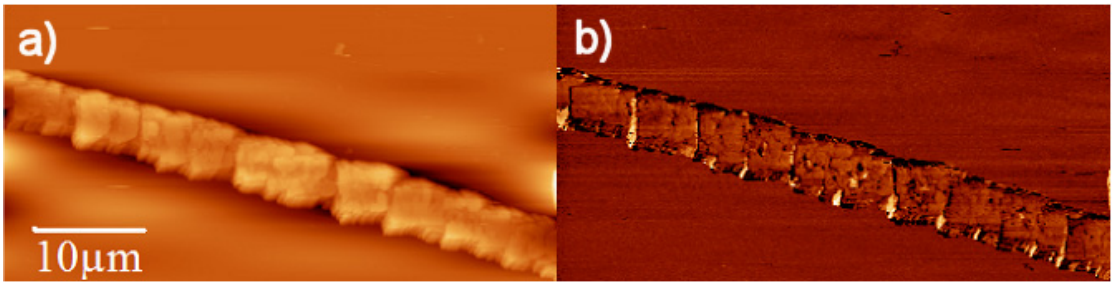

Fig. 3.41 AFM image showing the (a) topography and associated (b) out-of-plane piezoresponse of a PZT microwire.

3.3 Summary

The aim of this chapter was to produce freestanding PZT nanoparticles via the ex situ technique of hydrothermal synthesis. Initial attempts, following the work of Deng et al.[1], found the average size of the resultant particles to be two orders of magnitude

larger than that desired – namely, below 100 nm. Efforts were thus directed at modifying the technique in order to reduce particle size. The first variable to be altered was processing time. It was found that PZT, with a composition close to the MPB, was the major phase after just 30 min of processing at 160 °C, whilst full crystallisation was attained between 1.5 – 2 hr. However, particle sizes remained more or less unchanged, regardless of processing time. This suggested that the dissolution stage was the rate-limiting step in the overall reaction. Further evidence for this came when the effects of processing temperature were studied. Decreasing temperatures below 160 °C, whilst keeping processing times constant at 30 min, led to an increase in the amount of unreacted TiO_2 precursor remaining after the reaction. The PZT particles that did form, however, were of a similar morphology and size as those observed at higher temperatures. It was therefore concluded that reductions in processing temperature had had a large effect on the dissolution rate of the precursors, but only a limited effect on the precipitation rate of PZT crystals.

The initial Zr/Ti precursor ratio was altered in order to synthesise PZT compositions above and below the MPB. These experiments were undertaken to gain an insight into the reaction mechanism involved in the hydrothermal process. Unexpectedly, the resultant PZT composition was found to be independent of the initial Zr/Ti precursor ratio and lay close to the MPB. The subsequent excesses of Zr or Ti manifested themselves as amorphous $PbZrO_3$ and ZrO_2 above the MPB and TiO_2 below the MPB.

Increasing the initial Pb precursor concentration was found to modify the morphology but not the size of the resultant PZT particles. The cubic crystals were well faceted and less agglomeration had taken place. It is thought that an excess of Pb ions at the early stages of the reaction helped in the dissolution of the Zr-Ti precipitates. Finally, the internal structure of PZT particles produced using a Pb-excess exhibited an enhanced degree of crystallisation when compared to those produced from stoichiometric precursor solutions.

A brief study into the effect of alkali mineraliser type found that it was possible to produce phase-pure PZT when KOH was substituted for NaOH. The morphology of particles was unaffected, however the average size fell by 40% when NaOH was used.

A number of different surfactants were tested for their ability to disrupt the hydrothermal reaction during the precipitation stage and thus impede crystal growth. Using a 2% Triton X-100 solution it was possible to reduce the average PZT particle size by 60% in comparison to those synthesised without surfactants. The other surfactants were less effective and resulted in the production of large quantities of amorphous or partially crystallised material.

The final study on freestanding particles involved the hydrothermal crystallisation of a PZT sol precursor. It was hoped that the homogeneous sol would be more amenable in terms of the required mineraliser concentration necessary to promote a reaction. Processing the sol for 30 min at 160 °C using a 3.3 M KOH concentration resulted in a mixture of agglomerated, micron-sized PZT cubes and amorphous material. Increasing the reaction time to 24 hr, whilst keeping the other variables constant, led to the production of pyramidal fibres that, in some cases tapered to nanosized points.

Since the various studies on freestanding hydrothermal particles failed to produce crystals of the desired dimensions, the decision was taken to investigate epitaxial hydrothermal growth of PZT on single-crystal $SrTiO_3$ substrates. Long processing times of 24 hr resulted in the formation of micron thick PZT films, with inhomogeneous substrate coverage. Islands with dimensions approaching 100 nm were also observed. XRD analysis showed the structures to be highly (100)-oriented which was due to the good lattice match between PZT and $SrTiO_3$. Processing times of 30 minutes led to the formation of isolated PZT islands as well as “microwires”, up to a millimetre in length, composed of individual islands that had coalesced in one dimension. It was thought that these features were the result of preferred nucleation sites on the substrate due to polishing. Unfortunately, the size of the individual islands did not scale with reaction time. This suggests that the nanometric islands observed in the extended processing time experiment were the result of local inhomogeneities in the precursor mixture.

The ferroelectric properties of individual PZT islands and microwires were analysed using PFM. All of the crystalline material displayed a weak piezoresponse, whilst adjacent amorphous material did not.

References

[1] Y. Deng, L. Liu, Y. Cheng, C.W Nan and S. Zhao, *Mater. Lett.* 57, 1675 (2003)

[2] S. Fushimi and T. Ikeda, *J Am. Ceram. Soc.* 50, 3, 129 (1967)

[3] M. Traianidis, C. Courtois and A. Leriche, *J. Euro. Ceram. Soc.* 20, 2713 (2000)

[4] A. Boutarfaia and S. E. Bouaoud, *Ceram. Int.* 22, 281 (1996)

[5] T.R.N. Kutty and R. Balachandran, *Mater. Res. Bull.* 19, 1479 (1984)

[6] H. Cheng, J. Ma, B. Zhu, and Y. Cui, *J. Am. Ceram. Soc*. 76, 3, 625 (1993)

[7] M. M. Lencka, A. Anderko and R. E. Riman, *J. Am. Ceram. Soc.* 78, 10, 2609 (1995)

[8] S-B. Cho, J-S. Noh, M. M. Lencka, R. E. Riman, *J. Euro. Ceram. Soc.* 23, 2323 (2003)

[9] A. Rujiwatraa, J. Jongphiphana, S. Anantab, *Mater. Lett.* 59, 1871 (2005)

[10] X. Li and J. Chang, *Chem. Lett.* 33, 11 (2004)

[11] L. Chen, Y. Liu, Z. Lu, D. Zeng, *J. Colloid Interface Sci.* 295, 440 (2006)

[12] W. Chen, J. Peng, L. Mai, H. Yu, Y. Qi, *Solid State Commun.* 132, 513 (2004)

[13] F. Luo, D. Wu, L. Gao, S. Lian, E. Wang, Z. Kang, Y. Lan and L. Xu, *J. Cryst. Growth*, 285, 534 (2005)

[14] Triton X-100 datasheet, Roche Applied Science

[15] A. T. Hubbard, Encyclopedia of Surface and Colloid Science, CRC Press

[16] J. H. Zeng, Z. H. Li, J. Su, L. Wang, R. Yan and Y. Li, *Nanotechnology*, 17, 3549 (2006)

[17] C. Y. Xu, P. X. Zhang and L. Yan J. Raman Spectrosc. 32, 862 (2001)

[18] S. Wei, J. Lu, W. Yu and Y. Qian, *J. Appl. Phys.* 95, 7, 3683 (2004)

[19] C.Y. Xu, P.X. Zhang and L. Yan, *Acta Phys. Sin.* 54, 11, 5089 (2005)

[20] R. Wendelbo, D. E. Akporiaye, A. Karlsson, M. Plassen and A. Olafsen, *J. Euro. Ceram. Soc.* 26, 849 (2006)

[21] S-B. Cho, M. Oledzka and R. E. Riman, *J Cryst. Growth*, 226, 313 (2001)

[22] S. H. Ahn, W. W. Jung, and S. K. Choi, *Appl. Phys. Lett.* 86, 172901 (2005)

[23] I. Szafraniak and M. Alexe, *Ferroelectrics*, 291, 19 (2003)

[24] G. B. Cho, M. Yamamoto, Y. Endo, *Thin Solid Films* 464, 80 (2004)

[25] R. Tiruvalam, A. Kundu, A. Soukhojakb, S Jesse and S. V. Kalinin, *Appl. Phys. Lett.* 89, 112901 (2006)

Chapter 4: Solid Phase Synthesis

4.1 Introduction

Since the hydrothermal synthesis technique was unsuccessful in producing PZT particles of the desired scale, efforts were directed towards developing the in situ technique of solid-phase synthesis for the production of ferroelectric nanoislands. The work of Sidorkin et al. demonstrated the feasibility of producing $PbTiO_3$ films using this technique.[1] However, little detail of the film morphology is reported in their papers. Likewise, Stankus et al. followed a similar processing route, but stopped short of testing the ferroelectric properties of their $PbTiO_3$ films.[2] Therefore, it was felt worthwhile to begin by investigating the structure and morphology of $PbTiO_3$ thin films before moving on to an analysis of their ferroelectric properties. This would provide a deeper insight into the reaction mechanisms involved during solid-phase synthesis and hopefully lead to an understanding of the observed film microstructure. Comparisons could also be made between the ferroelectric properties of thin films and nanoislands - provided the latter could be synthesised successfully.

4.2 Attempts to synthesise $PbTiO_3$ films on SiO_2/Si substrates

4.2.1 Evolution of phases

In order to track the development of the perovskite $PbTiO_3$ phase, a sample consisting of a 100 nm Pb layer on top of a 50 nm Ti layer was subjected to consecutive 1 hr annealings in air, between 300 – 700 °C. The thickness of each layer was chosen in accordance with the molar volumes of Pb and Ti to give the correct $PbTiO_3$ stoichiometric ratio, with a 15% Pb-excess to account for losses during annealing. Fig. 4.1 shows the phase evolution that occurred within the bilayer, after each annealing. Oxidation of the Pb layer to tetragonal PbO (litharge, PDF card no. 05-0561) was more or less complete after the first annealing. Between 300 – 500 °C there is little change in phase composition visible in the XRD patterns. However, it is likely that several amorphous compounds form within the Ti-PbO solid solution at these temperatures. After the 600 °C annealing, peaks for PbO disappeared as the perovskite $PbTiO_3$ phase began to form. By 700 °C, $PbTiO_3$ formation has completed;

the prominent reflections associated with this phase are shown in Fig. 4.1. Annealing for longer times and/or higher temperatures brought about little change in the pattern. Therefore it seems reasonable to conclude that the optimum annealing temperature necessary to crystallise the perovskite phase lies between 600 – 700 °C. Single, 1 hr annealings at 650 °C provided confirmation of this.

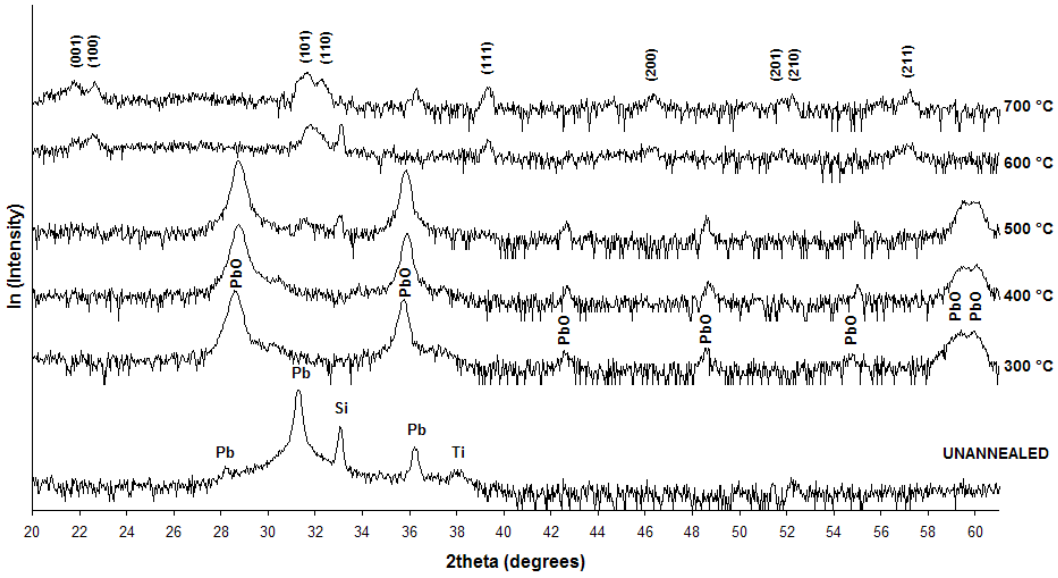

Fig. 4.1 XRD data for a Pb/Ti/SiO_2/Si sample after consecutive 1 hr annealings in air between 300 – 700 °C (indexed peaks correspond to the accepted values for tetragonal $PbTiO_3$, PDF card no. 06-0452).

Iijima et al.[3] define the *c*-axis orientation ratio of a $PbTiO_3$ film to be equal to:

$$\alpha = \frac{I(001)}{I(001) + I(100)} \qquad \text{Eqn. 4.1}$$

where $I(001)$ and $I(100)$ are the intensities of the (001) and (100) peaks in the XRD pattern, respectively. The value of α for $PbTiO_3$ powder is 0.29, whilst α derived from the 700 °C data in Fig. 4.1 is equal to 0.48. This suggests the substrate had a limited influence on the crystallographic orientation of the film.

The lone peak at approximately 36.3° in the 700 °C pattern, from Fig. 4.1, indicates the presence of an impurity phase in the sample. Phase identification from a single peak is difficult and inherently unreliable, but the fact that it appears at high

temperature would suggest a form of oxidised Ti is responsible. Three such candidates from the ICDD database, that are known to have strong intensities near to this location, include TiO_2 (PDF card no. 211276), $TiO_{1.04}$ (PDF card no. 43-1295) and δ-TiO (PDF card no. 080386).

4.2.2 Initial attempts at measuring electrical properties

4.2.2.1 Si substrates

Having established the crystallisation conditions for solid-phase $PbTiO_3$ thin films on thermal oxide wafers, it was necessary to switch to using conductive substrates in order to characterise their electrical properties. Initially, platinised Si wafers with an 8 nm Ti adhesion layer and a 100 nm Pt layer, were tested. This combination was found to be unsuitable however, since the Pt reacted with the bare Si, in a two-stage process, to form PtSi, when the structure was annealed (Fig. 4.2). The effect was exacerbated by the Pb/Ti overlayers which inhibited the diffusion of O_2, from the atmosphere, towards the Ti adhesion layer. Consequently, the titania diffusion barrier that would otherwise have formed, was suppressed, leading to a near complete conversion of the Pt into PtSi. A more exhaustive investigation of this effect is presented in a paper that can be found in *Appendix A*.

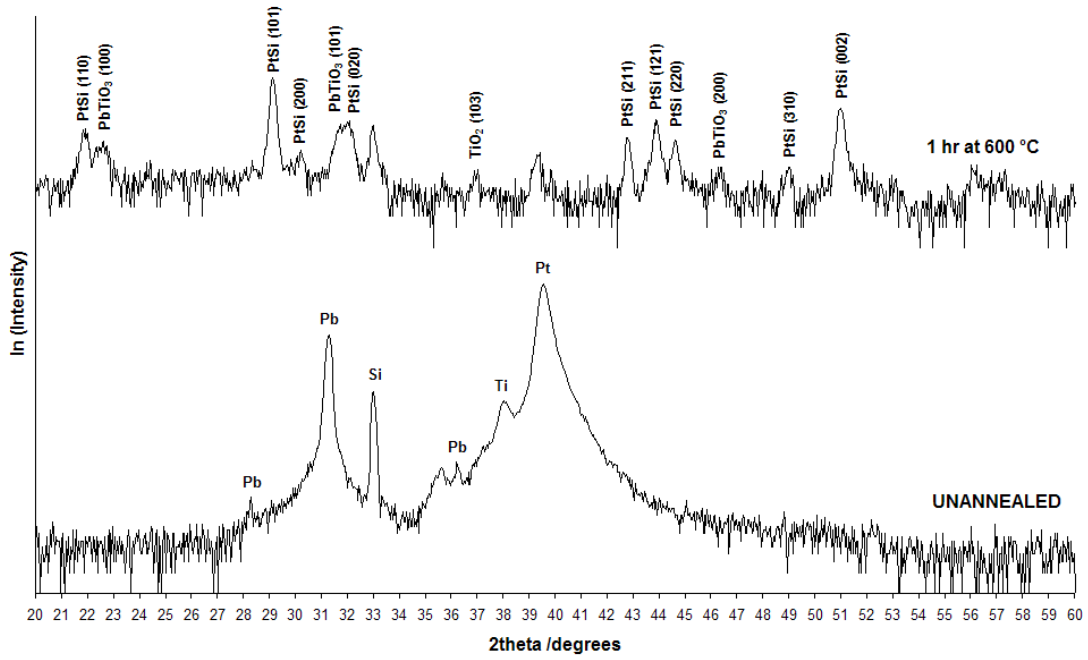

Fig. 4.2 XRD data indicating the formation of PtSi when a Pb/Ti/Pt/Ti/Si sample was annealed in air for 1 hr at 600 °C.

Although PtSi is conductive, its presence beneath the $PbTiO_3$ film is unwelcome since Si can also react with Pb to form lead silicates. Depositing the Pt/Ti back electrodes on thermal oxide Si wafers alleviated this problem. Both Sidorkin et al. and Stankus et al. chose to use Si substrates for their $PbTiO_3$ film experiments.[1, 2] However, as mentioned previously, only Sidorkin et al. measured the electrical properties of their films.[1] To achieve this, they deposited an In-Ga eutectic on top of the Si substrate to act as a bottom electrode. From their paper it is not clear how they prevented Si and/or PbO from diffusing through the electrode layer.

4.2.2.2 SiO_2/Si substrates

The same electrode structure (Pt/Ti) as used in combination with Si wafers was retained for the experiments involving thermal oxide wafers. Fig. 4.3 shows the XRD pattern of a Pb/Ti/Pt/Ti/SiO_2/Si sample annealed in air for 1 hr at 650 °C. The thickness of the Pb and Ti layers was kept at 100 nm and 50 nm, respectively. No peaks corresponding to platinum silicide phases were detected. In contrast, most of the peaks associated with the perovskite $PbTiO_3$ phase were easily identifiable. The α-

ratio (see Eqn. 4.1) for the film was equal to 0.23, which suggests the substrate has had little or no effect on the crystallographic orientation of the film.

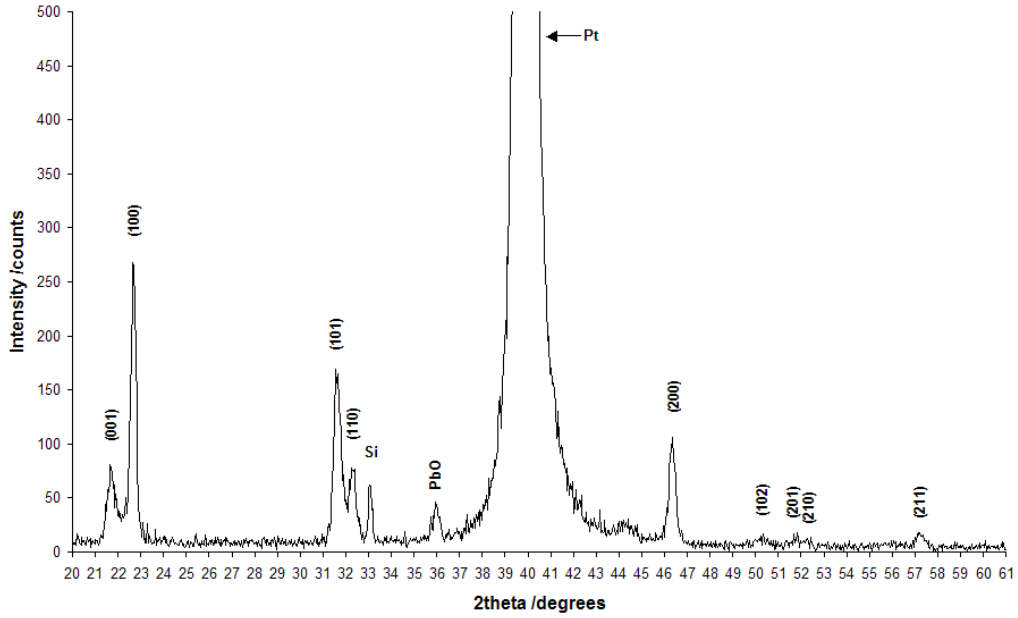

Fig. 4.3 XRD data for a Pb/Ti/Pt/Ti/SiO_2/Si sample annealed in air for 1 hr at 650 °C (indexed peaks correspond to the accepted values for tetragonal $PbTiO_3$, PDF card no. 06-0452).

Top electrodes were deposited onto the annealed sample in order to test the ferroelectric properties of the film. However, DC resistance measurements indicated the presence of shorts, thus making the acquisition of a hysteresis loop impossible. An inspection of the surface morphology of the film revealed the most probable cause of the shorts. The film was composed of close-packed grains that were predominantly nanosized. However, at many points across the surface, the film had detached from the back electrode to form circular blisters (Fig. 4.4). Often, pinholes were observed at the summits of these blisters and, more occasionally, at random points elsewhere on the film. From SEM observations, the areal density of the blisters was estimated to be on the order of 10^7 cm^{-2}. This corresponds to several thousand possible shorting paths over the area of a single top electrode, even accounting for the fact that not all of the blisters possessed pinholes. It is therefore reasonable to assume that these defects were responsible for the observed high conductivity.

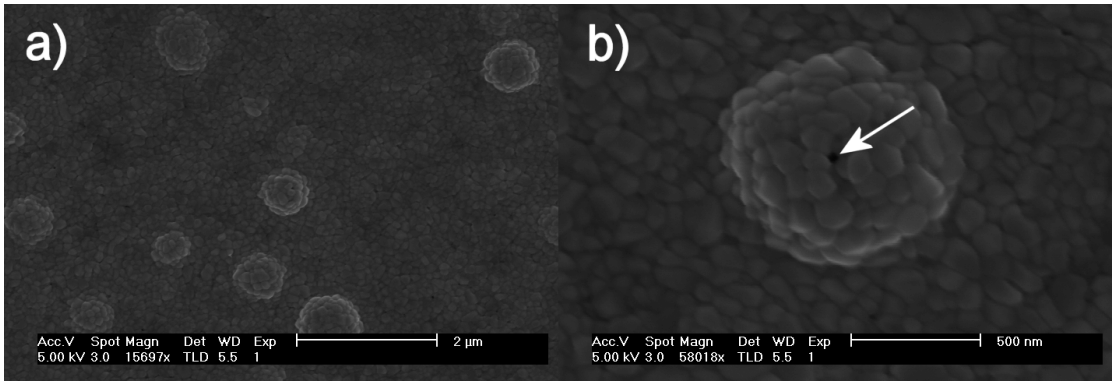

Fig. 4.4 SEM images of an annealed Pb (100 nm) /Ti (50 nm)/Pt/Ti/SiO_2/Si sample showing (a) the extent of blistering across the surface of the film and (b) a possible shorting path to the back electrode, through a pinhole, at the summit of one of the blisters.

As it was quite important to get a thin film ferroelectric measurement, considerable effort was expended to produce an intact film in order to overcome the issue of shorting. The following sections document the experimental work conducted to achieve this objective.

4.2.3 Attempts to overcome the shorting

4.2.3.1 Increasing film thickness

The first variable altered in an effort to produce intact $PbTiO_3$ films was the initial bilayer thickness. Generally, thinner films are more susceptible to shorting since there is a greater likelihood of a pinhole reaching the bottom electrode. Furthermore, shorting can occur through regions of loosely packed grains when the film thickness approaches the average grain size. With this in mind, a thicker 1 µm bilayer was prepared by depositing 370 nm of Ti onto the Pt back electrode, followed by 630 nm of Pb. These values were chosen in order to maintain the stoichiometric ratio necessary to produce perovskite $PbTiO_3$. The surface morphology of such a sample was analysed, after being annealed in air for 1 hr at 650 °C (Fig. 4.5). It is clear that blistering has not been suppressed by using a thicker bilayer, as originally anticipated. In fact, the average diameter of the blisters increased from below 1 µm to 10 µm, when compared with the 150 nm bilayer film (Fig. 4.5a). Also, the level of distortion exhibited by some of the blisters led to the formation of large cracks that exposed the bottom electrode (Fig. 4.5b). The average grain size was found to increase with film thickness; an observation also noted in the sol-gel synthesis of $PbTiO_3$ thin films.[4]

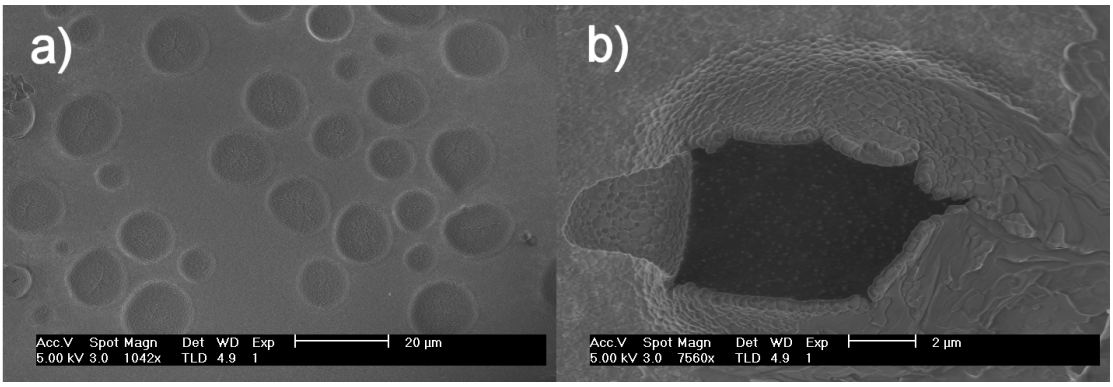

Fig. 4.5 SEM images of a 1 µm Pb/Ti-bilayer sample after annealing for 1 hr at 650 °C.

In order to gain further insight into the mechanism of blister formation, cross-sectional SEM images of the annealed 150 nm and 1 µm bilayer films were acquired (Fig. 4.6). These revealed the presence of voids in the SiO_2 layer and, in the case of the 1 µm sample, severe damage to the Pt back electrode. The severity of the distortion in the 1 µm sample caused the film to lose adhesion to the Pt electrode. PbO diffusion through the Pt layer was confirmed through EDAX analysis of the substrate. It is likely that the PbO reacted with SiO_2 to form one or more of the many lead silicate glass phases present in the PbO-SiO_2 system under such conditions.[5]

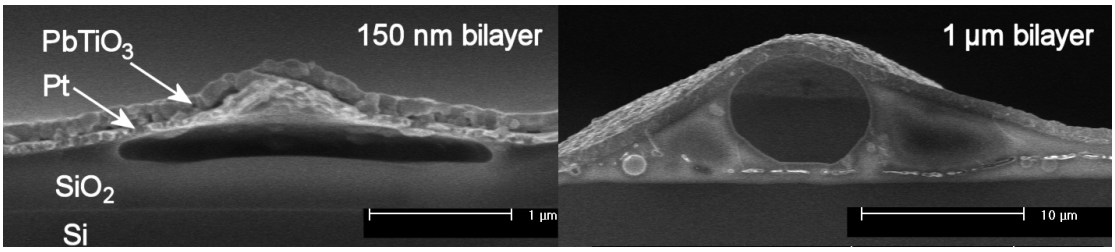

Fig. 4.6 SEM cross-sectional images of thin and thick Pb/Ti-bilayer samples after annealing for 1 hr at 650 °C.

An interesting feature was observed in many of the high magnification SEM cross-sectional images of the film. Groups of parallel striations were present on the surface of the $PbTiO_3$ grains, which, in certain cases, intersected with one another (Fig. 4.7).

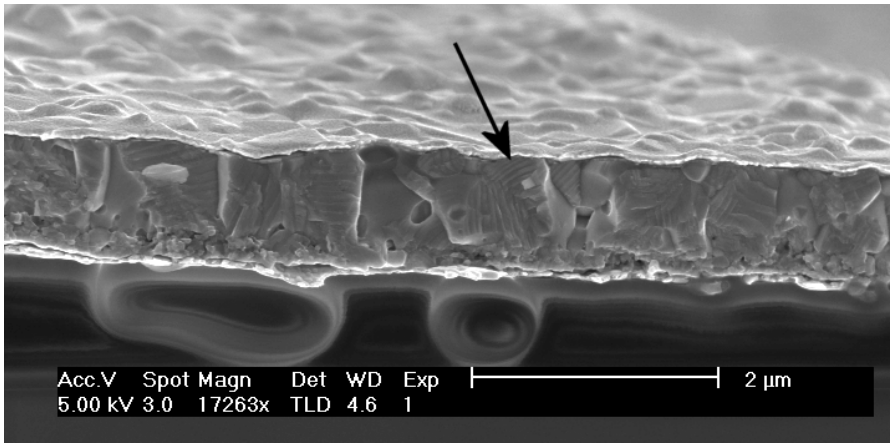

Fig. 4.7 SEM cross-sectional image of a Pb/Ti-bilayer sample showing striations within $PbTiO_3$ grains.

Two possible explanations for this effect were proposed. The features may simply have been fracture surface patterns that arose from cleaving the sample. However, if this were the case, it seems strange that the striations ran in different directions within a single grain (Fig. 4.8). Alternatively, it was thought that the striations could have been e-beam induced ferroelectric domain patterns. A number of papers have been written on the subject of ferroelectric domain imaging via SEM.[6-9]. The contrast mechanisms involved are complex and have been attributed to differences in the pyroelectric potential of positive and negative domains,[10] topographical changes due to the converse piezoelectric effect[11] and differences in secondary electron emission from positive and negative domains, due to their interaction with spontaneous polarisation charges[6]. However, in all cases, bar one, where the authors actively suppressed charging through the use of an environmental SEM[12], the domain images have been unstable. Furthermore, imaging of nanoscale domains is known to be very difficult since the contributions to surface potential from domains falls rapidly as their size decreases.[13] These factors would thus count against the observed striations having a ferroelectric origin. As a final test, the striations were exposed to a 20 keV e-beam for several minutes and then reobserved. The pattern remained identical, even at high magnification, so it is therefore safe to assume the striations were a static morphological feature of the grains. The unusual nature of the fracture surface may be attributable to inhomogenieties within individual grains as a result of stresses endured during their growth.

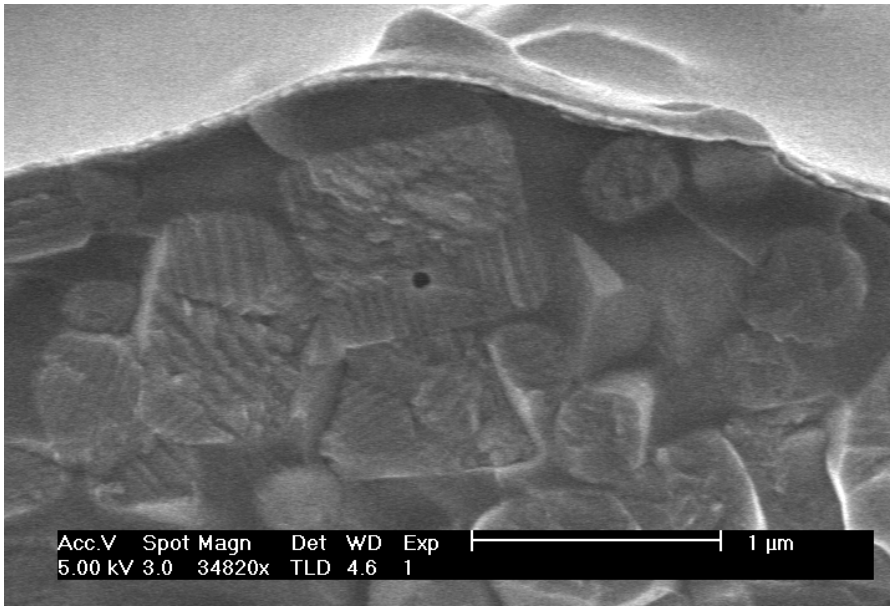

Fig. 4.8 SEM image showing striations running in different directions within single $PbTiO_3$ grains.

4.2.3.2 Alternative adhesion layers

4.2.3.2.1 Rutile titania

At this stage it was unclear whether the blisters were the result of the diffusion of PbO from the film into the substrate or an inevitable consequence of the Pb/Ti solid phase reaction. When annealed above 500 °C in an oxidising environment, Ti from an adhesion layer can diffuse through Pt grain boundaries and oxidise forming titania precipitates that can reach the surface of the electrode.[14] The volume expansion associated with the formation of titania forces the columnar Pt grains apart and allows species such as PbO to diffuse downwards towards the substrate.[15] One method of overcoming this problem is to oxidise the Ti adhesion layer prior to depositing Pt, by annealing in air. Titania, in particular the rutile polymorph, is less susceptible to diffusion through Pt grain boundaries[16] and can also act as a diffusion barrier, thus preventing PbO from reaching the substrate.[15] These favourable characteristics were the motivation for an experiment designed to assess the feasibility of substituting the Ti adhesion layer with titania, in order to overcome the blistering problem. A test sample, consisting of a 450 nm Ti layer sputtered onto a bare Si substrate, was annealed in air for 2 hr at 700 °C. XRD analysis showed peaks corresponding to the rutile TiO_2 phase (PDF no. 211276) and also gave an indication that $TiSi_2$ (PDF no.

350785) had formed (Fig. 4.9). The reaction to produce the latter is facilitated by the breakdown, through reduction, of the thin native SiO_2 layer present on Si wafers, by Ti.[17] An analysis of the relative peak intensities indicated that the rutile film grew without a preferred crystallographic orientation.

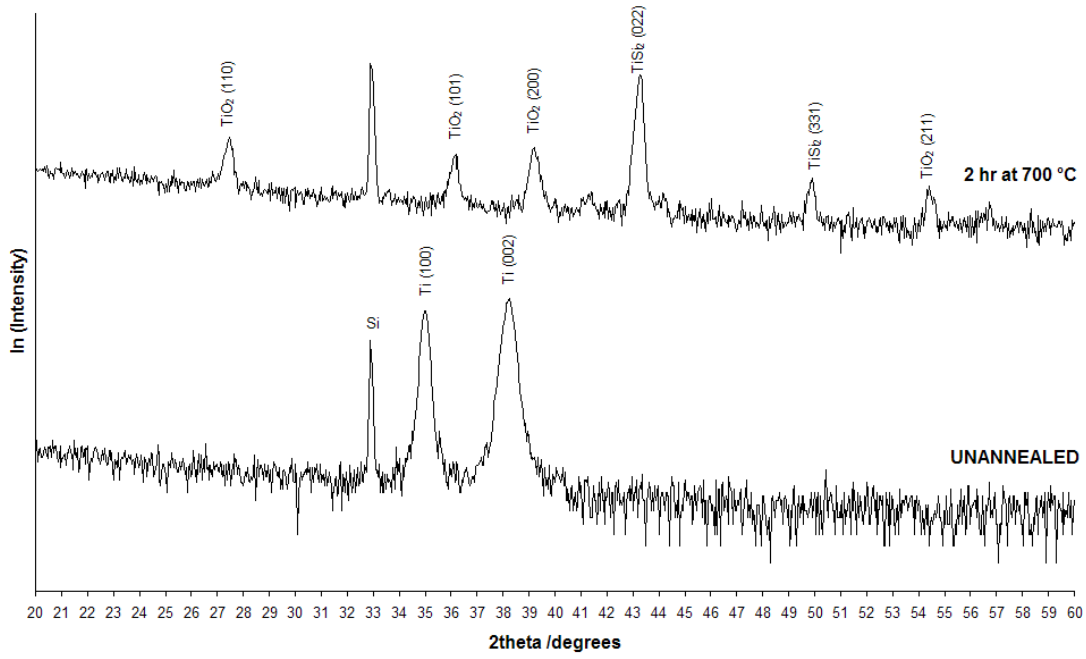

Fig. 4.9 XRD for a Ti (450 nm)/SiO_2/Si sample before and after annealing in air for 2 hr at 700 °C. The indexed peaks correspond to the accepted values for Ti (PDF no. 441294), rutile TiO_2 (PDF no. 211276) and $TiSi_2$ (PDF no. 350785).

Having demonstrated that relatively thick Ti layers could be annealed in air to form rutile, the next step was to reduce the film thickness to a scale suitable for use as an adhesion layer, whilst simultaneously retaining diffusion barrier properties. To prevent the formation of silicides thermal oxide-coated Si wafers were used. The standard Ti adhesion layer thickness was increased from 8 nm to 30 nm, which, after annealing for 2 hr at 700 °C, resulted in a TiO_2 film thickness of approximately 45 nm. This time, the XRD data indicated the formation of (200)-oriented rutile without any secondary silicide phase (Fig. 4.10). This result agrees with that found by Abe et al. who annealed 20 nm Ti films on SiO_2/Si, under O_2 at 700 °C, to produce rutile adhesion layers.[16] Ting et al. also studied rutile films that were produced by annealing Ti layers on fused silica substrates.[18] They found that the degree of preferential growth of (200)-oriented films was inversely proportional to their thickness and attributed this effect to the reduced levels of strain energy in thinner films.

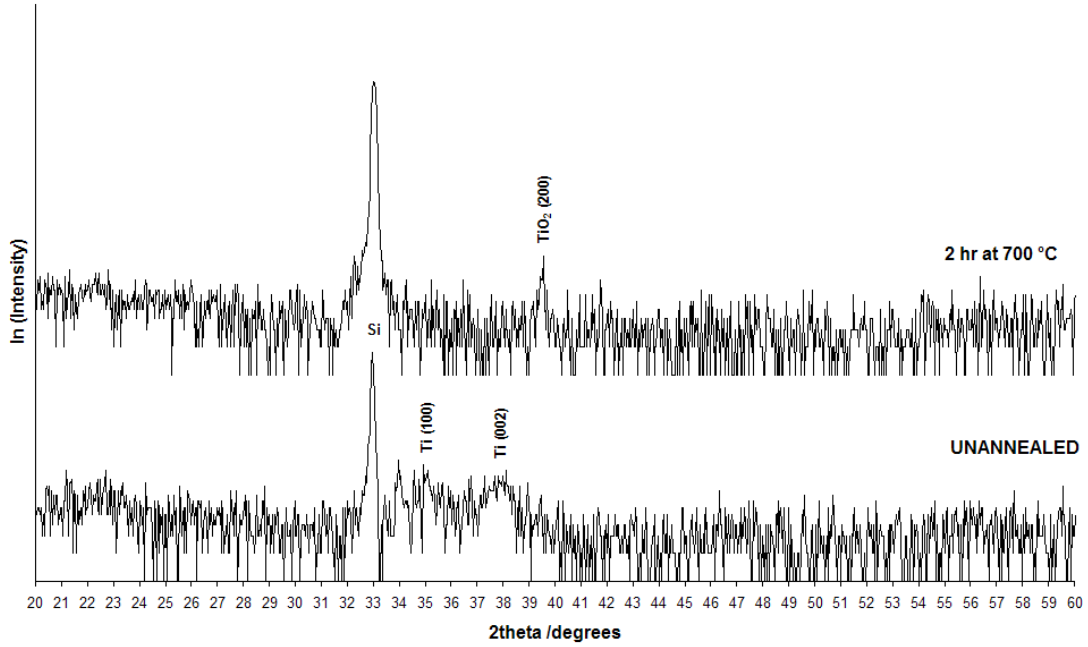

Fig. 4.10 XRD data for a Ti (30 nm)/SiO_2/Si sample before and after annealing in air for 2 hr at 700 °C. The indexed peaks correspond to the accepted values for Ti (PDF no. 441294) and rutile TiO_2 (PDF no. 211276).

Unfortunately, after depositing 100 nm of Pt onto the rutile adhesion layer a tape adhesion test resulted in the partial removal of the film. In contrast, Pt/Ti structures subjected to the same test remained intact. This result gave a qualitative indication of the inferior adhesion properties associated with Pt films deposited onto rutile. Kim et al. found the opposite to be true when they compared the adhesion properties of Pt/Ti and Pt/TiO_2 structures.[19] However, the authors concentrated on thinner adhesion layers (< 10 nm) and their annealing regime, conducted at a lower temperature, led to the formation of the anatase titania polymorph as opposed to rutile. Anatase has a greater tendency to migrate through Pt grain boundaries than rutile[16], which prohibited its use in this study. Finally, our results agree with Maeder et al. who found that Pt adhered poorly to 10 nm Ti adhesion layers that were previously annealed under O_2.[15] Their paper does not state the annealing temperature, however, so it is not certain whether rutile or anatase was produced.

Although the adhesion of the Pt back electrode was questionable, it was still thought worthwhile to deposit a stoichiometric 1 μm Pb/Ti-bilayer onto the Pt/TiO_2/SiO_2/Si structure, in order to test the diffusion suppression properties of the rutile layer. After

annealing for 1 hr at 650 °C the $PbTiO_3$ phase was seen to develop, but the integrity of the film was poor. All of the Au/Cr electrodes, deposited after annealing, were shorted. This result indicated that replacing the usual Ti adhesion layer with rutile was insufficient to prevent PbO diffusion and the subsequent distortion that occurs during $PbTiO_3$ film formation.

4.2.3.2.2 Zirconium

After the adhesion problems encountered during the deposition of Pt onto rutile, the focus of the investigation switched to an alternative metallic adhesion layer. In comparison to Ti, Zr atoms have a larger radius are thus less apt to diffuse through Pt grain boundaries during thermal processing.[15] Additionally, Zr is also more reactive than Ti and so it was anticipated to possess superior adhesion properties when deposited onto SiO_2/Si substrates. Therefore, the use of Zr as an adhesion layer would appear to bring the combined benefits of stability and improved adhesion to an electrode structure.

Thermal oxide Si wafers were used throughout the investigation, onto which 18 nm of Zr was deposited, followed by 100 nm of Pt. Two Pb/Ti-bilayer samples were prepared with total thicknesses of 150 nm and 1 μm. After annealing for 1 hr at 650 °C the $PbTiO_3$ phase was produced, as expected, however significant quantities of tetragonal α-PbO (litharge) and orthorhombic β-PbO (massicot) were also detected in the thicker film (Fig. 4.11). The tetragonal to orthorhombic PbO phase transition occurs at 490 °C, but massicot can exist in a metastable state at room temperature.[20, 21]

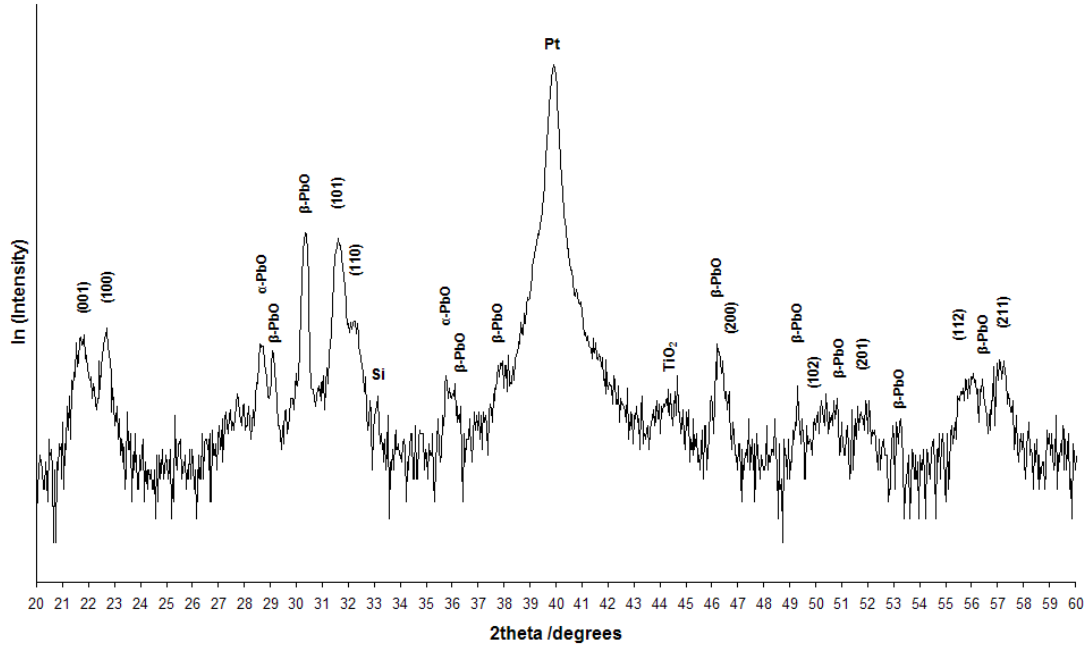

Fig. 4.11 XRD data for a 1 µm Pb/Ti-bilayer deposited onto a Pt/Zr/SiO_2/Si substrate and annealed in air for 1 hr at 650 °C (indexed peaks correspond to the accepted values for tetragonal $PbTiO_3$, PDF card no. 06-0452).

The morphology of the films was inspected via SEM, after annealing (Fig. 4.12). The size and shape of the $PbTiO_3$ grains was similar to those observed in films grown on Pt/Ti/SiO_2/Si substrates (cf. Fig. 4.4). Blistering was also present, to a similar extent, across both films. As observed previously, the size of the blisters increased with bilayer thickness.

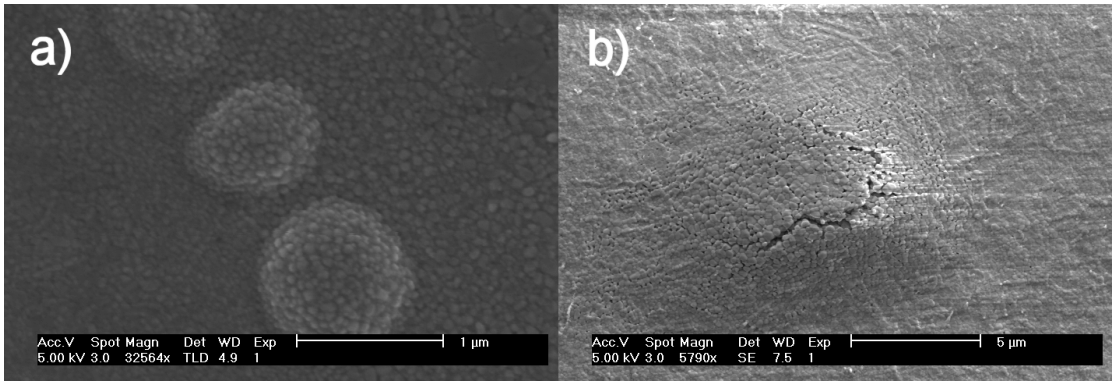

Fig. 4.12 SEM images showing examples of blister formation on annealed (a) 150 nm and (b) 1 µm Pb/Ti-bilayers deposited on Pt/Zr/SiO_2/Si substrates.

Cross-sectional SEM images of the annealed 1 µm bilayer film showed evidence of PbO diffusion through the Pt electrode (Fig. 4.13). Voids in the SiO_2 layer were often

located below the base of a blister. It is likely that as the blister forms, the pressure exerted on the Pt electrode at these contact points increases. This helps to open the Pt grain boundaries and initiate PbO diffusion. Of course, this also implies that an interaction between PbO and the substrate is not a prerequisite for blister formation, but rather a consequence of it.

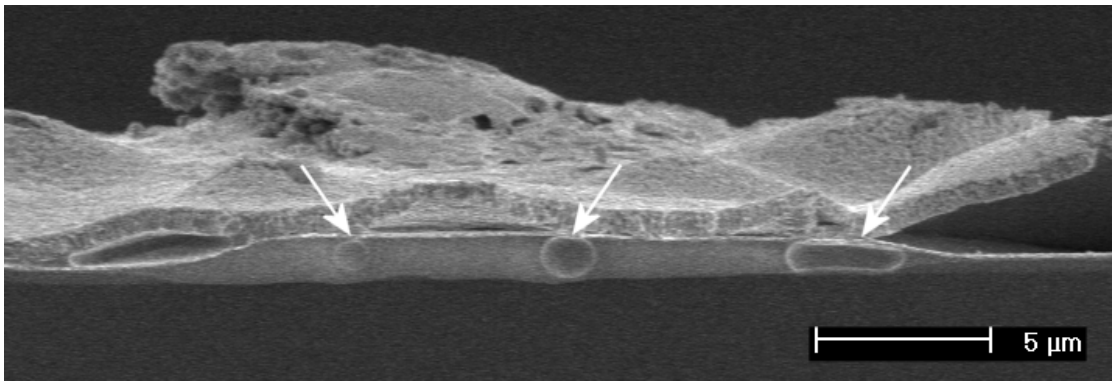

Fig. 4.13 Cross-sectional SEM image of blisters on a Pb/Ti/Pt/Zr/SiO_2/Si sample. Note the location of voids in the SiO_2 layer beneath the bases of each blister.

Au/Cr electrodes were deposited onto the annealed 1 µm bilayer film in order to acquire ferroelectric hysteresis loop measurements. Unlike in previous samples, several of the electrodes were not shorted and possessed high values of DC resistance. Fig. 4.14 shows the ferroelectric hysteresis response of the sample for a number of applied maximum voltages. Above an applied voltage of 15 V the loops became heavily distorted, irrevocably, possibly indicating breakdown. The loop shape below this critical voltage was not characteristic of a typical ferroelectric material. Saturation was not reached and the loops had an elliptical shape, indicative of linear lossy dielectric behaviour. Furthermore, there was no measurable decrease in the switchable polarisation after a fatigue test conducted at 12 V for 10^{10} cycles. Both of these results suggest the dielectric behaviour was not attributable to ferroelectric hysteresis.

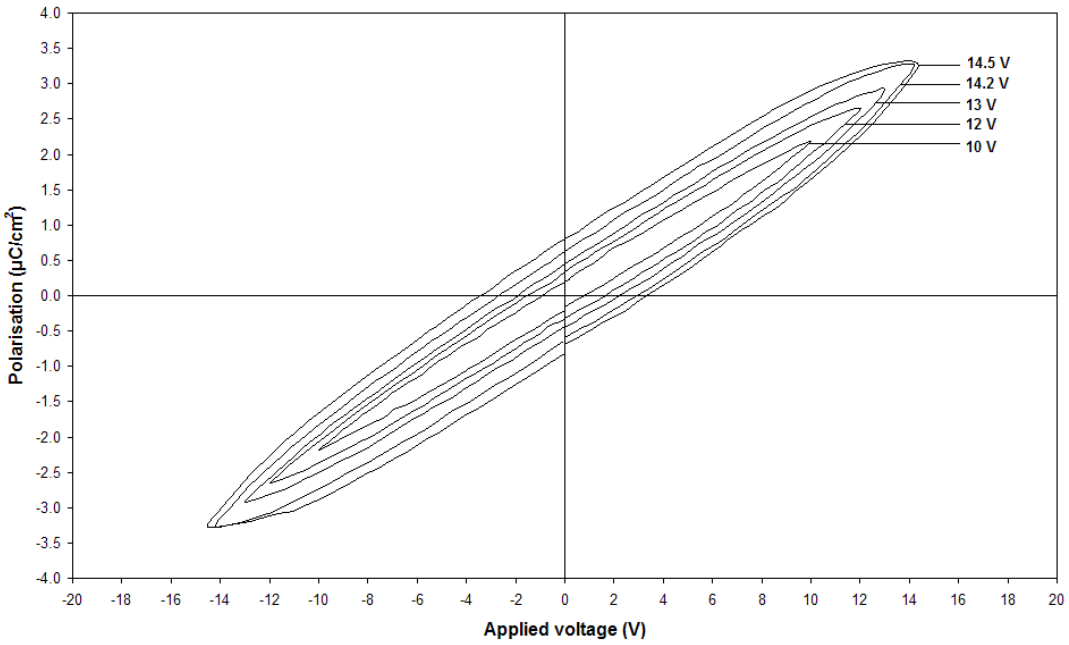

Fig. 4.14 Polarisation vs. applied voltage ferroelectric hysteresis loop data for a Pb/Ti/Pt/Zr/SiO_2/Si sample.

4.2.3.3 Alternative substrates

The next variable to be altered, in an attempt to produce intact films, was the choice of substrate. Naturally, in order to investigate the electrical properties of the ferroelectric films, any replacement for platinised Si would have to possess good electrical conductivity. Two such candidates were selected: ITO-coated glass and single-crystal Nb:$SrTiO_3$. Both have been successfully used as substrates for ferroelectric thin films in the past. Examples from the literature include, but are not limited to, $BaTiO_3$/ITO[22], PZT/ITO[23], $PbTiO_3$/ITO[24] and $PbTiO_3$/Nb:$SrTiO_3$[25]. Single-crystal Nb:$SrTiO_3$ was, of course, also used in the previous chapter, as a substrate during the hydrothermal deposition of PZT films and nanoislands.

4.2.3.3.1 ITO-coated glass

As in previous experiments, two, stoichiometric Pb/Ti-bilayer samples were prepared with total thicknesses of 150 nm and 1 μm. Upon annealing at 650 °C for 1 hr the thinner bilayer became transparent, whilst the thicker bilayer took on the texture and colour of fine $PbTiO_3$ powder (light-yellow). XRD analysis indicated the formation of the perovskite $PbTiO_3$ phase, but it was weak in intensity (Fig. 4.15). Several other

phases were also present, including both dimorphs of PbO. The Au peak originates from the circular top electrodes deposited after the annealing, in anticipation of electrical measurements on the film.

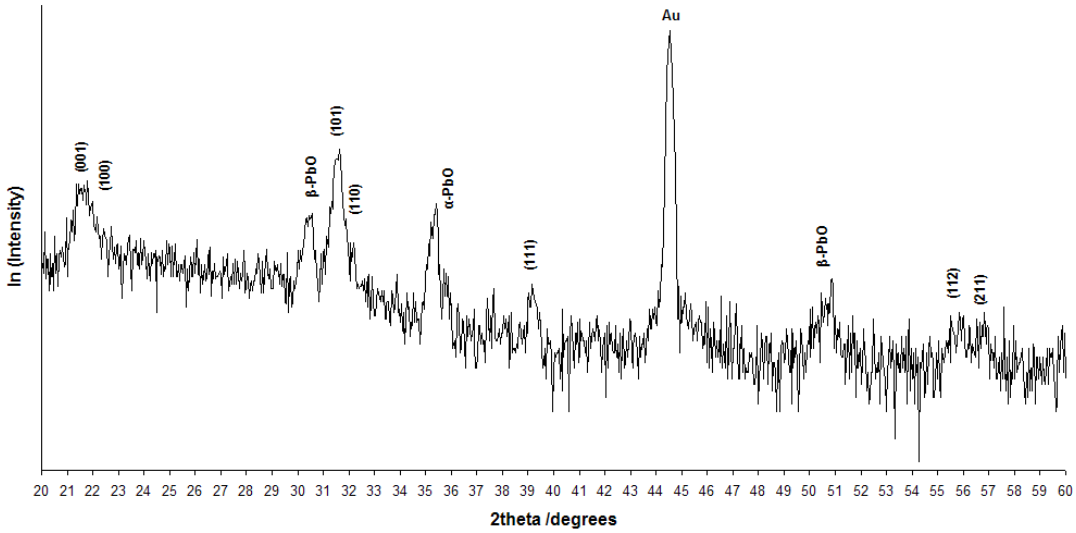

Fig. 4.15 XRD data for a 150 nm Pb/Ti-bilayer deposited onto an ITO-coated glass substrate and annealed for 1 hr at 650 °C (indexed peaks correspond to the accepted values for tetragonal $PbTiO_3$, PDF card no. 06-0452).

The surface morphology of the thin and thick bilayer $PbTiO_3$ films is shown in Fig. 4.16. The grain size was found to be on the nanoscale and hence comparable to that of films grown on platinised Si. In the case of the 150 nm bilayer film, the only defects that could be observed were pinholes – no blistering was seen. The 1 μm bilayer sample was even more heavily distorted than the equivalent deposited onto platinised Si. However, the distortions had the appearance of large wrinkles, as opposed to circular blisters. In some cases the length of the wrinkles was in excess of 200 μm. This would suggest that the adhesion of thicker, in situ $PbTiO_3$ films to ITO-coated glass substrates was inferior to that of films annealed on platinised Si.

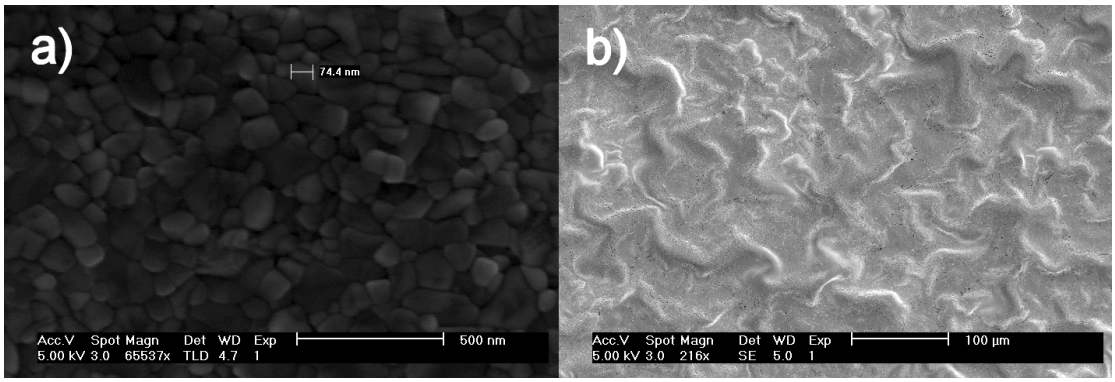

Fig. 4.16 SEM images showing the surface morphology of (a) 150 nm and (b) 1 µm Pb/Ti-bilayers deposited onto ITO-coated glass after annealing for 1 hr at 650 °C .

To better assess the level of film distortion and its possible impact on the substrate, cross-sectional SEM images of the annealed 1 µm bilayer were taken (Fig. 4.17). It appears that the ITO electrode delaminated from the glass substrate during the annealing, but remained relatively well adhered to the newly formed $PbTiO_3$ film. In all the images examined, no evidence of damage to the glass substrate, as a result of PbO diffusion, was found. This is in marked contrast to the results obtained for platinised Si wafers and lends support to the argument that film distortion is inherent to the formation of $PbTiO_3$, rather than as a consequence of substrate interactions.

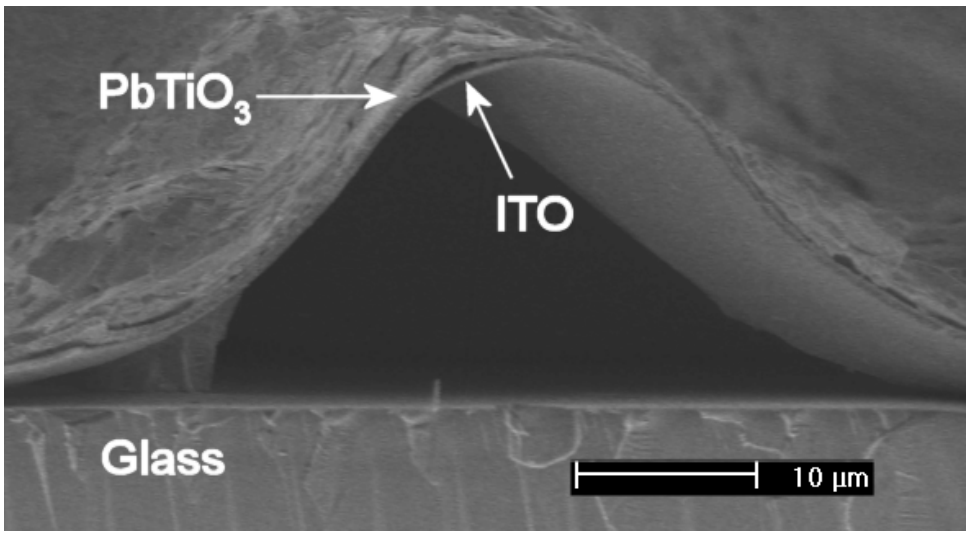

Fig. 4.17 SEM cross-sectional image showing the resultant distortion in a 1 µm Pb/Ti-bilayer (deposited onto ITO-coated glass) after annealing for 1 hr at 650 °C.

Several spherical features were observed on the surface of the thicker $PbTiO_3$ film after annealing (Fig. 4.18). Semi-quantitative EDAX analysis revealed them to

contain In, N and O. One possible source of these elements is the indium nitrate precursor commonly used during the commercial preparation of ITO-coated glass.[26] Although this particular compound could not have survived the $PbTiO_3$ annealing, its constituent elements, in a more stable form, may have remained as an impurity. Regardless of the compound's identity, the presence of In on the surface implies the upward diffusion of species from the electrode through the $PbTiO_3$ film.

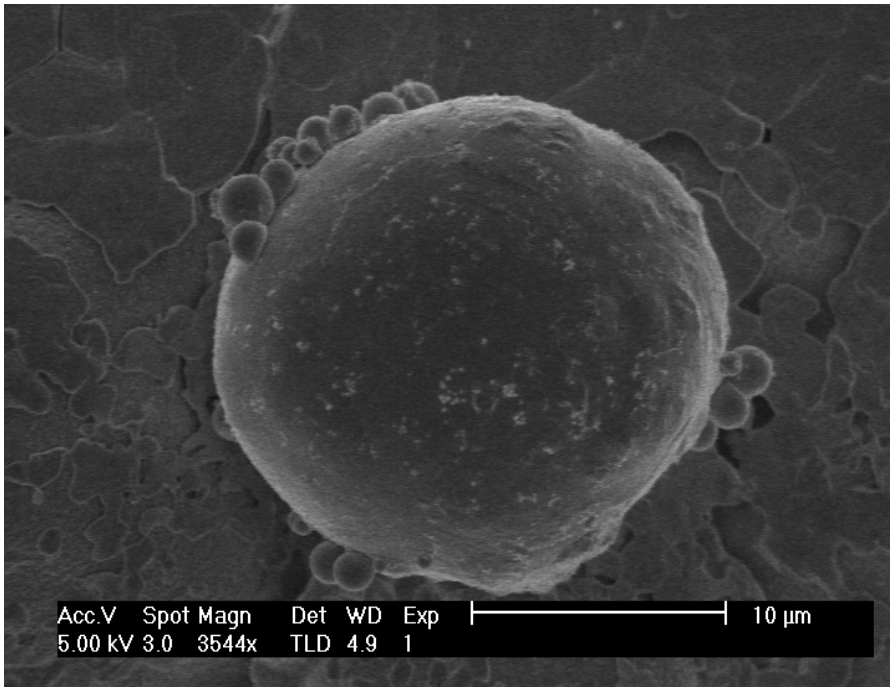

Fig. 4.18 SEM image of spheres containing In and N found on the surface of the $PbTiO_3$ film.

Attempts to measure the electrical properties of the annealed 150 nm and 1 µm bilayer films were not successful. Before annealing, the DC resistance of the bottom electrode was measured between two exposed points on either side of the deposited bilayers. Values of 25 Ω and 29 Ω were recorded for the 150 nm and 1 µm bilayer samples, respectively. After annealing, the electrode resistance of the 150 nm sample had increased to 980 Ω, whilst the value for the 1 µm sample increased to a point beyond the measurable limit. Similarly, the resistance of an uncovered section of ITO increased by approximately ten times from its original level, after the annealing. Therefore, it is likely that the combination of elevated temperatures and the disruption associated with $PbTiO_3$ formation led to the electrodes being damaged. In the case of the 1 µm sample, the distortion was so severe that the electrode failed completely and continuity was lost. All the Au/Cr top electrodes, deposited onto the 150 nm sample

after annealing, were shorted, which is concurrent with previous results on platinised-Si.

4.2.3.3.2 Single-crystal Nb:$SrTiO_3$

A single, stoichiometric Pb/Ti-bilayer, with a total thickness of 1 µm, was deposited onto a Nb:$SrTiO_3$ substrate and annealed for 1 hr at 650 °C. Fig. 4.19 shows the XRD data for the annealed film. The peaks corresponding to the perovskite $PbTiO_3$ phase were of a much greater intensity than those observed in previous experiments using different substrates. The film also appeared to be preferentially oriented in the (001) direction. These findings would suggest the (100)-oriented Nb:$SrTiO_3$ substrate enhanced the crystallisation and influenced the growth direction of the $PbTiO_3$ perovskite phase. Nevertheless, impurity phases still remained – most notably the high temperature PbO dimorph, massicot. The $PbTiO_3$ unit cell *c*-axis lattice parameter was calculated from the (002) peak and found to be 1% smaller than the accepted bulk value. This behaviour has been observed before in sol-gel derived and MOCVD $PbTiO_3$ films deposited on various substrates and has been attributed to stresses in the film[27, 28] or Pb-loss[29].

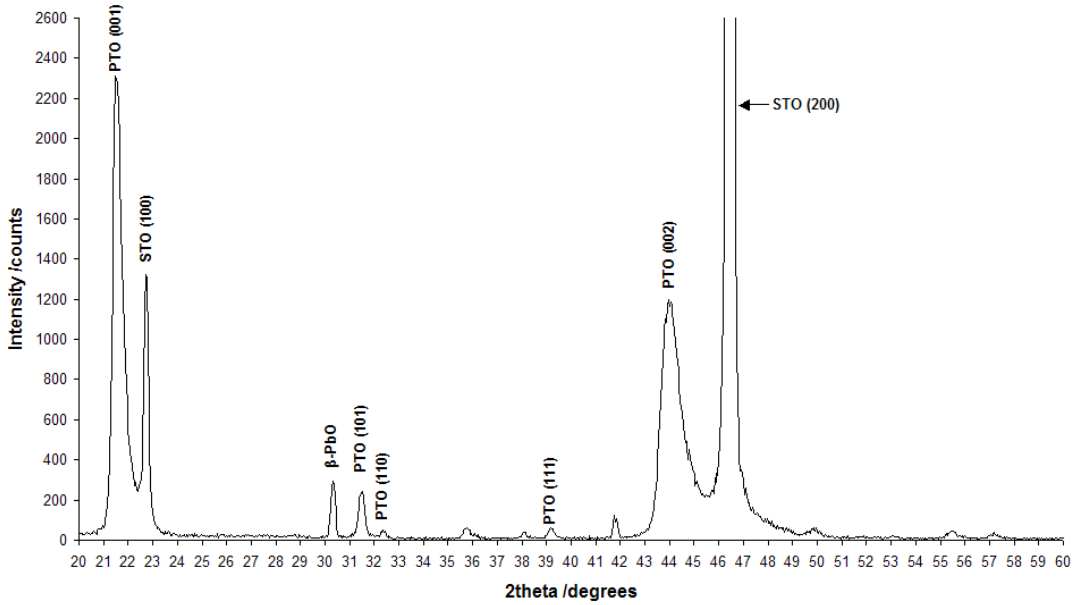

Fig. 4.19 XRD data for a 1 µm Pb/Ti-bilayer deposited on Nb:$SrTiO_3$ and annealed for 1 hr at 650 °C (indexed peaks correspond to the accepted values for tetragonal $PbTiO_3$ (PDF # 06-0452) and cubic $SrTiO_3$ (PDF # 35-0734)).

The morphology of the film was studied using SEM and found to consist of a mixture of tightly packed $PbTiO_3$ grains together with smooth PbO platelets (visible in the top right hand corner of Fig. 4.20a). The average $PbTiO_3$ grain size was larger than that observed in 1 μm bilayer films deposited on alternative substrates. One of the consequences of good lattice matching between film and substrate, as in the case of $PbTiO_3$ on $SrTiO_3$, is enhanced grain growth.[30] Extensive blistering was also observed over the entire film surface. In some areas, the blisters were so large that the affected area of film detached completely to reveal the underlying substrate (Fig. 4.20b). From these images it became clear that the substrate had remained intact during the annealing, as there were no signs of chemical interaction with diffusible species, such as PbO, from the film. We can therefore conclude that in this instance, as was the case with Pb/Ti-bilayers deposited onto ITO-coated glass, the substrate did not play a direct role in the formation of blisters.

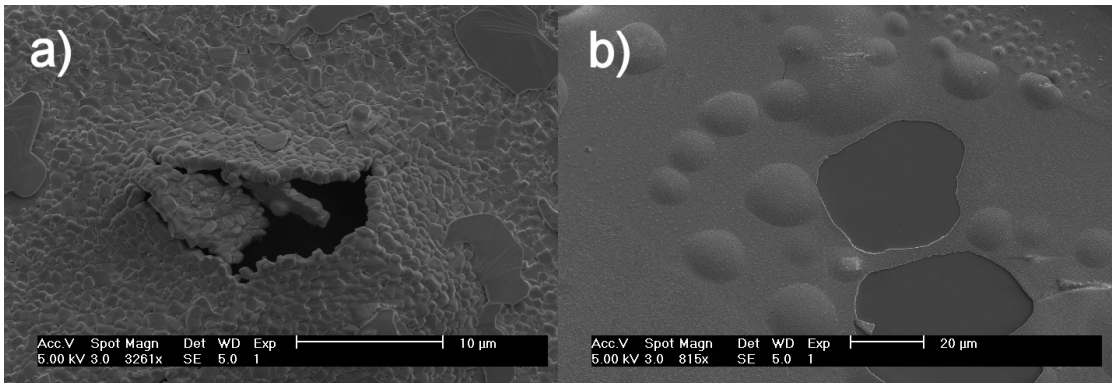

Fig. 4.20 SEM images showing a) grain morphology and b) blistering of a 1 μm Pb/Ti-bilayer deposited on Nb:$SrTiO_3$ and annealed for 1 hr at 650 °C.

4.2.3.4 Non-stoichiometric films

Further evidence demonstrating the lack of involvement of the substrate during initial blister formation came when a non-stoichiometric Pb/Ti-bilayer was annealed. In this experiment 370 nm of Ti and just 100 nm of Pb were deposited onto a $Pt/SiO_2/Si$ substrate, which was subsequently annealed in air for 1 hr at 650 °C. An SEM cross-sectional image of the sample is shown in Fig. 4.21. Through differences in grain morphology and a relatively well-defined interface, it is possible to discriminate between a surface layer composed of smooth $PbTiO_3$ grains and a dense underlying TiO_x layer. The titania is clearly acting as a diffusion barrier, effectively isolating the

$PbTiO_3$ layer from the Pt back electrode and the SiO_2/Si substrate. Blistering still occurs, but it is confined to the $PbTiO_3$ layer and fails to penetrate the $PbTiO_3$-TiO_x interface. Therefore it is feasible to assume that blister formation is initiated whenever Pb/Ti-bilayers react to form $PbTiO_3$, under the current annealing regime, regardless of the substrate on which they are deposited.

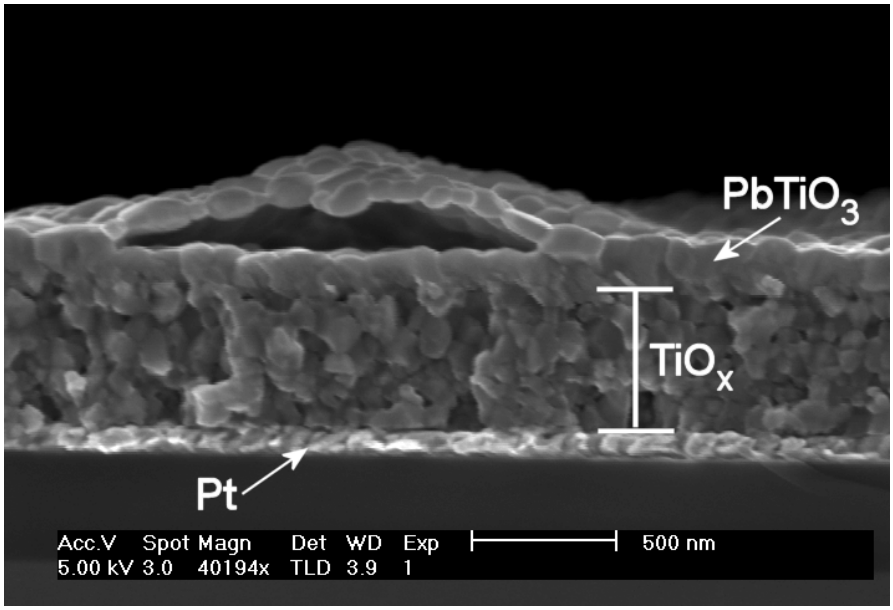

Fig. 4.21 SEM cross-sectional image of a non-stoichiometric Pb/Ti-bilayer annealed on a Pt/SiO_2/Si substrate.

4.2.3.5 Rapid thermal annealing

Conventional furnace annealing has the drawback that it exposes samples to elevated temperatures for extended periods. This can lead to enhanced diffusion of species from the film into the substrate. Rapid thermal annealing has been used in the past to alleviate this problem.[31] Shorter annealing times also help to reduce Pb-loss, which has been linked to crack formation in PZT thin films[32] and the formation of the pyrochlore phase, $PbTi_3O_7$, when attempting to produce $PbTiO_3$ thin films[3]. These benefits provided a justification for investigating the rapid thermal annealing technique as a way of overcoming the problem of blistering during solid phase synthesis.

As with the experiments that involved conventional annealing, stoichiometric Pb/Ti-bilayers of 150 nm and 1 μm were deposited onto Pt/Ti/SiO_2/Si substrates. After annealing the 150 nm sample for 30 s at 650 °C the perovskite $PbTiO_3$ phase was

evident in the XRD data (Fig. 4.22). A peak that corresponded to massicot PbO was also present. The *c*-axis orientation ratio, derived from the $PbTiO_3$ (001) and (100) peaks, was equal to 0.31. These results were very similar to those of samples conventionally annealed for 1 hr at 650 °C (c.f Fig. 4.3), which highlights the considerable processing time advantage of the rapid thermal annealing technique.

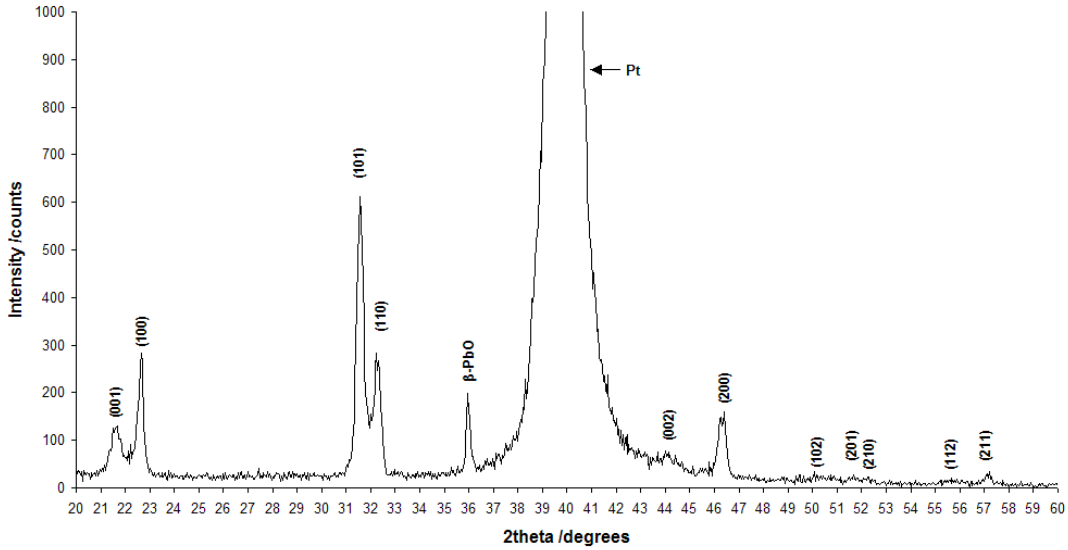

Fig. 4.22 XRD data for a 150 nm Pb/Ti-bilayer rapid thermally annealed for 30 s at 650 °C (indexed peaks correspond to the accepted values for tetragonal $PbTiO_3$, PDF card no. 06-0452).

The processing parameters used to anneal the 150 nm bilayer were retained when it came to annealing the thicker, 1 μm bilayer sample. XRD analysis revealed two strong peaks at 37.36° and 53.12° (Fig. 4.23a), which were not present after annealing the 150 nm bilayer sample. The peaks were found to diminish significantly after a second identical annealing (Fig. 4.23b), suggesting the possibility of a metastable phase. No single pattern from the ICDD database matched both peaks well. However, four patterns, each corresponding to a different TiO solid solution (TiO (PDF no. 080117), TiO (PDF no. 120754) $TiO_{1.04}$ (PDF no. 431296 and PDF no. 431295)), provided a good match to one or other of the peaks. Assigning the peaks to a TiO phase or phases would seem reasonable since the formation of $PbTiO_3$ in the bilayer system proceeds through various intermediate Pb and Ti solid solutions.[1] Likewise, the absence of these peaks from the spectra of samples annealed conventionally could be explained if they were to originate from a transient, metastable phase or phases.

Finally, a peak that matched well to the accepted value for Pt_xPb (111) (PDF card no. 060574) was also observed after the second annealing. From the work of Huang et al. it is understood that a metastable Pt_3Pb intermetallic precedes the crystallisation of the perovskite phase during the annealing of sol-gel PZT thin films on Pt coated substrates.[33] It is believed that this phase acts as a lattice matching buffer layer between the Pt and PZT. The same cannot be said in the current study since the $PbTiO_3$ perovskite phase started to form before the appearance of the Pt_xPb peak and the Pt layer had little influence on the orientation of the resultant film. Instead it seems that an excess of Pb may have reacted with the Pt.

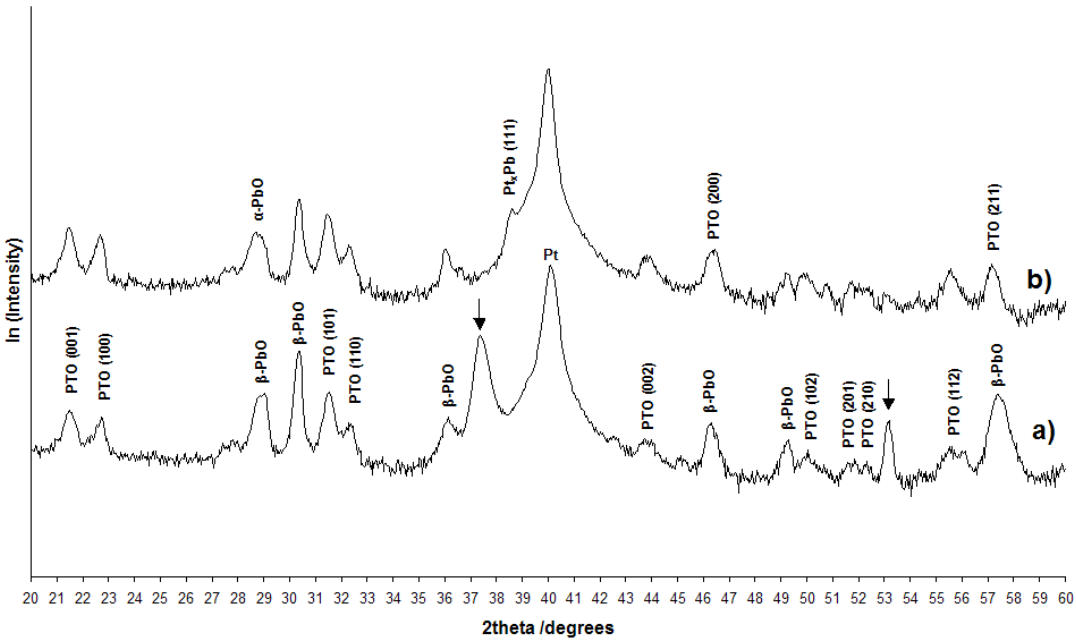

Fig. 4.23 XRD data for a 1 µm Pb/Ti-bilayer rapid thermally annealed for (a) 30 s at 650 °C and again for (b) 30 s at 650 °C. The peaks marked with arrows in (a) correspond to a possible metastable phase or phases that disappear after the second annealing.

The surface morphology of the rapid thermally annealed 150 nm bilayer film was similar to that of equivalent samples that had been conventionally annealed (Fig. 4.24a). Blister coverage was extensive across the film and the average grain size was below 100 nm. The thicker 1 µm bilayer film, in contrast, displayed few blisters but a large number of pinholes were visible between adjacent grains. As a consequence of these defects, all Au/Cr top electrodes deposited on the samples were found to be shorted.

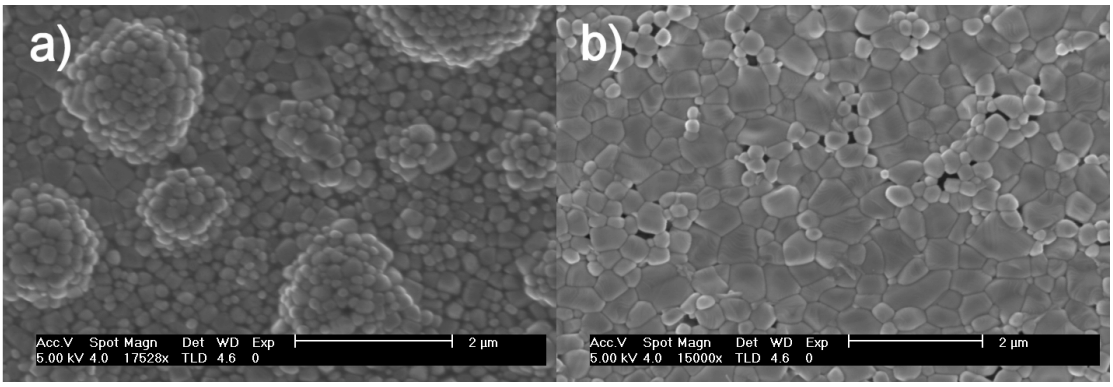

Fig. 4.24 SEM images showing the surface morphology of (a) 150 nm and (b) 1 µm Pb/Ti-bilayers deposited onto Pt/SiO_2/Si substrates after rapid thermal annealing for 30 s at 650 °C.

In conclusion, rapid thermal annealing significantly shortened the time required to crystallise the perovskite $PbTiO_3$ phase, however there were no improvements in the film quality, when compared to conventional annealing.

4.2.3.6 Attempts to synthesise PZT

The final series of experiments to produce ferroelectric thin films via the in situ method involved depositing a layer of Zr, in addition to the Ti and Pb layers, in an attempt to produce PZT. The question remains as to what caused the distortion in the $PbTiO_3$ films produced in previous experiments. If, as the evidence above suggests, the influence of the substrate was negligible, then an alternative explanation must be sought. It is known that large stresses can be generated in $PbTiO_3$ thin films and ceramics when they are cooled through the Curie point.[34] This is a result of the high tetragonality associated with the $PbTiO_3$ unit cell. By comparison, tetragonal 52:48 PZT has a smaller *c*/*a* ratio (1.03, in comparison to 1.07 for $PbTiO_3$) and is hence less susceptible to cracking, in thin film form. With this in mind, three trilayers were prepared to test the feasibility of producing a PZT thin film via the in situ technique. The thickness of each layer (Pb = 190 nm, Zr = 66 nm and Ti = 50 nm) was chosen, in accordance with the respective molar volumes, to result in a 50:50 PZT stoichiometry. Consecutive 1 hr annealings were conducted under air in a conventional furnace, replicating the regime used during the $PbTiO_3$ thin film experiments. However, the ultimate annealing temperature was raised to 900 °C as it was anticipated that the PZT phase would require more energy to crystallise.[35] Fig. 4.25 shows the evolution of phases for a Pb/Ti/Zr/SiO_2/Si sample that was subjected to consecutive annealings

between 300 – 900 °C. Both forms of PbO are the predominant phases found at lower temperatures, as was the case when Pb/Ti-bilayer films were annealed (Fig. 4.1). At 500 °C we observe the emergence of the monoclinic ZrO_2 phase (PDF card no. 371484), which reaches maximal intensity after the 600 °C annealing. Peaks corresponding to $PbTiO_3$ (PDF card no. 060452) also appear after the aforementioned annealing. Interestingly, no peaks corresponding to crystalline $PbZrO_3$ were found, up to the maximum temperature. Likewise, no PZT phase was observed, which would suggest that the conditions were insufficient to induce a reaction between the as-formed ZrO_2 and $PbTiO_3$. Unfortunately, increasing annealing temperatures above 900 °C was infeasible due to softening of the Si substrate.

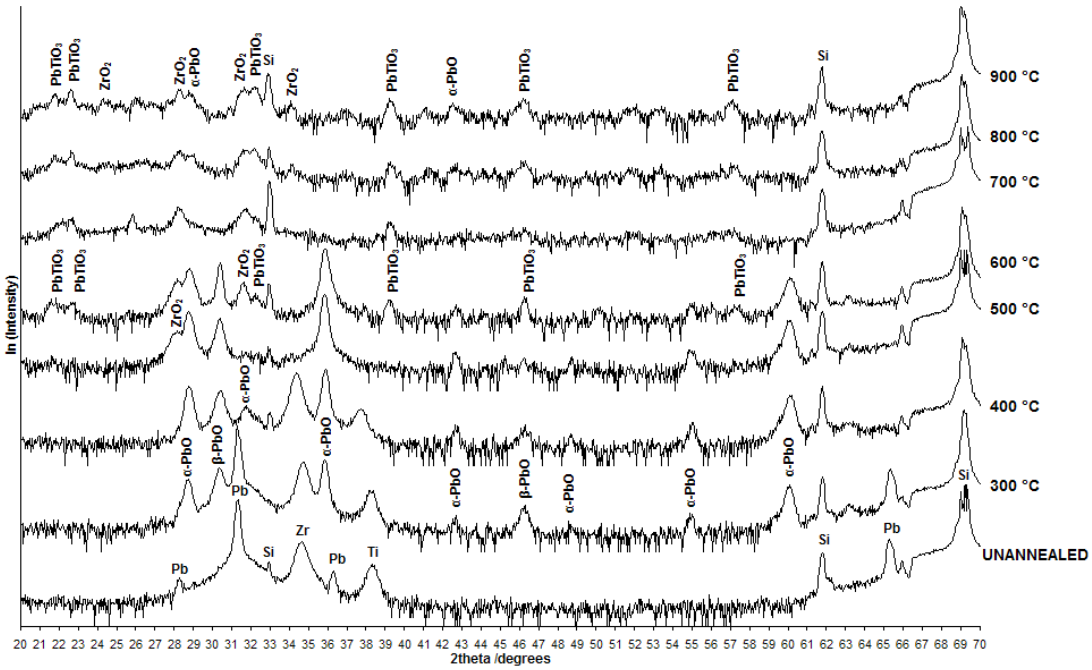

Fig. 4.25 XRD data for a Pb/Ti/Zr/SiO_2/Si sample after consecutive, 1 hr annealings in air between 300 – 900 °C.

The second multilayer combination to be tested was Pb/Zr/Ti/SiO_2/Si. XRD data for this sample, across the same annealing temperature range, is shown in Fig. 4.26. From the patterns we can see that, in contrast to the previous structure, the perovskite $PbTiO_3$ phase did not form until after the 700 °C annealing. This can be explained by considering the fact that the Pb and Ti layers were isolated by the partially oxidised Zr layer, which helped to suppress interdiffusion. The phase assemblage from the 700 °C annealing onwards bears a considerable resemblance to that of the Pb/Ti/Zr/SiO_2/Si sample. This suggests that the solid solution becomes homogenised at the higher

annealing temperatures. Once again, no PZT phase was visible in the patterns up to 900 °C.

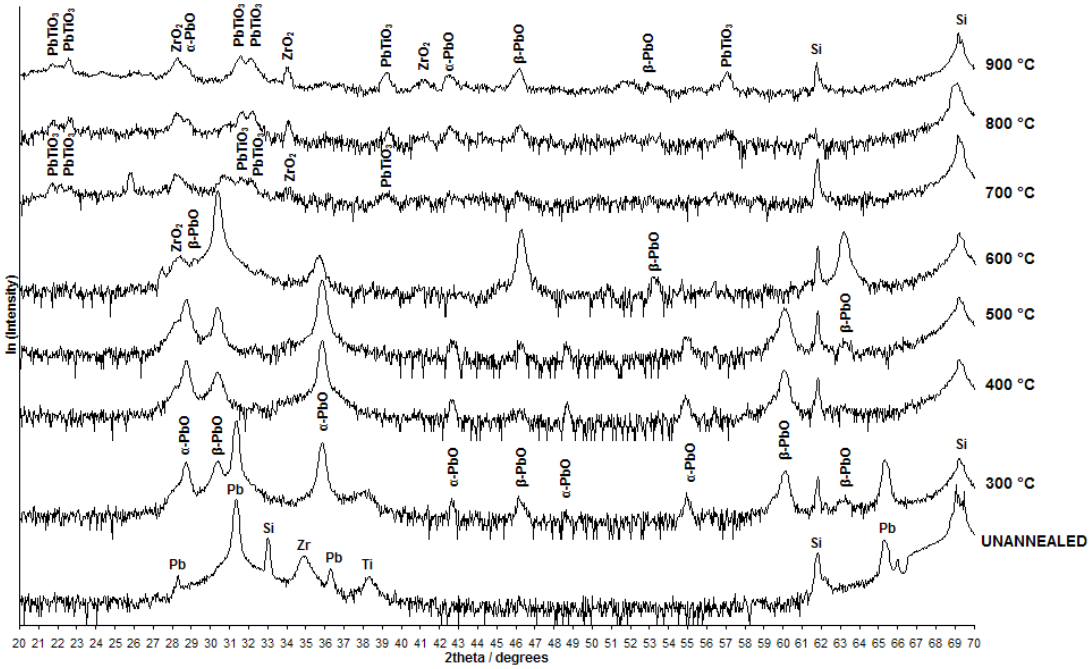

Fig. 4.26 XRD data for a Pb/Zr/Ti/SiO_2/Si sample after consecutive, 1 hr annealings in air between 300 – 900 °C.

The last sample to be analysed had the following structure: Ti/Pb/Zr/Pt/Ti/SiO_2/Si. Since the Pb layer was now closer to the SiO_2/Si substrate, a Pt back electrode was utilised to inhibit, as much as possible, the diffusion of PbO. Fig. 4.27 shows the evolution of phases for the Ti/Pb/Zr/Pt/Ti/SiO_2/Si structure across the same annealing temperature range as that employed previously. It is notable that the overlying Ti layer restricts PbO formation until after the 400 °C annealing. However, perovskite $PbTiO_3$ begins to crystallise after 600 °C, as witnessed in the Pb/Ti/Zr/SiO_2/Si sample. Three prominent peaks between 2theta = 25° – 28°, in the 900 °C pattern, were not conclusively identified. A partial match to the Pt_2Si_3 phase in the ICDD database (PDF card no. 41-0874) may indicate that the higher temperatures induced a reaction between the bottom electrode and the substrate. The absence of these peaks from the patterns of the previous two structures, together with the diminishment of the Pt (111) peak intensity in the latter case, would lend support to this view. Furthermore, it is known that Pt and Ti form a eutectic at 840 °C, which has been attributed to the degradation of Pt/Ti electrodes during prolonged high temperature

annealing.[36] Finally, as with the other multilayer structures, no PZT phase was identified, across the entire annealing temperature range.

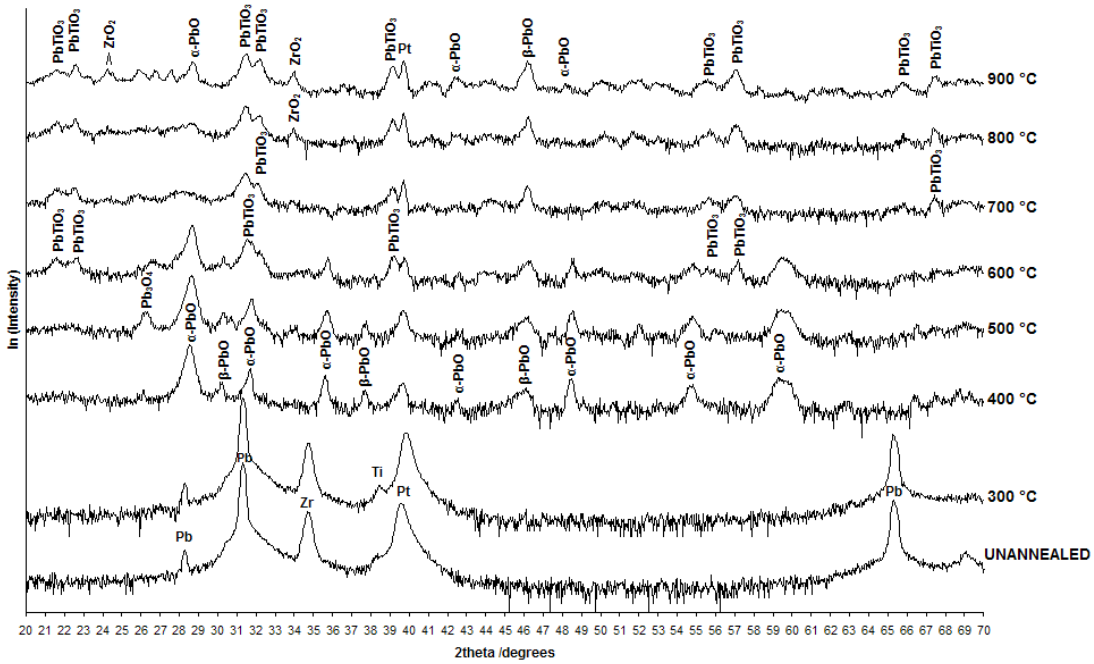

Fig. 4.27 XRD data for a Ti/Pb/Zr/Pt/Ti/SiO_2/Si sample after consecutive, 1 hr annealings in air between 300 – 900 °C.

4.2.4 Summary of solid phase film production

The heat treatment necessary to induce the formation of the perovskite $PbTiO_3$ phase via the in situ method led to unavoidable distortions in the resultant films. Examination of sample cross-sections, by SEM, revealed extensive diffusion of volatile PbO into the substrate when SiO_2/Si wafers were utilised. Alternative adhesion layers for the Pt back electrodes were investigated, in an attempt to limit the diffusion of PbO. By substituting Zr for Ti, as an adhesion layer, several of the deposited Au/Cr top electrodes were found to be intact. However, the shape of hysteresis loops recorded from these electrodes corresponded to a lossy dielectric as opposed to a ferroelectric response from the film.

The focus of the investigation then moved towards replacing the thermal oxide Si wafers with substrates less susceptible to PbO diffusion. Film distortion of similar or even greater magnitude was evident when alternative substrates were tested, but SEM images showed that, if PbO diffusion had occurred, it had not led to the destruction of

the upper regions of the substrates, as was the case for SiO_2/Si. This result suggested that the distortion present in the films was not a consequence of the interaction between volatile species and the substrate. Experiments with non-stoichiometric bilayers on thermal oxide wafers supported this idea, since the resultant films exhibited blistering, whilst remaining isolated from the substrate by a thick TiO_x diffusion barrier.

The question remains as to what caused the distortions during the formation of the $PbTiO_3$ films. If the influence of the substrate can be neglected, then it seems likely that the actual cause of blistering and delamination was a result of stresses generated during the transformation into the $PbTiO_3$ perovskite phase. Unfortunately, undoped $PbTiO_3$ is difficult to prepare in both ceramic and thin-film form due to its high *c*/*a* ratio resulting in a large internal stress when the ceramics (or ceramic film) are cooled through the Curie point. These stresses often cause cracking and delamination of pure $PbTiO_3$ thus preventing its applications in bulk and thin-film devices.[34] In their work on the solid phase synthesis of $PbTiO_3$, Sidorkin et al. make no reference to the morphology of their films.[1, 37] It is therefore hard to assess the extent to which their films suffered from the problems discussed above. Stankus et al. observed blistering in Pb/Ti films annealed at 600 °C for 1 hr on Si (111) substrates.[38] They attributed this effect to the release of gases from the film when heating at lower temperatures. Samples annealed at 700 °C appeared not to suffer from this phenomenon, contrary to the results from the current study. Also, Stankus et al. observed differences in film morphology when depositing onto Si substrates of different orientation and yet we found that the crystallographic properties of the substrate had little influence on the structural properties of the films.

4.3 Attempts to synthesise $PbTiO_3$ nanoislands via the solid phase method

4.3.1 Generating discrete Pb nanoislands

Observations of the as-deposited Pb layers, used during the solid phase thin film experiments, showed them to possess a textured morphology. This provided an impetus to investigate the production of Pb nanoislands by adapting the deposition technique. During the thermal evaporation process Pb particles nucleate in-flight

between the crucible and substrate. After hitting the substrate these particles coalesce to form nanoislands and ultimately thin films. The key requirement for nanoisland formation, under such circumstances, is limited wettability of the deposited material on the substrate. Fig. 4.28 shows the effects of reducing evaporation time on the size of Pb nanoislands deposited onto Si substrates. After evaporating for 8 s a continuous film, consisting of more than one layer of ~ 100 nm Pb nanoislands, was seen. Discontinuous Pb films formed when evaporation times were reduced to 5 s. The resultant nanoislands exhibit an irregular morphology due to the significant coalescence that had taken place. Reducing evaporation times still further led to the formation of spherical nanoislands with an average size that was proportional to evaporation time. The size distribution of the nanoislands was between 5 – 30 nm after a flash evaporation lasting 0.5 s.

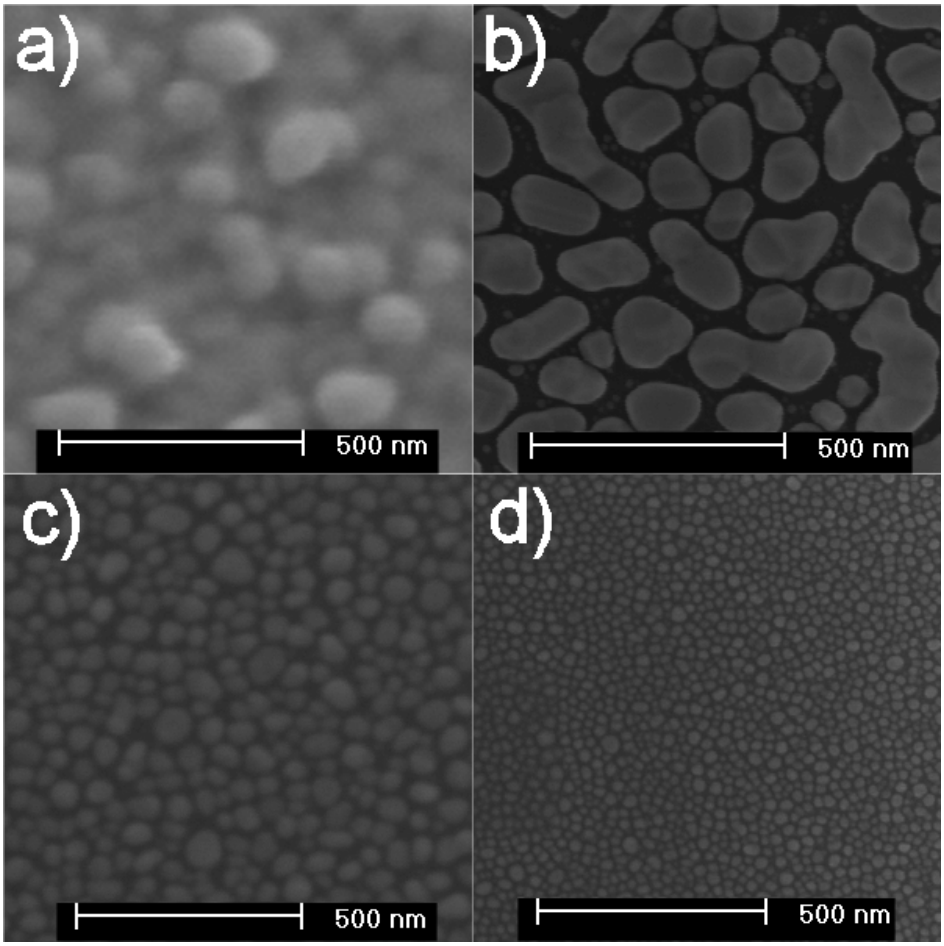

Fig. 4.28 SEM images showing the effects of evaporation time on Pb nanoisland morphology: (a) A continuous thin film, consisting of more than one layer of nanoislands, forms after evaporating for 8 s; (b) Reducing evaporation time to 5 s results in the formation of a discontinuous film with irregular morphology. Further reductions lead to the production of discrete, spherical nanoislands with diameters proportional to evaporation time: (c) 1 s, 30 – 80 nm; (d) 0.5 s, 5 – 30 nm.

4.3.2 Annealing Pb nanoislands

Attempts were made to produce $PbTiO_3$ nanoislands by annealing the Pb nanoislands in contact with an underlying Ti layer, 10 nm in thickness. Experiments showed that the morphology and size distribution of Pb nanoislands deposited onto Ti were identical to those on Si substrates. It was important, in terms of analysing ferroelectric size effects, that the nanoparticles remained discrete throughout their solid phase synthesis. However, the melting point of spherical Pb particles decreases from the bulk value of 327.5 °C as their diameter decreases.[39] This is due to the high surface-to-volume ratio associated with particles of small radii. More than half the bonds of an atom at the surface of a metal are dangling bonds.[40] Since the cohesive energy of a solid depends on the number of bonds each atom forms with its neighbours, these dangling bonds lead to a depression in the melting point. Qi and Wang[41] derived the following equation that predicts the adjusted melting point of a metallic nanoparticle after taking into account size and shape effects:

$$T_m = T_{mb}\left(1 - 6\alpha\frac{r}{D}\right) \qquad \text{Eqn. 4.2}$$

where T is the adjusted melting point, T_{mb} is the bulk melting point, α is the shape factor, r is the atomic radius of the material and D is the nanoparticle radius. Fig. 4.29 shows a graph of the variation in melting point as a function of the inverse diameter of Pb nanoparticles.

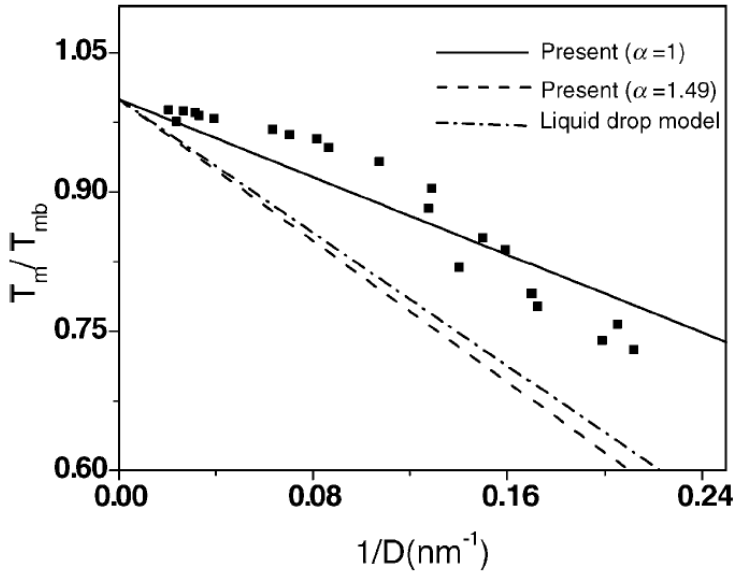

Fig. 4.29 Variation of the melting temperature as the function of the inverse diameter of Pb nanoparticles. The symbols (■) represent experimental values.[41]

Assuming a perfectly spherical shape (α = 1), the adjusted melting point of a 10 nm Pb nanoparticle is approximately 90% of the bulk value, or 270 °C. In fact the nanoislands in this investigation were not perfectly spherical, but disc-like, due to their orientation on the substrate. This increased the shape factor (α > 1.15, according to Qi and Wang[41]), which in turn decreased the predicted melting point to a value approaching 250 °C. This posed a problem when attempting to anneal at the elevated temperatures necessary to form the $PbTiO_3$ phase.

The first solution investigated was to pre-anneal the samples at a lower temperature, below the melting point of the Pb nanoparticles, but above that necessary for their oxidation. PbO, in its bulk form, has a much higher melting point (888 °C) than Pb. Therefore, it was speculated that PbO nanoparticles might be able to withstand the higher temperatures necessary to form $PbTiO_3$, whilst remaining discrete. Fig. 4.30 shows XRD data taken before and after annealing a Pb/Si nanoisland sample for 2 hr at 200 °C, in air. As can be seen, all of the Pb was oxidised to litharge and massicot PbO. Meanwhile, the SEM image in Fig. 4.31 shows that the morphology of the nanoislands was retained after the annealing and no melting occurred.

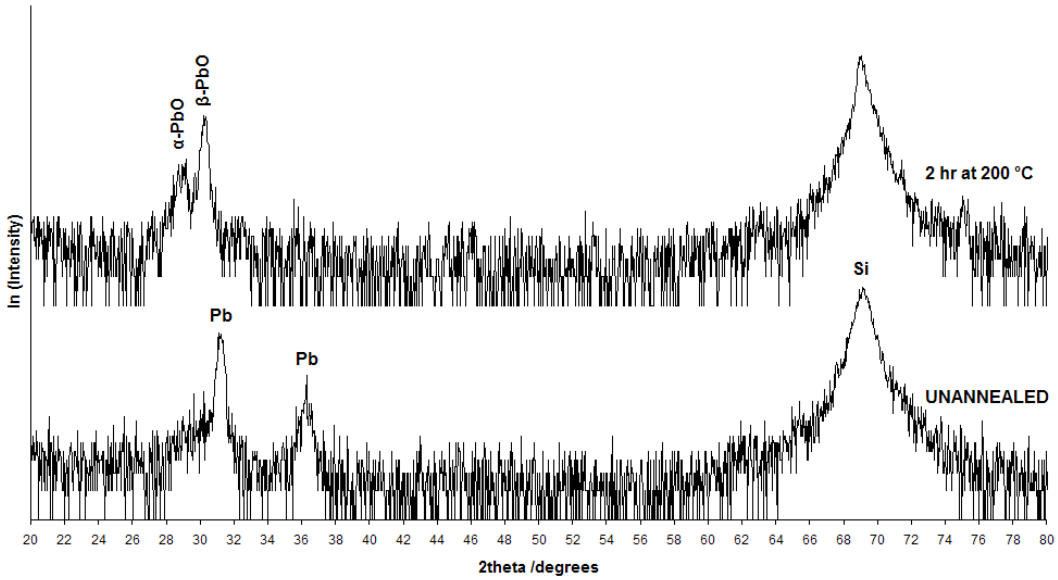

Fig. 4.30 XRD data for a Pb nanoisland sample before and after annealing in air for 2 hr at 200 °C.

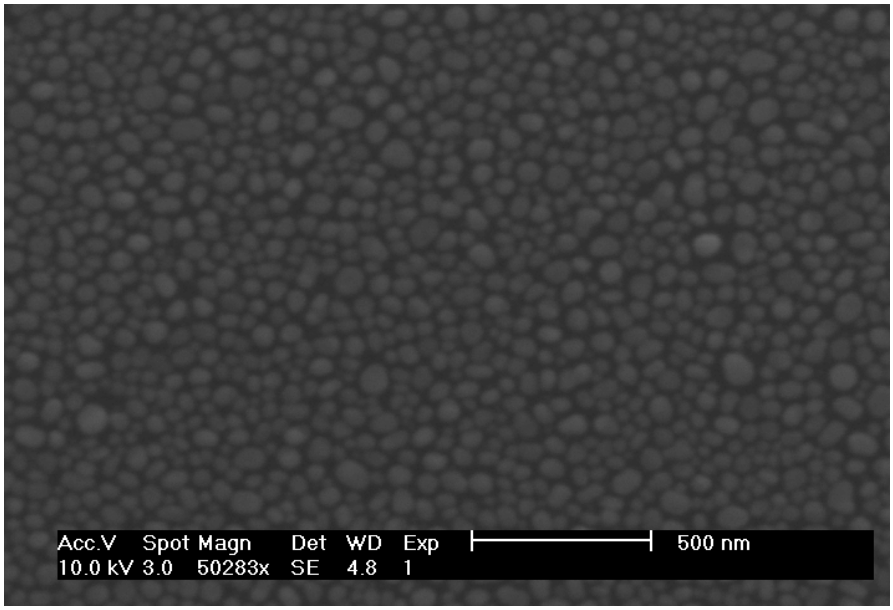

Fig. 4.31 SEM image showing discrete PbO nanoislands produced by annealing Pb nanoislands for 2 hr at 200 °C in air.

Unfortunately, after the main annealing, which was conducted at 650 °C for 1 hr, the morphology of the nanoislands was lost. The increased temperature led to the coalescence of groups of PbO nanoislands on the surface, through sintering (Fig. 4.32).

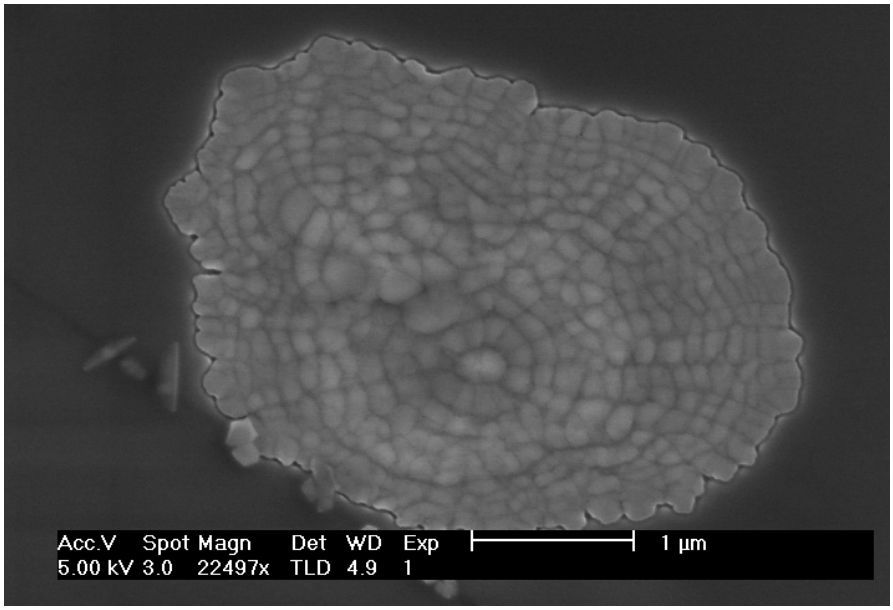

Fig. 4.32 SEM image showing the sintering of PbO nanoislands after annealing for 1 hr at 650 °C in air.

This development meant that another strategy had to be found in order to retain nanoisland morphology. There is evidence to suggest that $PbTiO_3$ can form, through the solid-state reaction of PbO and TiO_2 powders, at temperatures as low as 375 °C, after extended annealing.[42] Since the reactivity of the metallic Pb/Ti nanoisland system is greater than that of mixed oxide powders, it was hypothesised that the formation temperature for $PbTiO_3$ might be even lower. To test this, a Pb/Ti nanoisland sample was annealed in air for 40 hr at 300 °C. Fig. 4.33 shows the morphology of the nanoislands after annealing. Melting appears to have occurred, as the areal density of the nanoislands was noticeably lower when compared to before the annealing. However, large quantities of nanoislands with diameters $\leq$ 30 nm remained discrete and were thus suitable for ferroelectric analysis via PFM.

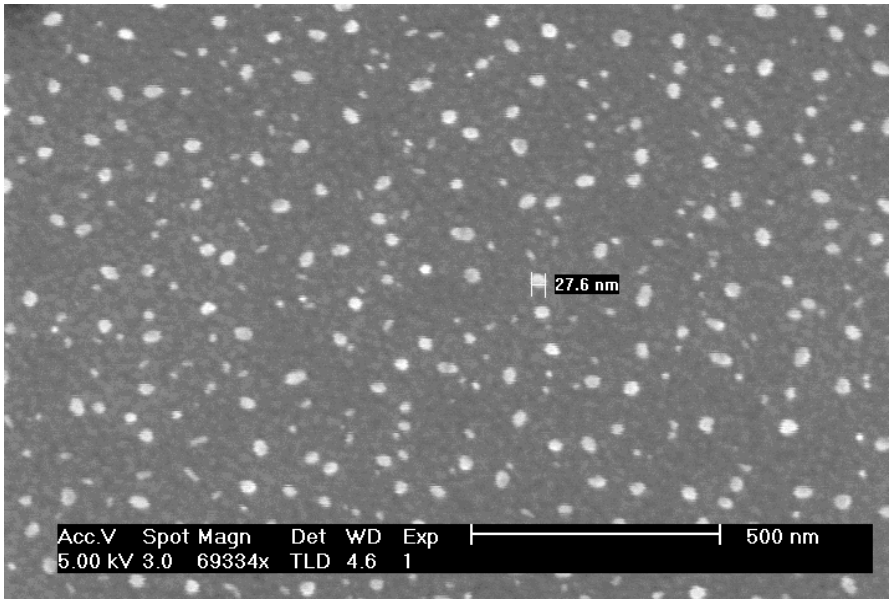

Fig. 4.33 SEM image showing changes in nanoisland morphology after annealing for 40 hr at 300 °C.

Very brief, high temperature annealings were also trialled as a means of crystallising $PbTiO_3$ nanoislands, whilst preserving their morphology. Rapid thermal annealings, for 1 s, were conducted at 500 °C, 600 °C and 650 °C whilst a hot plate was used to anneal samples at 550 °C, also for 1 s. Fig. 4.34 shows the morphology of nanoislands exposed to 500 °C for 1s using the former technique. Clearly significant coalescence has taken place to an extent whereby the grains appear similar to those found on rapid thermally annealed Pb/Ti films (cf. Fig. 4.24a). As temperatures were increased to 600 °C, prominent blisters were observed which confirmed the transformation from isolated nanoislands to an extremely thin Pb/Ti film (Fig. 4.35). Interestingly, the morphology of grains on a sample annealed at 650 °C was rougher in comparison to those annealed at lower temperatures (Fig. 4.36). The grains also appeared to be more loosely packed. This may have been due to Pb-loss from the as-formed $PbTiO_3$ film, since the initial volume of Pb was very small.[43] Although the rapid thermal annealing experiments were unsuccessful in terms of retaining discrete nanoislands, it was thought worthwhile to conduct PFM on the samples, since the ferroelectric properties of ultrathin $PbTiO_3$ films may have differed significantly from thicker films.

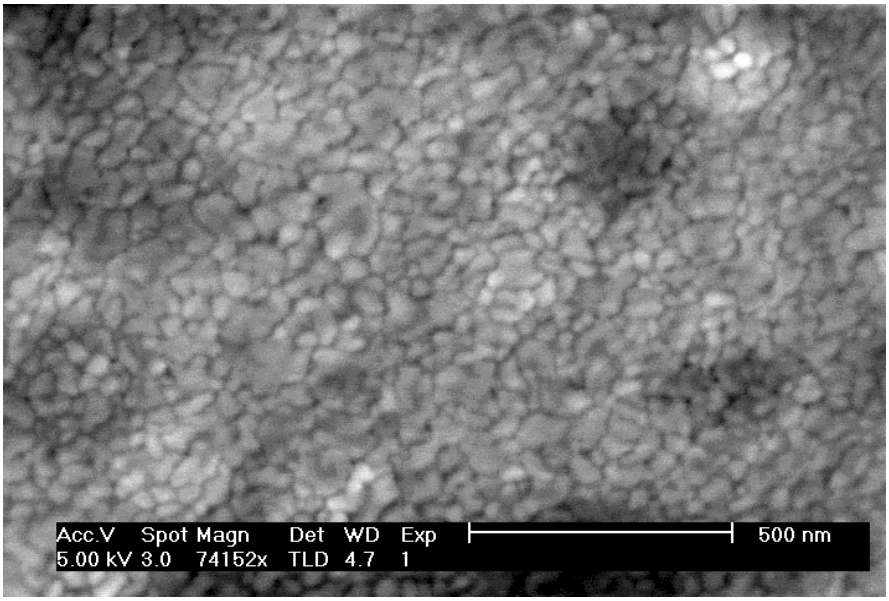

Fig. 4.34 SEM image showing the surface of a Pb/Ti nanoisland sample after rapid thermal annealing for 1s at 500 °C.

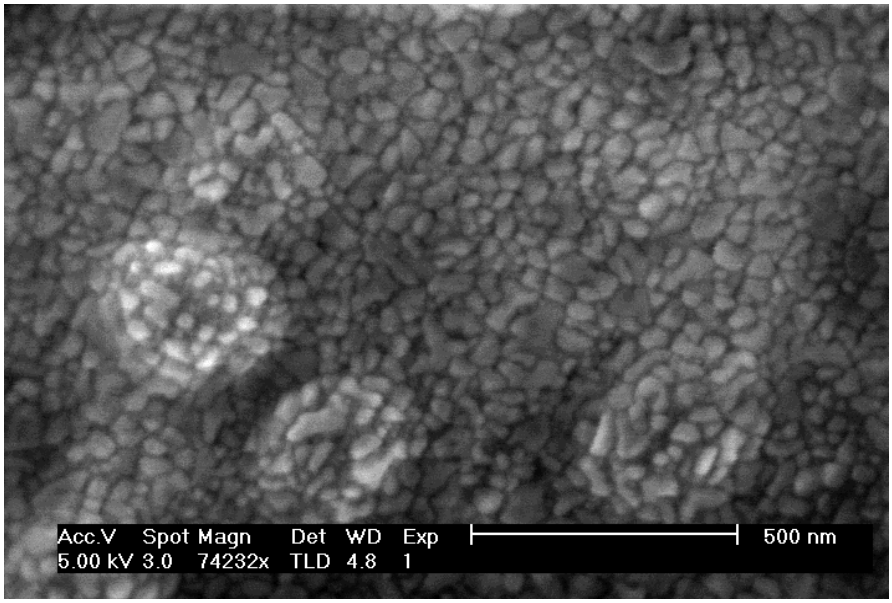

Fig. 4.35 SEM image showing the surface of a Pb/Ti nanoisland sample after rapid thermal annealing for 1s at 600 °C.

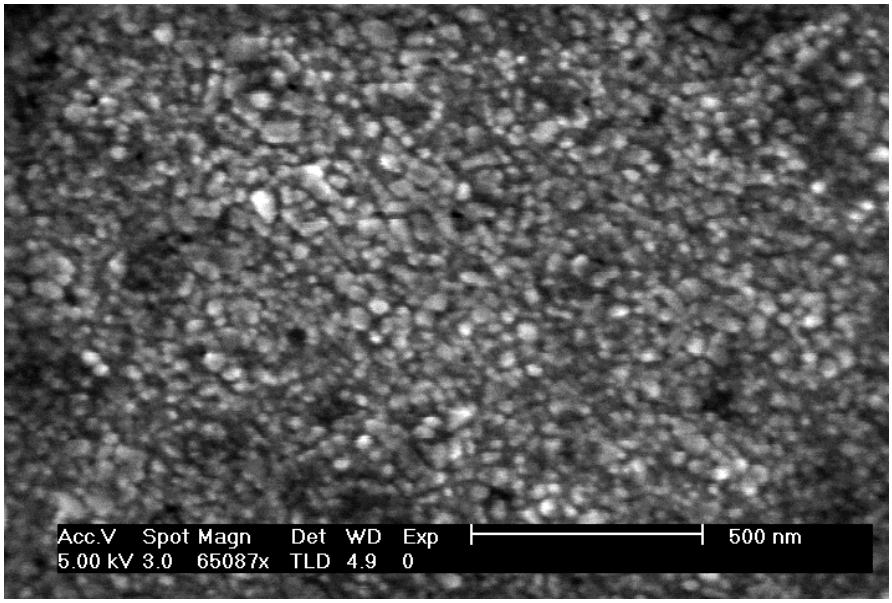

Fig. 4.36 SEM image showing the surface of a Pb/Ti nanoisland sample after rapid thermal annealing for 1s at 650 °C.

By annealing a sample on a hot plate, in air at 550 °C for 1 s it was possible to preserve the morphology of nanoislands that were, in some cases, smaller than 30 nm (Fig. 4.37). Coalescence through melting was still observed, however nanoislands over a relatively wide size range remained discrete. This result was in contrast to that of the rapid thermally annealed samples and can probably be explained by procedural differences related to the two techniques. The hot plate sample was removed immediately after annealing for 1 s, whilst the rapid thermally annealed samples had to endure a longer cooling period from the target temperature. This was an unavoidable limitation associated with the RTA, which could not be opened above a temperature of 200 °C on the grounds of safety.

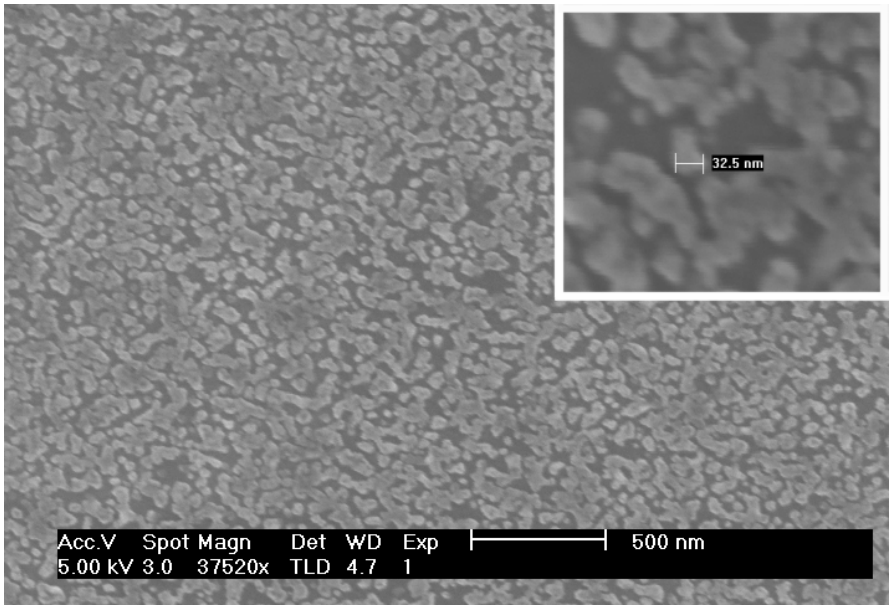

Fig. 4.37 SEM image showing the partial melting that occurred after annealing a Pb/Ti nanoisland sample at 550 °C for 1 s. The inset image shows nanoislands, with diameters ≤ 30 nm, which remained discrete.

4.3.3 Summary of solid phase nanoisland production

This section attempted to adapt the in situ, solid phase synthesis technique for the production of $PbTiO_3$ nanoislands. By utilising flash evaporations, lasting approximately 0.5 s, it was possible to produce Pb nanoislands with a size distribution of between 5 – 30 nm. Annealing the nanoislands under the same regime as that used during the thin film experiments led to the loss of their morphology through melting. Pre-annealing the samples at a temperature below the melting point of Pb to oxidise the nanoislands was posited as a solution to this problem. Unfortunately, during the subsequent high temperature annealing the PbO nanoislands sintered and coalesced. To overcome this problem an extended low temperature annealing was adopted. Limited melting and coalescence still occurred, but a significant number of nanoislands in the size range of interest remained on the substrate.

Rapid thermal and brief, hot plate annealings were also investigated as a means of crystallising the $PbTiO_3$ nanoislands while retaining their morphology. Samples subjected to rapid thermal processing exhibited a grain structure similar to that of in situ $PbTiO_3$ thin films. In contrast, the nanoislands on samples annealed using the hot plate coalesced to a lesser extent. This difference was attributed to the extended cooling period that the rapid thermally annealed samples had to endure.

References

[1] A. S. Sidorkin, A. S. Sigov, A. M. Khoviv, S. O. Yatsenko and O. B. Yatsenko, *Phys. Solid State*, 42, 4, 745 (2000)

[2] V. Stankus and J. Dudonis, *Mater. Sci. Eng. B*, 109 178 (2004)

[3] K. Iijima, T. Yoshihiro, R. Takayama and I. Ueda, *J. Appl. Phys.* 60 1 361 (1986)

[4] C. J. Lu, S. B. Ren, H. M. Shen, J. S. Liu and Y. N. Wang, *J. Phys.: Condens. Matter*, 8, 8011 (1996)

[5] R. M. Smart and F. P. Glasser, *J. Am. Ceram. Soc.* 57, 9, 378 (1974)

[6] R. Le Bihan, *Ferroelectrics*, 97, 19 (1989)

[7] A. A. Sogr, *Ferroelectrics*, 97, 47 (1989)

[8] V. Aristov and L. Kokhanchik, *Ferroelectrics*, 126, 353 (1992)

[9] D. V. Roshchupkin and M. Brunel, *Scanning Microscopy* 7, 543 (1993)

[10] S. Zhu and W. Cao, *Phys. Stat. Sol.* 173, 495 (1999)

[11] G. Rosenman, A. Skliar, I. Lareah, N. Angert, M. Tseitlin and M. Roth, *Phys. Rev. B: Condens. Matter Mater. Phys.* 54, 9, 6222 (1996)

[12] S. Zhu and W. Cao, *Phys. Rev. Lett.* 79, 13, 2558 (1997)

[13] U. Lev and E. Zolotoyabko, *J. Appl. Phys.* 99, 044106 (2006)

[14] K. Sreenivas, I. Reaney, T. Maeder, N. Setter, C. Jagadish and R. G. Elliman, *J. Appl. Phys.* 75, 1, 232 (1994)

[15] T. Maeder, L. Sagalowicz and P. Muralt, *Jpn. J. Appl. Phys.* 37, 2007 (1998)

[16] N. Abe, Y. Otani, M. Mitake, M. Kurita, H. Takeda, S. Okamura and T. Shiosaki, *Jpn. J. Appl. Phys.* 42, 2791 (2003)

[17] D. Pramaltik, A.N. Saxena, Owen K. Wu, G.G. Peterson and M. Tanielian, *J. Vac. Sci. Technol. B*, 2, 775 (1984)

[18] C-C. Ting, S-Y. Chen and D-M. Liu, *Thin Solid Films*, 402 290 (2002)

[19] Y. J. Kim, Y. S. Lee and H. C. Lee, *Jpn. J. Appl. Phys.* 44, 6167 (2005)

[20] M. J. Munson and R. E. Riman, *J. Therm. Anal. Calorim.* 37, 2555 (1991)

[21] L. Douillard, M. Gautier-Soyer, J. P. Duraud, A. Fontaine and F. Baudelet, *J. Phys. Chem. Solids*, 57, 4, 495 (1996)

[22] H. X. Zhang, C. H. Kam, Y. Zhou, X. Q. Han, Y. L. Lam, Y. C. Chan and K. Pita, *Mater. Chem. Phys*, *Volume*, 63, 2, 174 (2000)

[23] S. Dunn and R. W. Whatmore, *J. Euro. Ceram. Soc*, 22, 6, 825 (2002)

[24] T. W. Kim, D. U. Lee, Y. S. Yoon, C. H. Wang, S. S. Yom, S. J. Lee and C. O. Kim, *Solid State Commun.* 96, 2, 95 (1995)

[25] C. Lichtensteiger and J. Triscone, *Integ. Ferro.* 61, 1, 143-148 (2004)

[26] M-S. Tsai, C-L. Wang and M-H. Hon, *Surf. Coat. Technol.* 172, 95 (2003)

[27] G. Guzman, P. Barboux and J. Perrière, *J. Appl. Phys.* 77, 2, 635 (1995)

[28] S. D. Cheng, C. H. Kam, Y. Zhou, W. X. Que, Y. L. Lam, Y. C. Chan and W. S. Gan, *Thin Solid Films*, 375, 109 (2000)

[29] Y-F. Chen, L. Sun, T. Yu, J-X. Chen and N-B. Ming, *Appl. Phys. Lett.* 67, 23, 3503 (1995)

[30] D. Bao, X. Yao, K. Shinozaki and N. Mizutani, *J. Phys. D: Appl. Phys.* 36, 2141 (2003)

[31] M. L Calzada, I. Bretos, R. Jiménez, H. Guillon and L. Pardo, *Adv. Mater.* 16, 18, 1620 (2004)

[32] R. Thapliyal, P. Schwaller, M. Amberg, F.J. Haug, G. Fortunato, D. Hegemann, H.J. Hug and A. Fischer, *Surf. Coat. Technol.*, 200, 1051 (2005)

[33] Z. Huang, Q. Zhang and R. W. Whatmore, *J. Mater. Sci. Lett.* 17, 1157 (1998)

[34] A. L. Kholkin, I. Bdikin, Yu. I. Yuzyuk, A. Almeida, M. R. Chaves, M. L. Calzada and J. Mendiola, *Mater. Chem. Phys.* 85, 1, 176 (2004)

[35] S. S. Chandratreya, R. M. Fulrath and J. A. Pask, *J. Am. Ceram. Soc.* 64, 7, 422 (1981)

[36] S. L. Firebaugh, K. F. Jensen and M. A. Schmidt, *J. MEMS*, 7, 1 (1998)

[37] A. S. Sidorkin, L. P. Nesterenko, I. A. Bocharova,V. A. Sidorkin, and G. L. Smirnov, *Ferroelectrics*, 286, 335 (2003)

[38] V. Stankus, J. Dudonis, L. Pranevicius, L.L. Pranevičius, D. Milcius, C. Templier and J.-P. Riviere, *Thin Solid Films*, 426, 78 (2003)

[39] C. R. M. Wronski, *Brit. J. Appl. Phys.* 18, 1731 (1967)

[40] C. Solliard and M. Flueli, *Surf. Sci.* 156, 1, 487 (1985)

[41] W. H. Qi and M. P. Wang, *Mater. Chem. Phys* 88, 280 (2004)

[42] S. S. Cole and H. Espenschied, *J . Phys. Chem.* 41, 445 (1937)

[43] E. Sato, Y. Huang, M. Kosec, A. Bell, and N. Setter, *Appl. Phys. Lett.* 65, 21, 2678 (1994)

Chapter 5: Ferroelectric Analysis of $PbTiO_3$ Nanostructures

5.1 Introduction

This section describes the attempts to analyse the ferroelectric properties of solid phase synthesised $PbTiO_3$ nanoislands and thin films using PFM.

5.2 Nanoislands

The samples discussed in this section consisted of Pb nanoislands deposited via thermal evaporation onto Ti/Pt/Ti/SiO_2/Si substrates, which were subsequently annealed under different conditions. The diameter range of the nanoislands, prior to annealing, was between 5 – 30 nm.

5.2.1 Low temperature annealing

This sample was prepared by conventional annealing for 40 hr at 300 °C, in air. PFM images were acquired by applying an AC voltage with a magnitude of 0.5 V and frequency of 62 kHz between a conductive $PtIr_5$-coated Si tip and the bottom electrode of the sample. The tip had a nominal resonant frequency and spring constant of 14 kHz and 0.2 N/m, respectively. Fig. 5.1 shows the topography and associated out-of-plane piezoresponse amplitude signal from an area of the sample. Several of the nanoislands in the topography image appear to possess a piezoresponse. Notable examples with particularly strong response are circled in both images. From the literature, it is understood that $PbTiO_3$ grains analysed using PFM exhibit a monodomain structure below 40 nm.[1] The nanoislands shown in Fig. 5.1 appear substantially larger than this, but no domain structure can be resolved. However, analysis of the piezoresponse phase image (Fig. 5.2) shows that the larger nanoislands are in fact agglomerates of smaller grains, which probably coalesced during the annealing.

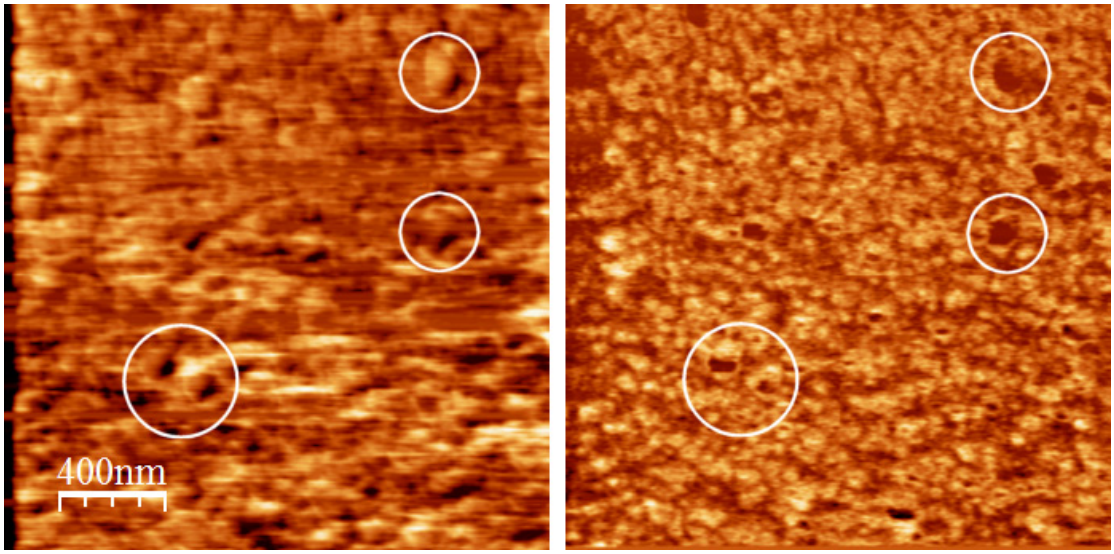

Fig. 5.1 Topography (left) and associated out-of-plane piezoresponse amplitude signal (right) from an area of a Pb/Ti -nanoisland sample conventionally annealed for 40 hr at 300 °C, in air.

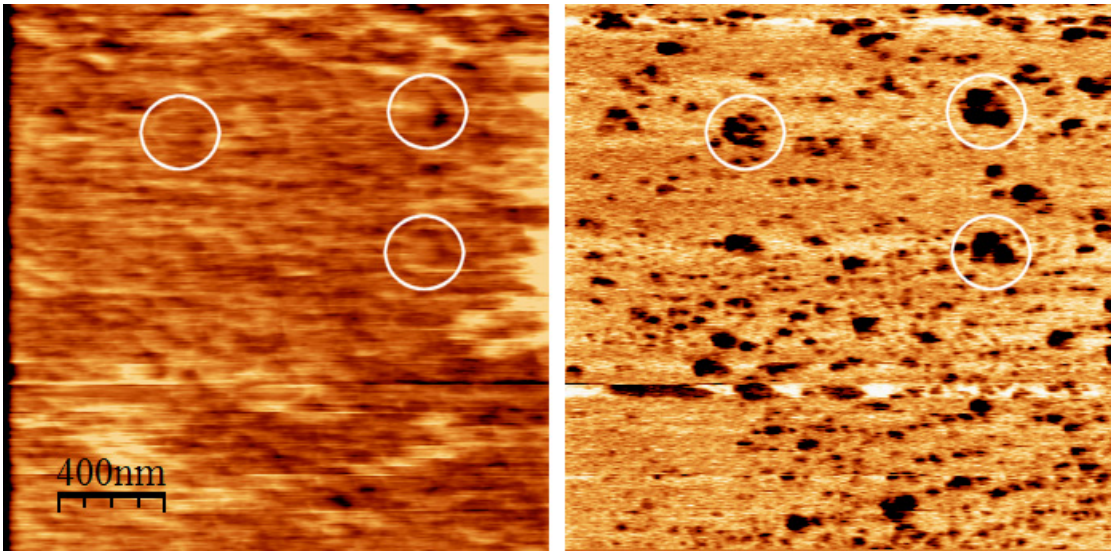

Fig. 5.2 Topography (left) and associated out-of-plane piezoresponse phase signal (right) from an area of a Pb/Ti -nanoisland sample conventionally annealed for 40 hr at 300 °C, in air.

In order to rule out the possibility of the PFM signal being an artefact associated with the topography of the nanoislands, as opposed to a true piezoresponse, a second sample was prepared for analysis. This time, Pb nanoislands were deposited directly onto a $Pt/Ti/SiO_2/Si$ substrate and annealed under the same conditions to produce a control sample with similar morphology but that was known to be non-ferroelectric. Fig. 5.3 shows the topography and associated out-of-plane piezoresponse phase signal from an area of the sample. As can be seen, the morphology of the nanoislands bears a

strong resemblance to those shown in Fig. 5.1 and Fig. 5.2, however there is no discernible piezoresponse, above background noise, in the phase image.

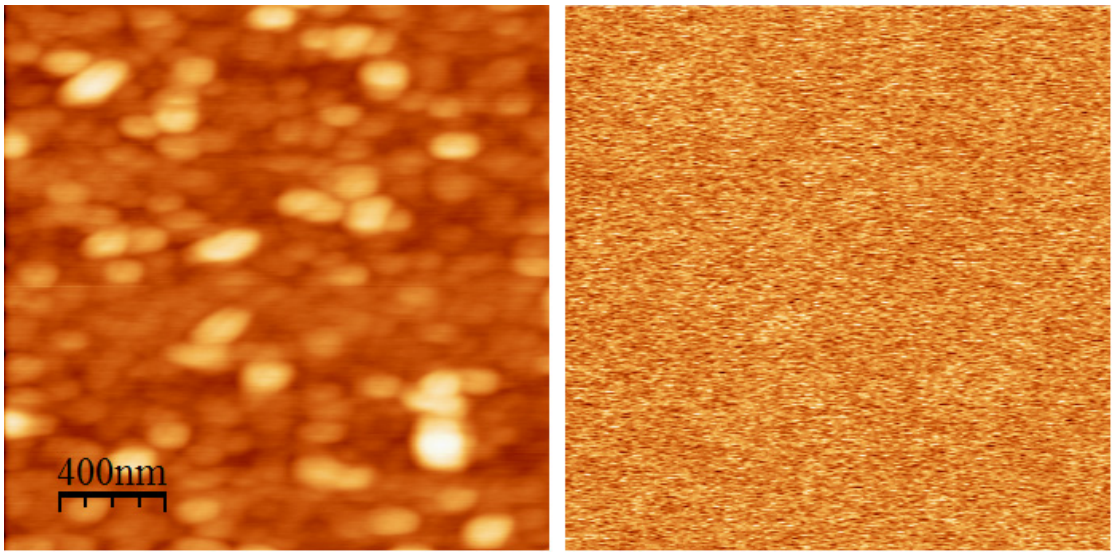

Fig. 5.3 Topography (left) and associated out-of-plane piezoresponse phase signal (right) from an area of a Pb -nanoisland sample conventionally annealed for 40 hr at 300 °C, in air.

5.2.2 Hot plate annealing

The next sample to be analysed consisted of Pb nanoislands deposited onto a $Ti/Pt/SiO_2/Si$ substrate that was subsequently annealed for 1 s at 550 °C, on a hotplate. PFM images were acquired under the same conditions as those discussed in the preceding section. Fig. 5.4 shows the topography and associated out-of-plane piezoresponse phase signal from an area of the sample. The majority of the grains appear to possess a response and, in some of the larger grains, domain structure.

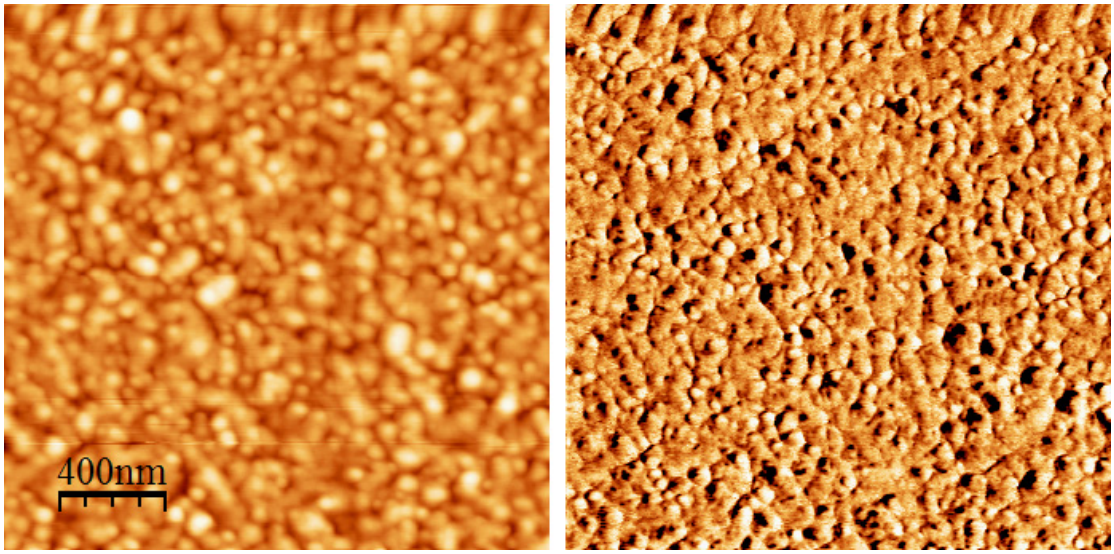

Fig. 5.4 Topography (left) and associated out-of-plane piezoresponse phase signal (right) from an area of a Pb/Ti -nanoisland sample annealed for 1 s at 550 °C, on a hotplate.

Once again, checks were made to rule out the possibility that the signal had been misinterpreted as a true piezoresponse rather than an artefact related to topography. An area of the sample was selected that had been masked during the Pb nanoisland deposition. This site consisted solely of a thin titania layer on top of the Pt back electrode. As can be seen from Fig. 5.5, the titania grains had a similar morphology to the nanoislands in Fig. 5.4, yet they exhibited no detectable piezoresponse, as one would expect.

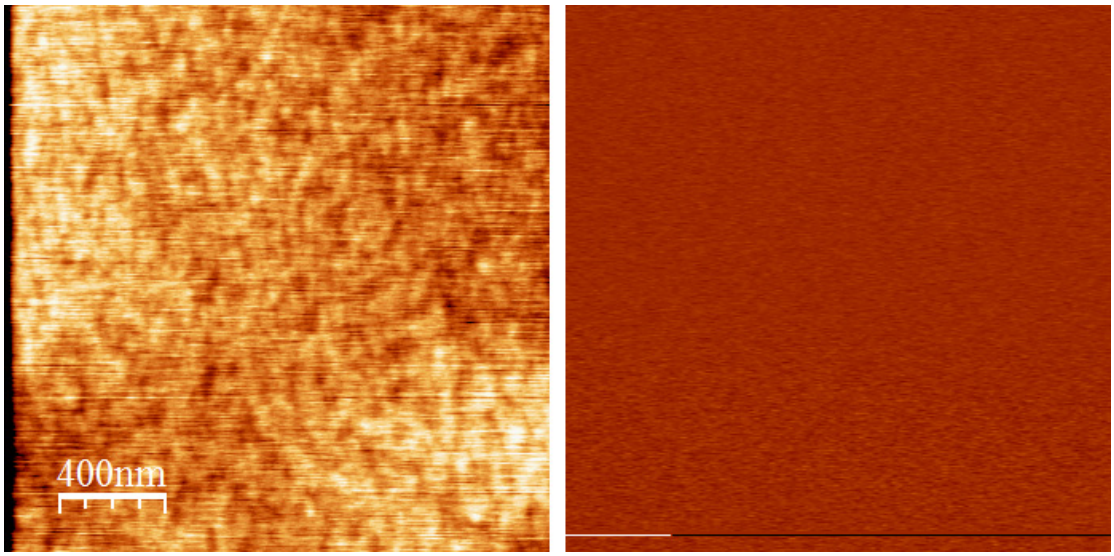

Fig. 5.5 Topography (left) and associated out-of-plane piezoresponse phase signal (right) from an area of titania on the sample analysed in Fig. 5.4.

5.2.3 Attempts to switch the polarisation of nanoislands

In order to verify whether the nanoisland samples were indeed ferroelectric, it was necessary to demonstrate that their polarisation could be switched. This involved applying a DC voltage between the tip and the bottom electrode and scanning a region of the sample that contained nanoislands. PFM scans of the area before and after the poling treatment would have revealed changes in contrast, if switching had taken place. Unfortunately this strategy was unsuccessful, with no evidence of changes in piezoresponse with applied voltages up to 5 V. Attempts to increase voltages above this level led to local destruction of the sample and/or the tip due to dielectric breakdown or shorting through defects in the underlying titania layer. This problem was also encountered when localised hysteresis measurements were made on individual nanoislands. The coercive field of $PbTiO_3$ nanoislands has been reported to be anomalously high – in some cases up to 5 MV/cm.[2] For a nanoisland with a height of 30 nm this corresponds to a coercive voltage of 15 V. Other researchers have suggested that an air gap between the tip and the sample is responsible for the extreme coercive fields measured in PFM experiments.[3] Therefore it is likely that the fields necessary to switch the polarisation orientation of the nanoislands, in the current investigation, were unattainable.

5.2.4 Nanoisland morphology loss through rapid thermal annealing

As discussed towards the end of the previous chapter, it was not possible to retain the morphology of the rapid thermally annealed nanoislands. Instead, SEM observations revealed a surface composed of grains with morphologies similar to those of $PbTiO_3$ films produced earlier in the investigation. PFM images of the rapid thermally annealed samples were acquired by applying an AC voltage with a magnitude of 0.5 V and frequency of 40 kHz between a conductive $PtIr_5$-coated Si tip and the bottom electrode. Fig. 5.6 shows the topography and associated out-of-plane piezoresponse phase signal from a sample that was rapid thermally annealed for 1 s at 500 °C. The piezoresponse image reveals areas of dark and light contrast that represent the c^+ and c^- domains, but few areas of intermediate contrast. On the whole, the grains exhibit a single domain structure, which is to be expected since most are below 50 nm. There appears to be a preference in favour of one domain orientation, since there are far

more light-coloured grains than dark. This can be indicative of self-polarisation, which has been observed in many ferroelectric thin film studies.[4-7]. Explanations for this effect are wide-ranging and encompass both electrical and mechanical origins. Pronin et al. studied the influence of stresses on self-polarisation in ferroelectric thin films.[8] They contested that differences in the thermal expansion coefficients of $PbTiO_3$ and Si led to mechanical compression in films of the former deposited on the latter. This, in turn, led to strong self-polarisation as the stresses helped to orient the polarisation vector along the normal to the substrate plane. The substrate had a negligible influence on the growth of thicker films studied in the current investigation, since the buckling and blistering that occurred during the transformation to $PbTiO_3$ quickly led to the delamination of the films before cooling. However, it is likely that the situation was different for the rapid thermally annealed nanoisland samples as the total film thickness and hence distortions were very small. This means the films would have remained in better contact with the underlying substrate, throughout the heat treatment. Furthermore, other groups have reported that the magnitude of self-polarisation increases as film thickness is reduced, because the domains responsible are local to the film-substrate interface.[9] Taking these results into consideration, it seems feasible that the self-polarisation evident in the piezoresponse image could have originated from substrate induced compressive stress.

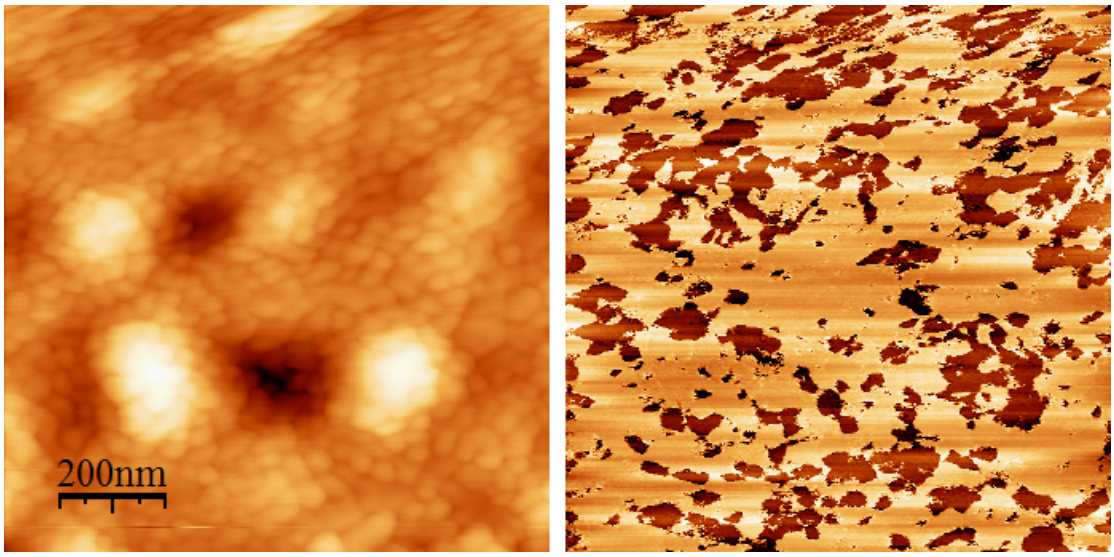

Fig. 5.6 Topography (left) and associated out-of-plane piezoresponse phase signal (right) from an area of a Pb/Ti/Pt/SiO_2/Si-nanoisland sample rapid thermally annealed for 1 s at 500 °C. The large number of bright grains in the piezoresponse image suggests the film was self-polarised.

Fig. 5.7 shows the topography and associated out-of-plane piezoresponse phase signal from an area of a sample rapid thermally annealed for 1 s at 650 °C. In contrast to the sample annealed at 500 °C, the net polarisation across the scanned region is close to zero. This apparent contradiction may stem from the differences in grain morphology that were noticeable in SEM images of the two films (Figs. 34 and 36 in previous chapter). The loose-packed nature of the grains associated with the sample annealed at 650 °C might have helped to minimise stresses in the film during the heat treatment.[10] Consequently any mechanically induced self-polarisation effects would also be limited.

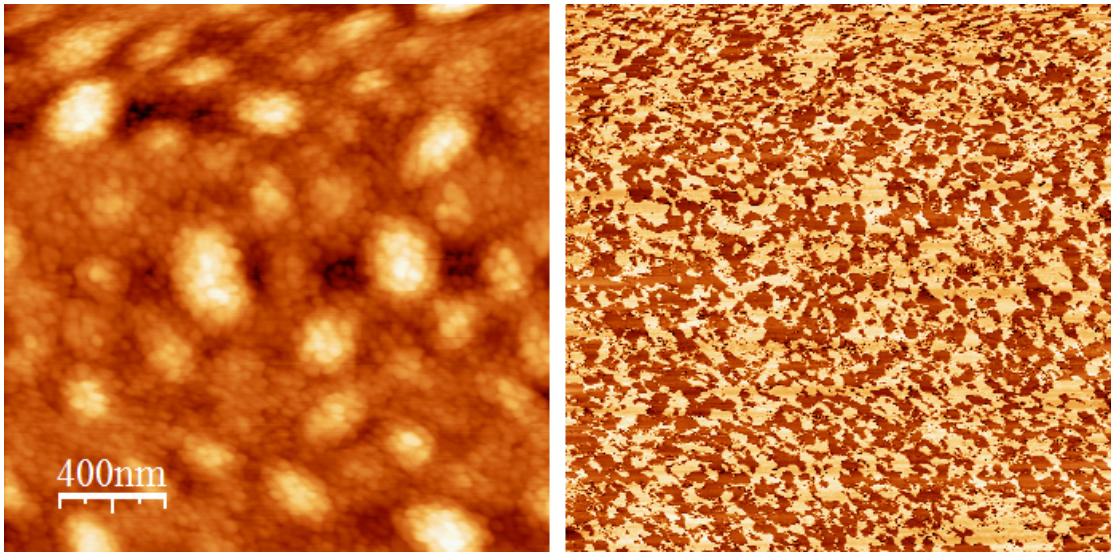

Fig. 5.7 Topography (left) and associated out-of-plane piezoresponse phase signal (right) from an area of a Pb/Ti/Pt/SiO_2/Si-nanoisland sample rapid thermally annealed for 1 s at 650 °C.

5.3 Thin films

The films analysed in this section consisted of Pb/Ti bilayers deposited onto Pt/Ti/SiO_2/Si substrates that were subsequently annealed conventionally, in air. PFM images were acquired under the same conditions as those described in the preceding section, however the magnitude of the applied AC voltage was raised to 1.5 V to compensate for the increase in sample thickness. Fig. 5.8 shows the topography and associated out-of-plane piezoresponse phase signal from an area of a Pb (100 nm)/Ti (50 nm) bilayer sample that was conventionally annealed for 1 hr at 700 °C. The grains visible in the topographic image appear to be spherical, around 100 nm in diameter and agglomerated. The piezoresponse image shows areas of c^+ and c^-

domains that are pinned by the grain boundaries. Areas with intermediate contrast are either non-ferroelectric or polarized in the plane of the film. The average piezoresponse across the scan area is approximately zero indicating little or no self-polarisation. This agrees well with the findings of Gruverman et al. who analysed $PbTiO_3$ thin films, synthesised via a sol-gel technique, using PFM.[11]

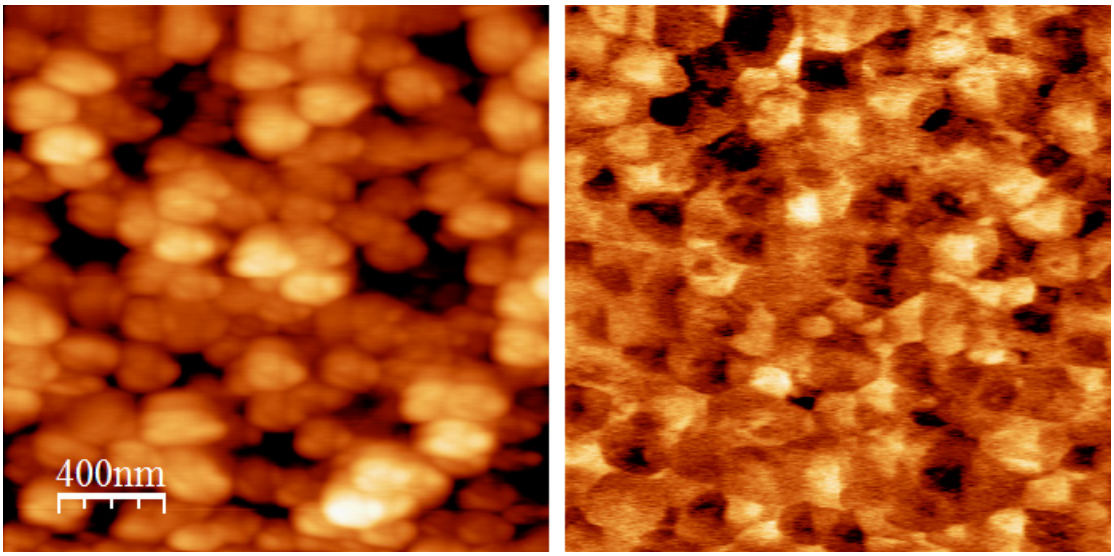

Fig. 5.8 Topography (left) and associated out-of-plane piezoresponse phase signal (right) from an area of a Pb/Ti/Pt/SiO_2/Si thin film sample conventionally annealed for 1 hr at 700 °C.

5.3.1 Attempts to switch the polarisation of films

Once again, it was important to verify the ferroelectric nature of the films by demonstrating that the polarisation of the grains could be switched. However, as was the case with the nanoisland samples, difficulties were often encountered when applying large DC voltages between the tip and bottom electrode. Fig. 5.9 shows the topography and associated out-of-plane piezoresponse phase signal from an area of a sample shortly after applying a +10V DC poling voltage to the same region. A large area visible on the right-hand side of the topographic image has been damaged, through melting, most probably due to Joule heating associated with high currents that passed through a defect. Interestingly, the clarity of the images is testament to the fact that, in this instance the tip appears to have remained intact. Analysis of the piezoresponse image reveals filaments that emanate from the centre of the shorted region. Such changes to the piezoresponse may have been caused by local temperature increases that approached the Curie point of the film.

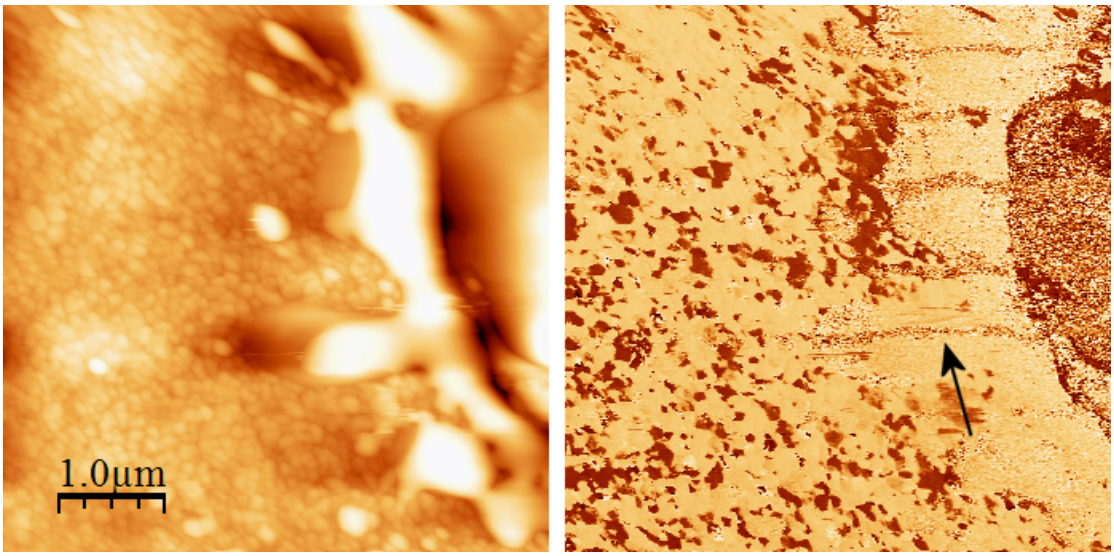

Fig. 5.9 Topography (left) and associated out-of-plane piezoresponse phase signal (right) from an area of a $PbTiO_3$ thin film damaged by poling. Note the apparent piezoresponse beneath the ejecta from the shorted region.

Fig. 5.10 shows the topography and associated out-of-plane piezoresponse from a different area of the same sample, before and after applying a +10 V poling voltage to the central 2.5 μm × 2.5 μm region. The absence of any changes in topography, after poling, indicated that the sample had remained intact this time (cf. Fig. 5.9). Within the central poled region, however, there can clearly be seen a change in the contrast in the piezoresponse image. The majority of the grains have switched to an intermediate contrast, between light and dark. This may represent 90° switching, whereby the polarisation vectors of grains that once faced out-of-plane now lie within the plane of the film. In fact, it is known that 180° switching in perovskites proceeds through two 90° steps as opposed to a direct translational motion of the B-site atom through the plane of symmetry.[12] Alternatively, the intermediate contrast may be due to an internal electric field within the film resulting from a proposed Schottky barrier at the ferroelectric-bottom electrode interface.[13] This field has also been attributed to the self-polarisation effect, since it exists close to the film-electrode interface and has sufficient magnitude to polarise parts of the film in this region. When an external field is applied anti-parallel to the internal field, polarisation reversal can be restricted to the upper part of the grain. This results in the formation of a "tail-to-tail" domain structure and leads to the intermediate contrast observed in piezoresponse phase images.[14]

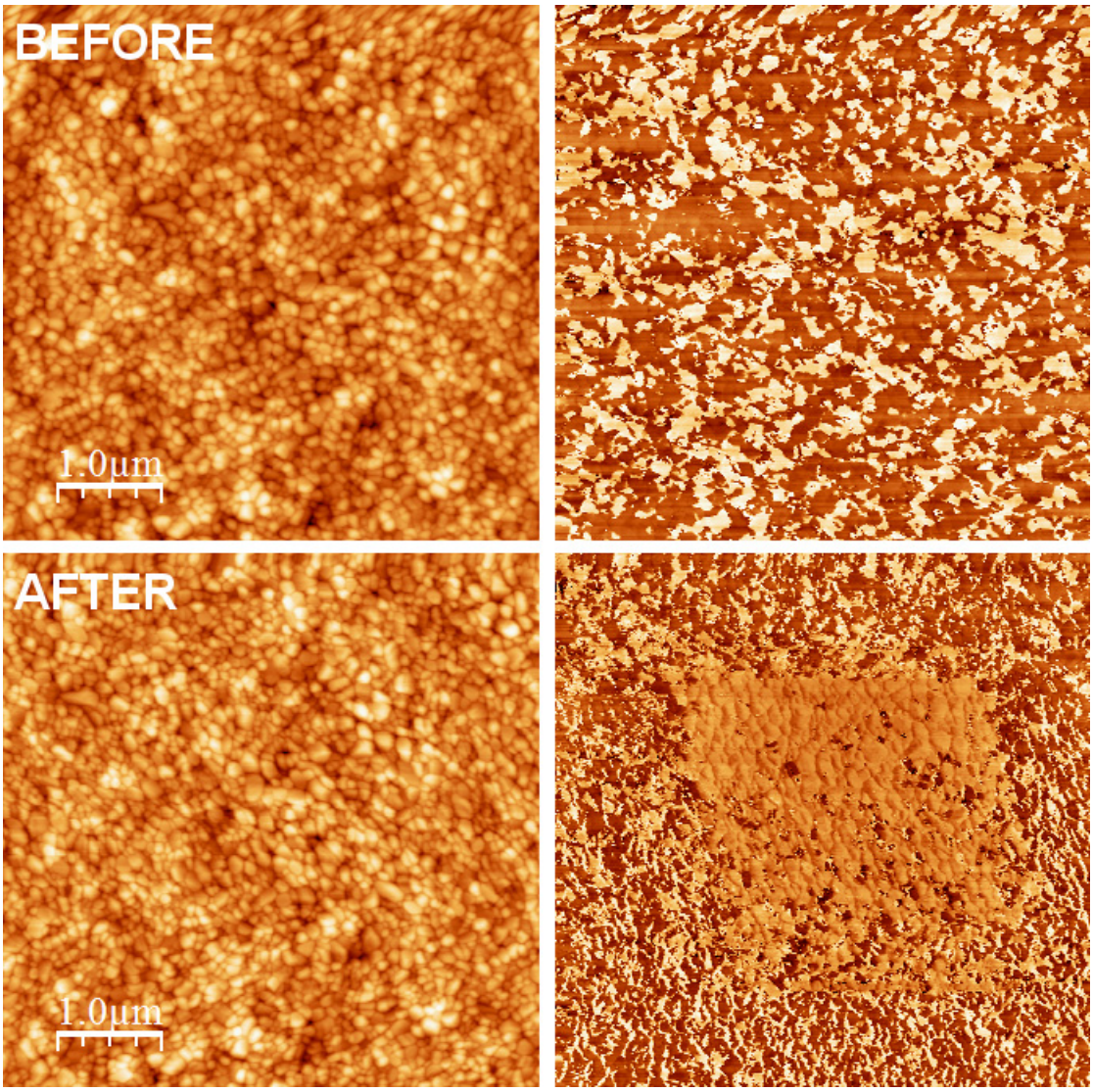

Fig. 5.10 Topography (left) and associated out-of-plane piezoresponse phase signal (right) from an area of a Pb/Ti/Pt/SiO_2/Si thin film sample conventionally annealed for 1 hr at 700 °C, before (top row) and after (bottom row) poling the central region.

5.3.2 Piezoresponse from non-stoichiometric films

The final film to be analysed was a non-stoichiometric sample, composed of a Pb (100 nm)/Ti (370 nm) bilayer, that was annealed for 1 hr at 650 °C. Fig. 5.11 shows the topography and associated piezoresponse phase signal from a region of the sample. Interestingly, the number of grains possessing 180 ° striped domain patterns was substantially larger than that of stoichiometric sample processed in a similar manner.

The explanation for this effect is not clear, however, it is perhaps the result of differing levels of stress in films originating from stoichiometric and non-stoichiometric Pb/Ti bilayers. Fig. 5.12 shows a piezoresponse phase image from an area highlighted in Fig. 5.11 and subsequently rescanned. We can see in more detail the 180 ° striped domain patterns in the top left-hand corner as well as possible 90 ° domain patterns in a large grain on the right hand side.

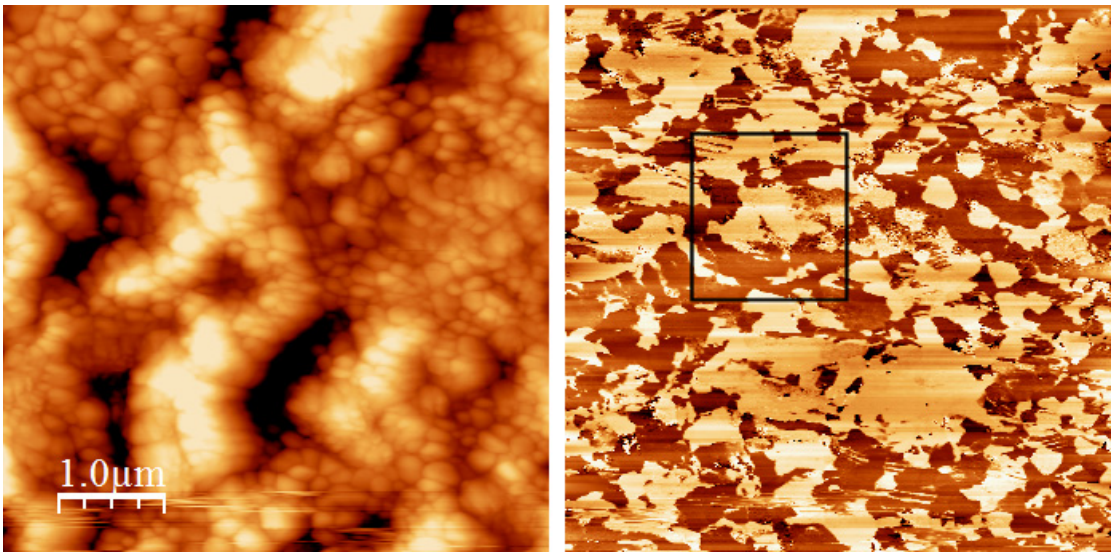

Fig. 5.11 Topography (left) and associated out-of-plane piezoresponse phase signal (right) from an area of a non-stoichiometric Pb/Ti/Pt/SiO_2/Si thin film sample conventionally annealed for 1 hr at 650 °C. The region bounded by a square was rescanned and is shown in Fig. 5.12.

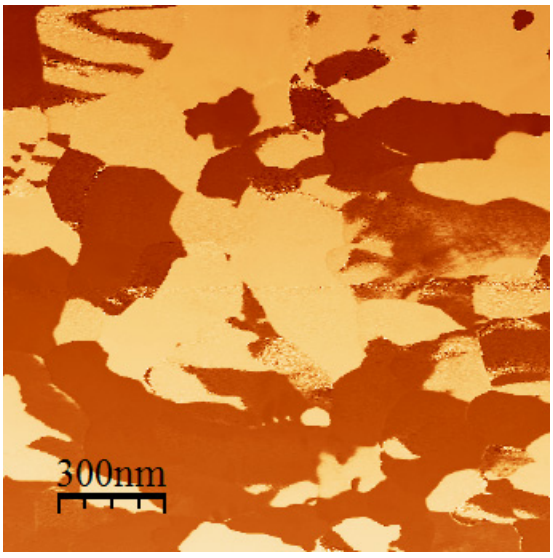

Fig. 5.12 Out-of-plane piezoresponse phase image from the rescanned region highlighted in Fig. 5.11. Note the presence of 180° striped domain patterns in the upper left-hand corner.

5.4 Summary

PFM was conducted on various nanoisland and thin film samples that were produced by the in situ technique. Nanoisland samples subjected to prolonged conventional annealings at 300 °C and brief hot plate annealings at 550 °C exhibited a non-zero piezoresponse. Attempts were made to rule out the possibility that the piezoresponse was spurious by analysing control samples that were known to be non-ferroelectric, yet shared a similar morphology. In all cases the piezoresponse of the control samples was found to be zero. Definitive evidence of ferroelectricity in the nanoisland samples could not be demonstrated, however, as the poling attempts were unsuccessful. The application of DC voltages necessary to exceed the coercive field led to the destruction of the sample and/or tip, as a result of shorting.

Nanoisland samples exposed to rapid thermal annealings between 500 – 650 °C were also analysed. The morphology of these samples resembled that of thin films, since the processing treatment had induced the melting and coalescence of nanoislands. Self-polarisation, attributed to compressive stress in the film, was evident in the sample annealed at 500 °C. The open grain structure of the sample at annealed at 650 °C was thought to relieve stress and thus help to prevent the appearance of self-polarisation.

$PbTiO_3$ thin films produced by annealing Pb/Ti bilayers displayed clear *c*+ and *c*- ferroelectric domains that were mostly pinned by the grain boundaries. Little evidence of self-polarisation was found, since the average piezoresponse across the image was close to zero. This result is typical of polycrystalline $PbTiO_3$ films synthesised by other techniques such as sol-gel. Poling the thin films was found to be challenging, yet not impossible. However, the resultant piezoresponse images showed the presence of intermediate contrast that was interpreted as either partial switching (90 °) or evidence of “tail-to-tail” domain structure formation.

References

[1] H. Zeng, S. Lu, L. Dai, J. Liu, Z. Wang, C. Zuo, *Mater. Lett.* 59, 2808 (2005)

[2] H. Fujisawa, M. Okaniwa, H. Nonomura, M. Shimizu, H. Niu, *J. Euro. Ceram. Soc.* 24, 1641 (2004)

[3] T. Hidaka, T. Maruyama, I. Sakai, M. Saitoh, L. A. Wills, R. Hiskes, S. A. Dicarolis, J. Amano, and C. M. Foster, *Integ. Ferro.* 17, 319 (1997)

[4] M. Adachi, T. Matsuzaki, T. Yamada, T. Shiosaki and A. Kawabata, *Jpn. J. Appl. Phys.* 26, 550 (1987)

[5] S. A. Impey, Z. Huang, A. Patel, R. Beanland, N. M. Shorrocks, R.Watton, and R. W Whatmore, *J. Appl. Phys.* 83, 2202 (1998)

[6] A. R. Zomorrodian, N. J. Wub, H. Linb, and A. Ignatiev, *Thin Solid Films* 335, 225 (1998)

[7] R. Koehler, G. Suchaneck, P. Padmini, T. Sandner, G. Gerlach and G. Hoffmann, *Ferroelectrics* 225, 57 (1999)

[8] I. P. Pronin, E. Yu. Kaptelov, A. V. Gol'tsev and V. O. Afanas'ev, *Phys. Solid State*, 45, 9, 1769 (2003)

[9] A. L. Kholkin, K. G. Brooks, D. V. Taylor, S. Hiboux, N. Setter, *Integ. Ferro*. 22, 1, 525 (1998)

[10] W. C. Goh, K. Yao and C. K. Ong, *Appl. Phys. Lett.* 87, 072906 (2005)

[11] A. Gruverman, B. J. Rodriguez, R. J. Nemanich, and A. I. Kingon, *J. Appl. Phys.* 92, 5, 2734 (2002)

[12] H. Sahota, *Continuum Mech. Thermodyn.* 16, 163 (2004)

[13] J. F. Scott, *Integ. Ferro.* 9, 1, 1 (1995)

[14] A. Gruverman, A. Kholkin, A. Kingon and H. Tokumoto, *Appl. Phys. Lett.* 78, 18, 2751 (2001)

Chapter 6: Conclusions and Further Work

6.1 Introduction

The aim of this thesis was to produce nanoscale PZT and $PbTiO_3$ structures. Two very different techniques were proposed to achieve this goal, after an extensive review of the existing literature on the subject. The first, namely hydrothermal synthesis was selected for its numerous advantages over competing ex situ techniques. These included: low processing temperature requirements, the ability to produce ultra pure crystals and the relative simplicity of the technique. Furthermore, nucleation and growth of hydrothermal crystals occurs in isolation, without possible influence from a substrate. Taking these advantages into account, it was felt that hydrothermal synthesis had the best chance of producing the "ideal" crystal – a prerequisite for studying intrinsic ferroelectric properties.

6.2 The ex situ technique of hydrothermal synthesis

Initial experiments contradicted the findings of Deng et al.[1] with respect to the scale of the PZT crystals produced, using a simple, one-stage hydrothermal synthesis. The resultant crystals were found to be micron-sized with a cubic morphology, as opposed to spherical and nanometric, as was reported. Efforts were thus directed at reducing the size of the resultant particles by altering various reaction parameters. It was found that the original processing time of 4 hr could be halved whilst still retaining full crystallisation. However, particle sizes remained more or less unchanged, regardless of processing time. This suggested that the dissolution stage was the rate-limiting step in the overall reaction. Attempts to reduce particle sizes by lowering the reaction temperature below 160 °C, led to incomplete dissolution of the precursors and no change to the average PZT crystal size. From these findings it was concluded that processing temperature had had a limited effect on the rate at which the PZT crystals had precipitated.

Increasing the initial Pb precursor concentration was found to modify the morphology but not the size of the resultant PZT particles. The cubic crystals were well faceted

and less agglomeration had taken place. It is thought that an excess of Pb ions at the early stages of the reaction helped in the dissolution of the Zr-Ti precipitates. Finally, the internal structure of PZT particles produced using a Pb-excess exhibited an enhanced degree of crystallisation when compared to those produced from stoichiometric precursor solutions.

A brief study into the effect of alkali mineraliser type found that it was possible to produce phase-pure PZT when KOH was substituted for NaOH. The morphology of particles was unaffected, however the average size fell by 40% when NaOH was used.

A number of different surfactants were tested for their ability to disrupt the hydrothermal reaction during the precipitation stage and thus impede crystal growth. Using a 2% Triton X-100 solution it was possible to reduce the average PZT particle size by 60% in comparison to those synthesised without surfactants. The other surfactants were less effective and resulted in the production of large quantities of amorphous or partially crystallised material.

The final study to produce freestanding particles via the hydrothermal method involved the treatment of an as-prepared 52:48 PZT sol precursor. It was hoped that the homogeneous sol would be more amenable in terms of the required mineraliser concentration necessary to promote a reaction. Processing the sol for 30 min at 160 °C using a 3.3 M KOH concentration resulted in a mixture of agglomerated, micron-sized PZT cubes and amorphous material. Increasing the reaction time to 24 hr, whilst keeping the other variables constant, led to the production of pyramidal fibres that, in some cases tapered to nanosized points.

Since the various studies on freestanding hydrothermal particles failed to produce crystals of the desired dimensions, the decision was taken to investigate epitaxial hydrothermal growth of PZT on single-crystal $SrTiO_3$ substrates. Long processing times of 24 hr resulted in the formation of micron thick PZT films, with inhomogeneous substrate coverage. Islands with dimensions approaching 100 nm were also observed. XRD analysis showed the structures to be highly (100)-oriented which was due to the good lattice match between PZT and $SrTiO_3$. Processing times of 30 minutes led to the formation of isolated PZT islands as well as “microwires”, up

to a millimetre in length, composed of individual islands that had coalesced in one dimension. It was thought that these features were the result of preferred nucleation sites on the substrate, created during polishing. Unfortunately, the size of the individual islands did not scale with reaction time. This suggests that the nanometric islands observed in the extended processing time experiment were the result of local inhomogeneities in the precursor mixture. Ferroelectric analysis of the PZT islands and microwires conducted using piezoresponse force microscopy showed them to possess a weak piezoresponse.

6.3 The in situ technique of solid phase synthesis

The second technique investigated for the production of ferroelectric nanostructures was solid phase synthesis. This involved the deposition of metals by magnetron sputtering and thermal evaporation onto a substrate and annealing the resulting heterostructures in air to crystallise the ferroelectric phase. Since this was an in situ technique the substrate could be expected to influence the ferroelectric properties of the heterostructures. Furthermore, the temperatures necessary to crystallise the ferroelectric phase were greater than the hydrothermal method studied previously, although less than competing in situ techniques such as sol gel. On the positive side, it was felt that the technique of solid phase synthesis could be developed to produce nanoislands of smaller dimension than any of the crystals produced in the hydrothermal experiments.

6.3.1 Synthesising $PbTiO_3$ thin films

Work began with a detailed investigation into the structure and morphology of $PbTiO_3$ thin films generated by the solid phase technique. This was in response to earlier work on the subject by Sidorkin et al.[2] and Stankus et al.[3] Consecutive 1 hr furnace annealings were conducted, in air, between 300 – 700 °C in order to track the evolution of crystalline phases in near-stoichiometric Pb/Ti-bilayers. From these studies the optimum conditions for crystallisation of the perovskite $PbTiO_3$ phase were ascertained to be 1 hr at 650 °C. In order to characterise the electrical properties of the films it was necessary to use conductive substrates. The first attempt using bare Si wafers and Pt back electrodes failed due to a reaction that consumed the Pt and

formed PtSi during the annealing. This led to the adoption of thermal oxide Si wafers, which, when used in conjunction with Pt electrodes, were stable at the elevated processing temperatures associated with solid phase synthesis. Unfortunately inspection of the resultant $PbTiO_3$ film morphology found extensive blistering across the surface. Consequently, measuring the dielectric properties of the films was impossible due to shorting, between the top and bottom electrodes, through pinholes at the blister sites.

Cross-sectional SEM images of the $PbTiO_3$ thin films revealed damage to the Pt bottom electrode and voids in the SiO_2 beneath the blisters. This was thought to be caused by PbO that had diffused through Pt grain boundaries during the annealing and formed lead silicates on contact with the SiO_2. At this stage it was unclear whether the distortions and blistering in the film were as a result of the damage to the substrate (possibly through the production of a gas), or vice-versa. To answer this question, two strategies were adopted with the overall aim of reducing the level of distortion observed in the films and thus facilitate dielectric measurements. The first involved finding a replacement for the Ti adhesion layer used with the Pt back electrodes. During an annealing, Ti has been known to diffuse through Pt grain boundaries and force them apart through the volume expansion that occurs upon oxidation. However, titania, in particular the rutile polymorph, is less susceptible to this diffusion and also has the added benefit of being a good diffusion barrier. A rutile adhesion layer was therefore prepared, by pre-annealing a Ti film prior to deposition of the Pt back electrode. The adhesion of Pt on rutile was found to be inferior to that of Pt on Ti, but work continued with the deposition of a Pb/Ti-bilayer to produce $PbTiO_3$. After annealing for 1 hr at 650 °C the $PbTiO_3$ phase was seen to develop, but the integrity of the film was poor and it was still not possible to record electrical measurements.

The adhesion problems encountered during the deposition of Pt onto rutile prompted a return to the use of metallic adhesion layers. Zr was selected as a possible candidate to replace Ti, since it possesses a larger atomic radius and greater chemical reactivity. These properties were predicted to lead to a reduction in the level of diffusion through Pt grain boundaries as well as improved adhesion. After depositing and annealing a Pb/Ti-bilayer, SEM observations showed blisters were still present across the resultant film. However, in contrast to the previous electrode configurations, it was possible to

record hysteresis measurements from a number of top electrodes. The loop shape indicated lossy dielectric behaviour as opposed to a ferroelectric response.

The second strategy to improve film quality involved replacing the thermal oxide Si substrates. ITO-coated glass and Nb:$SrTiO_3$ single-crystals were chosen for their conductivity and compatibility with ferroelectric films. In both cases it was possible to crystallise the $PbTiO_3$ phase using these substrates, but the level of distortion present in the films was the same or even greater than that present on thermal oxide Si substrates. However, in contrast to films deposited on the latter, the upper regions of the substrates remained intact and undamaged. This result suggested that the distortion present in the films was not a consequence of the interaction between volatile species and the substrate. Experiments with non-stoichiometric bilayers on thermal oxide wafers supported this idea, since the resultant films exhibited blistering, whilst remaining isolated from the substrate by a thick TiO_x diffusion barrier. If the influence of the substrate can be neglected, then it seems likely that the actual cause of blistering and delamination was a result of stresses generated during the transformation into the $PbTiO_3$ perovskite phase.

An attempt was made to synthesise MPB PZT thin films via the solid phase technique by adding a Zr layer to the Pb/Ti-bilayer structure. If the distortions present in $PbTiO_3$ films were a result of the large tetragonality of the $PbTiO_3$ lattice, then it was felt that attempting to produce PZT could be a solution. Three different trilayer combinations were assessed by conducting consecutive 1 hr annealings in the same manner as that of the $PbTiO_3$ experiments. An XRD analysis showed that ZrO_2 and $PbTiO_3$ started formed in all cases, above a temperature of 600 °C, but no evidence of any PZT phase was found, up to a maximum temperature of 900 °C. This indicated that there was insufficient thermal energy available to crystallise via PZT via the solid phase technique. Increasing the annealing temperature above 900 °C was not possible, due to softening of the Si substrate.

6.3.2 Adapting the technique to produce $PbTiO_3$ nanoislands

Following the work on thin films, the solid phase synthesis technique was adapted to produce $PbTiO_3$ nanoislands. By utilising flash evaporations, lasting approximately

0.5 s, it was possible to produce Pb nanoislands with a size distribution of between 5 – 30 nm. Annealing the nanoislands under the same regime as used during the thin film experiments led to the loss of their morphology through melting. Pre-annealing the samples at a temperature below the melting point of Pb to oxidise the nanoislands was posited as a solution to this problem. Unfortunately, during the subsequent high temperature annealing the PbO nanoislands sintered and coalesced. To overcome this problem an extended low temperature annealing was adopted. Limited melting and coalescence still occurred, but a significant number of nanoislands in the size range of interest remained on the substrate.

Rapid thermal and brief, hot plate annealings were also investigated as a means of crystallising the $PbTiO_3$ nanoislands while retaining their morphology. Samples subjected to rapid thermal processing exhibited a grain structure similar to that of in situ $PbTiO_3$ thin films. In contrast, the nanoislands on samples annealed using the hot plate coalesced to a lesser extent. This difference was attributed to the extended cooling period that the rapid thermally annealed samples had to endure.

6.3.3 Ferroelectric analysis of $PbTiO_3$ nanostructures

Piezoresponse force microscopy was conducted on various nanoisland and thin film samples that were produced by the in situ technique. Nanoisland samples subjected to prolonged conventional annealings at 300 °C and brief hot plate annealings at 550 °C exhibited a non-zero piezoresponse. Attempts were made to rule out the possibility that the piezoresponse was spurious by analysing control samples that were known to be non-ferroelectric, yet shared a similar morphology. In all cases the piezoresponse of the control samples was found to be zero. Definitive evidence of ferroelectricity in the nanoisland samples could not be demonstrated, however, as the poling attempts were unsuccessful. The application of DC voltages necessary to exceed the coercive field led to the destruction of the sample and/or tip, as a result of shorting.

Nanoisland samples exposed to rapid thermal annealings between 500 – 650 °C were also analysed. The morphology of these samples resembled that of thin films, since the processing treatment had induced the melting and coalescence of nanoislands. Self-polarisation, attributed to compressive stress in the film, was evident in the

sample annealed at 500 °C. The open grain structure of the sample at annealed at 650 °C was thought to relieve stress and thus help to prevent the appearance of self-polarisation.

Lead titanate thin films produced by annealing Pb/Ti bilayers displayed clear *c*+ and *c*- ferroelectric domains that were mostly pinned by the grain boundaries. Little evidence of self-polarisation was found, since the average piezoresponse across the image was close to zero. This result was typical of polycrystalline $PbTiO_3$ films synthesised by other techniques such as sol-gel. Poling the thin films was found to be challenging, yet not impossible. However, the resultant piezoresponse images showed the presence of intermediate contrast that was interpreted as either partial switching (90 °) or evidence of "tail-to-tail" domain structure formation.

6.4 Final remarks

This thesis set out to investigate two different synthesis routes for producing PZT and $PbTiO_3$ nanostructures. The ex situ method of choice, hydrothermal synthesis, although technically simple was unable to be modified for the task. All the fully crystallised, freestanding material observed in this research was microscale as opposed to nanoscale. The main issue hampering size control was the extremely rapid dissolution stage of the hydrothermal reaction. Unfortunately one of the disadvantages of the hydrothermal method is that it is impossible to monitor a reaction in real time and thus intervene at an earlier stage. The relatively slow cooling rate of the reinforced autoclave is another problem, since it distorts the actual length of the reaction time. Attempts to quench the reaction by rapid cooling were avoided due to the possible danger of the autoclave failing. Some "large" nanoscale material was observed, however, in the experiments involving heteroepitaxial growth of PZT on $SrTiO_3$ substrates. Of course, this meant sacrificing one of the inherent benefits of the hydrothermal technique, namely isolated growth, and was thus a less than favourable solution to the problem of producing nanoscale structures.

The focus of the investigation shifted towards the solid phase technique after it was realised that hydrothermal synthesis could not be used to produce nanoscale PZT crystals of the desired size. Work in this area began with the characterisation of

$PbTiO_3$ films synthesised using solid phase synthesis. Distortions present in the films were found to originate from stresses induced by the transformation into the perovskite $PbTiO_3$ phase. Many attempts were made to reduce the level of these distortions, but to no avail. As such the method was found to be inadequate for producing $PbTiO_3$ of sufficient quality for device applications. Attempts to produce PZT films, with the addition of a Zr layer to the original Pb/Ti-bilayer heterostructure, were also unsuccessful, since no crystalline PZT phase could be detected.

A method to produce Pb nanoislands via flash thermal evaporation was demonstrated and combined with the solid phase technique to produce $PbTiO_3$ nanoislands. The morphology of the former could be retained during the annealing by reducing temperatures to prevent melting and subsequent coalescence. Dwell times were increased significantly to compensate for the reduction in the rate of reaction.

Ferroelectric analysis via PFM was conducted on solid phase $PbTiO_3$ nanoislands and thin films. A non-zero response was detected from the nanoisland samples, which gave an indication that they were piezoelectric. However, due to limitations with the technique, it was not possible to pole the nanoislands and so ferroelectricity was not explicitly confirmed. The average piezoresponse from $PbTiO_3$ thin films was close to zero and there was plenty of evidence for domain structure within individual grains. Confirmation of ferroelectricity was achieved by scanning areas that were previously poled using an applied DC field.

6.5 Further work

6.5.1 Hydrothermal synthesis

The hydrothermal technique used to generate PZT in this investigation proved to be very robust. As such it is difficult to imagine small alterations in the starting variables and conditions ever producing crystals of the desired scale. It would probably be necessary to synthesise a tailored complex precursor solution, perhaps with the aid of surfactants. The investment in time necessary to design such a synthesis was beyond the scope of this investigation and detracts from the simplicity of the hydrothermal technique – one of the key benefits identified at the start of the study.

6.5.2 Solid phase synthesis

This investigation has shown that solid phase synthesis is unsuitable for producing high quality $PbTiO_3$ films. It is therefore imprudent to continue efforts in this direction. Utilisation of the technique to produce nanoislands, however, is more promising. A further development could be to analyse the interaction between polar molecules in a solution and the surface charge associated with the nanoislands. This would open up the possibility of using arrays of ferroelectric nanoislands as tools for molecular self-assembly.

Lateral PFM should be conducted on all the nanostructures, in particular the $PbTiO_3$ thin films, which exhibited grey domain contrast in the VPFM image. This analysis would answer the question as to whether the grains were non-ferroelectric or polarised in the film plane. It could also verify the presence of partial, 90 ° switching that may have occurred after the poling treatment. This analysis was beyond the scope of the current investigation, but would not be difficult to achieve assuming suitable apparatus was available.

References

[1] Y. Deng, L. Liu, Y. Cheng, C-W. Nan and S-J. Zhao, *Mat. Lett.* 57, 1675 (2003)

[2] A. S. Sidorkin, A. S. Sigov, A. M. Khoviv, S. O. Yatsenko and O. B. Yatsenko, *Phys. Solid State*, 42, 4, 745 (2000)

[3] V. Stankus and J. Dudonis, *Mater. Sci. Eng. B*, 109 178 (2004)

Appendix A: The effect of the Ti overlayer on the formation of platinum silicide in Ti/Pt/Ti/Si structures

The effect of the Ti overlayer on the formation of platinum silicide in Ti/Pt/Ti/Si structures

Scott Harada*[a] and Steve Dunn[a]

Pt and Ti thin films have been deposited via sputtering onto Si wafers to form Pt/Ti/Si and Ti/Pt/Ti/Si structures. The behaviour of both structures was compared after annealing in air and under Ar over a range of times (5 minutes to 24 hrs) and temperatures (400 – 700 °C). Powder XRD was used to track the evolution of phases within the structures after successive annealings. PtSi and Pt_2Si were seen to form after annealing Pt/Ti/Si structures for 1 hr at 500 °C. However, the reaction was inhibited by the presence of O_2 at the Pt_2Si reaction front and finally halted after the Ti adhesion layer became oxidised. The behaviour of Pt/Ti/Si structures annealed under Ar showed similarities to that of Ti/Pt/Ti/Si structures annealed in air. Therefore, it was proposed that the Ti overlayer had a role in preventing O_2 from reaching the Ti adhesion layer in the Ti/Pt/Ti/Si structures. Consequently, the diffusion barrier between Pt and Si that would normally form in Pt/Ti/Si structures, when annealed in air, was suppressed, allowing for almost complete conversion of Pt into PtSi.

1. Introduction

The high oxidation resistance of Pt makes it ideal for use as a bottom electrode in the manufacture of micro-electromechanical systems (MEMS) and oxide capacitors.[1-3] Many of these applications require processing at temperatures in excess of 500 °C. The piezoelectric material lead zirconate titanate (PZT) is used extensively in the manufacture of MEMS devices for sensing and actuation.[4,5] Sol-gel derived PZT thick films crystallise into the perovskite phase at approximately 550 °C.[6] Under such conditions, interdiffusion across the interfaces between metal layers and the substrate becomes an issue. An intermetallic Pt_3Pb phase is known to form when PZT, deposited on Pt/Ti electrodes, is annealed at 440 °C.[7] In this case the Pt_3Pb phase is transient and beneficial since it facilitates the growth of (111)-orientated perovskite PZT films. Often, however, the formation of intermetallics can have a detrimental effect on the performance of a thin film system. The electronics industry famously suffered from the "purple plague" when bonding Au to Al.[8] Au and Al react to form the brittle, purple intermetallic $AuAl_2$ at comparatively low temperatures (~150 °C). Consequently, Au-Al bonds tended to fail as a result of their reduced mechanical strength.[8]

When Si substrates are used in the fabrication of Pt electrodes, a thin layer of Ti is normally deposited first to ensure good substrate-electrode adhesion. Ti atoms are sufficiently reactive to break O-Si bonds, on the surface of the substrate, and make Ti-O or Ti-Si bonds. Pt, being a noble metal, does not adhere to Si in this way, but can form strong metallic bonds with Ti. Hence, the surface energy of the substrate-film interface can be reduced sufficiently, by way of the Ti adhesion layer, for Pt to bond to Si.[9] When Pt/Ti electrodes are annealed under an inert atmosphere, a reaction can occur between the Pt electrode and Si substrate that depends on the thickness of the Ti adhesion layer.[10] Ti layers less than 5 nm thick react with the native oxide present on the Si substrate to form a titania diffusion barrier that inhibits the Pt-Si reaction. Layers thicker than 5 nm lead to the formation of a Ti-O solid solution which does not hinder the Pt-Si reaction. In this paper, we discuss the effects of adding an overlayer of Ti to the Pt/Ti/Si system. Such structures are a prerequisite when forming ferroelectrics via solid-state reactions. For example, by depositing a layer of Pb on top of the Ti/Pt/Ti/Si structure and annealing in air, a thin film of the ferroelectric $PbTiO_3$ can be produced. Hence, the behaviour of Ti/Pt/Ti/Si structures annealed under Ar and air atmospheres has been compared to that of Pt/Ti/Si structures, under similar conditions.

2. Experimental details

Mechanical grade, boron-doped (100) Si wafers were used, after an IPA/acetone clean, throughout the investigation. A Nordiko 2500 sputtering system (base pressure $4.5 – 9.5 \times 10^{-5}$ Pa; Ar gas) was used to deposit the metallic thin films onto Si. A Ti adhesion layer was sputtered first, followed by Pt and in some experiments a final Ti overlayer. Deposition rates for Ti and Pt were established before this investigation by measuring step heights using a Dektak surface profilometer. Annealing took place in a box furnace in air and a tube furnace under Ar over a range of times (5 minutes up to 24 hrs) and temperatures (400 – 700 °C). The tube furnace was pumped down and back-filled to atmospheric pressure with Ar three times, prior to annealing, in order to minimise O_2 contamination. A Siemens D5005 x-ray diffractometer (Cu $K\alpha_1$ radiation $\lambda = 1.5406$ Å) was used to characterise the phase composition of the wafers.

[a] *Nanotechnology Group, Building 70, Cranfield University, Cranfield, Bedfordshire, MK43 0AL*
E-mail: s.harada.2003@cranfield.ac.uk; Fax: +44 (0) 1234 751346; Tel:+44 (0) 1234 750111 x2583

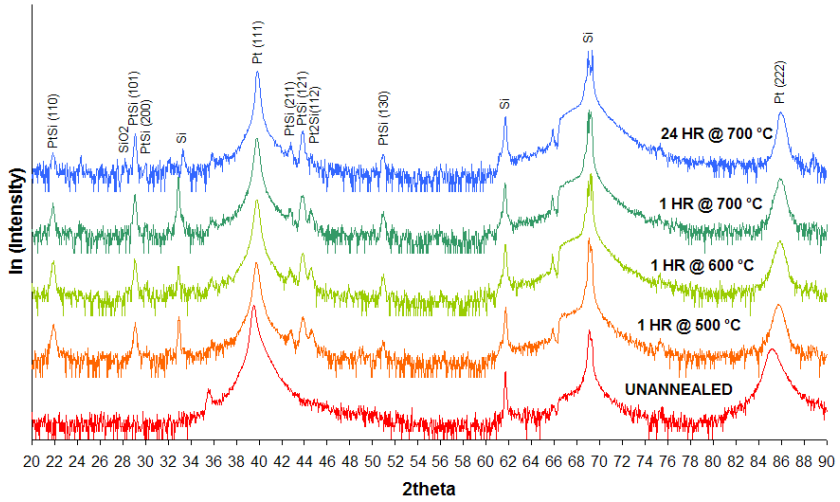

Fig. 1 XRD data for a Pt/Ti/Si structure showing the evolution of phases after successive annealings between 500 – 700 °C.

3. Results and Discussion

3.1. Annealing Pt/Ti/Si structures in air

The first experiment involved sputtering a 100 nm Pt film on top of an 8 nm Ti adhesion layer. These thicknesses satisfy the relevant criteria for bottom electrodes – namely good electrical conduction and adhesion. The XRD data in Fig. 1 shows the evolution of phases that occurred after successive annealings, between 500 – 700 °C, in air. Peaks representing PtSi and Pt_2Si (JCPDS card nos. 07-0251 and 17-0683, respectively) can be seen to form after 1 hr at 500 °C. However, the reaction does not consume the entire Pt layer, since a strong Pt (111) peak is still detected, even after annealing for 24 hrs at 700 °C. The lack of a significant increase in intensity of the PtSi peaks, with each successive annealing, suggests that the reaction is essentially complete after 1 hr at 500 °C. Larrieu et al.[11] found that complete silicidation of 15 nm Pt films into PtSi took less than 120 s at 300 °C under an inert atmosphere. Therefore, the observations are consistent with known results, although the presence of O_2 has an effect on the rate of reaction that will be discussed later. The mechanism of PtSi formation in thin films is known to be a two-step process.[12] In the first step, Pt diffuses into Si and a Pt-rich Pt_2Si phase is formed; in the second, Si diffuses into Pt_2Si to form PtSi (note the Pt_2Si (112) peak in Fig. 1. which diminishes with each annealing). Under an inert atmosphere, the two steps are sequential, so the Pt, Pt_2Si and PtSi phases cannot coexist. However, when O_2 is present in the sample, it tends to concentrate at the Pt_2Si reaction front. Consequently, diffusion of Pt can be inhibited to the point at which Pt_2Si growth is halted.[12] The reaction to form PtSi reaction then proceeds at the Pt_2Si/Si interface, leaving behind a layer of unreacted Pt on the surface of the sample. A second mechanism inhibiting silicide growth may occur if O_2 from the atmosphere reaches the Ti adhesion layer. In this case, a titania diffusion barrier will form, preventing Pt from reaching the Si substrate. The reaction to form the titania barrier will be limited by the rate at which O_2 diffuses through the Pt layer. As such, a significant quantity of silicide will be produced before the barrier can form.

A peak thought to represent SiO_2 (JCPDS 46-1242) was observed after annealing the sample for 24 hr at 700 °C. This behaviour has been noticed before [10, 11, 13] and is attributed to the outdiffusion and subsequent oxidation of Si during the PtSi reaction step.

The Pt (111) peak shifted during each annealing to reach a final 2theta value approximately + 0.3 ° from its starting position. This is thought to have been caused by annealing-induced stress as the Pt diffused into the Si.

3.2. Pt consumption during the annealing of Ti/Pt/Ti/Si structures in air

A second sample was prepared in which a 200 nm Ti overlayer was sputtered on top of the Pt (100 nm)/Ti (8 nm)/Si structure. Fig 2. shows XRD data for the Pt (111) peak of this wafer after successive 1 hr annealings between 400 – 550 °C. The peak shift observed in the previous experiment is again present. The peak intensity increases, after the 400 °C and 450 °C annealings, are due to the tendency of Pt atoms to arrange in a configuration with the lowest energy state on an amorphous layer – the (111) plane having the lowest free energy in the FCC crystal structure.[14] However, the peak area falls, between 450 – 550 °C, indicating a continuous conversion of Pt into PtSi. After the final annealing at 550 °C the Pt (111) peak becomes undetectable above the background intensity. This result is in marked contrast to the experiment in Section 3.1., involving the Pt/Ti/Si structure, in which the Pt (111) peak remained prominent, even after successive annealings up to 700 °C. Fig. 3 shows XRD data in the range 2theta = 20 – 60 ° for the sample after the last two annealings (500 °C and 550 °C). The disappearance of the Pt (111) peak in the data for the 550 °C annealing, along with an increase in

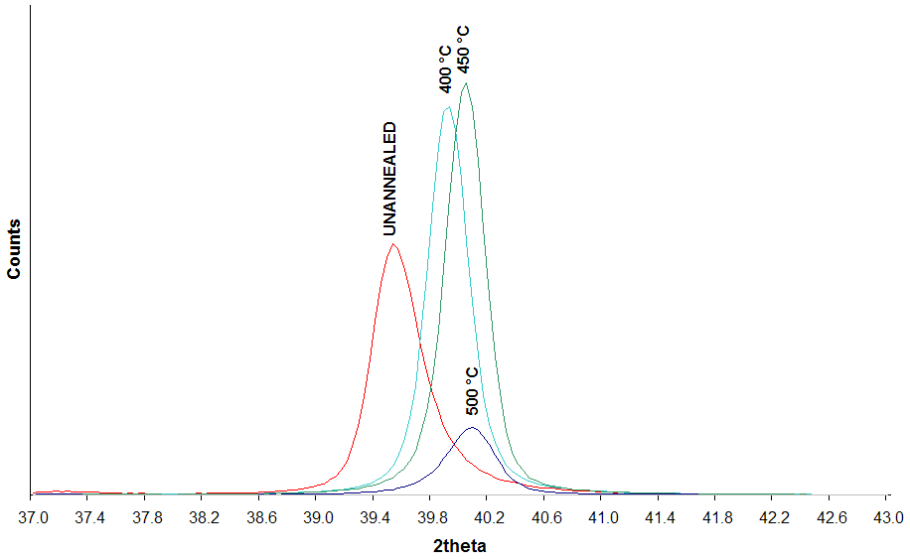

Fig. 2 XRD data showing the change in intensity of the Pt (111) peak in a Ti/Pt/Ti/Si structure after successive annealings.

intensity of the PtSi peaks, suggests a complete conversion of the available Pt, within the sample, into PtSi.

From XPS analysis, it is known that, during annealing, the Ti in the adhesion layer moves upward towards the surface of the sample.[10] While inside the Pt layer, the Ti undergoes a reaction to form PtTi. This phase (JCPDS 19-0917) has been detected via XRD and is shown in Fig. 3.

3.3. A comparison between Pt/Ti/Si structures annealed under Ar and Ti/Pt/Ti/Si structures annealed in air

To explain the observations noted under the preceding two Sections, a series of annealings was conducted using two different types of sample. The first had a 2 nm Ti adhesion layer on top of which 30 nm of Pt was sputtered. The second had a thicker, 200 nm, layer of Ti onto which 140 nm of Pt was sputtered. Fig. 4 shows the XRD results after annealing both samples under Ar for 30 minutes at 700 °C. No PtSi was detected after annealing the Pt (30 nm)/Ti (2 nm)/Si sample whereas almost complete conversion of Pt into PtSi occurred in the Pt (140 nm)/Ti (200 nm)/Si sample. This behaviour can be explained by considering the difference in thickness of the Ti layers in each sample. It is understood that a titania diffusion barrier forms when the Ti layer is thin enough (< 5 nm) to react with the native oxide on the Si substrate. Under these conditions, Pt cannot diffuse into the Si and the reactions leading to the formation of PtSi cannot proceed. Conversely, for Ti layers thicker than 5 nm, a Ti-O solid solution forms through which Pt can still diffuse.[10]

The final experiments involved sputtering a 50 nm Ti overlayer onto two unannealed samples of the type described above, producing the following structures: Ti (50 nm)/Pt (30

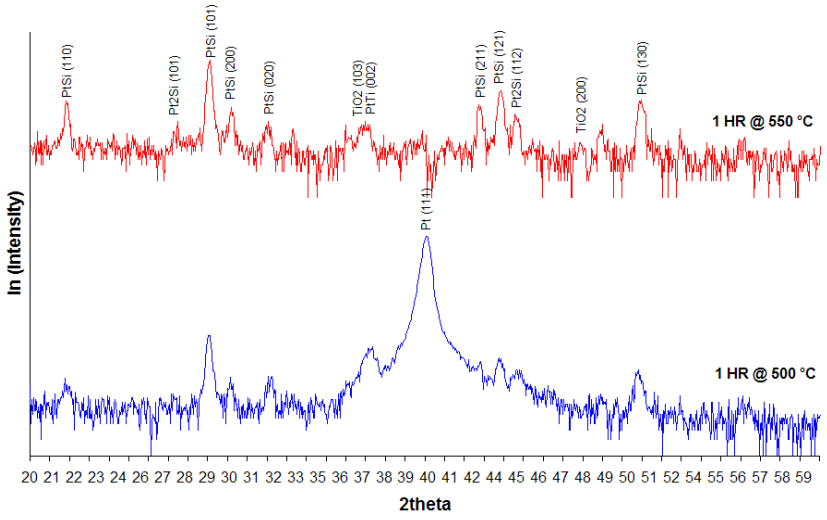

Fig. 3 XRD data for a Ti/Pt/Ti/Si structure indicating the consumption of Pt after annealing for 1 hr at 550 °C.

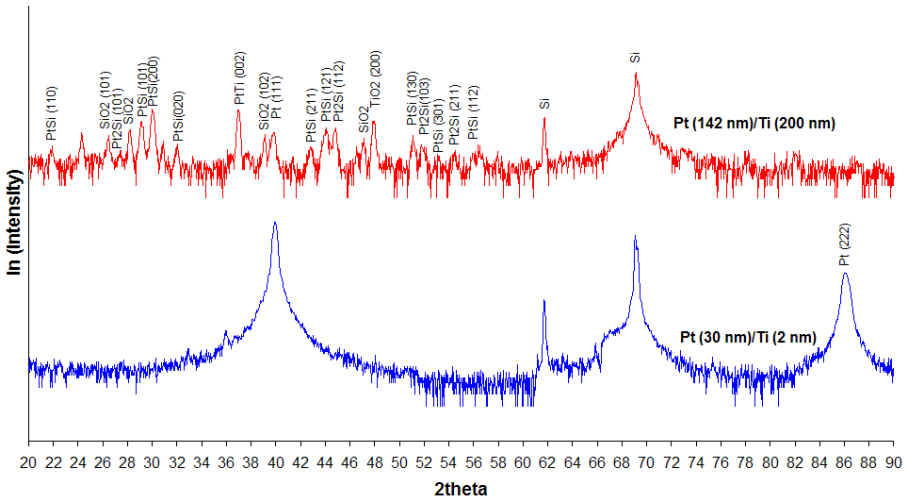

Fig. 4 XRD data for two different Pt/Ti/Si structures annealed under Ar for 30 mins at 700 °C.

nm)/Ti (2 nm)/Si and Ti (50 nm)/Pt (140 nm)/Ti (200 nm)/Si. Both were then annealed in air for 30 minutes at 700 °C. The XRD results of all four annealing experiments are shown in Fig. 5, for comparison. Ti/Pt/Ti/Si structures annealed in air appear to behave like Pt/Ti/Si structures that have been annealed under Ar. In the case of the Ti (50 nm)/Pt (140 nm)/Ti (200 nm)/Si sample it is likely that the Ti overlayer oxidised quickly forming titania. This would act as a barrier preventing O_2 from the atmosphere diffusing towards the underlying Ti adhesion layer. Any O_2 within the Pt layer would also be scavenged by the Ti, helping to sustain the PtSi reaction. We would expect the samples with a 2 nm Ti adhesion layer to behave similarly, regardless of annealing atmoshpere, since the diffusion barrier forms because of the native oxide present on the Si substrate.

4. Conclusions

We have discussed the behaviour of Pt/Ti/Si and Ti/Pt/Ti/Si structures annealed under Ar and air. PtSi formed in Pt/Ti/Si structures that were annealed in air, but the reaction failed to complete due to a combination of O_2 build up at the Pt_2Si reaction front and the oxidation of the Ti adhesion layer. The addition of a 50 nm Ti overlayer, to a fresh Pt/Ti/Si structure, resulted in complete conversion of Pt into PtSi after a series of 1 hr annealings between 400 – 550 °C. This behaviour was explained in Section 3.3. by comparing the results of Pt/Ti/Si and Ti/Pt/Ti/Si structures that had been annealed under Ar and air, respectively. The Ti overlayer was identified as having a role in preventing O_2 from reaching the Ti adhesion layer in the Ti/Pt/Ti/Si structures. Consequently, the diffusion barrier between the Pt and Si that would normally form was suppressed, allowing for almost complete conversion of Pt into PtSi. These results suggest that very thin (< 5 nm) Ti

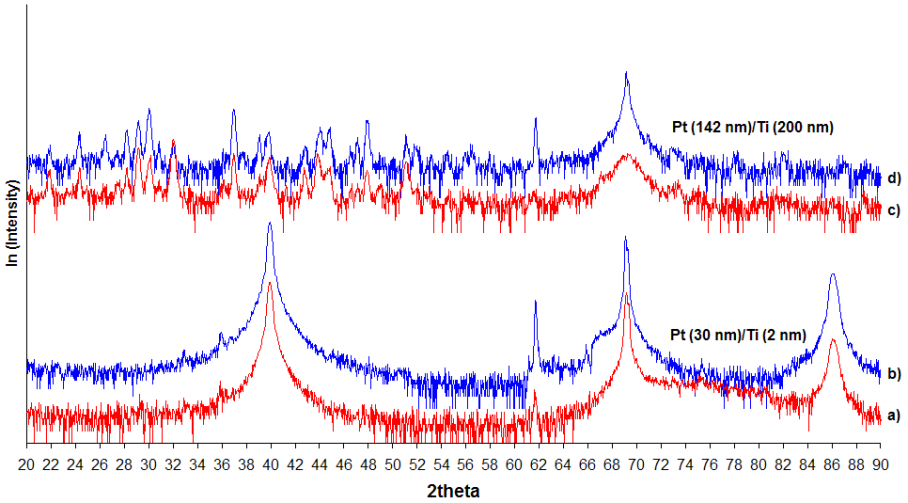

Fig. 5 XRD data for four structures annealed at 700 °C for 30 mins in air [a) Ti (50 nm)/Pt (30 nm)/Ti (2 nm)/Si and c) Ti (50 nm)/Pt (142 nm)/Ti (200 nm)/Si] and under Ar [b) Pt (30 nm)/Ti (2 nm)/Si and d) Pt (142 nm)/Ti (200 nm)/Si].

adhesion layers could be used in situations where it is important to retain the Pt layer – for example, when Pt is used as a bottom electrode.

Acknowledgements

This work was supported by a grant from the Engineering and Physical Sciences Research Council (EPSRC), UK.

References

1 C. C. Liu, D. F. Cui, *Microsyst. Technol.*, 2005, **11**, 1262.

2 Z. H. Zhang, W. G. Zhu, C. Chao, C. L. Zhao, X. F. Chen, *Surf. Coat. Technol.,* 2005, **198**, 384.

3 P. X. Yang, D. L. Carroll, J. Ballato, R. W. Schwartz, *Appl. Phys. Lett.* 2002, **81**, 4583.

4 F. Akasheh, T. Myers, J. D. Fraser, S Bose, A Bandyopadhyay, *Sens Actuators, A*, 2004, **111**, 275.

5 M. Alguero, A. J. Bushby, P. Hvizdos, M. J. Reece, R.W. Whatmore, Q. Zhang, *Integrated Ferroelectrics*, 2001, **41**, 1705

6 Q. Zhang, C. P. Shaw, Z. Huang, R. W. Whatmore, *Integrated Ferroelectrics*, 2004, **64**, 207.

7. Z. Huang, Q. Zhang, R. W. Whatmore, *J. Mater. Sci. Lett.*, 1998, **17**, 1157.

8 J. M. Poate, K. N. Tu, J. W. Mayer, *Thin Films: Interdiffusion and Reactions*, The Electrochemical Society, Princeton NJ, 1978, ch. 1, p. 3.

9 D. L. Smith, *Thin-Film Deposition: Principles & Practice*, McGraw-Hill, Inc. New York, 1995, ch. 5, pp. 144 – 145.

10 C. K. Lee, C. D. Hsieh, B. H. Tseng, *Thin Solid Films*, 1997, **303**, 232.

11 G. Larrieu, E. Dubois, X. Wallart, X. Baie, J. Katcki, *J. Appl. Phys*. 2003, **94**, 7801.

12 C. A. Crider, J. M. Poate, J. E. Rowe, T. T. Sheng, *J. Appl. Phys*. 1981, **52**, 2860.

13 M. J. Rand, J. F. Roberts, *Appl. Phys. Lett.*, 1974, **24**, 49.

14 J. M. Poate, K. N. Tu, J. W. Mayer, *Thin Films: Interdiffusion and Reactions*, The Electrochemical Society, Princeton NJ, 1978, ch. 5, p. 88.

Appendix B: Publications

Conferences

ISIF 2005, Shanghai, China
17th-20th April 2005
Poster presentation: *Characterisation of Nanocrystalline PZT Synthesised via a Hydrothermal Method*

Nanotech 2005, Los Angeles, USA
8th-12th May 2005
Poster presentation: *Characterisation of Nanocrystalline PZT Synthesised via a Hydrothermal Method*
Full paper published in special edition of Integrated Ferroelectrics (see below)

ISIF 2006, Honolulu, Hawaii, USA
23rd-27th April 2006
Oral presentation: *Synthesis and analysis of lead titanate nanoislands*
Full paper published in conference proceedings.

Rank Prize Funds Mini-Symposium on Electro-Optic Nanostructured Arrays 2006, Grasmere, UK
11th-14th September 2006
Oral presentation: *Synthesis and analysis of lead titanate nanoislands*

Papers

S. Harada and S. Dunn, *Synthesis and analysis of lead titanate nanoislands* Integrated Ferroelectrics, 87:1, 67 – 76 (2007)

S. Harada and S. Dunn, *Low temperature hydrothermal routes to various PZT stoichiometries*, Journal of Electroceramics, 20:2, 65 – 71 (2007)

S. Dunn and S. Harada, *Hydrothermal deposition of heteroepitaxial lead-zirconate-titanate nanostructures and thin films*, Journal of the European Ceramics Society (In press)

S. Harada and S. Dunn, *The effect of the Ti overlayer on the formation of platinum silicide in Ti/Pt/Ti/Si structures*, Submitted to Materials Chemistry and Physics